



UNIVERSITY OF
CAMBRIDGE

Structure in the cores of galaxy clusters

Jeremy Stephen Sanders

Pembroke College
Institute of Astronomy

This dissertation is submitted for the degree of Doctor of Philosophy

Contents

Declaration	xi
Summary	xiii
Acknowledgements	xvii
1 Introduction	1
1.1 Clusters of galaxies	1
1.1.1 The intracluster medium	2
1.1.2 Cooling of the ICM	3
1.1.3 Cooling flows	3
1.1.4 Inhomogeneous cooling flow models	4
1.1.5 Lack of low-energy emission lines	6
1.1.6 Evidence for cooling flows outside the X-ray band	7
1.1.7 Cold fronts	10
1.1.8 Metals in the ICM	11
1.1.9 Cluster mass distributions	13
1.1.10 Plasma codes	14
1.2 The <i>Chandra X-Ray Observatory</i>	14
1.2.1 The spacecraft module	17
1.2.2 The HRMA	18
1.2.3 The ISIM	19
1.2.4 The ACIS	19
1.2.5 Spatial resolution	22
1.2.6 Dithering	22
1.2.7 Energy resolution	22
1.3 X-ray data and analysis	23
2 Colour maps of cluster cores	27
2.1 Introduction	28
2.1.1 <i>ROSAT</i>	30
2.2 Observations and colour map analysis	32

2.2.1	Adaptive smoothing	34
2.2.2	Background removal	34
2.3	Results	35
2.4	Colour models	41
2.4.1	Fitting cooling flow models	50
2.4.2	Calculating intrinsic absorption	52
2.4.3	Fitting metallicity gradients	53
2.5	Discussion	55
2.5.1	Adaptively-smoothed images	55
2.5.2	The sample of clusters	55
2.5.3	Comparison with models	55
2.6	Conclusions	56
3	Adaptive binning	59
3.1	Introduction	59
3.1.1	ASMOOTH	60
3.1.2	Wavelet transforms	63
3.1.3	Adaptive binning	64
3.2	Intensity binning	65
3.2.1	Demonstration	66
3.2.2	Real example	67
3.2.3	Notes on the algorithm	70
3.2.4	Simulated cluster	73
3.3	Colour binning	77
3.3.1	Real example	77
3.3.2	Spectral fitting	81
3.4	Non-square bins	81
3.5	Binning by spectral fit	84
3.6	Availability	86
4	The Perseus and Abell 1795 clusters	87
4.1	The Perseus cluster	88
4.1.1	Introduction	88
4.1.2	The <i>Chandra</i> observation	91
4.1.3	X-ray colour analysis	91
4.1.4	Radio image	99
4.1.5	Discussion	99
4.2	Abell 1795	103
4.2.1	Introduction	103
4.2.2	The <i>Chandra</i> observations	104

4.2.3 Comparisons with the optical and radio emission	105
4.2.4 Discussion	112
5 The Centaurus cluster	117
5.1 Introduction	118
5.2 The X-ray image	118
5.3 Spectral fits	122
5.3.1 Spectrum of central 10 arcsec	122
5.3.2 Spectrum of the plume	125
5.4 Imaging analysis	129
5.4.1 Radial profiles	129
5.4.2 East-west anisotropy	133
5.4.3 Fits to adaptively-binned areas	133
5.5 Discussion	139
6 Conclusions	143
6.1 Introduction	143
6.2 Summaries of chapters	144
6.2.1 Colour maps of cluster cores	144
6.2.2 Adaptive binning	144
6.2.3 The Perseus and Abell 1795 clusters	144
6.2.4 The Centaurus cluster	145
6.3 Future work	145
7 References	147

List of Figures

1.1	Centaurus in optical and X-ray	2
1.2	Cold front in A3667	11
1.3	Spectra from different plasma models	15
1.4	Contribution to plasma from different elements	16
1.5	<i>Chandra</i> expanded view	17
1.6	<i>Chandra</i> mirrors and structures	18
1.7	<i>Chandra</i> predicted effective area	19
1.8	The ACIS focal plane	20
1.9	Event grade schematic	22
1.10	ACIS on-axis encircled energy	23
2.1	Simulated plasma spectrum, as absorption is varied	29
2.2	Simulated plasma spectrum, as temperature is varied	29
2.3	Simulated plasma spectrum, as metallicity is varied	30
2.4	Effective area of the <i>ROSAT</i> XMA	31
2.5	Perseus adaptively-smoothed images	38
2.6	Virgo adaptively-smoothed images	39
2.7	A2199 adaptively-smoothed images	40
2.8	Perseus contour colour maps	42
2.9	Virgo contour colour maps	43
2.10	Selection of C/D colour maps	44
2.11	Variation of B/D for sample of clusters	45
2.12	Variation of C/D for sample of clusters	46
2.13	Cooling flow flux against $S(C/D)$	47
2.14	Plot of cooling time against $S(C/D)$	47
2.15	Theoretical isothermal colour predictions	48
2.16	Theoretical cooling flow colour predictions	49
2.17	Cluster temperature profiles	50
2.18	Cluster cooling flow component profiles	53
2.19	Cluster intrinsic absorption profiles	54
3.1	Comparison of fixed binning and smoothing sizes	61

3.2	Adaptively-binned images of the Centaurus cluster	62
3.3	Simple adaptive binning example	66
3.4	Raw image of the Perseus cluster	68
3.5	Adaptively-binned image of the Perseus cluster (error 0.06)	68
3.6	Adaptively-binned image of the Perseus cluster (error 0.04)	69
3.7	Fractional error map of image in Fig. 3.6	69
3.8	Adaptively-smoothed image of the Perseus cluster	70
3.9	Adaptively-binned ACIS-I Perseus image	71
3.10	Simulated cluster images and reconstruction	74
3.11	Fractional differences between reconstructed images and the original	76
3.12	Distribution of fractional differences between pixels and binned images . .	78
3.13	Adaptively-binned colour map of bands 0/1	79
3.14	Adaptively-binned colour map of bands 1/2	80
3.15	4×4 half bins	82
3.16	2×2 half bins	82
3.17	Adaptively-binned images of the simulated cluster using half-bins	83
3.18	Deviation away from the model surface brightness with half-bins	84
3.19	Adaptively-binned images of the Centaurus cluster using half-bins	85
3.20	Adaptively-binned image of the Perseus cluster with half-bins	85
4.1	<i>ROSAT</i> HRI image of the Perseus cluster	89
4.2	H α image of the core of the Perseus cluster	90
4.3	Raw <i>Chandra</i> image of the Perseus cluster	92
4.4	Count profile across the centre of the Perseus cluster	93
4.5	X-ray RGB image of the Perseus cluster	94
4.6	Soft X-ray image and JKT <i>B</i> -band image of NGC 1275	95
4.7	Temperature and column density maps for Perseus	97
4.8	Adaptively-smoothed image of Perseus	98
4.9	Electron density and pressure maps for Perseus	100
4.10	Cooling time map for Perseus	101
4.11	Radio map of Perseus	101
4.12	Soft and hard X-ray images of A1795	106
4.13	A1795 ASMOOTHed filament and H α image	107
4.14	A1795 count rate profiles	108
4.15	A1795 temperature and absorption profiles	109
4.16	A1795 two-dimensional temperature map	110
4.17	A1795 electron density and cooling time maps	111
4.18	A1795 radio map	113
5.1	Colour X-ray image of the Centaurus cluster	119

5.2	Adaptively-smoothed image of the Centaurus cluster	120
5.3	Optical <i>HST</i> image of dust lane	121
5.4	Spectrum of inner 10 arcsec fitted with a MEKAL model	124
5.5	Contributions to χ^2 in the inner 10 arcsec	126
5.6	Spectrum of the plume, fitted with a 2-T APEC model.	127
5.7	Results of radial fits	130
5.8	Cumulative mass deposition profile	132
5.9	East and west profiles	134
5.10	Results of fits to adaptive bins	135
5.11	Radial bin distributions	137
5.12	Regions where a power-law improves the fit	138
5.13	Radial metallicity plot between 3 and 7 keV	140
5.14	Radiative cooling time of the gas	142

List of Tables

1.1	ACIS focal plane temperature variation	24
2.1	Energy bands	28
2.2	Sample of clusters examined	36
2.3	Mean distances of contours	37
2.4	Excess absorptions in clusters	51
5.1	Results of Centaurus spectral fits	128

Declaration

I hereby declare that my dissertation entitled *Structure in the cores of galaxy clusters* is not substantially the same as any that I have submitted for a degree or diploma or other qualification at any other University.

I further state that no part of my dissertation has already been or is being concurrently submitted for any such degree, diploma or other qualification.

This dissertation is the result of my own work and includes nothing which is the outcome of work done in collaboration, unless stated explicitly. Those parts of this dissertation which have been published, or are in press, are listed below.

1. Chapter 2 is based on the paper *X-ray colour maps of the cores of galaxy clusters*, J.S. Sanders, A.C. Fabian & S.W. Allen, 2000, *Monthly Notices of the Royal Astronomical Society*, 318, 733.
2. Chapter 3 is based on the paper *Adaptive binning of X-ray galaxy cluster images*, J.S. Sanders & A.C. Fabian, 2001, *Monthly Notices of the Royal Astronomical Society*, 325, 178.
3. Chapter 4 contains work published in *Chandra imaging of the complex X-ray core of the Perseus cluster*, A.C. Fabian, J.S. Sanders, S. Ettori, G.B. Taylor, S.W. Allen, C.S. Crawford, K. Iwasawa, R.M. Johnstone, P.M. Ogle, 2000, *Monthly Notices of the Royal Astronomical Society*, 318, L65, and *Chandra image of the X-ray core of Abell 1795*, A.C. Fabian, J.S. Sanders, S. Ettori, G.B. Taylor, S.W. Allen, C.S. Crawford, K. Iwasawa, R.M. Johnstone, 2001, *Monthly Notices of the Royal Astronomical Society*, 321, L33.
4. Chapter 5 is based on the paper *Spatially-resolved X-ray spectroscopy of the core of the Centaurus cluster*, J.S. Sanders & A.C. Fabian, 2002, in press, *Monthly Notices of the Royal Astronomical Society* (preprint astro-ph/0109336)¹.

This dissertation contains fewer than 60 000 words.

Jeremy Sanders
Cambridge, UK
18th January, 2002.

¹<http://www.arxiv.org/abs/astro-ph/0109336>

Summary

This dissertation explores the structure in the cores of clusters of galaxies. Galaxy clusters are the largest gravitationally bound objects in the universe, emitting X-ray radiation from a hot ($2 - 10 \times 10^7$ K) intracluster medium (ICM). In the centres of many of these clusters the mean radiative cooling time of the ICM is short ($< 10^{7-8}$ yr), therefore gas is expected to be cooling out of the X-ray band. More gas should then flow in under pressure to replace that which is deposited. Those clusters with evidence for cooling gas (a highly peaked luminosity profile) are known as cooling flow clusters.

I start by summarising the current understanding of the subject, and the observational evidence for it. An analysis of a sample of clusters using *ROSAT* archival data is then made, to look for the spectral evidence of cool gas and absorbing material in their cores, using the method of X-ray colours. Next, I discuss an original method developed to analyse spatial and spectral data from clusters, adaptive binning, which gives similar levels of signal to noise in each spatial bin. Such an algorithm is necessary to interpret the sub-arcsec resolution images of nearby clusters taken by the *Chandra X-Ray Observatory*.

I analyse a *Chandra* observation of the Perseus cluster, making temperature and absorption maps from X-ray colours, and looking at the interaction of the cooling ICM with the central radio source. For the Abell 1795 cluster I make similar maps to examine the structure of a 40 arcsec long filament found in the cluster, and hypothesise on its nature. Finally, I examine a *Chandra* observation of the core of the Centaurus cluster. Using imaging spectroscopy I make radial plots and maps of the temperature, absorption and metallicity distributions of the gas in the cluster. I discuss an unexpected drop in metallicity in the centre of the cluster, and also a plume-like feature found there.

*"The time has come," the Walrus said,
"To talk of many things:
Of shoes—and ships—and sealing-wax—
Of cabbages—and kings—
And why the sea is boiling hot—
And whether pigs have wings."*

—Lewis Carroll, Through the Looking Glass

Acknowledgements

This work would never have been made possible without the help of my supervisor, Andy Fabian. I would also like to thank the members of the X-Ray Group at the Institute of Astronomy, past and present, including Steve Allen, David Ballantyne, Carolin Crawford, Stefano Ettori, Roderick Johnstone, Kazushi Iwasawa, Julia Lee, Andrea Merloni, Raquel Morales, Glenn Morris, Poshak Gandhi, Robert Schmidt, Dave White, Richard Wilman, Kelvin Wu and Andy Young. I would also like to thank Greg Taylor for discussions. I would have never been able to write this dissertation without all the hard work of the *Chandra* team, making it such a superb instrument.

I would like to thank the anonymous referee who made very helpful comments about the paper on which Chapter 2 is based. I am also grateful to the referee Silvano Molendi for his comments about the paper on which Chapter 5 is based.

I am in great debt to those in my year of PhD students at the IoA for making my time here so enjoyable, including David Bacon, Andrew Dean, Andrew Firth, Chris Jordinson, Steve Moody, Celine Peroux, Rob Sharp, Mark Sullivan and Lisa Wright. I really can't mention all those bizarre lunchtimes (but how does one define normality?). Thanks must also go to Phil Kendall (for geek discussion), Colin Frayne (for you-know), Fraser Clarke, Sam Rix, Richard Massey, and Lynnette Dray. I am grateful to Eileen Fenlon for giving me a warm welcome when I first arrived at the department, and to Paul Aslin for being a great administrator. I've probably missed lots of important people, but the Institute of Astronomy is a wonderful place to work. I must also thank Linus Torvalds and Richard Stallman for helping me mess with computers. Douglas Adams superb writing convinced me that astronomy would be fun to work in, and Malcolm Longair's fascinating Christmas Lectures were far too interesting to ignore!

I am deeply grateful for my friends Angela Taylor, Sam Thompson and Amanda George, for putting up with me for several years. I must also mention Andrew Grantham, Becky Taylor, Joy Sarker, Mike Alexander, Emma Gibbins, David Henderson, Miriam Büttner and Daniel Coetzee at Pembroke College (unfortunately I can't name all the graduates there). Finally (and *definitely* not least), I must thank my family and Siggy for support.

Enjoy! :-)

1

Introduction

Summary

This chapter introduces some of the topics discussed in this dissertation. The first part of the chapter is an introduction to the subject of clusters of galaxies, in particular cooling flows. I then discuss recent X-ray observations of clusters, including cold fronts and the lack of low energy emission lines. The second part is a brief introduction to the *Chandra X-Ray Observatory*. Finally, I discuss the analysis of X-ray spectral data.

1.1 Clusters of galaxies

Clusters of galaxies are the largest gravitationally bound objects in the universe, with masses of around $10^{15} M_{\odot}$. About 5 per cent of galaxies are concentrated into clusters and groups with a density of greater than one galaxy per megaparsec (Dressler 1984). Clusters typically contain several hundred galaxies within a radius of 1 to 2 Mpc.¹ Galaxies in clusters are more likely to be of the so-called early type, i.e. elliptical or S0 galaxies, than later-type galaxies such as spirals or irregulars. Rich clusters often contain a single central dominant galaxy (Matthews et al. 1964), typically a giant elliptical or S0 with a dark-matter halo, known as a cD galaxy. Such galaxies are normally at rest in the bottom of the potential well of a cluster (Oegerle & Hill 1994) and are at the peak of the cluster X-ray emission (Jones et al. 1979).

¹A cosmology of $H_0 = 50 \text{ km s}^{-1} \text{ Mpc}^{-1}$, $\Lambda = 0$ and $\Omega = 1$ is assumed throughout this dissertation, unless stated otherwise.

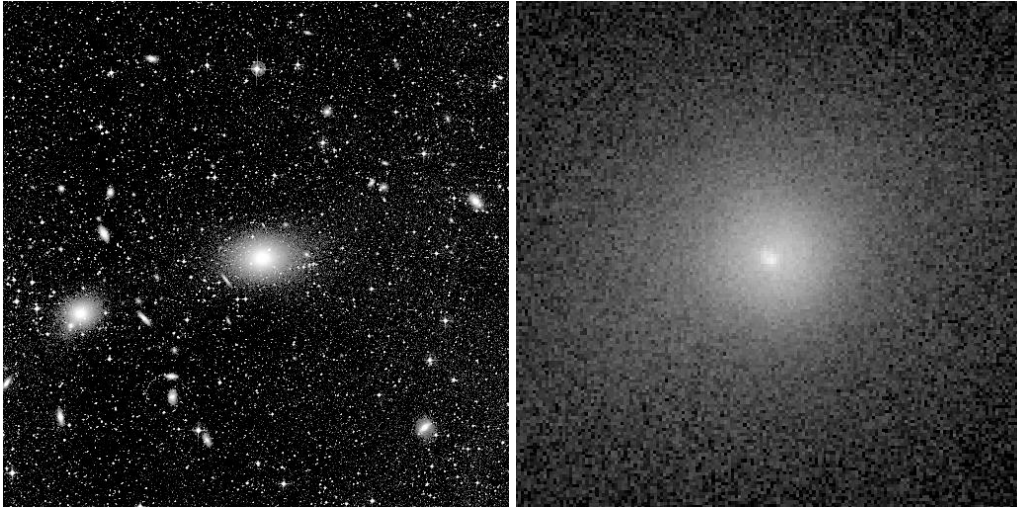


Figure 1.1: The appearance of the Centaurus cluster in the optical and X-ray bands. The image measures roughly 0.8 Mpc across (40 arcmin). The left image is an optical Digitised Sky Survey image. The right image is a *ROSAT* PSPC image. Images were taken from <http://www.astr.ua.edu/white/mug/cluster/clusters.html> of R. E. White III.

Historically, clusters were first catalogued in the optical waveband, by looking for overdensities in the galaxy number density, firstly by Abell (1958), and later by Zwicky et al. (1961). The optical emission from a galaxy cluster is mainly from the stars in the individual galaxies in the cluster.

1.1.1 The intracluster medium

The bulk of the baryonic matter in clusters consists of X-ray emitting plasma virialised at temperatures of tens of million Kelvin, known as the Intracluster Medium (ICM). The majority of X-ray emission from a cluster is from the ICM, and typical X-ray cluster luminosities range from 10^{42} to above $10^{45} \text{ erg s}^{-1}$ (Forman & Jones 1982). For a general review of X-ray emission from clusters of galaxies, see Sarazin (1998). Fig. 1.1 shows the appearance of the Centaurus cluster of galaxies in optical and X-ray wavebands. The images show that the X-ray emission (and so the ICM) is much more smoothly distributed than the optical emission. The ICM typically has densities of 10^{-4} to 10^{-2} cm^{-3} and temperatures of $2 - 10 \times 10^7 \text{ K}$. The total mass of gas in the ICM is of the order $\sim 10^{14} \text{ M}_\odot$.

Historically, X-rays were first detected from an extragalactic object when they were observed by a rocket experiment, emitted from the direction of M87 (Byram et al. 1966; Bradt et al. 1967). M87 is a galaxy lying in the centre of the Virgo cluster, which is our nearest rich cluster. Cavaliere et al. (1971) first claimed there to be X-ray emission from clusters of galaxies in general, after the detection of X-ray sources in the Coma cluster and the Perseus cluster (e.g. Fritz et al. 1971; Gursky et al. 1971). More detailed observations showed that the sources were extended (Forman et al. 1972), and had a

spectrum consistent with bremsstrahlung emission. An iron line was later detected in the X-ray radiation from the Perseus cluster (Mitchell et al. 1976).

1.1.2 Cooling of the ICM

The ICM in a cluster is likely to have been formed by the accumulation of gas when the cluster was built up from the hierarchical merger of smaller units of matter, such as groups, which themselves collapsed in areas of the universe which had an overdensity compared to the average. After a merger, the new gas reaches the virial temperature of the cluster. The ICM is a hydrostatic self supported atmosphere, and in order to support itself the sound speed of the gas must be close to the velocity dispersion of the cluster (typically 300 to 1200 km s⁻¹; Fabian 1994), so

$$\frac{k_B T}{\mu m} \sim \sigma_r^2, \quad (1.1)$$

where T is the temperature of the gas, μm is the average molecular mass, and σ_r is the line-of-sight velocity dispersion of the galaxies (Sarazin 1998).

The hot gas emits mainly in the X-ray waveband given its temperature. As it emits radiation it is continually cooling. The main processes for emission are thermal bremsstrahlung (free-free) and line emission. Bremsstrahlung radiation occurs by the interaction of an electron with a proton (or nucleus), and line emission occurs by the interaction of an electron and ion. Since bremsstrahlung is a 2-body process, the emissivity (power output per unit volume) is proportional to the electron density times the ion density. I discuss more detailed models for the emission from a plasma in Section 1.1.10.

The gas in the centre of the cluster is the densest, and so this gas cools more quickly than less dense regions. To support the hydrostatic atmosphere, the density of the cooling gas rises as its temperature decreases. The overlying gas must flow subsonically inwards to conserve volume if there is cooling. This is what is known as a *cooling flow* (see Fabian 1994 for a review).

1.1.3 Cooling flows

For X-ray emitting gas, the radiative cooling time is the time which gas takes to cool by the emission of X-ray radiation. Assuming isobaric cooling and bremsstrahlung emission, the cooling time of X-ray emitting gas is related to the initial temperature, T , and the density, n , by $t_{\text{cool}} \propto T^{1/2} n^{-1}$ (Sarazin 1998). A cooling flow is formed when t_{cool} is less than the age of the cluster, or the time since the cooling flow was disrupted by a major merger. For relaxed clusters (those which are fully virialised) this has often assumed to be $\sim H_0^{-1}$. Assuming spherical symmetry, the radius at which t_{cool} is less than the age of the cluster is defined as the cooling radius, r_{cool} .

So a cooling flow occurs when

$$t_{\text{grav}} < t_{\text{cool}} < t_{\text{age}}, \quad (1.2)$$

where t_{grav} is the gravitational free-fall time. The gravitational free-fall time is less than the cooling time in galaxy clusters. Radiative cooling dominates when condition (1.2) holds.

The rate of mass cooling out of the cooling flow is known as the mass deposition rate, \dot{M} . The mass deposition rate inside r_{cool} can be estimated from the surface brightness profile, $L(r)$. If condition (1.2) holds, the mass deposition rate is related to the luminosity, L_{cool} , of the cooling region (within a radius of r_{cool}) by

$$L_{\text{cool}} \approx \frac{5}{2} \frac{k_B T}{\mu m} \dot{M}, \quad (1.3)$$

where T is the temperature of the gas at r_{cool} and μm is the mean mass of the gas particles. The factor of 5/2 represents the enthalpy of the gas (the sum of the radiated internal energy of the gas, and the PdV of work done on the gas entering r_{cool}). For a cluster with a cooling flow, L_{cool} is typically 10 per cent of the total X-ray luminosity of the cluster. The estimate for the cooling luminosity in (1.3) does not include a contribution for the gravitational energy of the gas as it flows through the cooling radius, and relies on assumptions about the age of the cooling flow to find the cooling radius. Typical values of the mass deposition rate in clusters range from tens to hundreds of solar masses per year (e.g. Peres et al. 1998).

The first cooling flow models (Cowie & Binney 1977; Fabian & Nulsen 1977; Mathews & Bregman 1978) were invoked to explain the enhanced soft X-ray emission observed in the cores of the Perseus cluster (Fabian & Nulsen 1977) and the Virgo cluster (Mathews & Bregman 1978).

1.1.4 Inhomogeneous cooling flow models

The simple model above assumes that the gas is homogeneous, with a single temperature and density at each radius. However, when (1.3) was applied to images of the Perseus cluster from the *Einstein Observatory* (Fabian et al. 1984) and other clusters (Stewart et al. 1984b,a) at each radius, the mass deposition rate was found to vary (assuming no balancing heat source) as

$$\dot{M}(r) \propto r. \quad (1.4)$$

If this is true, then the gas in the flow is multiphase (Nulsen 1986; Thomas et al. 1987). At each radius, there is gas at more than one temperature and density.

The luminosity profile can be modelled by building up the cluster from a set of shells, each of which has a number of homogeneous phases. The shells allow the effects of pro-

jection to be taken into account. Assuming the gas in each shell is at constant pressure, the flow is modelled as successive cycles of constant pressure followed by adiabatic cooling as the gas moves from one shell to the next (Thomas et al. 1987). The model is calculated from the centre of the cluster, adding a new phase which cools out of the flow in each shell.

An alternative way to fit the data is spectrally with a cooling flow spectral model (Johnstone et al. 1992). The spectrum of the cooling gas should consist of the sum of the spectra of the phases below an upper temperature, T_{\max} . The spectra are normalised according to how long the gas stays at particular temperatures, which depends on the cooling function of the gas.

If a volume dV of gas is cooling isobarically from temperature T to $T - dT$, its luminosity is

$$dL_{\text{cool}} = n_e n_H \Lambda(T) dV = \frac{5}{2} \frac{\dot{M}}{\mu m} k_B dT, \quad (1.5)$$

a similar expression to (1.3), where n_e and n_H are the electron and proton densities, and $\Lambda(T)$ is the cooling function at temperature T . If ε_ν is the emissivity at a frequency ν , then the luminosity of the spectrum at each frequency is

$$dL_{\text{cool}}(\nu) = n_e n_H \varepsilon_\nu dV. \quad (1.6)$$

Combining (1.5) and (1.6), and integrating, we find

$$L_{\text{cool}}(\nu) = \frac{5k_B}{2\mu m} \dot{M} \int_0^{T_{\max}} \frac{\varepsilon_\nu}{\Lambda(T)} dT. \quad (1.7)$$

The spectrum of the cooling flow is therefore simply the sum of the emissivities at each temperature, weighted by the inverse of the cooling function at that temperature, and normalised by the overall mass deposition rate. The free parameters to the model are the mass deposition rate, \dot{M} , the upper temperature of the cooling gas, T_{\max} , and the metallicity of the gas which affects the cooling function $\Lambda(T)$.

An integrated spectrum of the cluster does not contain the spatial information about the cooling gas. This means a fit to this spectrum will give an upper limit to the mass deposition rate, as the model is not sensitive to the density of the cooling gas. The spectra of many clusters (taken by instruments predating *Chandra* and *XMM-Newton*) are well fit with a cooling flow spectral model (e.g. Allen & Fabian 1997; White 2000; Allen et al. 2001) if excess absorption is added.

In addition to the observed luminosity profiles and spectral signatures, clusters with cooling flows also show temperatures decreasing towards their centres, as expected from cooling flow models (e.g. Schwarz et al. 1992; Allen et al. 1993). Excess X-ray absorption has also been observed in cooling flow clusters (e.g. White et al. 1991b; Allen & Fabian 1997), but not in clusters without cooling flows. It was found that the quantity of inferred

absorbing matter observed in A478 is in good agreement with the amount a cooling flow could deposit over the lifetime of the cluster (Allen et al. 1993, 2001).

1.1.5 Lack of low-energy emission lines

Recent observations of cooling flow clusters using the RGS on *XMM-Newton* have shown that there is a lack of emission in low energy emission lines compared to what is expected from a cooling flow model (e.g. Peterson et al. 2001; Tamura et al. 2001). In order to explain these results, the gas must ‘disappear’ as it cools below 1 keV or there must be a mechanism to allow the gas to cool without emitting these lines.

The *XMM-Newton* X-ray observatory contains two Reflection Grating Spectrometers (the RGS) for medium-high ($E/\delta E = 100 - 200$) resolution X-ray spectroscopy (den Herder et al. 2001). This instrument has enabled individual X-ray spectral lines to be identified from cooling flows. It was found that standard cooling flow clusters lacked the characteristic emission lines of cool X-ray emitting gas, such as Fe XVII and Fe XX (e.g. Peterson et al. 2001, A1835; Tamura et al. 2001, A1795). The observations show there is gas cooling about 2 keV, but there is no spectral signature of gas cooling below these temperatures.

These results present some problems for standard cooling flow models. Tamura et al. (2001) found by fitting two temperature components to the RGS spectrum (inside a radius of 30-60 arcsec), that the emission measure of the cool temperature component in A1795 is less than 10 per cent of the hot component, when the cooler component is set to below 1 keV in the model. Using a cooling flow model for the low temperature component limits the mass deposition rate to $\sim 140 M_{\odot} \text{ yr}^{-1}$, smaller than the values of $\sim 250 M_{\odot} \text{ yr}^{-1}$ found by Allen et al. (2001) using *ASCA*. \dot{M} is strongly constrained by the lack of Fe XVII emission lines. A model which fits the data well is a cooling flow model in which the gas cools from an upper temperature to a minimum temperature of 1-2 keV, however the gas must ‘disappear’ at this point which appears rather unphysical.

Possible explanations for the observations are discussed by Fabian et al. (2001b). A heat source is not realistic, as the gas heated from 3 keV should be visible but it just appears to vanish. The heating would need to be targeted towards the cooler gas, and the mechanism would have to maintain the distribution of gas at higher X-ray temperatures to mirror that expected from cooling gas. It is difficult to see how sporadic heating could solve the problem, as the gas takes much longer to cool from several keV to 2 keV (which there is evidence for), than it does to cool from 2 keV out of the X-ray band.

A further possibility for the lack of emission lines is that cool gas at 10^4 K could mix with the cooling X-ray gas at 10^7 K, effectively making it invisible. The final temperature of the mixed gas will be approximately $\sqrt{T_{\text{hot}} T_{\text{cold}}}$ (Begelman & Fabian 1990). Gas at 3×10^7 K mixing with gas at 3×10^3 K produces gas at roughly 3×10^5 K. This theory might be testable by UV observations. If the UV is then reprocessed, then this could

explain the optical emission line results mentioned in Section 1.1.6, something which is possible energetically.

A third explanation is that absorption causes the lack of low energy emission lines. If the cooler gas occupied the same region as absorbing material (which itself could have been deposited by the cooling flow), then the low energy lines could be removed without changing the emission from the high temperature gas. Resonant scattering, a process by which certain emission lines can be scattered out of the line of sight, could also be important. Lines missing in the RGS spectra are weakened in solar spectra by resonant scattering processes (Rugge & McKenzie 1985).

Fabian et al. (2001b) also discuss a new hypothesis. If most of the metals in the gas are concentrated into metal-rich clumps occupying a small volume, then the emission of the cooling gas will be quite different from a homogeneous gas. If 10 per cent of the gas has twice solar abundance and 90 per cent has zero metallicity, then the spectrum of the gas will appear to be from gas of $0.2 Z_{\odot}$. At high temperatures the gas will cool by bremsstrahlung emission, but as the temperature decreases line cooling will become more important, and even more so for the higher metallicity clumps (Böhringer & Hensler 1989). Therefore most of the line emission would come from the high metallicity clumps. High metallicity clumps would only contain a small fraction of the internal energy of the total gas, and so the emission lines would be smaller than expected for an evenly mixed ICM.

1.1.6 Evidence for cooling flows outside the X-ray band

If the gas in the cooling flow continues to cool then we should observe it at longer wavelengths. However, over 90 per cent of the thermal energy of the cooling gas is radiated in the X-ray waveband. When the gas has finally cooled, then it would be expected to form stars unless there is some mechanism to stop star formation.

Optical observations

The evidence for cooling flows is indirect in the optical waveband. The cooling gas is spread out over too large an area to be detectable directly (Fabian 1994). The central regions of cooling flows however do show optical-line nebulosity. Filaments were seen around NGC 1275 in the Perseus cluster (Kent & Sargent 1979; also see Section 4.1.1), around M87 in the Virgo cluster (Ford & Butcher 1979), and in A496 (Fabian et al. 1981b). Line emission has also been observed in many clusters (e.g. Heckman 1981; Crawford et al. 1995, Crawford et al. 1999). The filaments in some cases extend over regions of 10-50 kpc and can emit $10^{43} \text{ erg s}^{-1}$ in H α radiation.

The amount of material emitting optically by line emission is a small fraction of the quantity of matter seen in X-ray absorption and is concentrated into a smaller region (Heckman et al. 1989). Not all clusters with cooling flows show optical emission lines.

70-90 per cent of the clusters examined by Edge et al. (1992) were found to have evidence for the existence of a cooling flow, but only ~ 40 per cent showed the presence of optical emission lines. This was also found to be true at higher redshifts (Allen et al. 1992; Crawford et al. 1995).

Blue continuum emission is also seen in several large clusters with cooling flows. The emission is extended over a few kpc in the central cD, but is much brighter than expected from galaxies of that type. Blue continuum emission is often a signature of star formation, as it is emitted from high mass stars which have a limited lifetime. Indeed, Rubin et al. (1977) found strong Balmer line absorption from NGC 1275 in the Perseus cluster which indicates the presence of A or late B stars. However, the blue light could be scattered light from a central active galactic nucleus, scattered by dust or electrons towards us. McNamara & O'Connell (1993) discovered a correlation in the position of emission of blue light and the radio axes of A1795 and A2597. However, the continuum emission is better described by star formation rather than by a power-law process, and there are probably very large numbers of O stars present in the most massive systems (Allen 1995). Carlson et al. (1998) found using *HST* imaging that there are a number of very blue stellar clusters in NGC 1275.

Ultraviolet observations

Evidence for star formation has also been found at UV wavelengths (where the direct emission from young stars is most visible), in A1795 by Smith et al. (1997), and more recently by Mittaz et al. (2001) using the optical monitor on *XMM-Newton*. In general, however, the estimated levels of star formation found do not correspond to the mass deposition rate of the cooling flow. A possible explanation is that the initial mass function (IMF), the distribution of stellar masses produced by star formation, may be biased in cooling flows towards the formation of low mass stars, which are difficult to observe, especially in the UV (Fabian et al. 1982).

A very interesting recent result was the recent detection of UV emission lines from cooling gas in the A1795 and A2597 clusters (Oegerle et al. 2001). As the gas cools from X-ray temperatures ($\sim 10^7$ K) through 3×10^5 K it should emit strongly in the O VI $\lambda\lambda 1032, 1038$ resonance lines. O VI $\lambda 1032$ was detected from A2597 (indicating a mass deposition rate of $\sim 40 M_\odot \text{ yr}^{-1}$), and C III $\lambda 977$ was detected from both of the clusters. These observations provide direct evidence of gas with temperatures between that of the X-ray gas and the gas in the optical emission line filaments.

Infrared observations

Observations by *IRAS* detected emission of infrared radiation from several sources coincident with cooling flows in clusters. For example, Bregman et al. (1990) found that 30 per cent of their sample of central cluster galaxies were detected at $12/25 \mu\text{m}$, whilst

46 per cent were detected at 60/100 μm . The ratio of infrared to optical emission is an order of magnitude greater than for elliptical and S0 galaxies. Others have also observed infrared emission from the regions of cooling flows (e.g. de Jong et al. 1990; Grabelsky & Ulmer 1990, Allen et al. 2001). The source of the radiation is probably emission from dust, however the nature of the energy source for this radiation is still controversial (e.g. Edge et al. 1999). If cooling flows are leading to star formation, then the dust-enshrouded stars which are forming are expected to emit in the infrared and sub-mm.

Wilman et al. (2000) found using infrared spectroscopy that there are at least $2.3 \times 10^8 M_\odot$ of H₂ gas within 5 kpc of the nucleus of the Cygnus-A cluster. If this material were deposited over 10^9 yr, then that would require a $10 M_\odot \text{ yr}^{-1}$ mass deposition rate within that radius. Recently, molecular gas has also been detected in sixteen clusters with powerful cooling flows (Edge 2001). The detection of CO transitions indicates levels of $10^{9-11.5} M_\odot$ of warm molecular gas within 50 kpc radius of the central galaxy. Interestingly, CO emissions were not detected from clusters with powerful radio sources.

Radio observations

Many galaxies with cooling flows also contain a strong radio source (e.g. Bijleveld & Valentijn 1983; Ball et al. 1993). The lobes of radio sources have been found to displace the X-ray emitting gas in many clusters, as exemplified by NGC 1275 (Böhringer et al. 1993). I discuss this further for the Perseus cluster in Section 4.1.1. In M87 (Böhringer et al. 1995) the situation is different: the X-ray emission shows some correlation with the radio emission. However, the spectrum of the X-ray emission rules out inverse-Compton emission. In the case of this cluster there is evidence for the radio lobes being buoyant blobs of radio plasma which have brought up cool X-ray emitting gas from the core of the cluster (e.g. Churazov et al. 2001).

For there to be a cooling flow, then there cannot be significant classical (known as Spitzer; Spitzer 1956) heat conduction in the X-ray gas. Evidence for the suppression of conduction is also indicated by the existence of cold fronts (see Section 1.1.7). To suppress thermal conduction, tangled magnetic fields are often invoked to reduce the thermal conduction (e.g. Chandran & Cowley 1998), however some authors claim that this is not a realistic effect (e.g. Pistinner & Shaviv 1996). The magnetic field in a cluster can be estimated by examining the polarisation of the radio emission. If polarised electromagnetic radiation passes through an ionised medium, the rate of change of the plane on the polarisation is (e.g. Dreher et al. 1987)

$$\frac{d\chi}{ds} = 0.81 \lambda^2 n_e B_{\parallel}, \quad (1.8)$$

where χ is the position angle in radians of the electric field of the radiation, B_{\parallel} is the component of the magnetic field along the line of sight in μG , λ is the wavelength of

the radiation in m, n_e is the electron density in cm^{-3} , and s is the path length in parsec. If the radiation source is behind the plasma, the rotation measure (RM) is defined by $\chi(\lambda) = \chi_0 + \text{RM } \lambda^2$, so

$$\text{RM} = 0.81 \int n_e B_{\parallel} \, ds. \quad (1.9)$$

Observations of the rotation measure and depolarisation of many radio sources in the centres of cooling flows (e.g. Dreher et al. 1987; Ge & Owen 1993) show that the magnetic field and pressure increase towards the centre of the cluster. Assuming equipartition, the pressures obtained agree with those derived from X-ray observations. An alternative mechanism to lower the thermal conduction in a cluster could be electromagnetic instabilities driven by the the temperature gradient (e.g. Pistinner et al. 1996).

Diffuse radio emission is also seen in some clusters. If the emission is located in the centre, it is known as a radio halo, otherwise it is called a radio relic (see Buote 2001 and references within). Radio halos have synchrotron spectra, and are only associated with clusters in a state of merger. Roughly 10 per cent of clusters have a radio halo. The shape of a radio halo is well correlated with X-ray emission (Govoni et al. 2001). There is also a correlation with the radio power of the halo at 1.4 Ghz and the X-ray temperature of the gas (Colafrancesco 1999). See Buote (2001) for further discussion.

1.1.7 Cold fronts

Recent observations by *Chandra* with its unsurpassed spatial resolution in the X-ray band, have revealed that many clusters contain sharp discontinuities in their surface brightness profiles, a feature which has been named ‘cold fronts’, and first discovered in the cluster A2142 (Markevitch et al. 2000). A cold front is distinguished by a sharp drop outwardly in surface brightness and gas density, and a sharp rise in temperature. The pressure of the gas is continuous over the front. Cold fronts are not shocks, as the denser side of the edge has a lower temperature.

A possible explanation for a cold front, given by Markevitch et al. (2000), is that the inner region is a dense body of gas which is a surviving core from a merged subcluster, and is being stripped by a less dense surrounding gas. The edge is where the dense core is in pressure equilibrium with surrounding gas. Any gas in the core at lower pressure would have been stripped off as a tail on the subcluster. A cooler dense core surviving during a merger was discussed by Fabian & Daines (1991) who concluded that a dense core was not necessarily shock heated during a merger.

Other clusters containing cold fronts include A3667 (Vikhlinin et al. 2001b; see Fig. 1.2), RX J1720.1+2638 (Mazzotta et al. 2001b), MS 1455.0+2232 (Mazzotta et al. 2001a) and A1795 (Markevitch et al. 2001). However, some of these systems are not merging and are apparently relaxed, containing cooling flows. If cold fronts are the results of mergers then they must be long lived phenomena.

An interesting feature of cold fronts is that the width of the discontinuity is smaller

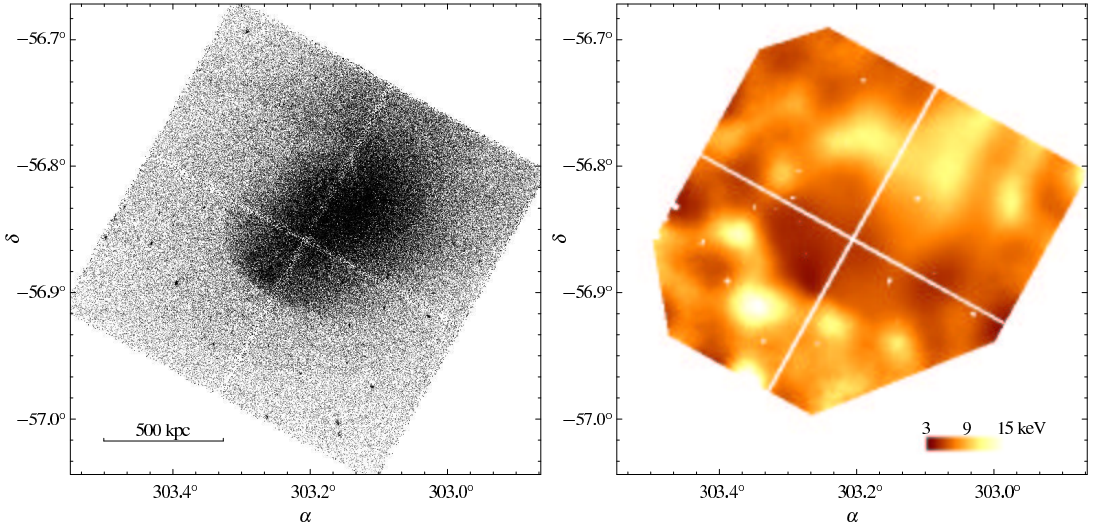


Figure 1.2: Cold front in A3667. Left panel shows the raw *Chandra* X-ray image in the 0.5-4 keV band. The right panel shows a temperature map. Taken from Vikhlinin et al. (2001b).

than the Coulomb mean free path. This means that thermal conduction is suppressed (Ettori & Fabian 2000; Vikhlinin et al. 2001b). Ettori & Fabian (2000) claim thermal conduction is suppressed by at least a factor of between 250 and 2500. They also speculate that cooler gas dumped in a cluster core by a merger would be part of a different magnetic structure, and would be thermally isolated.

More evidence for the suppression of thermal conduction in clusters can be seen in the non-cooling-flow Coma cluster (Vikhlinin et al. 2001a). Both of the dominant galaxies in the cluster retain $\sim 10^8 M_{\odot}$ of central cool interstellar gas at temperatures of 1-2 keV, in an intracluster gas at ~ 9 keV. This indicates conduction is suppressed by factors of 30-100.

1.1.8 Metals in the ICM

The ICM is enriched by metals. The X-ray spectra of rich clusters contains strong emission from the iron K-shell lines. In low redshift clusters the iron abundance is roughly 1/3 solar (Edge & Stewart 1991). ASCA observations found that the relative abundances of different elements are consistent with enrichment by Type II supernovae (Mushotzky et al. 1996). This corresponds well with the earlier observation that the mass of iron in a cluster is well correlated with the total optical emission from elliptical and lenticular galaxies (Arnaud et al. 1992). The mass of material in the ICM exceeds that in cluster galaxies by a factor of 2-5 (Arnaud et al. 1992; David et al. 1995; White & Fabian 1995), indicating there must be an efficient process by which to enrich the ICM. There appears to be little evolution in the iron abundance in clusters between the present epoch and a redshift of 0.3 (Mushotzky & Loewenstein 1997). If that is the case, most of the metal production and intracluster enrichment must have occurred at high redshifts.

More recently, however, *ASCA* results have shown there is significant SN Ia contamination in the cores of some clusters, including the Perseus cluster, the Virgo cluster and A496 (e.g. Dupke & White 2000; Dupke & Arnaud 2001; Allen et al. 2001). Typically 70 per cent of the iron enrichment in the core of these clusters is due to Type Ia supernovae. Dupke & White (2000) hypothesise that the Type Ia enrichment is caused by a metal-rich wind from the cD galaxy, and that the Type II enrichment was caused by a more energetic protogalactic wind.

When fitting the spectrum of a plasma, it is common to assume that the metals are in the same proportion as those measured in the Sun (even though they may be more similar to those in Type II or Type Ia supernova ejecta). The most commonly used tables of relative abundances used in X-ray astronomy are those of Anders & Grevesse (1989), which I use consistently throughout this dissertation.

Metals in clusters with cooling flows

Clusters with cooling flows have higher *emission-weighted* metal abundances than those without, by a factor of roughly 1.8 (Allen & Fabian 1998). Abundance gradients in cooling flow clusters are also common (e.g. De Grandi & Molendi 2001; Fukazawa et al. 1994; Matsumoto et al. 1996), and clusters without cooling flows do not show strong abundance gradients (e.g. Tamura et al. 1996). Cooling flow clusters are observed to have high metallicities in the centre, and lower metallicities in the outer regions. Clusters with cooling flows have bright cores, so an explanation for their higher average metallicities is that the metallicity we observe is emission weighted to the central region (Allen & Fabian 1998). In addition, if they undergo a merger which destroys the cooling flow, the high abundance gas in the core will get mixed with the gas in the outer regions, destroying the metallicity gradient.

There are several possible mechanisms to create abundance gradients in clusters. The centre of the cluster is in the deepest part of the potential well, so stars could have been forming there for the longest time, and so they would have generated more metals, which could enhance the formation of massive stars, and would retain the metals there (Allen & Fabian 1998). Star formation is also associated with the cores of cooling flows, leading to greater metal production than the outer regions. Other models include the cooling flow concentrating metals from Type Ia supernovae in the outer part of the cD galaxy (Reisenegger et al. 1996), although this may only work in low-luminosity clusters. Another possibility is that the metals are stored in large grains with a long lifetime (Allen & Fabian 1998). In a cooling flow the high density means that the grains are increasingly sputtered, which releases metals into the gas in the centre.

1.1.9 Cluster mass distributions

The visible mass in clusters is a small fraction of the mass required for them to be gravitationally bound (Zwicky 1933). The accepted explanation for this observation is the presence of dark matter in galaxy clusters (see Trimble 1987 for a review).

To model the gas distribution in clusters the equation of hydrostatic equilibrium is often assumed. In order for this to be correct the timescale of collisions within the gas must be much smaller than the timescale for any cooling or dynamical processes, there must also be no large flows in the cluster. If there is hydrostatic equilibrium, then

$$-\frac{d\phi}{dr} = \frac{1}{\rho_{\text{gas}}} \frac{dP_{\text{gas}}}{dr} = -\frac{GM(r)}{r^2}, \quad (1.10)$$

where ρ_{gas} is density of the gas at the radius, P_{gas} is the pressure, ϕ is the gravitational potential, and $M(r)$ is the total mass within radius r . The pressure and density of the gas are related by the ideal gas law (assuming that the only contribution to the pressure is thermal):

$$P_{\text{gas}} = \frac{\rho_{\text{gas}} k_B T_{\text{gas}}}{\mu m}. \quad (1.11)$$

Therefore by measuring the temperature of the gas as a function of radius and measuring its density from the surface brightness profile, it is possible to generate a mass profile (see Sarazin 1998). To account for projection effects one must deproject the data (Fabian et al. 1981a).

The cluster potential is often approximated to be that of a hydrostatic isothermal sphere (dominated by the mass of the dark matter). An approximation to this potential is the King model (King 1962). If the potential is given by the King model and the gas and galaxies are in hydrostatic equilibrium, then (Sarazin 1998)

$$\rho_{\text{gas}} = \rho_{\text{gas},0} \left[1 + \left(\frac{r}{r_c} \right)^2 \right]^{-3\beta/2}, \quad (1.12)$$

where $\beta = \mu m \sigma_r^2 / (k_B T)$, where σ_r is the velocity dispersion of the galaxies in the cluster, and r_c is the core radius of the King model. The King model has a flat density profile inside r_c .

Cosmological N-body simulations (e.g. Navarro et al. 1995) have shown that the dark matter potential is better described by a profile steeper than an isothermal one. The potential (known as the NFW potential) has the following form:

$$\rho_{\text{NFW}} = \frac{\rho_s}{x(1+x)^2}, \quad (1.13)$$

where $x = r/r_s$, ρ_s is the scale (dark matter) density, and r_s is the scale radius. Using this

result with the hydrostatic equation (1.10) the gas density follows (Ettori & Fabian 1999)

$$\rho_{\text{gas}} = \rho_0 (1 + x)^{\eta/x}, \quad (1.14)$$

where $\eta = 4\pi G \rho_s r_s^2 \mu m / (k T_{\text{gas}})$.

The original method of calculating the mass profile of a cluster was by measuring the line-of-sight velocities of the galaxies in the cluster and using a dynamical model. Unfortunately such studies are difficult.

Gravitational lensing is another independent method for mass determination (see Mellier 1999 for a review). A combined analysis of the X-ray and lensing data can provide better determination of the dark matter profile (Allen 1998).

1.1.10 Plasma codes

For an optically thin thermal X-ray plasma with a single phase (the same density, temperature and metallicity at all points), the emission is the sum of bremsstrahlung and more complex processes such as line emission. Theoretical models of the emission have been developed, including the Raymond-Smith model (Raymond & Smith 1977), the MEKAL model (Mewe et al. 1985, 1986; Liedahl et al. 1995), and more recently the APEC model (Brickhouse et al. 2000). The MEKAL model is the most commonly in use today. Fig. 1.3 shows the spectra predicted by the three different plasma codes, absorbed by 10^{20} cm^{-2} (using the PHABS model; Balucinska-Church & McCammon 1992) to represent some galactic absorption. The contribution to the emission from different elements in the plasma are shown in Fig. 1.4 for a solar metallicity 1 keV plasma. Iron, by far, provides the largest line-contribution to the total spectrum. At higher temperatures, there is less contribution to the emission by line emission, as there are fewer likely transitions. Spectra of a gas with varying temperature, abundance and absorption are shown in Section 2.1.

1.2 The *Chandra* X-Ray Observatory

The *Chandra* X-Ray Observatory (Weisskopf et al. 2000; Chandra X-ray Center 2000) is one of NASA's Great Observatories. It has an X-ray telescope capable of spatial resolutions of $\leq 1/2$ arcsec, and includes instruments for high-resolution X-ray imaging and spectroscopy. The observatory was in planning from the 1980s and was launched on 1999 July 23 by the Space Shuttle Columbia. The spacecraft was placed (by means of an integral propulsion system) into a highly elliptical orbit, with an apogee of $\sim 140,000$ km and a perigee of $\sim 10,000$ km in order to minimise the amount of time it spends in the Earth's radiation belts. An X-ray telescope needs to be positioned above the Earth's atmosphere, as X-rays have a short mean-free-path in air.

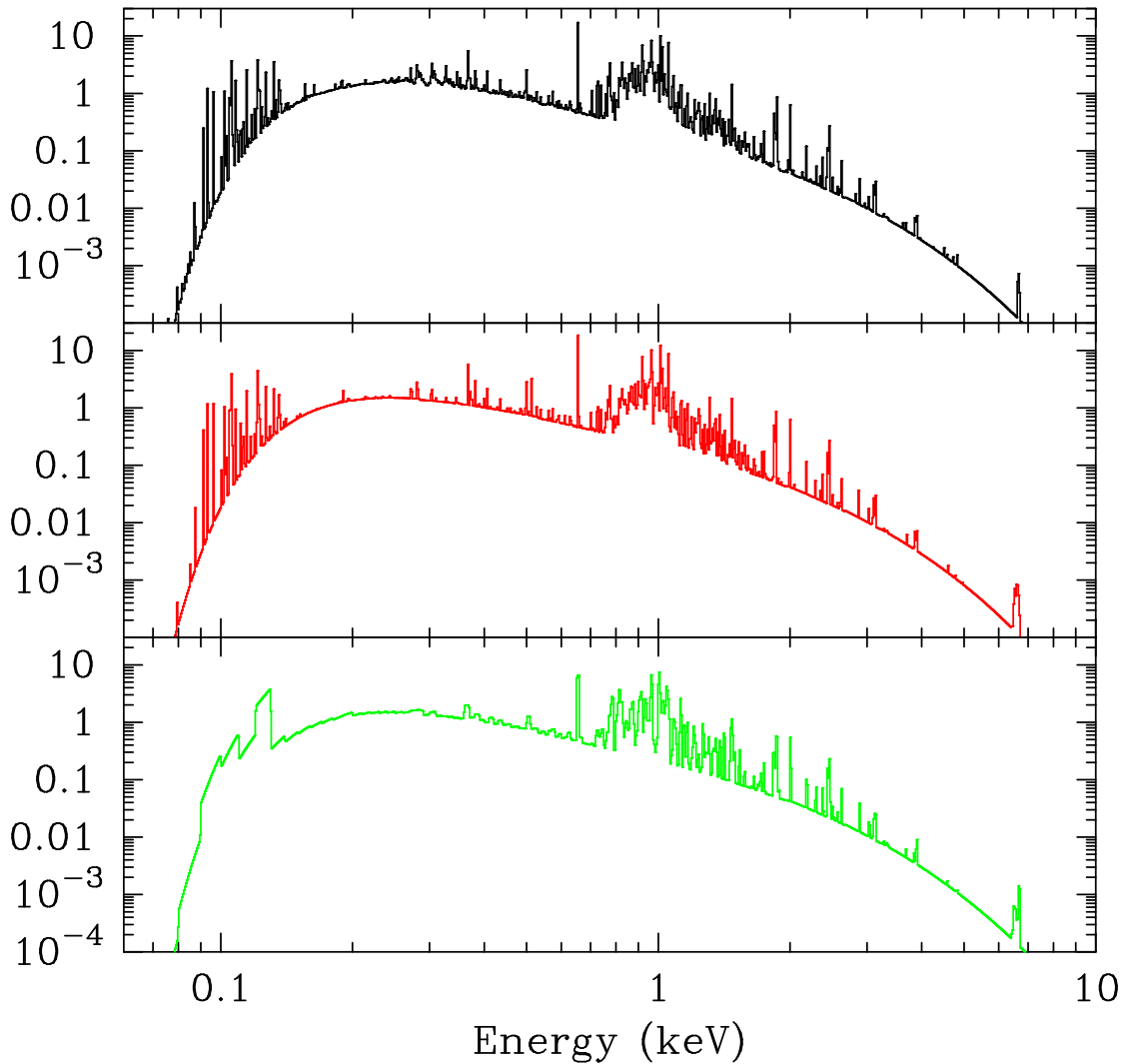


Figure 1.3: Predicted spectra of a 1 keV plasma, absorbed by a PHABS model of 10^{20} cm^{-2} , and with a metallicity of $1 Z_{\odot}$. The top panel shows the spectrum using an APEC model, the second panel is from a MEKAL model, and the lower panel is a Raymond-Smith model spectrum. Created using XSPEC version 11.1.0. Plots show normalised photon flux per keV.

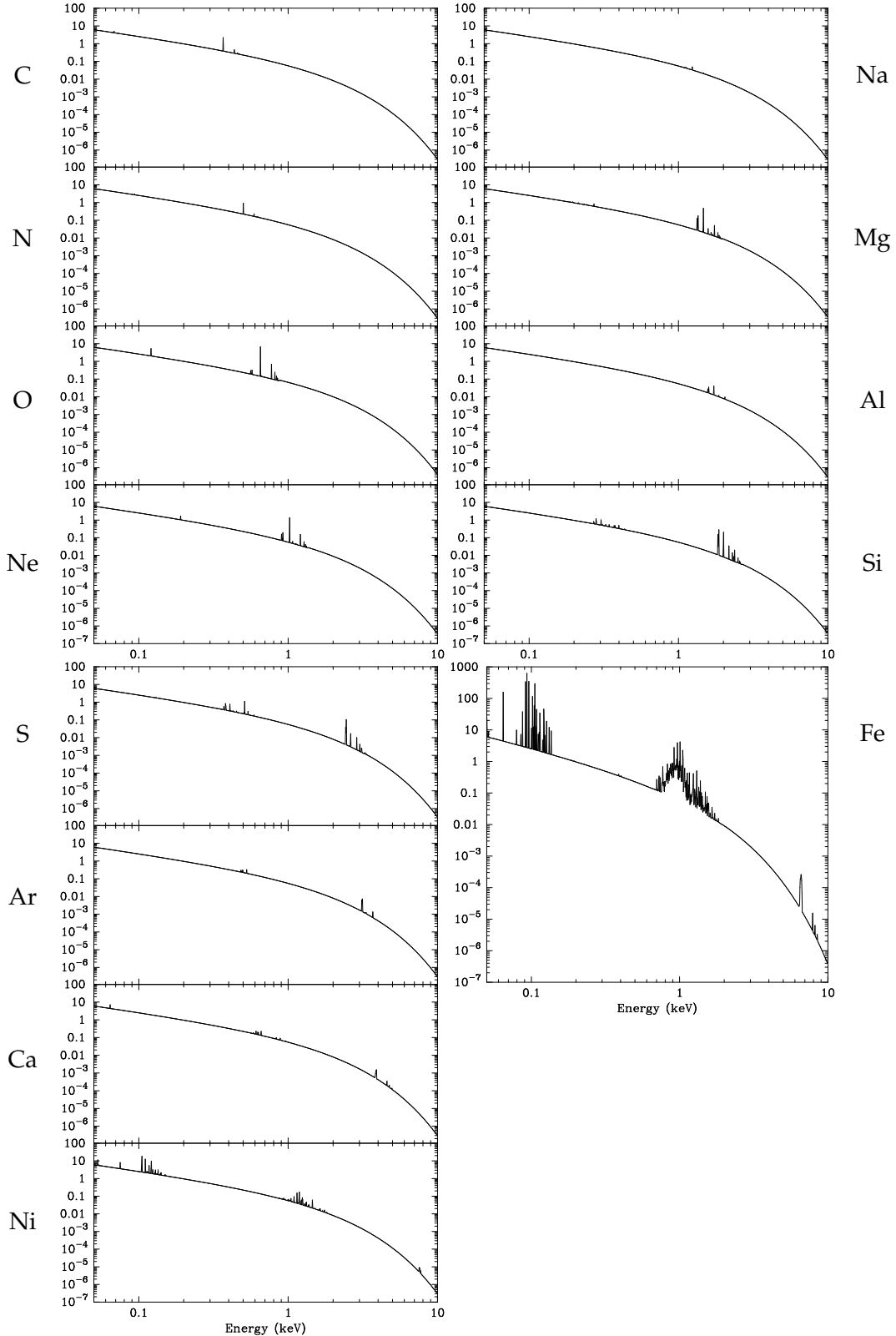


Figure 1.4: The contribution to the spectrum from different elements, for a MEKAL model at 1 keV and $1 Z_{\odot}$, each summed with the contribution from H and He. Top-left panel, going down: C, N, O, Ne. Top-right panel: Na, Mg, Al, Si. Bottom-left panel: S, Ar, Ca, Ni. Bottom-right: Fe. Plots show normalised photon flux per keV. I am grateful for R.G. Morris for producing the data files for these plots.

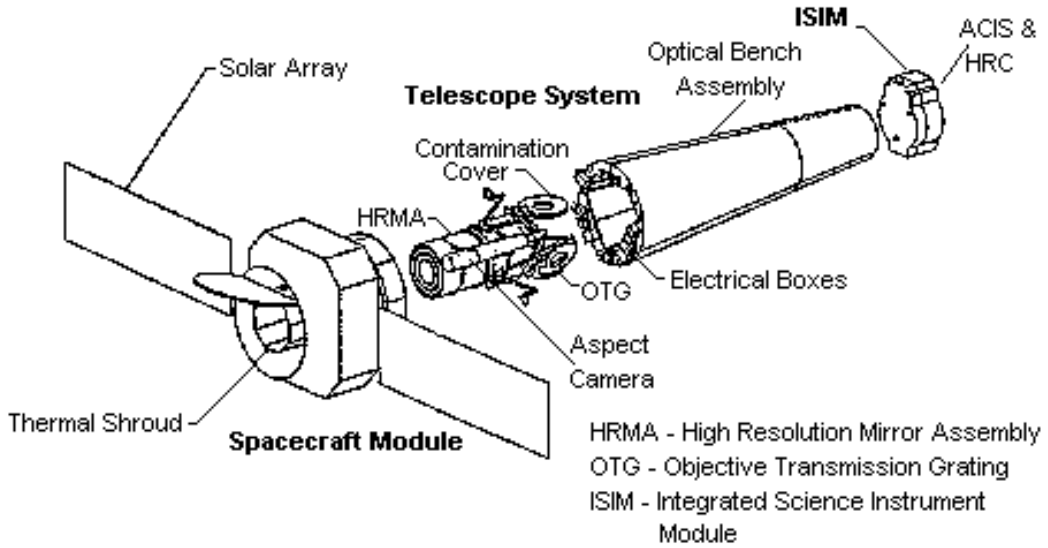


Figure 1.5: Expanded view of the *Chandra* subsystems. Taken from Weisskopf et al. (2000). TRW drawing.

The observatory presents spatial resolutions an order of magnitude greater than those before (e.g. ROSAT, Trümper 1983), and has extraordinary spectral resolution ($E/\Delta E \sim 1000$ between 0.4 and 10 keV) using its gratings.

An expanded view of the subsystems of *Chandra* is shown in Fig. 1.5. At one end of the observatory (nearest us in the figure) lies the spacecraft module, containing those systems necessary for the control of the spacecraft. Next is the High Resolution Mirror Array (HRMA), which is actually positioned at the end of the spacecraft. The HRMA contains the grazing-incidence mirrors for focusing the X-ray radiation, and the gratings. The X-ray radiation passes through the Optical Bench Assembly (OBA), to the Integrated Science Instrument Module (ISIM).

1.2.1 The spacecraft module

The spacecraft module should not be so relevant to the scientific performance of the observatory, but nevertheless there are constraints given by this aspect of the system so I will list its components (taken from Weisskopf et al. 2000):

1. The pointing control and aspect determination subsystem, which controls the solar arrays, slewing, pointing, dithering and spacecraft momentum. It also determines the attitude of the observatory.
2. The communication, command, and data management subsystem, which communicates data and commands to and from ground stations. It stores and processes incoming commands, does data acquisition and storage, provides a timing reference, and switches the electrical power or other parts of the spacecraft.

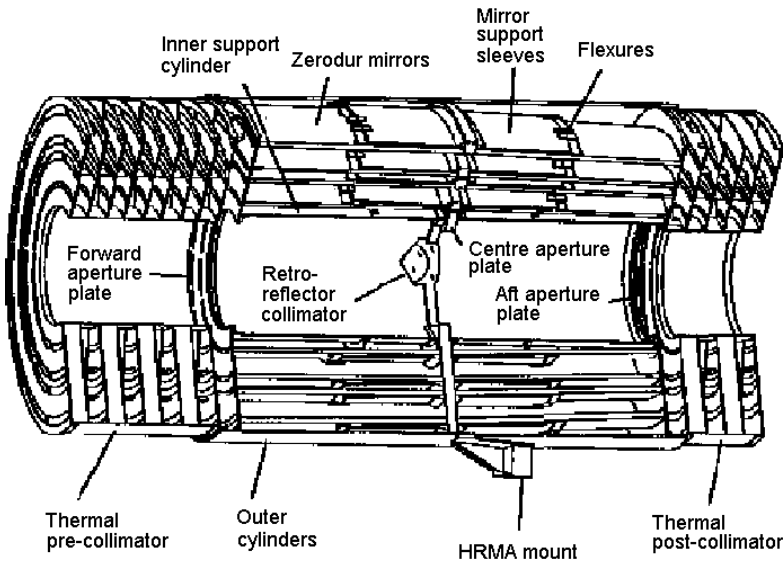


Figure 1.6: *Chandra* mirrors and structures. Taken from Chandra X-ray Center (2000).

3. The electrical power subsystem, which generates, regulates, stores, distributes, conditions, and controls the primary electrical power.
4. The thermal control subsystem, which passively controls the temperature of subsystems, if possible, and also uses heaters and thermostats for active temperature control.
5. The structures and mechanical subsystem, including the spacecraft structures, and the mechanical interfaces between the spacecraft subsystems.
6. The propulsion subsystem, which is the integral propulsion unit used to get into the correct orbit. The unit is now deliberately disabled.
7. The flight software, containing software for attitude finding and control, command and telemetry processing and storage, and thermal and electrical power monitoring and maintenance.

1.2.2 The HRMA

The mirror assembly in *Chandra* (shown in Fig. 1.6) consists of a nested set of four paraboloid-hyperboloid (Wolter-1) grazing-incidence X-ray mirror pairs. The largest mirror has a diameter of 1.2 m. The focal length of the system is 10 m. A diagram showing the total raytrace-predicted on-orbit effective area is shown in Fig. 1.7. The performance of the mirror tested on-ground is very close to those predicted values (van Speybroeck et al. 1997). The effective area of the mirror is greatest below 2 keV. The structure below 2 keV is due to the iridium M-edge.

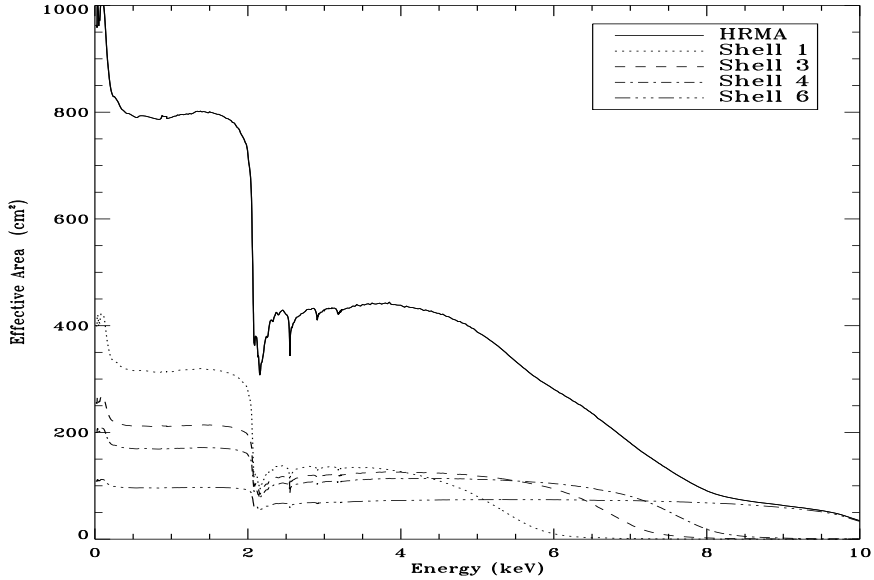


Figure 1.7: *Chandra* HRMA predicted effective area as a function of energy. Taken from Chandra X-ray Center (2000).

The Point Spread Function (PSF) of the mirror measures the amount of energy a point source produces inside a certain radius at the focus. This, in itself, is not a completely useful quantity as the detector also has a significant effect on the total PSF. In-flight observations show that 50 per cent of the energy is encircled by 0.4 arcsec for an on-axis source. 90 per cent of the energy is encircled by 0.9 arcsec. Off-axis there is significant distortion due to the Wolter-1 mirror arrangement.

1.2.3 The ISIM

The ISIM contains two instruments – the Advanced CCD Imaging Spectrometer (ACIS) and the High Resolution Camera (HRC). I will only consider the ACIS detector in detail, as the HRC (a microchannel plate device) does not have comparable spectral resolution to ACIS. Imaging spectroscopy requires moderate spectral resolution.

1.2.4 The ACIS

The ACIS detector is a complex instrument. The layout for the ACIS flight focal plane is shown in Fig. 1.8. The device is made up of 10 1024×1024 pixel CCDs (charge-coupled devices). There is a 2×2 array for imaging (known as the ACIS-I), and a linear array of 6 chips (known as the ACIS-S) which can be used for imaging or for the projection of spectra from the gratings. Two of the CCDs are back-illuminated (BI), and eight are front-illuminated (FI). The distinction is important as the front-illuminated CCDs were damaged by low-energy protons early in the mission (discussed in Section 1.2.7).

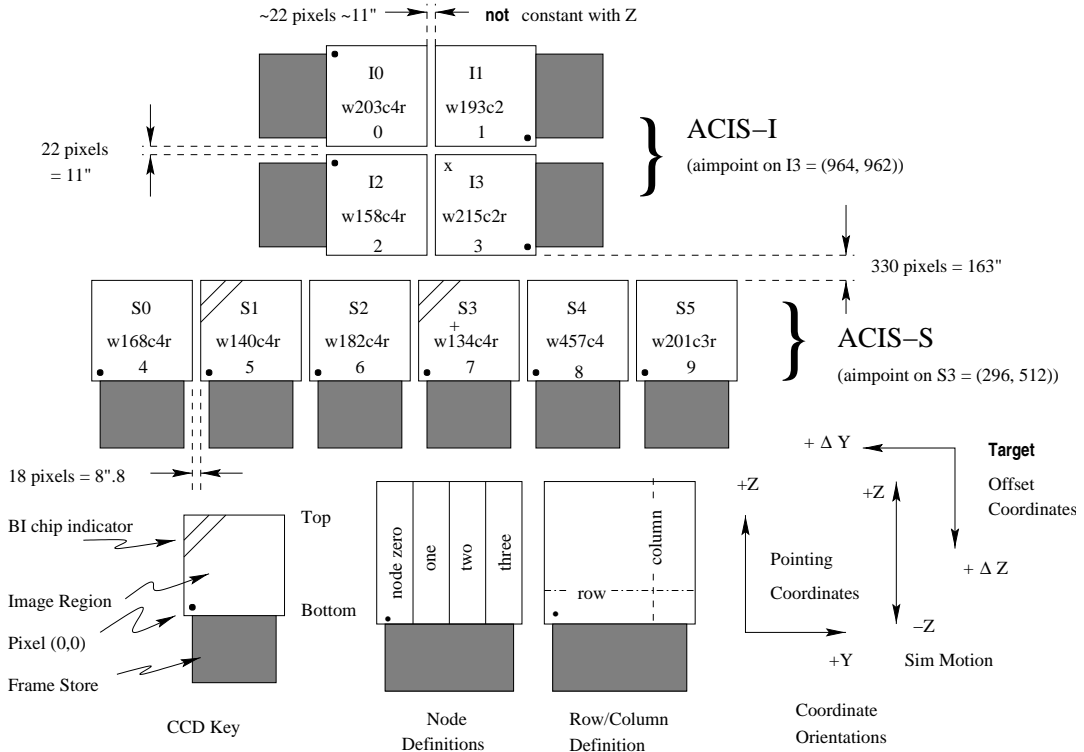


Figure 1.8: The ACIS focal plane. Taken from Chandra X-ray Center (2000).

CCDs

A CCD is a semiconductor (usually silicon) chip which contains a two-dimensional array of gates, which make up the pixels of the device. An X-ray photon entering a gate is photoelectrically absorbed, and releases electrons from the semiconductor into a conduction band. The number of electrons released is proportional to the energy of the incoming photon. The electrons are confined using an electric field in the gate. By varying the electric field (adjusting the voltages on the gate), the charge can be passed to the neighbouring gate. The gates are arranged in rows, and this technique is known as "clocking". The stored charges are measured at the edge of the CCD with a readout detector. One wishes to read the CCD often enough so that at most a single photon is absorbed by each gate. If this is the case, the voltage measured for each pixel will be proportional to the energy of the photon absorbed by the gate. If the CCD is not read often enough, individual photons cannot be identified. "Pile-up" is the term for when too many photons are detected in too short a time. It is very hard to analyse data from a region with pile-up.

The ACIS contains two types of CCDs: front-illuminated and back-illuminated. In both cases the gate lies on top of a silicon substrate. With a front-illuminated chip the X-rays enter from the top of the device: the gates face the incident X-rays. With a back-illuminated chip the X-rays enter from below. However, the silicon which is not sensitive

to X-rays has been removed from beneath the gate.

Factors which lead to an accurate determination of the photon energy are:

1. the fraction of charge collected in the gate,
2. the fraction of charge lost when clocking the charge down rows,
3. the sensitivity of the readout detectors,
4. the readout noise (less than 2 electrons RMS for ACIS), and
5. the noise in off-chip electronics (2-3 electrons RMS for ACIS).

The CCDs have two regions: an “active” region exposed to the incoming radiation and the frame store region, which holds the charges which are next for reading. This arrangement minimises the amount of time the CCD spends not recording incoming photons. A typical sequence for observing is as follows:

1. The active region is exposed to the incoming radiation for a period (~ 3.2 s for the full-frame observation mode).
2. The charges are then quickly shuffled into the frame store in about 40 ms.
3. The active region is exposed again.
4. Whilst the active region is recording photons, the charge in the frame store region is interpreted by a processing unit. First the bias in each pixel is removed (the voltage without any input signal), then “events” are identified on the chip.

Events are characterised by a peak in charge distribution over several pixels. By examining the shape of the distribution, each event is “graded” to signify whether the event was likely to have been created by an incoming photon. The event is then passed down to a ground station. As events are sent to the ground in real-time, there are a maximum number of events which can be received per unit time in each observing mode. If one is observing particularly bright objects, then small sky regions must be observed (to reduce the number of events) and CCD exposures have to be shortened (to reduce the effect of pileup).

Event grades Events are graded by finding the local maximum of counts and then examining the surrounding pixels. Each surrounding pixel is assigned a number, and if the charge in that pixel exceeds a threshold background level, it is summed. The numbers assigned to each neighbouring pixel is a power-of-two, which are shown in Fig. 1.9.

Events with particular event grades are discarded in the observatory, to reduce the amount of data sent to the telemetry stream. Only particular events grades are used

32	64	128
8	0	16
1	2	4

Figure 1.9: Values summed to give the event-grade. If a neighbouring pixel has a charge above a background threshold, it is summed to give a total event grade.

for the calibration data. The event grades chosen were found to maximise the signal-to-noise of the events if there is no pileup. The event grades are listed in Chandra X-ray Center (2000).

1.2.5 Spatial resolution

When using the ACIS for on-axis imaging, the HRMA is not the limitation for spatial resolution but the ACIS CCD pixel size is (~ 0.492 arcsec). At 1.49 keV 90 per cent of the encircled energy lies within 4 pixels radius (2 arcsec) of the aimpoint. At 6.4 keV this fraction of energy lies within 5 pixels (2.5 arcsec).

Off-axis, the CCD is not the dominating factor for spatial resolution but the HRMA is more important. Off-axis, point sources can have cusp-like appearances of a few arcsec in size. Ghost sources can also be present outside of the central 29 arcmin diameter. These are due to non-reflected, or singly reflected, rays from strong off-axis sources.

1.2.6 Dithering

The spacecraft is normally dithered during observing. The dithering ensures that areas of the sky which lie between gaps of the CCDs are observed, and pixel-to-pixel variations in the response are removed. The pattern which is followed is a Lissajous figure with a 16 arcsec peak-to-peak magnitude for ACIS. The dithering is removed by the on-ground processing of the data, before it is passed to the observer.

1.2.7 Energy resolution

Early in the mission, the ACIS FI CCDs were close to the theoretical limit for their energy resolution, whilst the BI CCDs had lower energy resolution. However the FI CCDs were damaged during the mission and now have an energy resolution which is a function of CCD row number.

The FI CCD damage was caused by low energy protons, which were unexpectedly focused by the HRMA onto the FI detectors. The source of the protons was the Earth's

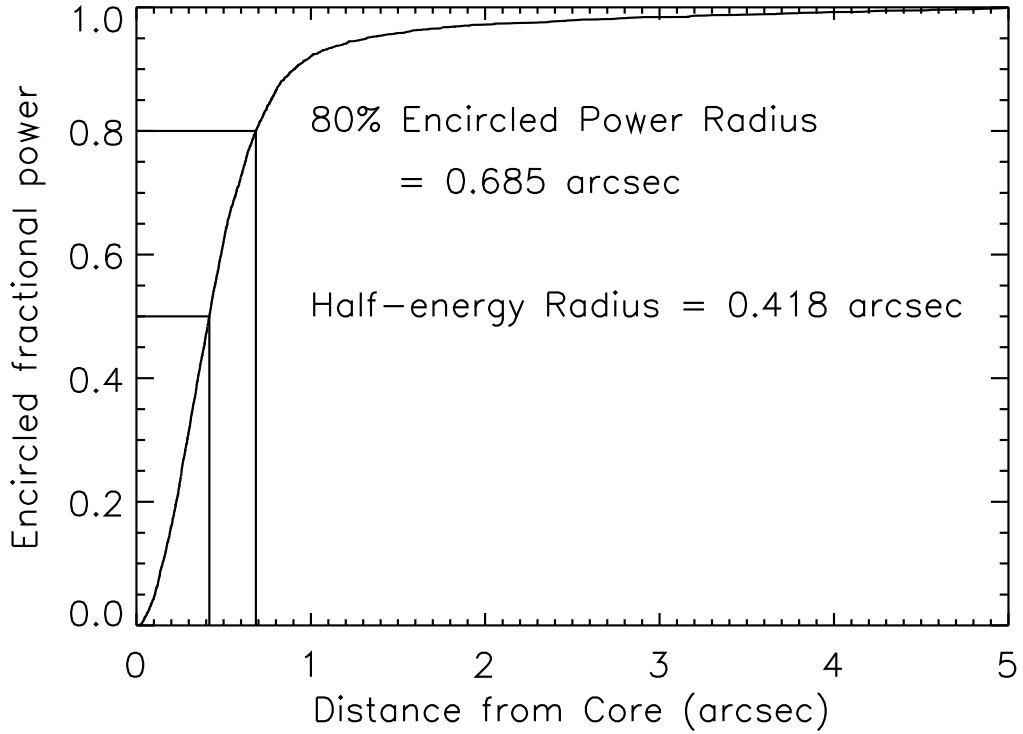


Figure 1.10: The encircled energy inside a particular radius for the object PG 1634-706 (effective energy 1 keV) measured in orbit. Taken from Chandra X-ray Center (2000).

radiation belt. The ACIS detector was left at the focus of the telescope during radiation belt passages. It is now moved from the focus at the times of belt passage, a procedure which has eliminated further damage. The BI CCDs were unaffected, as it is harder for a proton to pass through the silicon substrate to damage the gates.

It is difficult to analyse the spectral information from the ACIS-I detector due to the proton damage. A further complication for the analysis of ACIS data is that the focal plane temperature of the detector has been lowered during the lifetime of the mission. It is currently at the lowest temperature safely achievable, $\sim -120^{\circ}\text{C}$. Table 1.1 shows the variation in the focal plane temperature (taken from Markevitch 2001) as a function of time. Each time period requires different response-matrices and background files to analyse the data spectrally.

1.3 X-ray data and analysis

The end-user data from an X-ray telescope consists of a series of events, including the position of the event on the detector (DETX, DETY), the time the event occurred (TIME, limited in resolution to how often the CCD is read out), the energy-channel of the event (known as PHA, pulse height analyser, for historical reasons), and the grade of the event. There are also derived numbers such as the projected position of the sky in detector

Period	Dates	Temperature (°C)	Notes
A	First light to 1999 Sep 16	-100	Rapid CTI (charge transfer inefficiency) growth in FI chips.
B	1999 Sep 17 to 2000 Jan 29	-110	CTI stable, particle background down by 20-30 per cent relative to A.
C	2000 Jan 30 to present	-120	Slightly lower background than B, though varying by 15 per cent over the time period.

Table 1.1: ACIS focal plane temperature variation

coordinates (X, Y), the PI energy channel (pulse invariant; the PHA channel corrected for detector variations), and an ENERGY channel which estimates the energy of the event. *Chandra* data also include columns specifying which ACIS chip received the event, and the position of the event on the individual chip.

The mapping of a particular PI channel into energy is performed using a response matrix file (or RMF). For a particular energy of an incoming photon, there are a range of possible PI channels which could be activated. The RMF file gives the probability of the energy of the photon being in certain energy bins, given the PI (or PHA) value of the event. An X-ray spectrum consists of a table listing the number of events with a particular PI or PHA value. If the actual spectrum of the source as a function of energy is $f(E)$, then the number of counts in detector channel PI , D_{PI} , is given (Arnaud & Dorman 2001; ignoring the effective area of the telescope and the X-ray background) by

$$D_{PI} = \int_{E=0}^{\infty} f(E) \text{RMF}(PI, E) dE. \quad (1.15)$$

The obvious way to test whether the source spectrum is the same as the model spectrum is to deconvolve the RMF from the data. Unfortunately, the deconvolution is non-unique, and unstable to small changes in D_{PI} .

The RMF is used by a spectral fitting package (such as XSPEC, Arnaud 1996), along with an ARF (Ancillary response file, incorporating effects like the effective area of the telescope as a function of energy) to fit the data. A model spectrum is convolved with the RMF and multiplied by the ARF. The model can then be compared to a real spectrum by the χ^2 of the fit. The χ^2 for a fit is formally (Bevington & Robinson 1992)

$$\chi^2 = \sum_{j=1}^N \frac{[h(x_j) - NP(x_j)]^2}{\sigma_j(h)^2}, \quad (1.16)$$

where x_j is a measured value (when binned), $h(x_j)$ is its frequency, N is the total number of measurements, $P(x_j)$ is the probability of the measured value (predicted by a model), and $\sigma_j(h)$ is the standard deviation associated with the uncertainty in the observed frequency $h(x_j)$. If there are sufficient counts in each bin, we can write when

fitting a spectrum that

$$\chi^2 = \sum_{\text{PI}=\text{min}}^{\text{max}} \frac{(D_{\text{PI}} - M_{\text{PI}})^2}{D_{\text{PI}}}, \quad (1.17)$$

where D_{PI} is the number of counts in the PI bin, M_{PI} is the number of counts predicted in the PI bin, when the model has been convolved with the response of the telescope. The counting error on D_{PI} counts in the spectral bin is roughly $\sqrt{D_{\text{PI}}}$, providing D_{PI} is about 20 or more. min and max specify the minimum and maximum PI channels to consider. These are chosen to lie in the range where the telescope is well calibrated and the model is known to apply. If there are too few counts in each PI channel, it is common to bin PI channels with the neighbouring channel until there are a minimum number of ~ 20 counts in the new channel.

A model is fit by varying the parameters of the model to reduce the χ^2 . The parameters which give the lowest χ^2 are the best fitting parameters. If a model is a good description of the data, the reduced- χ^2 , χ^2_ν , equal to χ^2/ν , where ν is the number of degrees of freedom in the fit, should be approximately 1 (Bevington & Robinson 1992). The number of degrees of freedom in a spectral fit is the number of spectral channels (i.e. $\text{max} - \text{min} + 1$ if unbinned) minus the number of free parameters to the model.

2

Colour maps of cluster cores

Summary

This chapter details a study I made of a sample of the structure of 33 bright clusters from the brightest 55 X-ray cluster survey (Edge et al. 1990). The data were publicly available and were taken from the *ROSAT* LEDAS data archive¹. This chapter formed the basis of the paper *X-ray colour maps of the cores of galaxy clusters* (Sanders et al. 2000).

The aim of the study was to analyse the publicly available *ROSAT* cluster data sets, and use the method of X-ray colours (Allen & Fabian 1997) to spatially analyse the clusters for temperature and absorption gradients. The method used in this chapter takes account of the spatial structure in the image, rather than forming simple radial contours.

Using a colour sensitive to cooling gas, those clusters which have evidence for significant cooling flows showed a colour gradient into their centres, indicating the gas is at lower temperatures in their cores. A second colour sensitive to absorption also showed gradients, implying there are significant levels of absorbing gas in the cooling flow clusters. A metallicity gradient instead of absorption was unable to explain the results. Those clusters without cooling flows did not show evidence of increased absorption or cooling gas. These results provide more evidence that cooling flows accumulate absorbing material.

¹Hosted at Leicester University, <http://ledas-www.star.le.ac.uk/>

Band	Energy range (keV)
A_1	0.10–0.20
A_2	0.20–0.40
B	0.41–0.79
C	0.80–1.39
D	1.40–2.00
F	0.41–2.00

Table 2.1: Definition of the energy bands (Allen & Fabian 1997).

2.1 Introduction

Allen & Fabian (1997) undertook a study of the spatial distributions of cooling gas and intrinsic X-ray absorbing material in a sample of nearby clusters using X-ray colour profiles, formed from the ratio of flux in selected bands, using data from the *ROSAT* Position Sensitive Proportional Counter (PSPC). They found that the profiles indicated that there were significant central concentrations of cooling gas in those clusters with evidence for cooling flows, becoming approximately isothermal at larger radii. Their profiles also showed large levels of X-ray absorption in the cluster cores, increasing with decreasing radius (See Section 1.1.4 for a review of the evidence for absorption in cooling flow clusters).

The data were analysed in bands shown in Table 2.1. The ratio between the counts in each band in an annulus was used to make an *X-ray colour*, though in practise they used two colours B/D and C/D .

Band C contains most of the strong emission lines from a plasma of temperature ~ 1 keV including the Fe-L transitions (See Fig. 1.4). Column densities of $\sim 10^{21}$ cm $^{-2}$ absorb the spectrum below 0.8 keV by a large amount affecting band B . Band D is rather unaffected by emission lines. Therefore the colour C/D is sensitive to the presence of cool gas (here around 1 keV), and the colour B/D is sensitive to absorption. To quantify the temperature and absorption, they fitted the colours to those expected from different spectral models. The spectral models used were the plasma code of Kaastra & Mewe (1993), and a cooling flow model based on that plasma model (See Section 1.1.4). A redshift of 0.01 was assumed. The clusters examined have low redshifts, so it is unlikely for significant lines to move into a different band as the redshift varies.

The effects of changing absorption and temperature can be seen in the simulated plasma spectra shown in Fig. 2.1 and Fig. 2.2. The spectra were simulated assuming a redshift of 0, and a metallicity of $0.3 Z_{\odot}$. The plots show that the B band is sensitive to absorption, and the C band is sensitive to cooling gas. For completeness I show the effect of varying the abundance in a 1 keV plasma in Fig. 2.3. The plot highlights there are degeneracies between absorption, abundance and temperature in the three bands (See Section 2.5.3).

In this chapter I extend the analysis of Allen & Fabian (1997). Instead of a simple

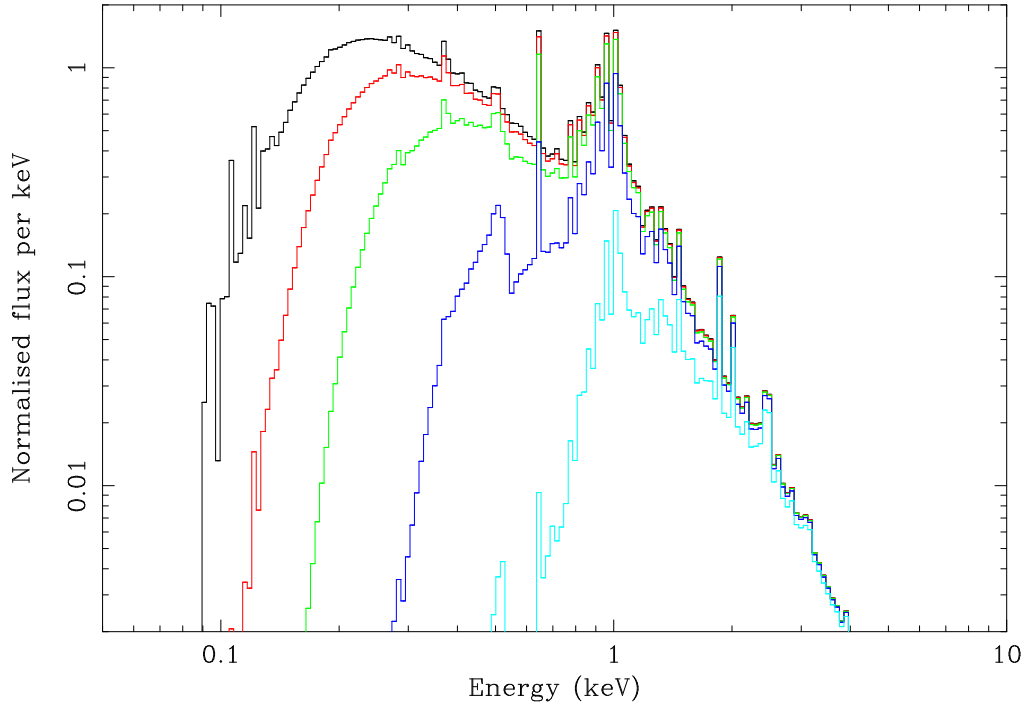


Figure 2.1: A simulated MEKAL spectrum of a gas at 1 keV, abundance of $0.3 Z_{\odot}$, varying the level of PHABS absorption from (1 [black], 2 [red], 5 [green], 20 [blue] and 80 [cyan]) $\times 10^{20} \text{ cm}^{-2}$. The simulated spectrum is binned into 200 logarithmic energy bins from 0.05 to 10 keV.

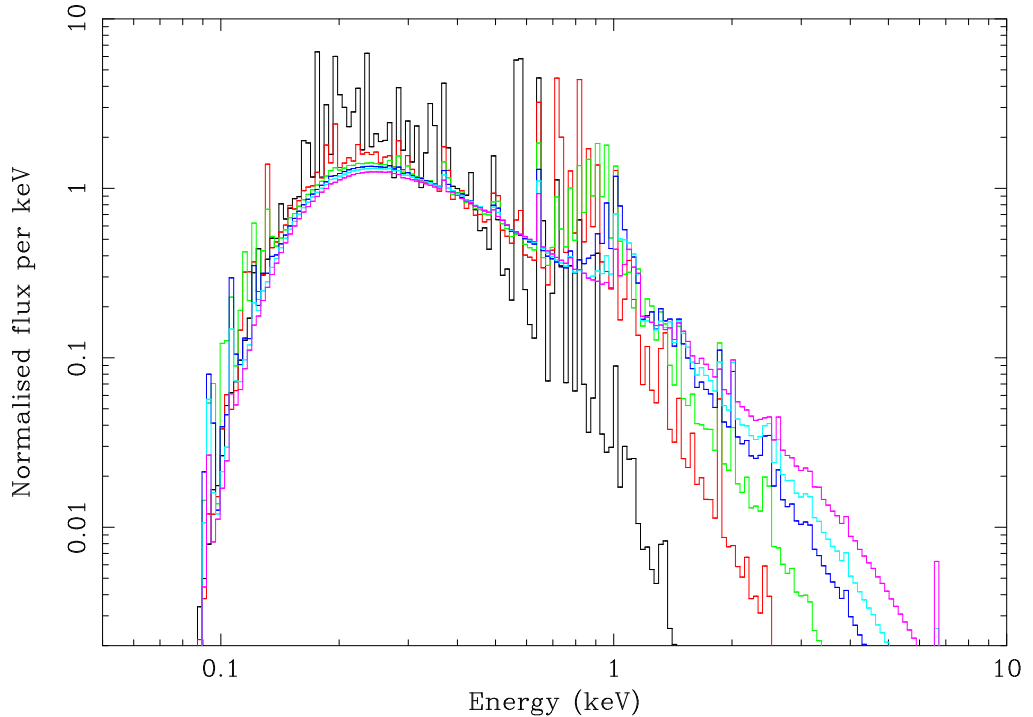


Figure 2.2: A simulated MEKAL spectrum of a gas with an abundance of $0.3 Z_{\odot}$, absorbed by 10^{20} cm^{-2} , varying the temperature of the gas from (0.2 [black], 0.5 [red], 0.8 [green], 1.2 [blue], 1.5 [cyan] and 2.0 [magenta]) keV. The simulated spectrum is binned as in Fig. 2.1.

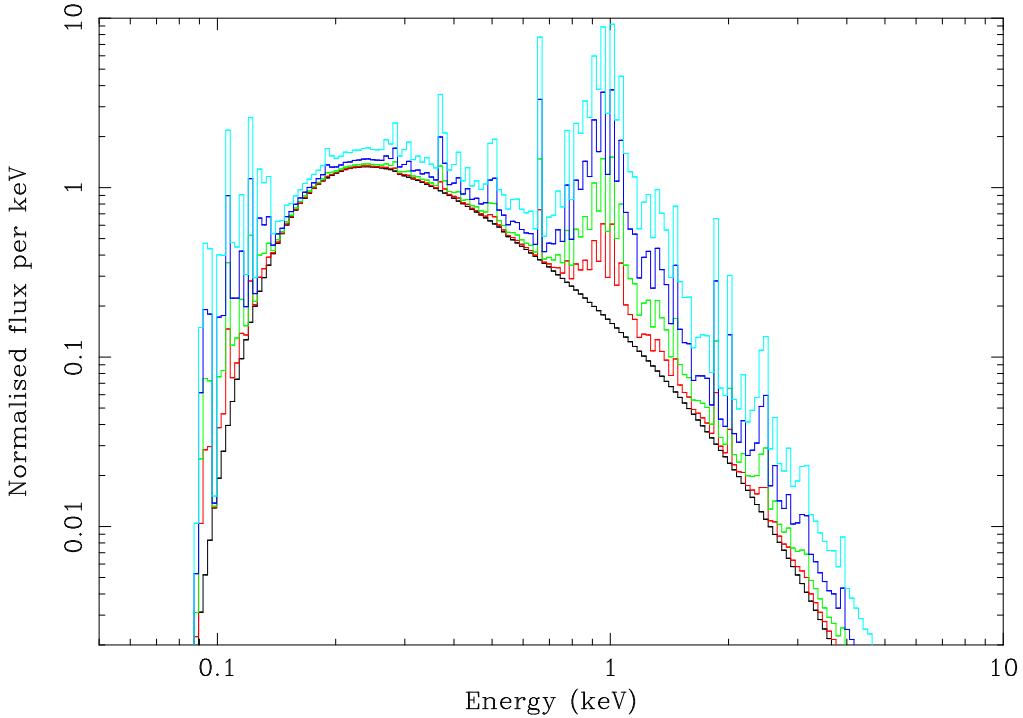


Figure 2.3: A simulated MEKAL spectrum of a gas with a temperature of 1 keV, absorbed by 10^{20} cm^{-2} , varying the abundance of the gas from (0 [black], 0.1 [red], 0.3 [green], 0.8 [blue] and 2.0 [cyan]) Z_\odot . The simulated spectrum is binned as in Fig. 2.1.

radial profile study of each cluster, which is inappropriate unless the cluster is known to have spherically-symmetric structure, I have developed a technique to take account of the two-dimensional structure of the image. The method also works better than simple binning does. Binning works as long as the number of counts per pixel does not vary significantly over the image, but this is not the case with images of clusters. If a small bin size is used, then areas with a small count rate have large errors on their X-ray colours. However, a large bin size would destroy any spatial information in areas with high count rates. This method attempts to make statistically useful X-ray colours whilst preserving spatial resolution. In Chapter 3 I present a more general method for doing this.

2.1.1 ROSAT

The *ROSAT* observatory (Trümper 1983) was a predecessor to *Chandra*, and a joint collaboration between Germany, the UK, and the US. Its name comes from a shortened version of the German word *Röntgensatellit* ('X-ray satellite'). The main aim of the mission was to be the first all-sky survey of the X-ray sky with a sensitivity much greater than that of previous missions. This aspect of *ROSAT*'s mission is yet to be bettered. *ROSAT* was launched on 1990 June 1, and was expected to have a nominal lifetime of 18 months. It carried an imaging X-ray telescope (XRT; sensitive from $\sim 0.12 - 2.4 \text{ keV}$) and a Wide Field XUV Camera (WFC; sensitive from $\sim 0.05 - 0.21 \text{ keV}$). The all-sky

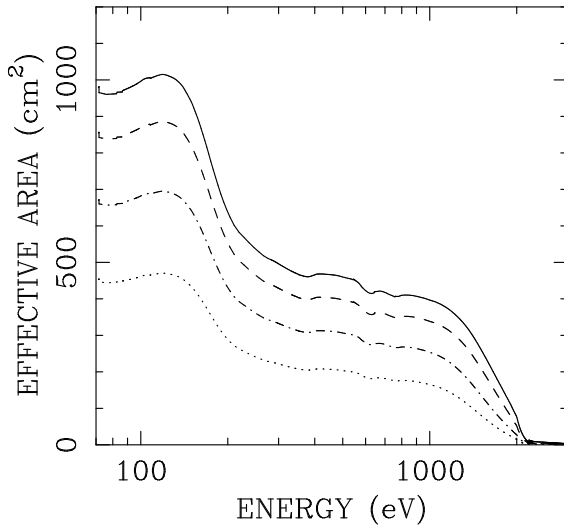


Figure 2.4: The effective area of the *ROSAT* XMA as a function of energy for (from top-to-bottom) off-axis angles 0, 20, 40 and 55 arcmin. Taken from Aschenbach (1990).

survey detected over 6×10^4 sources (Voges et al. 1996). The survey was followed by a series of pointed observations, of the type I show the analysis of in this chapter. *ROSAT* was finally switched off on 1999 February 12.

The XRT pointed observations made use of one of two detectors: the Position Sensitive Proportional Counter (PSPC) or the High Resolution Imager (HRI). The HRI was the higher-resolution device, but had little spectral resolution. The PSPC had the ability to distinguish the energy of incoming X-rays.

The *ROSAT* X-ray mirror assembly (XMA)

The XMA on *ROSAT* was a grazing incidence (like *Chandra*; Section 1.2.2) four-fold nested Wolter type I configuration. The mirrors were made from a glass ceramic with small thermal expansion, coated with a thin gold layer. The aperture of the telescope was 84 cm. Its effective area at several off-axis angles is shown in Fig. 2.4. The effective area is a function of:

1. the decreasing reflectivity of the mirror as a function of energy,
2. vignetting (the lower effective area of the mirror as the angle of incidence of the X-ray increases), and
3. scattering by the XMA.

The on-axis spatial resolution (half energy width) of the mirror was 5 arcsec.

The PSPC

The PSPC (Pfeffermann & Briel 1983) was a device (two were installed in *ROSAT*) to measure the position and energy of incoming X-rays. The PSPC consists of two separate counters (to help with background rejection). Each electrode (there are two cathodes and an anode) is a wire grid. The grids are sealed behind a thin plastic window in a gas mixture. When an X-ray photon passes through the detector it is absorbed by the gas releasing a photo-electron, which then produces a primary electron cloud. The cloud drifts through the cathode to the anode. The electric field near the anode causes an amplification of the cloud, with a gain of 5×10^4 . The charge is then detected on the anode, and an induced signal is found on the cathodes. The FWHM (full width half maximum) for the *ROSAT* telescope as a whole is about 0.5 arcmin. For 0.94 keV photons the energy resolution is 45 per cent. The energy resolution is approximately inversely proportionally to the square root of the energy of the incoming photons.

2.2 Observations and colour map analysis

I analysed archival *ROSAT* PSPC data for a sample of 33 clusters. The clusters I examined are shown in Table 2.2. The sample was mainly chosen to include known strong cooling flow clusters (taken from Peres et al. 1998), with a few non-cooling-flow clusters to enable comparisons to be made. I used the bands of Allen & Fabian (1997) in this analysis (See Section 2.1). These bands were optimised for the study of gas which is cooling in clusters at low redshift. Using the same bands also makes the results directly comparable with the earlier work. Unfortunately the choice of bands meant I could not use the extended object analysis package of Snowden & Kuntz (1998). I did follow many of the procedures they used, using modified versions of their routines.

The full analysis procedure for each cluster is as follows.

1. I removed time periods from the observation dataset where the Master Veto count rate averaged over ~ 30 s was greater than 220 counts s^{-1} (Snowden et al. 1994). Doing so removes time periods containing contaminating X-ray flares, which of course have a different spectrum from the source intended to be observed.
2. A modified version of Snowden's `CAST_DATA` routine was used to create binned 512×512 pixel images of the cluster, with a pixel size of approximately 15×15 arcsec 2 (the conventional binning factor for *ROSAT* PSPC data). I created images of the cluster in the *B*, *C* and *D* bands. To create the images I summed the number of events inside each pixel in the energy range of each band.
3. I background corrected each of the images (See Section 2.2.2).
4. Using the higher energy *D* band image I created an adaptively-smoothed (Ebeling et al. 2002) image (See Section 2.2.1) of the innermost 64×64 pixels (16 arcmin)

or for some clusters 128×128 pixels (32 arcmin), using a significance level of 6σ . The larger image size was for clusters whose angular extent were too large for the smaller image size. I chose the image size by visual inspection.

5. I created linear contours in the adaptively-smoothed image (in count rate), by simply taking the difference between the maximum and minimum count rates and dividing by the number of contours.
6. The total background-corrected counts in each of the bands were summed for those pixels between two particular contours (or inside the first contour, or outside the last).
7. The counts for those pixels between each two neighbouring contours were added in each of the background corrected B , C and D images.
8. I used the count totals to generate average B/D and C/D colours for each contour. The error on each result is

$$\left(\frac{\sigma_r}{r}\right)^2 = \frac{\sum_{\text{pixels}} (N_i^X + C_i^X)}{\left[\sum_{\text{pixels}} (N_i^X - C_i^X)\right]^2} + \frac{\sum_{\text{pixels}} (N_i^Y + C_i^Y)}{\left[\sum_{\text{pixels}} (N_i^Y - C_i^Y)\right]^2}, \quad (2.1)$$

where r is the X/Y average ratio, and σ_r is the error on the ratio. N_i^X is the uncorrected number of photons in pixel i in band X , and C_i^X is the background correction for pixel i in band X . This expression does not take account of systematic background uncertainties. I ignored pixels that were suspected to contain point sources (See Section 2.2.2) outside the core.

9. An iterative procedure was used to change the contour levels in the adaptively-smoothed image, to minimise the total error squared in the contours for both colours, or the value

$$x = \sum_{\text{contours}} \left\{ \left[\sigma_{(B/D)_i} \right]^2 + \left[\sigma_{(C/D)_i} \right]^2 \right\}. \quad (2.2)$$

The result of moving the contour levels to minimise x creates contour levels which contain similar numbers of counts and signal to noise ratios. The procedure produces colour ratios with roughly equal fractional uncertainties for each contour.

I used six contours to process the cluster images. This was a good compromise between showing detail and keeping statistical errors low. The results were stable to small changes in the number of contours.

2.2.1 Adaptive smoothing

Adaptive smoothing is a technique to smooth an image and retain significant small-scale structure (Ebeling et al. 2002). Smoothing is required because it is often the case, especially in X-ray data, that there are few photons per pixel. However, convolving an image with a Gaussian kernel leads to broadening of features and loss of small-scale structure. An algorithm is required which retains information on all scales. In Section 3.1.1 I discuss adaptive smoothing further, and present a method for retaining structure on different scales in Section 3.1.3: adaptive binning.

An adaptive kernel smoothing (AKS) algorithm applies a kernel with a varying size to an image. A part of the image with few counts is smoothed with a large kernel, whilst a part with many counts is smoothed with a small kernel. The algorithm decides what is the ‘natural’ smoothing scale for a part of an image. AKS algorithms differ on how they choose an appropriate kernel size. I used the ASMOOTH algorithm of Ebeling et al. (2002) to adaptively smooth the cluster images. ASMOOTH is unusual in that it uses the local signal-to-noise ratio to adjust the size of the kernel. The minimum signal-to-noise ratio of the part of the image smoothed by the kernel is a parameter to the algorithm. A level of 6σ seemed to produce the best results; it appeared not to generate false detail from spurious pixels. I used a Gaussian rather than top-hat adaptive kernel.

Other methods for revealing structure in data include, for example, wavelet analysis (Starck & Pierre 1998). Different methods have other advantages, but the ASMOOTH algorithm is particularly simple and quick to perform.

2.2.2 Background removal

The raw data contains counts not from the observed source. In order to do analysis of the data, especially spectral analysis, it is necessary to subtract these background counts. The background in the detector includes the following.

1. The X-ray background (e.g. Fabian & Barcons 1992; Mushotzky et al. 2000; Hasinger et al. 2001), which comes through the aperture of the telescope and is observed with the same vignetting response of the telescope as the object.
2. Solar X-ray emission, which is highly variable. Periods with high solar activity will be removed by Step 1 in Section 2.2.
3. The particle background (Plucinsky et al. 1993), which is diffuse and is caused by high energy cosmic rays. The flux of the particle background is approximately constant across the detector.

These components vary in strength with X-ray energy, so they must be removed to make X-ray colours.

To estimate the background I took the average count from the 30–35 arcmin region, beyond the ‘ribs’ in the field of the PSPC. From this count I subtracted an estimate of the particle background from Plucinsky et al. (1993), of 4×10^{-6} counts pixel $^{-1}$ s $^{-1}$ arcmin $^{-2}$ keV $^{-1}$. I corrected the result for vignetting. The corrected count and the particle background was removed from all pixels.

Accounting for the total background reduces the scatter of the observed data points. It also hardens the emission from the outermost parts of clusters which emit few photons.

Three clusters, A2142, A1795 and A2029, contained obvious point sources in their fields outside the cluster core. I removed the point sources using a mask which excluded the affected region around them. Those pixels inside the mask were not included in the sum of counts inside a contour.

2.3 Results

I created adaptively-smoothed images of the sample of clusters in the *B*, *C* and *D* bands, using an ASMOOTH minimum significance of 6σ . Fig. 2.5, 2.6 and 2.7 show the images for the Perseus, Virgo and A2199 clusters, respectively. As mentioned in Section 1.1.6, ROSAT HRI images of the centres of the Perseus cluster, NGC 1275, and the Virgo cluster, M87, have been examined by Böhringer et al. (1993) and Böhringer et al. (1995), respectively. They found the thermal plasma was displaced by the radio lobes of 3C 84 at the centre of the Perseus cluster (See Section 4.1.1). M87 is interesting, as the radio and X-ray emission appears to be correlated. The spectrum of the X-ray emission rules out inverse-Compton emission. In the case of this cluster, there is evidence for the radio lobes being buoyant blobs of radio plasma which have dragged up cool material from the core (Churazov et al. 2001).

Fig. 2.8 and 2.9 are colour contour maps of the Perseus and Virgo clusters. The maps show the average X-ray colours between each of six contours. The scale below each map shows the value and statistical uncertainty of the colour of each contour. The extreme error bars on the softest and hardest points are not shown on the scales. Note that darker shades in these plots indicate softer emission. Table 2.3 shows the mean physical distance from the cluster centre of each contour in each cluster in pixels. It also identifies which clusters were examined using a 64×64 pixel image or a 128×128 image.

Fig. 2.10 shows a sample of six colour contour maps. Four of the clusters are non-cooling-flow clusters, showing interesting spatial features. Two are cooling flow clusters, a category which makes up most of the sample, and reveal little substructure. The point source in A2142 is shown, but is not included in the contour statistics.

Fig. 2.11 and 2.12 show the average *B/D* and *C/D* colours for the contours of each of the sample of clusters. The clusters are listed in decreasing cooling flow flux order

Cluster	Sequence ID	Exposure/s	z	$\dot{M}/(M_{\odot} \text{ yr}^{-1})$	$t_{\text{cool}}/\text{Gyr}$	$S(B/D)$	$S(C/D)$
Virgo	rp800187n00	10536	0.0037	39^{+2}_{-9}	$0.2^{+0.0}_{-0.0}$	4.9	21
Perseus	rp800186n00	4711	0.0183	556^{+33}_{-24}	$0.9^{+0.0}_{-0.0}$	5.9	8.4
2A 0335+096	rp800083n00	10220	0.0349	325^{+32}_{-43}	$0.9^{+0.0}_{-0.0}$	2.6	7.1
Centaurus	rp800192n00	7793	0.0109	30^{+10}_{-5}	$0.8^{+0.0}_{-0.0}$	1.9	14
A2199	rp800644n00	40999	0.030	154^{+18}_{-8}	$1.9^{+0.0}_{-0.1}$	7.8	10
Ophiuchus	rp800279n00	3932	0.028	127^{+48}_{-94}	$3.0^{+0.4}_{-0.3}$	-1.2	0.3
Klemola 44	rp800354n00	3353	0.0283	87^{+25}_{-19}	$2.3^{+0.6}_{-0.2}$	-1.6	0.1
A2052	rp800275n00	6211	0.0348	125^{+26}_{-6}	$2.5^{+0.1}_{-0.1}$	2.1	4.6
A262	rp800254n00	8686	0.0164	27^{+6}_{-3}	$1.5^{+0.1}_{-0.1}$	2.2	5.1
PKS 0745-191	rp800623n00	10473	0.1028	1038^{+116}_{-68}	$2.2^{+0.1}_{-0.1}$	2.6	2.7
A1060	rp800200n00	15764	0.0124	15^{+5}_{-7}	$4.7^{+0.4}_{-0.3}$	0.3	0.1
A1795	rp800105n00	36273	0.0627	381^{+41}_{-23}	$1.9^{+0.1}_{-0.1}$	4.6	5.9
Hydra-A	rp800318n00	18398	0.0522	264^{+81}_{-60}	$2.0^{+0.0}_{-0.0}$	3.8	5.5
A2029	rp800249n00	12542	0.0767	556^{+44}_{-73}	$2.9^{+0.1}_{-0.1}$	4.4	5.2
A496	rp800024n00	8857	0.033	95^{+13}_{-12}	$1.8^{+0.1}_{-0.1}$	1.4	3.8
MKW3s	rp800128n00	9984	0.0449	175^{+14}_{-46}	$3.0^{+0.1}_{-0.1}$	-0.1	0.8
A478	rp800193n00	21969	0.0882	616^{+63}_{-76}	$2.8^{+0.1}_{-0.1}$	-0.8	2.1
A85	rp800250n00	10238	0.0521	198^{+53}_{-52}	$2.4^{+0.1}_{-0.1}$	1.5	2.9
A3112	rp800302n00	7598	0.0746	376^{+80}_{-61}	$1.9^{+0.1}_{-0.1}$	1.4	3.6
Cygnus-A	rp800622n00	9442	0.057	244^{+26}_{-22}	$2.6^{+0.1}_{-0.1}$	0.6	1.6
AWM7	rp800168n00	13088	0.0172	41^{+6}_{-6}	$1.9^{+0.2}_{-0.2}$	-0.4	2.2
A4059	rp800175n00	5439	0.0478	130^{+27}_{-21}	$3.4^{+0.6}_{-0.4}$	0.9	1.9
A3571	rp800287n00	6062	0.0391	72^{+56}_{-31}	$5.8^{+0.9}_{-1.0}$	6.7	3.4
A2597	rp800112n00	7163	0.0824	271^{+41}_{-41}	$2.3^{+0.1}_{-0.1}$	-0.3	1.4
A644	rp800379n00	10246	0.0704	189^{+106}_{-35}	$6.8^{+0.4}_{-0.4}$	2.8	1.4
A2204	rp800281n00	5357	0.1523	852^{+127}_{-82}	$3.1^{+0.1}_{-0.1}$	2.8	3.4
A2142	rp150084n00	7734	0.0899	350^{+66}_{-133}	$5.2^{+0.4}_{-0.3}$	1.0	1.0
A3558	rp800076n00	29490	0.0478	40^{+39}_{-10}	$10.2^{+0.3}_{-0.2}$	-0.2	1.2
A401	rp800235n00	7457	0.0743	42^{+82}_{-42}	$10.6^{+4.0}_{-1.8}$	-0.6	-1.3
Coma	rp800005n00	21140	0.0232	0^{+1}_{-0}	$17.7^{+6.7}_{-4.1}$	1.7	0.9
A754	rp800550n00	8156	0.0542	0^{+29}_{-0}	$15.0^{+3.1}_{-2.2}$	1.6	2.5
A2256	rp800162a01	4747	0.0581	0^{+14}_{-0}	$15.0^{+4.0}_{-3.6}$	0.2	0.9
A119	rp800251n00	15197	0.044	0^{+2}_{-0}	$19.2^{+12.2}_{-8.6}$	-0.9	-1.8

Table 2.2: The sample of clusters examined. z is the redshift taken from the NASA/IPAC Extragalactic Database (NED), and the values of \dot{M} , the mass deposition rate are PSPC observation derived values taken from Peres et al. (1998) as are the central cooling time values, t_{cool} . The sequence identification and exposure time give PSPC observation details. $S(B/D)$ and $S(C/D)$ are the significance of a colour gradient, larger values imply a larger colour gradient (§2.3). The clusters are listed in cooling flow flux order, \dot{M}/z^2 .

Cluster	1	2	3	4	5	6
2A 0335+096	2.1	3.8	5.9	8.7	13.8	28.7
A1060*	6.9	13.2	19.2	26.5	37.0	60.7
A119*	7.5	14.6	20.8	27.5	37.0	60.4
A1795	2.6	4.2	6.6	9.6	14.7	28.9
A2029	2.7	4.3	6.4	9.5	13.7	28.5
A2052	3.0	5.0	7.9	10.5	14.9	28.9
A2142	3.1	5.2	8.3	12.2	18.3	29.5
A2199	3.6	7.0	10.5	14.4	20.3	31.1
A2204	2.8	2.9	3.6	5.5	8.0	26.9
A2256*	7.4	11.9	16.7	20.8	25.6	56.1
A2597	2.4	2.9	3.7	5.3	8.1	27.0
A262*	6.3	11.8	18.1	24.8	33.4	59.1
A3112	3.3	3.7	5.2	8.0	13.1	28.5
A3558*	7.1	12.5	17.0	21.0	27.6	56.8
A3571*	5.5	10.2	14.4	21.7	32.1	58.0
A401	3.0	6.4	9.7	12.8	16.9	29.6
A4059	3.3	5.7	8.5	11.5	17.5	30.3
A478	2.4	3.6	5.1	7.6	11.2	27.8
A496	2.8	5.7	9.4	13.9	20.1	31.0
A644	3.8	6.1	8.7	11.8	16.4	29.0
A754*	12.0	25.7	27.7	30.7	36.6	57.2
A85	2.9	5.9	10.0	14.0	19.5	30.8
AWM7*	7.9	14.4	21.1	27.7	36.5	60.0
Centaurus*	5.7	12.3	18.5	27.2	39.2	60.9
Coma*	14.0	22.5	29.4	36.7	46.6	63.0
Cygnus A	4.6	5.3	6.2	8.8	16.5	29.5
Hydra A	2.6	3.8	6.7	9.6	13.4	28.4
KLEM44	4.3	6.0	8.9	12.4	17.8	29.8
MKW3s	2.4	4.7	7.0	9.2	12.9	28.2
Ophiuchus	7.3	12.2	15.2	19.1	24.4	31.3
Perseus*	4.2	8.4	13.5	22.2	34.8	59.3
PKS 0745-191	2.4	3.1	4.0	6.2	9.6	27.3
Virgo*	7.4	14.2	21.7	30.2	41.1	62.2

Table 2.3: Mean distance of the pixels in each contour from the cluster centre. Distances are measured in pixels (15 arcsec). The contours are numbered from 1 (inner) to 6 (outer). Clusters marked with an asterix (*) were examined using a 128×128 pixel adaptively smoothed image, rather than a 64×64 image.

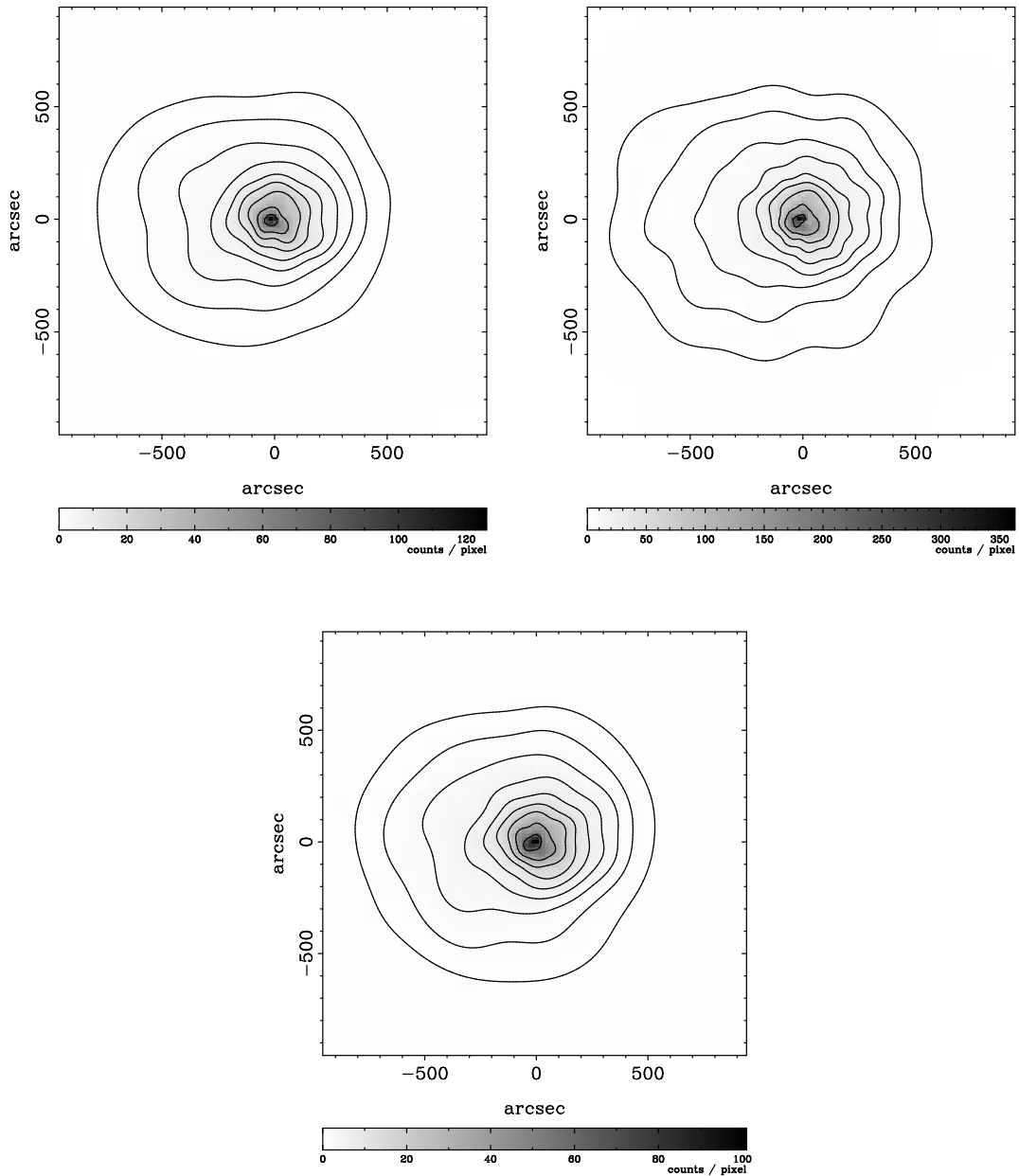


Figure 2.5: Adaptively-smoothed images of the Perseus cluster. The images are shown in bands B (top-left), C (top-right) and D (bottom). The greyscale is linear and the contours are logarithmic in smoothed counts.

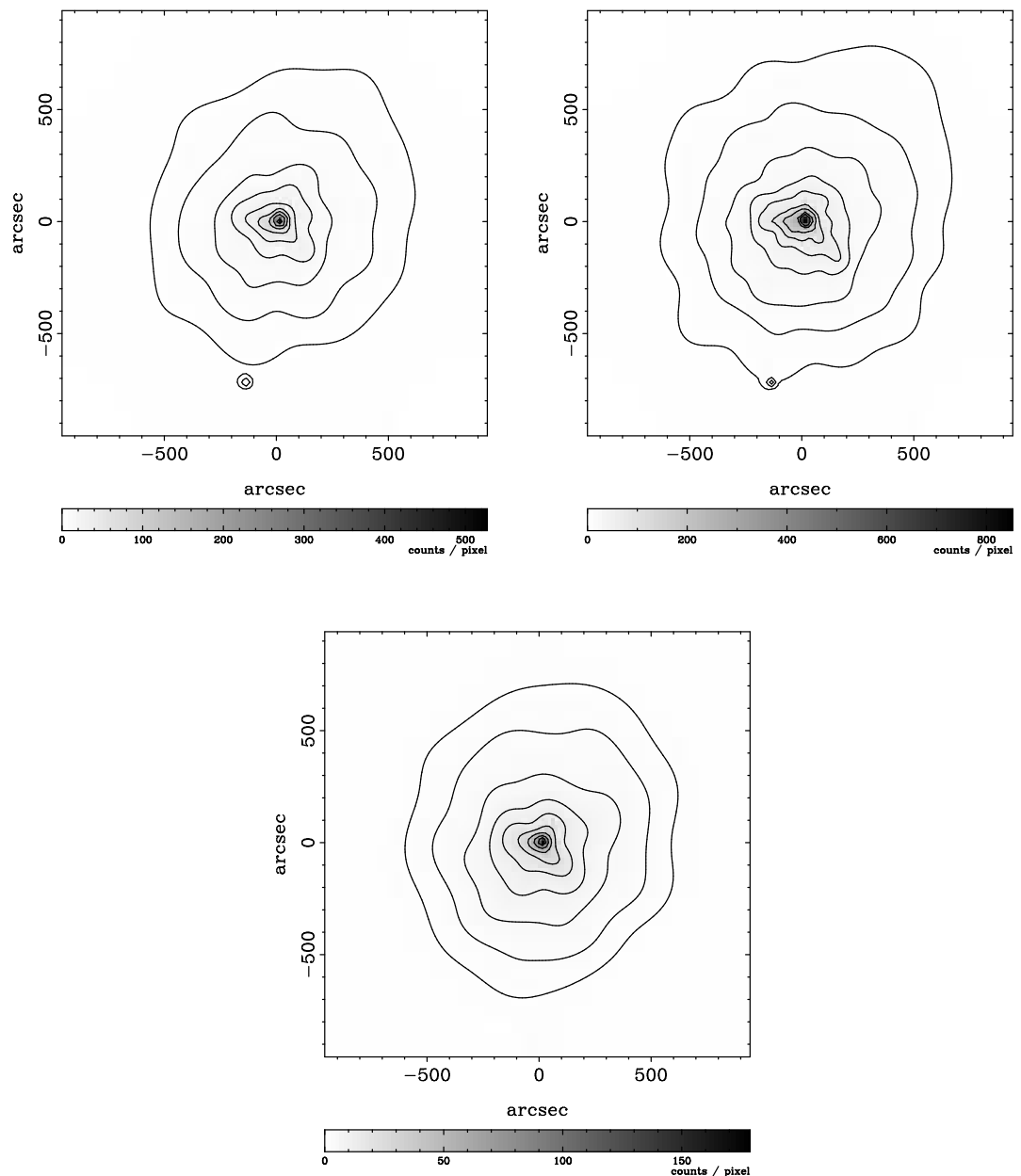


Figure 2.6: Adaptively-smoothed images of the Virgo cluster (see Fig. 2.5 for a description).

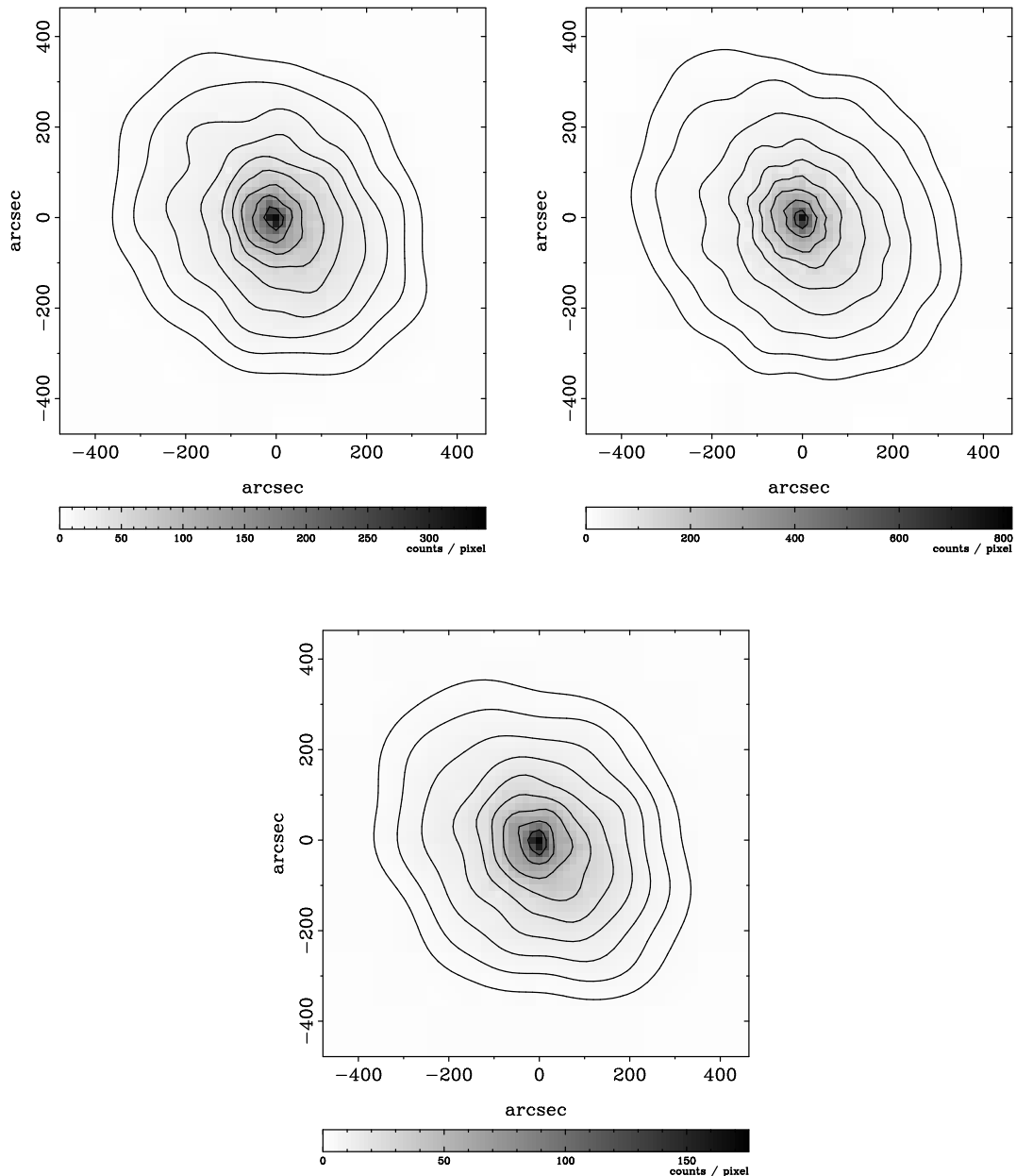


Figure 2.7: Adaptively-smoothed images of A2199 (see Fig. 2.5 for a description).

(\dot{M}/z^2 , where \dot{M} is the mass deposition rate, and z is the redshift of the cluster) using the PSPC \dot{M} values obtained by Peres et al. (1998). However, some of the clusters have highly uncertain mass deposition rates so the ordering is not definite.

Table 2.2 shows a significance measure of the change in colour from the outside to the inner region for each cluster. For a cluster with contours of colour X_i , the significance measure is calculated using

$$S(X) = \frac{1}{\sqrt{3/2} \sigma_X} [X_1 - (X_5 + X_6)/2], \quad (2.3)$$

X_1 is the innermost colour value, X_5 and X_6 are the two outermost colours, σ_X is the statistical uncertainty in each colour. The uncertainties are almost the same for each contour, due to the method of choosing contour levels (Section 2.2). $\sqrt{3/2}$ is a numerical factor to make $S(X)$ a measure of the number of 1- σ errors. I take the mean outer two colours to decrease the chance of background contamination. The background is a large fraction of the total number of counts in the outer contour in several clusters, for example A3571, A2204, A3558 and A262.

Fig. 2.13 shows the variation of the significance of the C/D colour, presumably due to the presence of cool gas, with the cooling flow flux, \dot{M}/z^2 , for the sample of clusters. Fig. 2.14 shows the significance plotted against central cooling time, t_{cool} . There is a clear anti-correlation between t_{cool} and the significance of a C/D colour gradient. Clusters with $t_{\text{cool}} \leq 2$ Gyr show colour gradients with $S(C/D) > 2$. t_{cool} is a measure of the quality of data for a cooling flow: cooling flow clusters with short cooling times have enough counts to make their central bins small in area.

Some of the results obtained are dependent on the choice of significance measure. If the cluster has a large soft core, as A3571, Hydra-A and A2204 seem to have in B/D , then using a measure based on $X_3 + X_4$ instead of $X_5 + X_6$ in equation (2.3) gives a much lower significance value. A significance based on $X_3 + X_4$ would be less affected by background noise but throws away much of the data. A more complex significance measure might be useful, but for those clusters where it might be important noise is probably a more limiting factor.

2.4 Colour models

By comparing the B/D and C/D ratios with theoretical models, it is possible to estimate the effective temperature, metallicity and absorbing column density. I reevaluated the theoretical curves of Allen & Fabian (1997) using a more recent model of an isothermal gas: the XSPEC 10 MEKAL model based on the calculations of Mewe and Kaastra with Fe L calculations by Liedahl (Mewe et al. 1985; Liedahl et al. 1995) with an absorbing PHABS screen (Balucinska-Church & McCammon 1992).

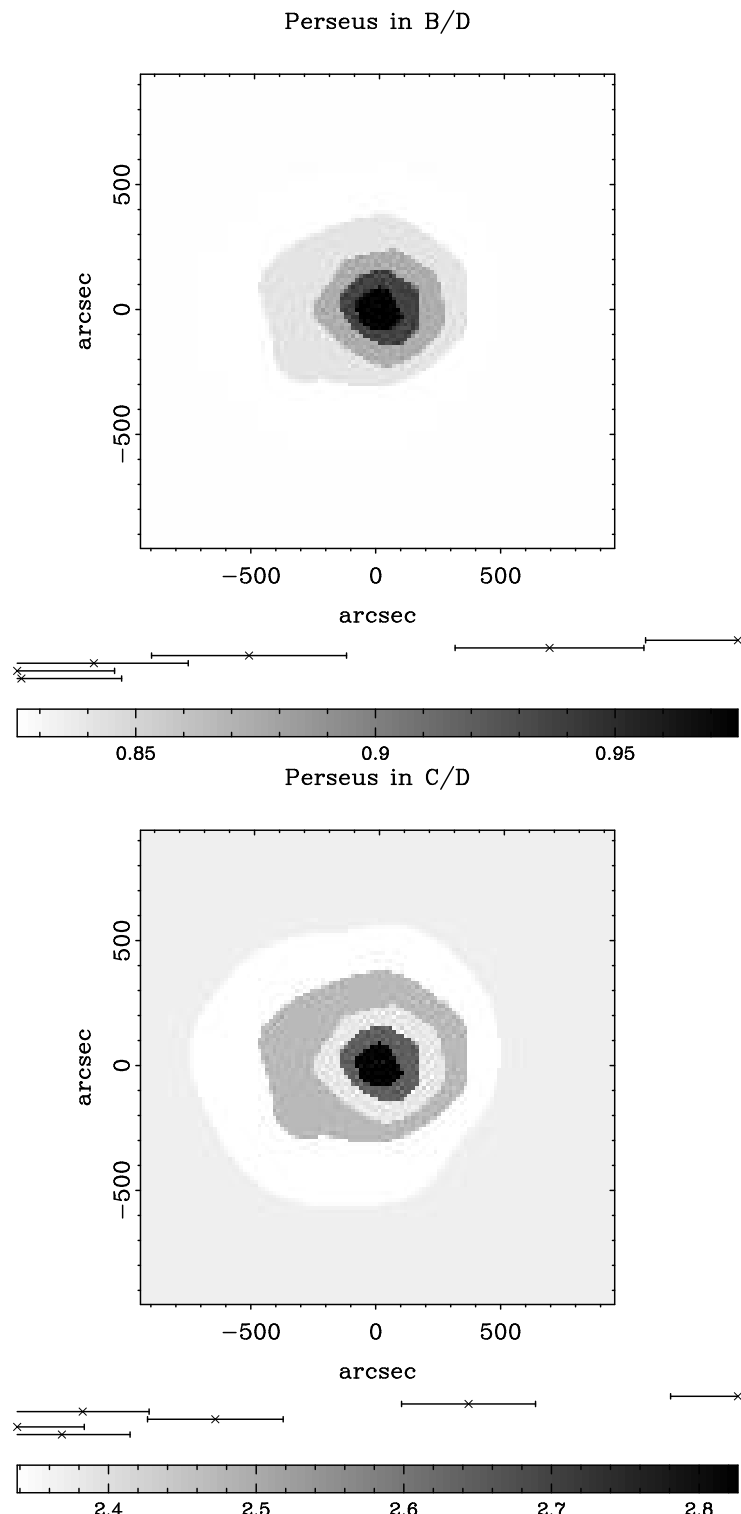


Figure 2.8: Contour colour maps of the Perseus cluster. Areas between contours are coloured by their average X-ray colour. The points below the maps show the numerical colours, with $1-\sigma$ errors. The most central contours are the uppermost points. Darker areas indicate softer emission.

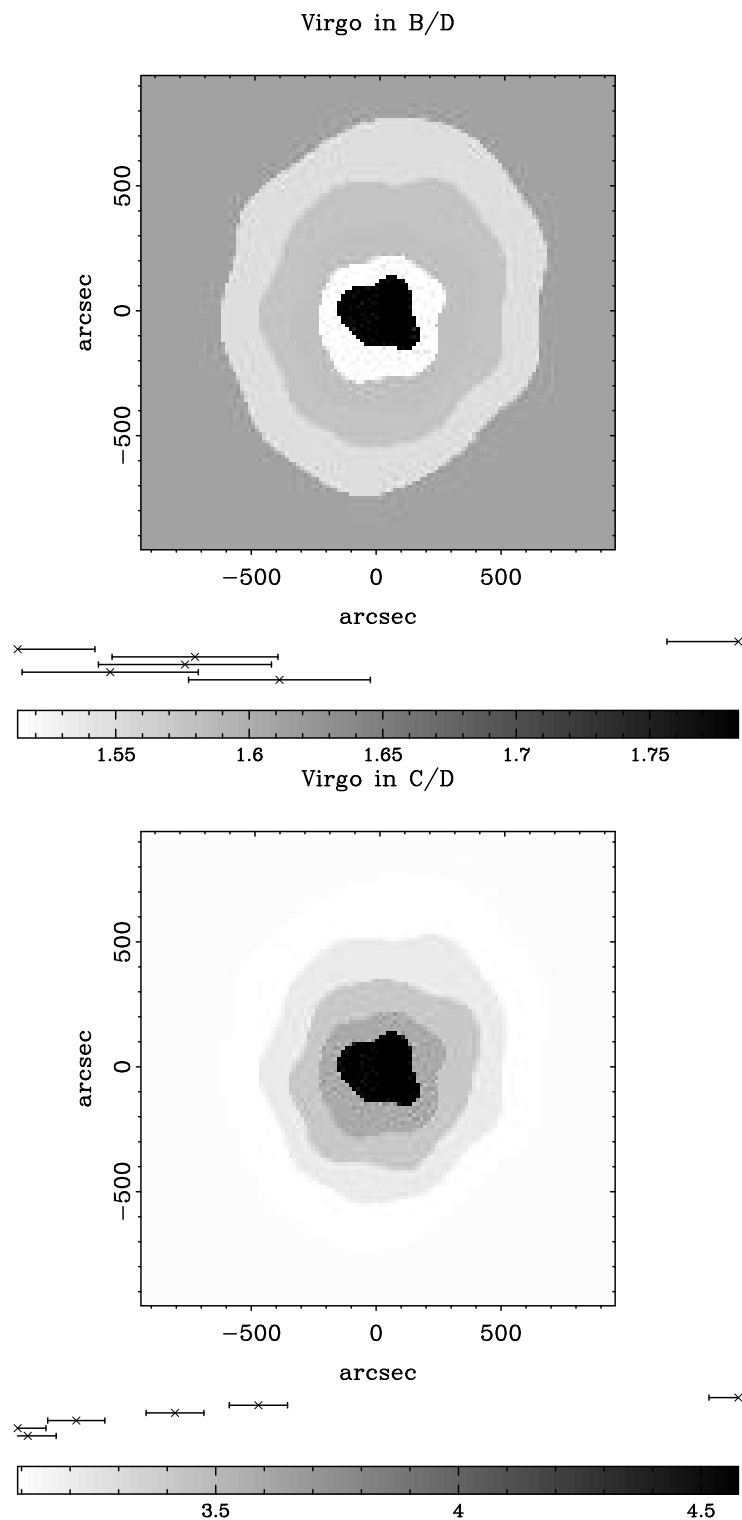


Figure 2.9: Contour colour maps of the Virgo cluster (see Fig. 2.8 for a description).

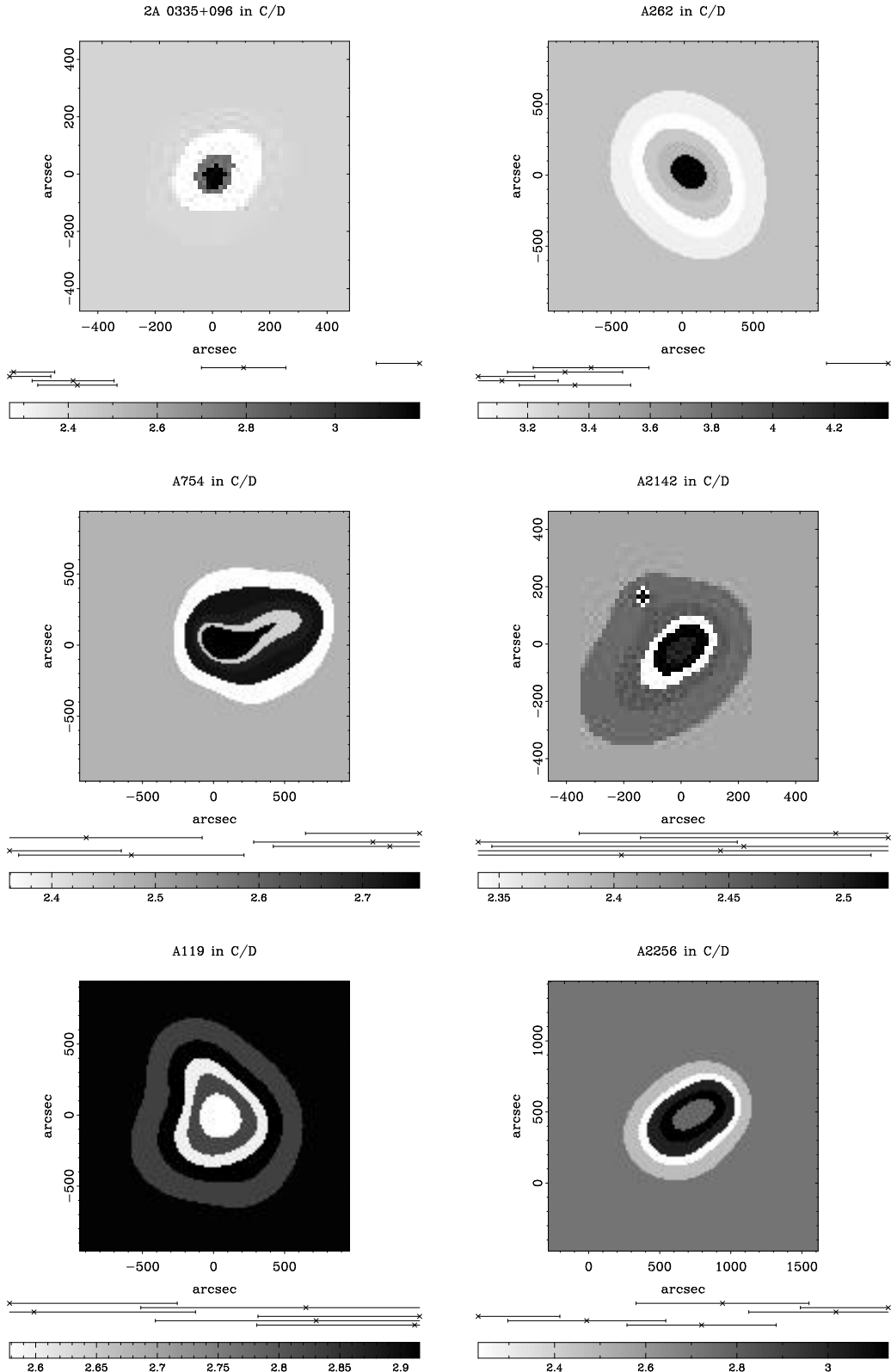


Figure 2.10: A selection of C/D contour colour maps (see Fig. 2.8 for a description). The upper two clusters contain cooling flows. The others are non-cooling-flow, or low \dot{M} cooling flow, clusters.

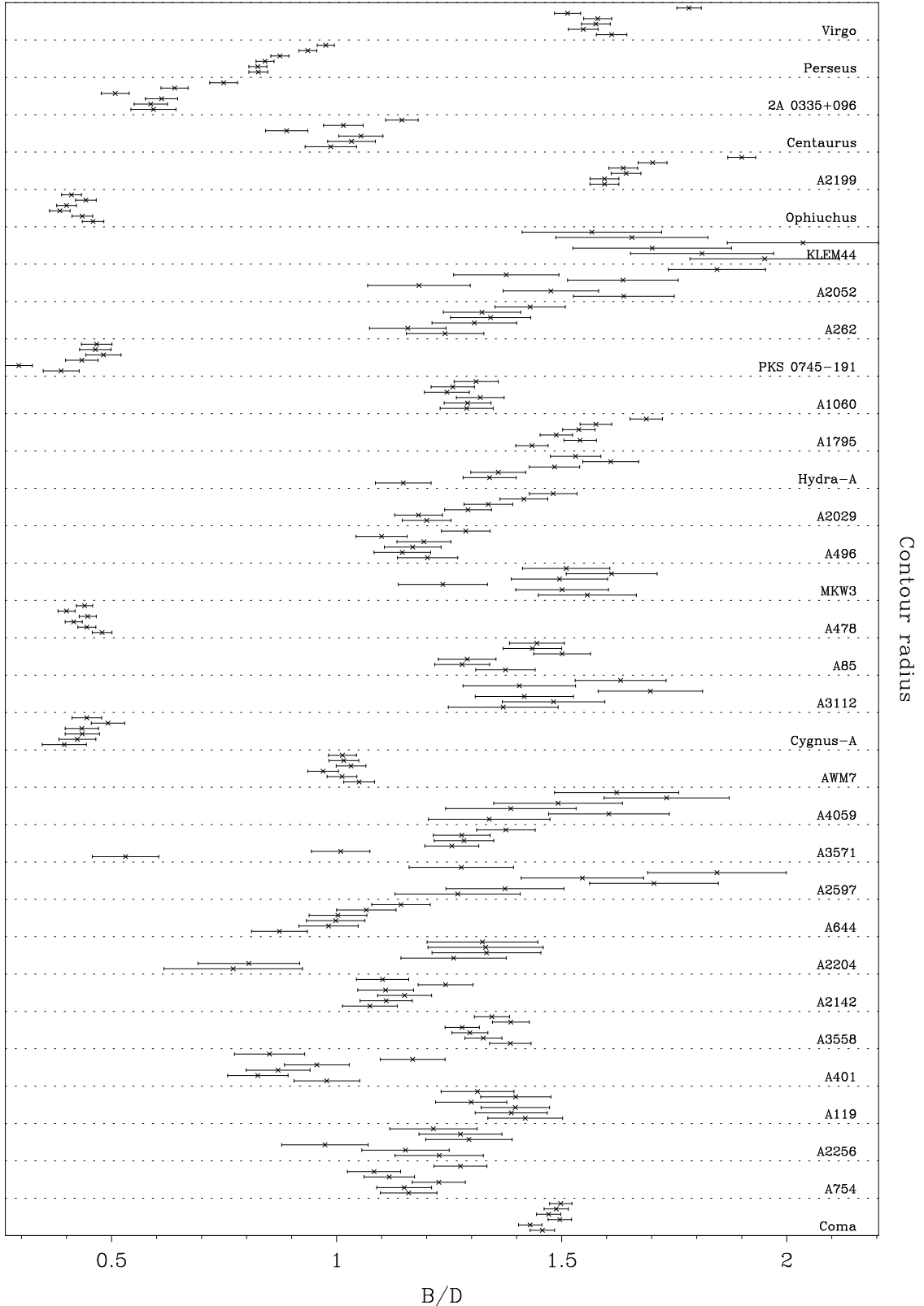


Figure 2.11: Variation of the ratio B/D for the sample of clusters. Each point represents the colour of a contour. The uppermost points represent the innermost contours, numbered 1.

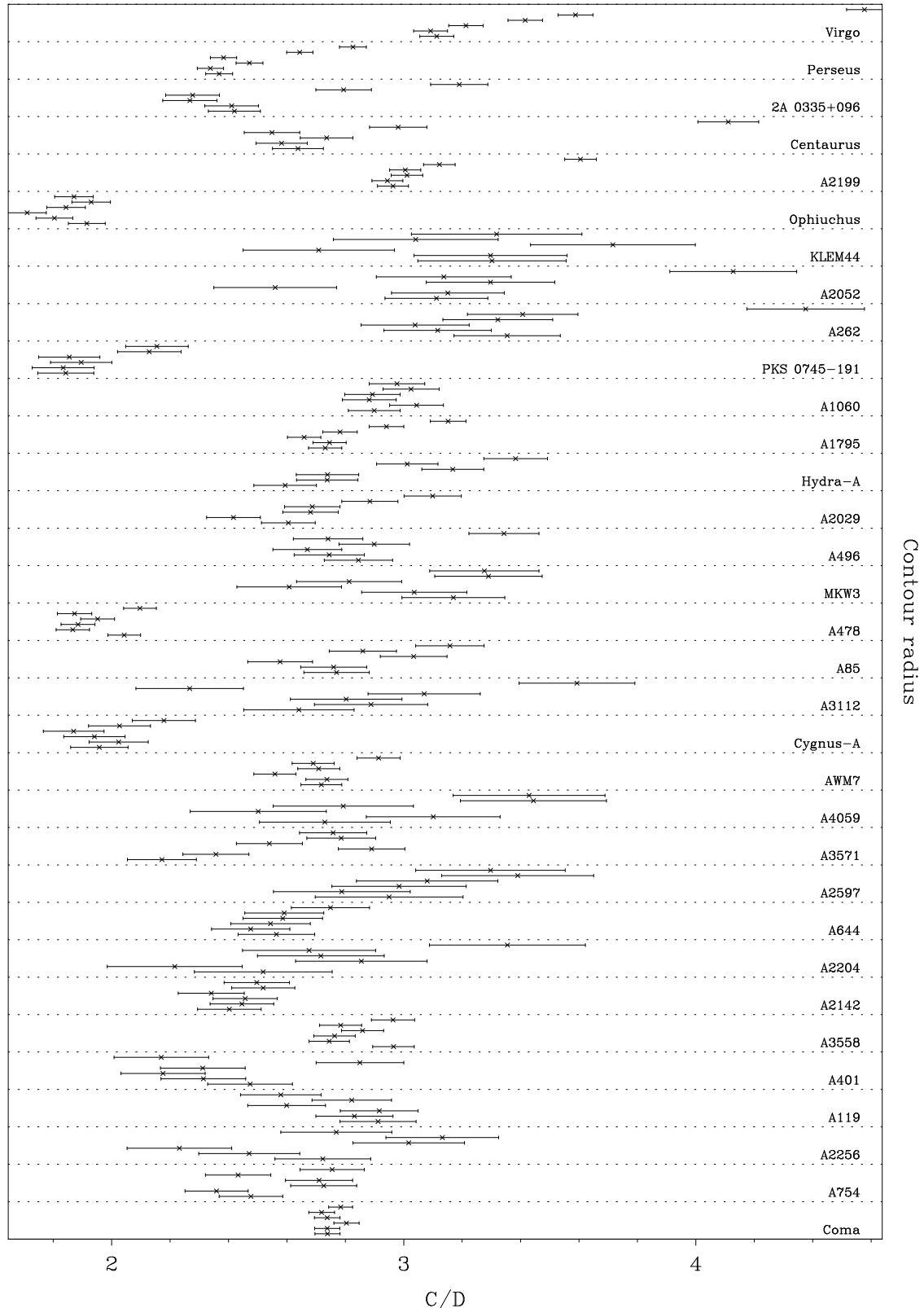


Figure 2.12: Variation of the ratio C/D for the sample of clusters. Each point represents the colour of a contour. The uppermost points represent the innermost contours, numbered 1.

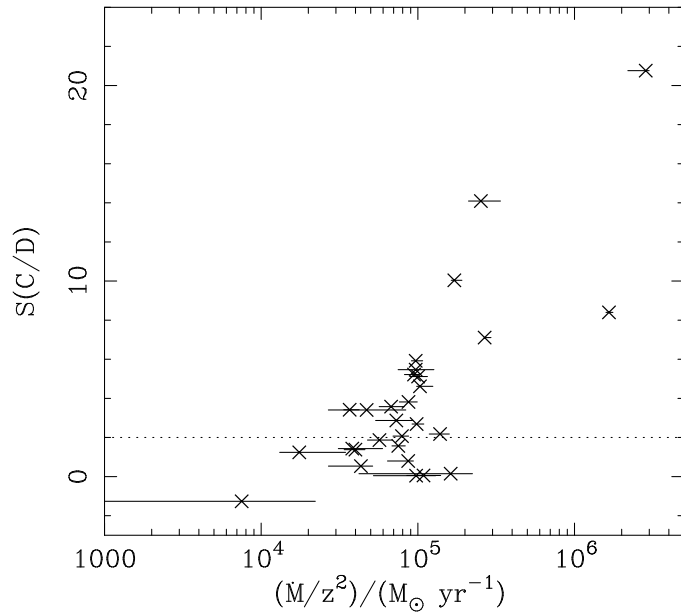


Figure 2.13: Plot of cooling flow flux, \dot{M}/z^2 , against the significance measure of a colour gradient $S(C/D)$ (See Section 2.3). The 2- σ significance level is indicated by a dotted line.

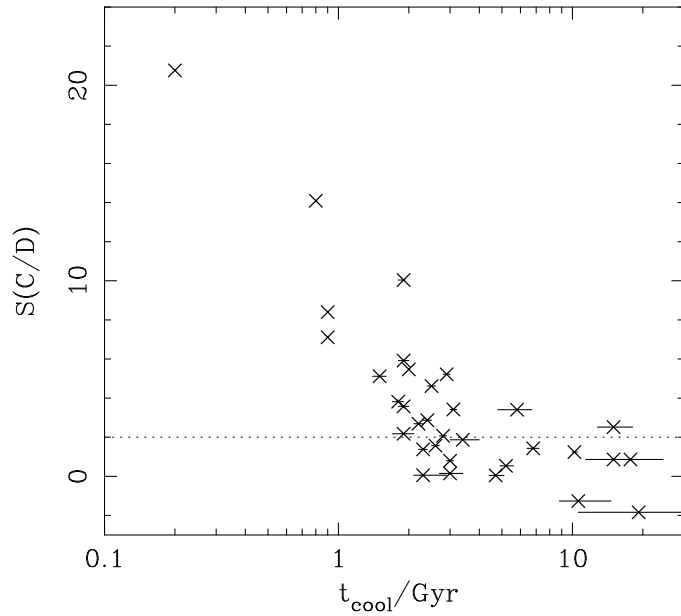


Figure 2.14: Plot of the central cooling time, t_{cool} , against the significance measure of a colour gradient $S(C/D)$ (See Section 2.3). The 2- σ significance level is indicated by a dotted line.

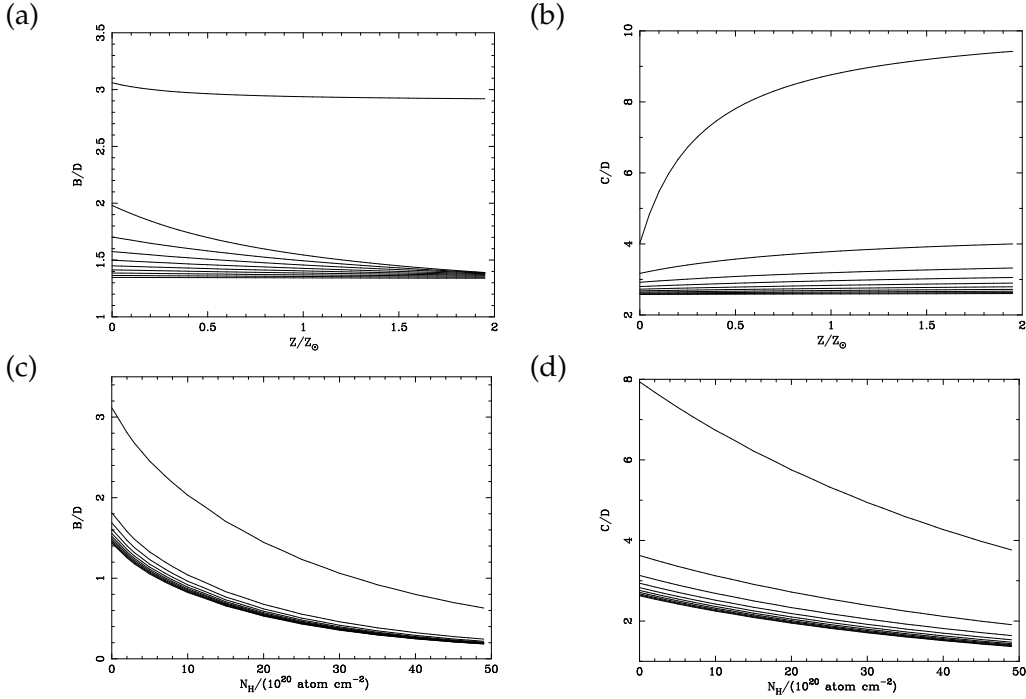


Figure 2.15: Theoretical predictions for the B/D and C/D ratios for an isothermal gas at temperatures of 1–10 keV. The lines show steps of 1 keV in temperature. The lowest temperature is the highest ratio on the vertical axis. (a) B/D and (b) C/D as functions of metallicity at fixed column density ($N_H = 10^{20}$ atom cm $^{-2}$). (c) B/D and (d) C/D as functions of column density at fixed metallicity ($Z = 0.5Z_\odot$).

I iterated the calculation of the B/D and C/D colour ratios over the parameter space $0 \leq N_H/(10^{20} \text{ cm}^{-2}) \leq 20$, $0 \leq Z/Z_\odot \leq 2$, and $1 \leq k_B T/\text{keV} \leq 10$, where N_H is the column density of the absorbing screen, and Z and T are the metallicity and temperature of the plasma. Projections of the ratios for constant Z or N_H are shown in Fig. 2.15. The colours were calculated for an object of redshift of 0.01. The clusters in the sample examined are all at low redshift, therefore it can be assumed that they are all at a redshift of 0.01 (See Section 2.1). The predictions of the model show some differences from those of Allen & Fabian (1997), particularly at low temperatures where the colour ratios are higher than those predicted before.

I calculated, too, the colour ratios expected for a cooling flow model (Johnstone et al. 1992) with an absorbing screen (shown in Fig. 2.16). The gas was modelled cooling to 0.001 keV over the same range of abundance, upper temperature and absorbing column density as the isothermal gas model.

A first step was to fit the C/D colour ratios for the contours of a cluster with a single component isothermal model. I assumed galactic absorption, $N_{H,\text{gal}}$, for each cluster and a constant metallicity of $Z_{\text{clust}} = 0.3 Z_\odot$. By taking the average fitted temperature of the outer three contours I derived an isothermal temperature of each cluster, T_{iso} . Table 2.4 shows the fitted isothermal temperature for each cluster with the galactic absorption

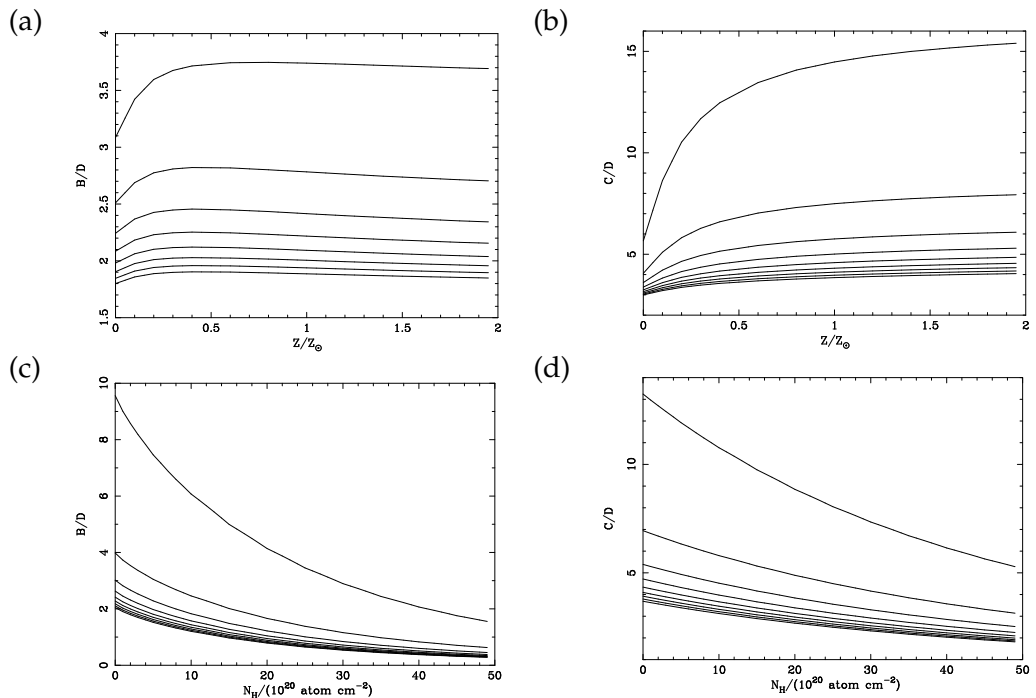


Figure 2.16: Theoretical predictions for the B/D and C/D ratios for an gas cooling from temperatures of 1–10 keV to 0.001 keV. The lines show steps of 1 keV in temperature. The lowest temperature at the highest ratio on the vertical axis. (a) B/D and (b) C/D as functions of metallicity at fixed column density ($N_H = 10^{20}$ atom cm $^{-2}$). (c) B/D and (d) C/D as functions of column density at fixed metallicity ($Z = 0.5Z_{\odot}$).

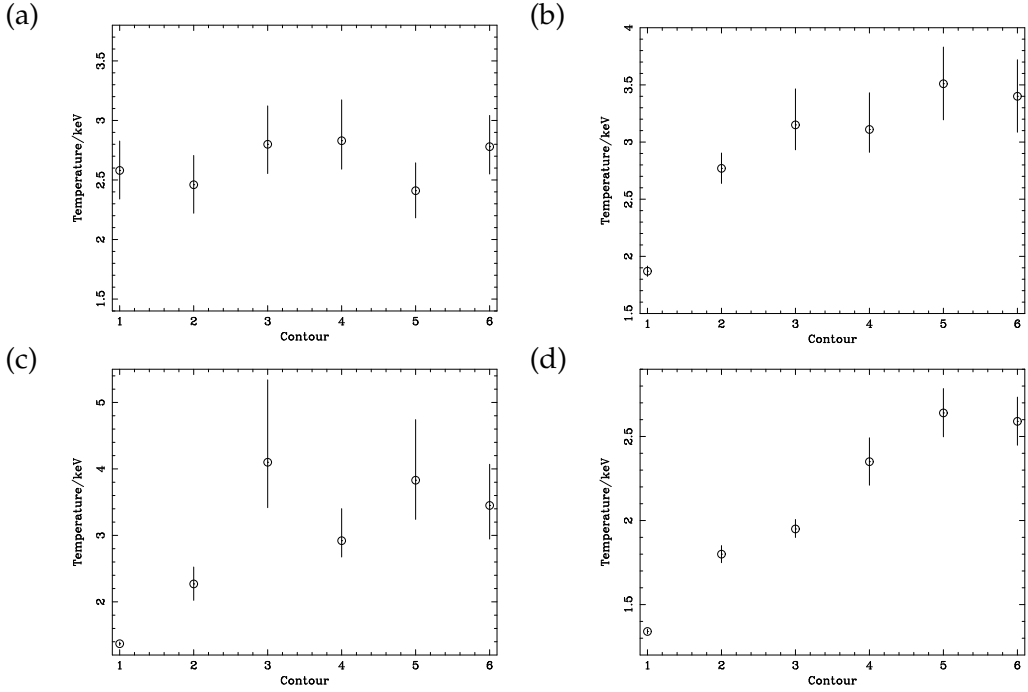


Figure 2.17: Temperature profiles generated by fitting constant galactic obscuring column density and constant $0.3 Z_{\odot}$ abundance to the C/D colour profile. The clusters are (a) A1060 (non-cooling-flow), (b) A2199, (c) Centaurus and (d) Virgo. The errors are $1-\sigma$, generated from the errors in C/D . The contours are numbered from innermost to outermost.

used. The galactic column densities listed were obtained using the FTOOLS NH program (Dickey & Lockman 1990), except for A478, PKS 0745-191 and A3112, for which I used the values quoted in White (2000) obtained by spectral fitting, where the values were significantly different from the Dickey & Lockman (1990) results.

Temperature profiles were created by fitting the C/D colours with an isothermal model with fixed absorption and metallicities. They are shown for a sample of four clusters in Fig. 2.17. The errors in the temperatures were propagated directly from the errors in the observed C/D ratio (The errors in the abundances and absorptions were assumed to be zero). Three of the clusters are known cooling flow clusters. Applying the isothermal model to each contour shows a temperature decrease from the outer regions of the clusters to their centres. For the non-cooling-flow cluster there is no evidence of this temperature change. This is generally the case for this sample of clusters. Those with strong cooling flows show a temperature decrease, except for those masked by a strong galactic column.

2.4.1 Fitting cooling flow models

To test whether a contribution from a cooling flow model was appropriate to fit the C/D colour of the cluster, I added a cooling flow component to the isothermal model. If the number of counts observed in a particular band is denoted by X_{obs} , an isothermal model

Cluster	$N_{H,\text{gal}}$	ΔN_H	$S(\Delta N_H)$	$k_B T_{\text{iso}} / \text{keV}$
Virgo	2.54	13.7 ± 0.7	19.0	2.5 ± 0.1
Perseus	14.9	3.1 ± 1.1	2.8	3.4 ± 0.2
2A 0335+096	17.8	10.0 ± 4.5	2.2	3.1 ± 0.4
Centaurus	8.06	22.7 ± 2.4	9.3	3.4 ± 0.4
A2199	0.86	1.2 ± 0.4	2.9	3.3 ± 0.2
Ophiuchus	20.3	4.7 ± 3.4	1.4	> 10.0
KLEM44	1.56	4.1 ± 1.6	2.5	3.3 ± 1.5
A2052	2.71	4.7 ± 2.8	1.7	4.3 ± 0.8
A262	5.37	13.1 ± 3.7	3.6	2.2 ± 0.2
PKS 0745-191	35.0	-5.0 ± 5.8	-0.9	3.2 ± 0.7
A1060	5.47	-0.5 ± 1.5	-0.3	2.7 ± 0.2
A1795	1.19	0.6 ± 0.4	1.5	5.8 ± 0.8
Hydra A	4.94	2.4 ± 1.4	1.7	4.1 ± 0.9
A2029	3.05	1.0 ± 1.3	0.7	7.0 ± 1.1
A496	4.58	5.3 ± 2.2	2.4	3.7 ± 0.7
MKW3s	3.04	2.2 ± 2.2	1.0	3.8 ± 1.3
A478	30.0	9.0 ± 3.0	3.0	3.7 ± 0.5
A85	3.45	2.1 ± 1.5	1.4	4.8 ± 1.3
A3112	4.0	5.0 ± 1.7	3.0	3.8 ± 1.9
Cygnus A	34.7	5.4 ± 6.6	0.8	2.6 ± 0.3
AWM7	9.81	4.3 ± 1.6	2.7	3.0 ± 0.2
A4059	1.10	2.6 ± 2.4	1.0	6.1 ± 1.6
A3571	3.71	-3.8 ± 3.0	-1.3	7.7 ± 0.2
A2597	2.49	7.4 ± 2.9	2.6	3.3 ± 1.7
A644	6.82	-3.9 ± 2.9	-1.3	5.0 ± 1.9
A2204	5.67	-3.4 ± 5.3	-0.6	6.2 ± 1.5
A2142	4.20	0.7 ± 1.8	0.4	> 10.0
A3558	3.89	1.5 ± 1.0	1.4	3.5 ± 0.3
A401	10.5	-2.7 ± 3.3	-0.8	6.8 ± 1.4
Coma	0.918	-0.3 ± 0.4	-0.8	5.2 ± 0.4
A754	4.37	1.6 ± 1.8	0.9	7.4 ± 0.7
A2256	4.10	1.8 ± 3.2	0.6	7.7 ± 0.8
A119	3.44	-1.4 ± 1.6	-0.8	3.2 ± 0.5

Table 2.4: Table showing the clusters and their calculated excess absorption ΔN_H (units $10^{20} \text{ atom cm}^{-2}$). Also shown is the used galactic column density, $N_{H,\text{gal}}$ (units $10^{20} \text{ atom cm}^{-2}$), and the significance of the excess absorption, $S(\Delta N_H)$. The clusters are listed in cooling flux order (\dot{M}/z^2). The outer contour of A3571 was ignored as it was suspected to have background contamination. T_{iso} is the isothermal temperature calculated from the outer contours, which is limited to a maximum of 10 keV.

predicts a count of $X_{\text{iso}}(Z, T, N_H)$, a cooling flow model predicts $X_{\text{cf}}(Z, T, N_H)$, where T in this case denotes the upper cooling temperature, and the models are normalised by the values N_{iso} and N_{cf} , then we can write

$$B_{\text{obs}} = N_{\text{iso}} B_{\text{iso}}(Z, T, N_H) + N_{\text{cf}} B_{\text{cf}}(Z, T, N_H), \quad (2.4)$$

$$C_{\text{obs}} = N_{\text{iso}} C_{\text{iso}}(Z, T, N_H) + N_{\text{cf}} C_{\text{cf}}(Z, T, N_H), \text{ and} \quad (2.5)$$

$$D_{\text{obs}} = N_{\text{iso}} D_{\text{iso}}(Z, T, N_H) + N_{\text{cf}} D_{\text{cf}}(Z, T, N_H). \quad (2.6)$$

By solving the above equations we can find the cooling flow fraction in a particular band. In Band C the cooling flow fraction is

$$\begin{aligned} f_C &= \frac{N_{\text{cf}} C_{\text{cf}}}{N_{\text{iso}} C_{\text{iso}} + N_{\text{cf}} C_{\text{cf}}} \\ &= \frac{C_{\text{cf}}(C_{\text{iso}} - [\frac{C}{D}]_{\text{obs}} D_{\text{iso}})}{[\frac{C}{D}]_{\text{obs}} (D_{\text{cf}} C_{\text{iso}} - C_{\text{cf}} D_{\text{iso}})}. \end{aligned} \quad (2.7)$$

Note that the model predictions, X_{iso} and X_{cf} are functions of metallicity, absorbing column density and temperature. I made the assumption of constant metallicity, isothermal temperature (or upper cooling temperature) and obscuration by galactic column. Those clusters with strong cooling flows show large cooling flow fractions at their centres. In Fig. 2.18 the C band cooling flow fraction profiles are shown for the four example clusters. The errors plotted take account only of the uncertainties in the C/D ratio.

2.4.2 Calculating intrinsic absorption

By rearranging equations (2.4), (2.5) and (2.6), we can predict the observed B/D colour from the C/D colour and the models. Rearranging,

$$\left[\frac{B}{D} \right]_{\text{pred}} = \frac{\left[\frac{C}{D} \right]_{\text{obs}} - \frac{C_{\text{cf}}}{D_{\text{cf}}}}{\frac{C_{\text{iso}}}{B_{\text{iso}}} - \frac{C_{\text{cf}} D_{\text{iso}}}{B_{\text{iso}} D_{\text{cf}}}} + \frac{\left[\frac{C}{D} \right]_{\text{obs}} - \frac{C_{\text{iso}}}{D_{\text{iso}}}}{\frac{C_{\text{cf}}}{B_{\text{cf}}} - \frac{C_{\text{iso}} D_{\text{cf}}}{B_{\text{cf}} D_{\text{iso}}}}. \quad (2.8)$$

Using this equation, I found that the predicted B/D colour did not match the observed value for most of the inner regions of the cooling flow clusters. The B/D ratio is more sensitive to absorption than the C/D ratio (Fig. 2.15 and 2.16). Assuming the difference between the observed and predicted values of B/D is due to intrinsic absorption, then it is possible to use the above equation to find the increase in absorption. I varied the obscuring column density to find $\{B, C, D\}_{\{\text{iso}, \text{cf}\}}$ until the predicted B/D ratio from equation (2.8) was the same as the observed one.

Profiles were created showing the required extra absorption above galactic as a function of contour for each cluster. Those clusters with strong cooling flows show an increase in absorption at their centres. Fig. 2.19 shows profiles of the required extra ab-

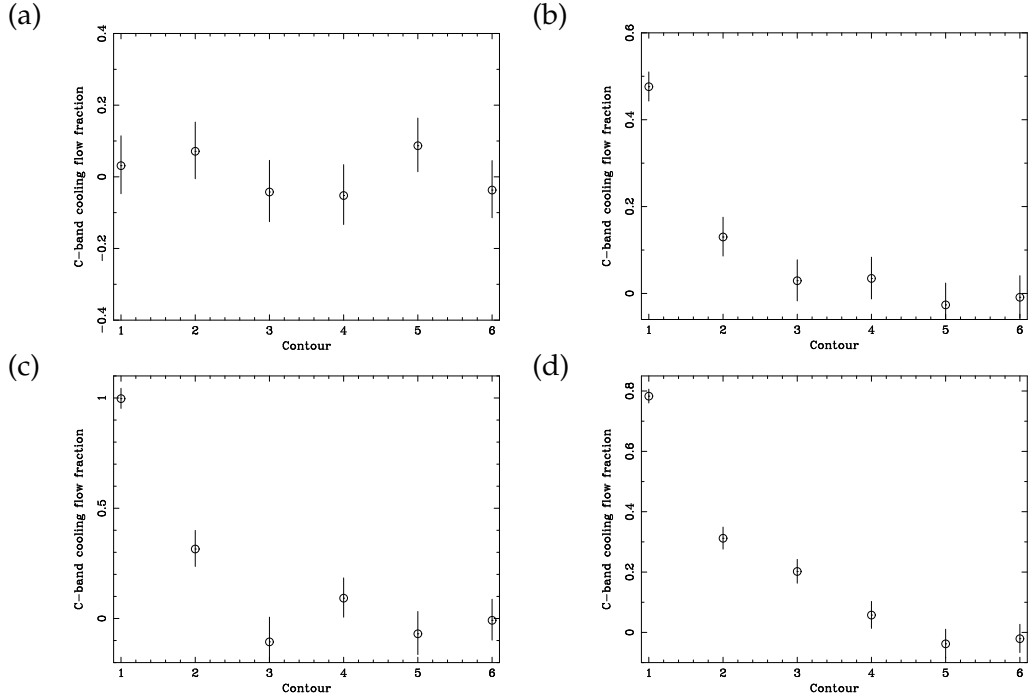


Figure 2.18: Profiles showing how the fractional cooling flow component must increase to fit the C/D ratio assuming isothermal gas in each contour, constant galactic column density and constant $0.3 Z_{\odot}$ abundance. The clusters are (a) A1060 (non-cooling-flow), (b) A2199, (c) Centaurus and (d) Virgo. The errors are $1-\sigma$, generated from the errors in C/D . The contours are numbered from innermost to outermost.

sorption for the four example clusters. Listed in Table 2.4 are the required absorption increases for each cluster in the sample. This value is the difference between the absorption in the central contour and the mean of the two outer ones. The mean of the two outer contours was taken to decrease the chance of background contamination. I looked at the difference in absorption between the centre and outside of the cluster, rather than the absolute difference from the central absorption to the galactic absorption, because the galactic absorption value is uncertain for many clusters. The errors on the values assume that all uncertainty is due to the observed B/D ratio. $S(\Delta N_H)$ shows the significance of the increased absorption using an expression with the same form as equation (2.3).

2.4.3 Fitting metallicity gradients

In the previous calculations I assumed that the metallicity in the cluster was constant. In order to test whether the required extra absorption could instead be fitted by metallicity variations, I minimised the function

$$\chi^2(Z) = \left\{ \frac{[B/D]_{\text{obs}} - [B/D]_{\text{iso}}(Z, T_{\text{iso}}, N_{H,\text{gal}})}{\sigma_{[B/D]_{\text{obs}}}} \right\}^2$$

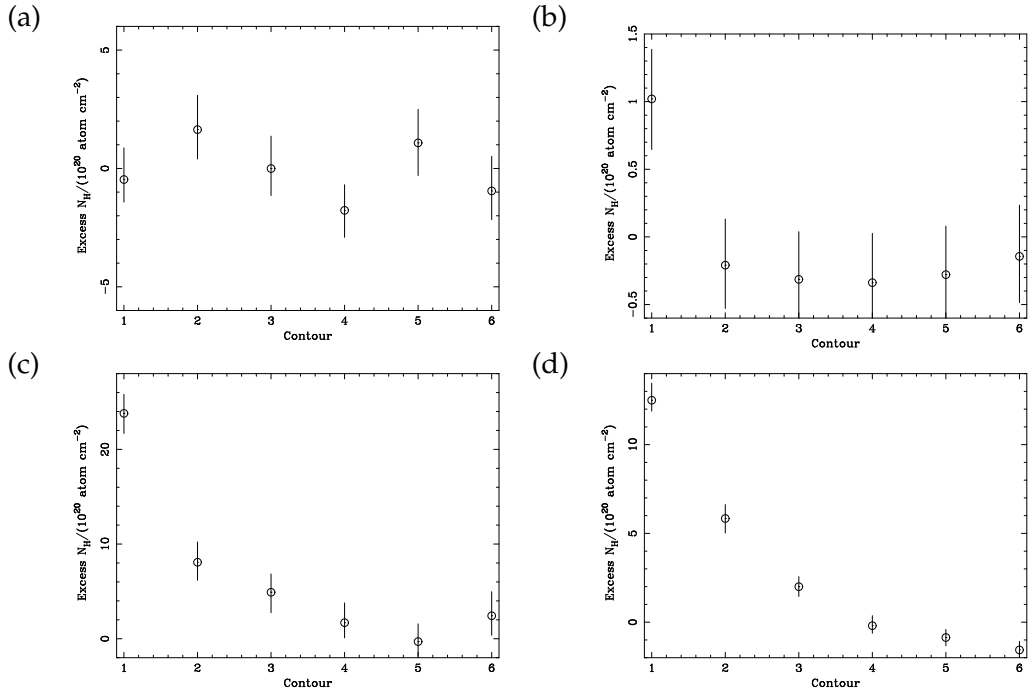


Figure 2.19: Profiles showing how the intrinsic absorption must increase assuming an isothermal temperature, constant galactic column density and a constant $0.3 Z_{\odot}$ abundance. These were calculated by assuming the cooling flow components above, and calculating the extra required column density above galactic to explain the B/D ratio, assuming constant $0.3 Z_{\odot}$ abundance. The errors are $1-\sigma$, and were generated from the error in B/D , the error in the cooling flow component is ignored. The clusters are (a) A1060 (non-cooling-flow), (b) A2199, (c) Centaurus and (d) Virgo. The contours are numbered from innermost to outermost.

$$+ \left\{ \frac{[C/D]_{\text{obs}} - [C/D]_{\text{iso}}(Z, T_{\text{iso}}, N_{H,\text{gal}})}{\sigma_{[C/D]_{\text{obs}}}} \right\}^2, \quad (2.9)$$

to find the optimum value of Z , where $[B/D]_{\text{obs}}$ and $[C/D]_{\text{obs}}$ are the observed contour colour values, $\sigma_{[B/D]_{\text{obs}}}$ and $\sigma_{[C/D]_{\text{obs}}}$ are their respective errors, and $[B/D]_{\text{iso}}$ and $[C/D]_{\text{iso}}$ are the predicted isothermal values as a function of Z .

This analysis showed that simply using an isothermal gas with a metallicity gradient was not a good fit to the observed data in the inner parts of the clusters. The fitted metallicity was $0.9Z_{\odot}$ for the inner contour of the Virgo cluster data, but the χ^2 value was ~ 600 , and so the fit was very poor. Most of the other strong cooling flows showed similar results.

2.5 Discussion

2.5.1 Adaptively-smoothed images

Many of the cooling flow clusters in the sample show relatively featureless elliptical images after adaptive smoothing. I show some interesting ones, those of the Perseus, Virgo and A2199 clusters, in Fig. 2.5, 2.6 and 2.7. The clusters show structure which appears to vary between the different bands. It is difficult to assess how significant the variation is.

2.5.2 The sample of clusters

Fig. 2.11 and 2.12 show that clusters with low galactic latitude, or those masked by regions of high absorption, show low B/D and C/D colours. These clusters include, for example, Ophiuchus, PKS 0745-191 and Cygnus A. Looking at Fig. 2.1, we would expect high absorption to give a low B/D ratio and a reduced C/D ratio.

Those clusters with strong cooling flows show large C/D ratios, or softer X-rays, at their centres, with large C/D gradients moving towards their centres. These include, for example, Virgo, Perseus, 2A 0335+096, Centaurus and A2199. They therefore contain cool gas at small radii, within a few arcminutes of the centre. This can be seen by comparison with the theoretical curves in Fig. 2.15. The only way of achieving the gradient is by adding cooler gas (Section 2.4.3). Those clusters without strong cooling flows do not show this strong colour gradient, for example, Coma, A2256 and A119.

2.5.3 Comparison with models

The isothermal temperatures derived using the isothermal model in the outer regions of the clusters agree in most cases with those derived from *ASCA* data (White 2000). There are a few clusters, most of which are absorbed by high galactic column densities, for

which I find unusually low temperatures. These include Perseus, PKS 0745-191, A478 and Cygnus-A. I was able to reproduce the Perseus *ASCA* temperature result using a column of 10^{21} cm^{-2} .

Those clusters with strong cooling flows show good evidence of absorbing material at their centres. For example Virgo, Centaurus, Perseus and A478 all show significant increased levels of absorption. There is no evidence for absorbing material in those clusters without cooling flows. Abundance gradients in cooling flow clusters have been observed, for example in the Centaurus cluster (Fukazawa et al. 1994), the Virgo cluster (Matsumoto et al. 1996) and AWM7 (Ezawa et al. 1997), with metallicities decreasing outwards from their cores. There is some degeneracy between the level of the absorption and the metallicity of the gas within the *B/D* colour. At low temperatures metallicity has its strongest effect (Fig. 2.15), so if I have overestimated the levels of absorption, then it will be primarily for those clusters with metallicity gradients. However, I found that metallicity gradients were not sufficient by themselves to account for the observed colour gradients.

The PSPC detector limits the energy bounds of the observations. There are too few independent energy bands to make more than two colours, which limits the complexity of the model (and number of parameters) I can fit to the data. More colours will help to completely resolve any degeneracy between metallicity and absorbing column density. Data from *Chandra* will help solve this problem. The increased effective area of the telescope will also improve the statistics, reducing the uncertainties in the colours, or allowing us to sample smaller areas of the clusters.

Allen & Fabian (1997) used a partial screening model in conjunction with a deprojection method on their data. Using a partial screening model results in larger column densities than those predicted without. Doing a similar analysis would show larger levels of absorption in the clusters, however it would add unnecessary complexity to the procedure. I also did not take the absorption results from the *B/D* colour to check for consistency with the *C/D* ratio, but I do not expect increased absorption to modify the *C/D* colour significantly.

The contouring method presented in this chapter has one main limitation: the assumption that colour gradients are mirrored by brightness gradients. If the brightness of the cluster stays constant over an area where the spectrum changes, then this method will not allow the change to be seen. I address this problem with the adaptive binning method in Chapter 3.

2.6 Conclusions

I have presented an analysis of X-ray colour maps. The analysis technique attempts to group areas of the image together in order to maximise the signal to noise of the results, but preserving information about the structure of the object. The data from telescopes

such as *Chandra* and *XMM-Newton* will show large variations in count rate, and will need analysis which is more intelligent than simple binning.

I created colour X-ray maps of the cores of a sample of 33 clusters, almost doubling the sample of Allen & Fabian (1997). The profiles generated from these maps show that there is cooling gas at the centres of those clusters with strong cooling flows. There is no evidence for cooling gas in clusters inferred from imaging deprojection or other methods to have weak, or no, cooling flow. I find a clear anti-correlation between the central cooling time of a cluster and the C/D colour gradient significance. The central cooling time is an indicator of the quality of cooling flow data. I also find a correlation between the cooling flow flux and the C/D significance. The maps of the non-cooling-flow clusters contain more structure as a group than those clusters with cooling flows.

I fitted a single-phase isothermal model to the C/D colour of each of the contours of a sample of clusters. Those clusters with strong cooling flows show a significant decrease in the fitted temperatures of their inner contours relative to their outer contours. I added a cooling flow component to the model with the same upper temperature as the isothermal plasma. Those clusters with cooling flows required the addition of a significant fraction of a cooling flow model in their centres to account for the C/D colour. To fit the observed B/D colour I required the addition of extra absorbing material at the centres of the strong cooling flow clusters. An isothermal gas with a varying metallicity instead of absorption was also not able to fit the data. This provides more evidence that cooling flows accumulate cold material (as in Section 1.1.6). There was no evidence for intrinsic absorbing material in those clusters without cooling flows.

3

Adaptive binning

Summary

This chapter describes the method of *adaptive binning*, an original method I have developed to bin images according to the local count rate. The algorithm can create colour maps and intensity maps where the fractional error on the colour or intensity is less than a threshold value across the map. This chapter formed the basis of the paper *Adaptive binning of X-ray galaxy cluster images* (Sanders & Fabian 2001).

Firstly, I describe the reasons for the development of the algorithm, and other possible ways of approaching the problem. I then describe the algorithm in detail, in particular applying it to real and simulated examples. Finally I discuss modifications to the basic method and their implications.

3.1 Introduction

A problem often encountered with the processing of images, especially those from X-ray telescopes, is that there is a large dynamic range present in intensity. In order to examine the structure of emission in regions of an image where there are few photons, it is necessary to bin the data using bins of large angular size. An alternative is to smooth the data with a Gaussian kernel of large angular size. Conversely, to examine structure in areas of high emission a small bin-size or kernel is sufficient. If one wishes to examine regions with a wide variation in count-rate, then some procedure which has a variable bin or kernel is required to create statistically optimal maps.

Another related problem, which motivated the work which led to this chapter, is the creation of optimal colour maps. The ratio of photon counts in different energy bands in a low intensity region will have a large associated statistical error, so the counts need to be averaged over a large region to form the ratio. The algorithm needs to account for the statistical accuracy in the separate bands, not just the total image.

This problem led onto another related problem: the problem of creating optimal maps showing the two-dimensional distribution of a parameter to a model fitted to spectra extracted from the image.

These problems can be illustrated with some examples. Fig. 3.1 shows colour images of a *Chandra* observation of the centre of the Centaurus cluster (which I discuss in Chapter 5). It shows the soft (0.5-1.5 keV) to hard (1.5-7 keV) ratio formed by a variety of methods. (a) and (b) were made by binning the two individual bands into 2 and 4 arcsec bins, respectively, and then dividing. The individual bands in (c) and (d) were binned into 1 arcsec bins, and then smoothed with a Gaussian of width $\sigma = 1$ arcsec and 2 arcsec, respectively, and then dividing. The images show that if the count-rate in an image significantly varies, it is impossible to show detail and eliminate noise by simple binning. Before I describe adaptive binning, I show in Fig. 3.2 it applied to the image of the Centaurus cluster.

3.1.1 ASMOOTH

One technique which allows structure on a wide range of scales to be revealed is adaptive kernel smoothing (Ebeling et al. 2002; Huang & Sarazin 1996). The ASMOOTH algorithm of Ebeling et al. (2002) convolves an image with a Gaussian kernel (or alternately top-hat) which varies in size over the image. If the signal within the kernel when applied to part of an image is of a chosen minimum significance above the local background, then the convolved signal is added to the output image. The kernel is increased in size until all the counts in the input image are added to the output image.

This following section describes the ASMOOTH routine in more detail (the description is condensed from Ebeling et al. 2002). If the input data to the smoothing routine is $I(\vec{r})$, the position on the image is given by \vec{r} , and the kernel function which describes the smoothing is \mathcal{K} , then the smoothing is given by the convolution

$$I'(\vec{r}) \equiv I(\vec{r}) \otimes \mathcal{K}(\vec{r}) = \int_{\mathbb{R}^2} \mathcal{K}(\vec{r} - \vec{r}') I(\vec{r}') d\vec{r}' \quad (3.1)$$

$$\left(\int_{\mathbb{R}^2} \mathcal{K}(\vec{r}) d\vec{r}' = 1 \right)$$

ASMOOTH adjusts its smoothing scale so that at each position in the output image, each pixel has the same signal-to-noise above the background (specified by the input parameter τ_{\min}).

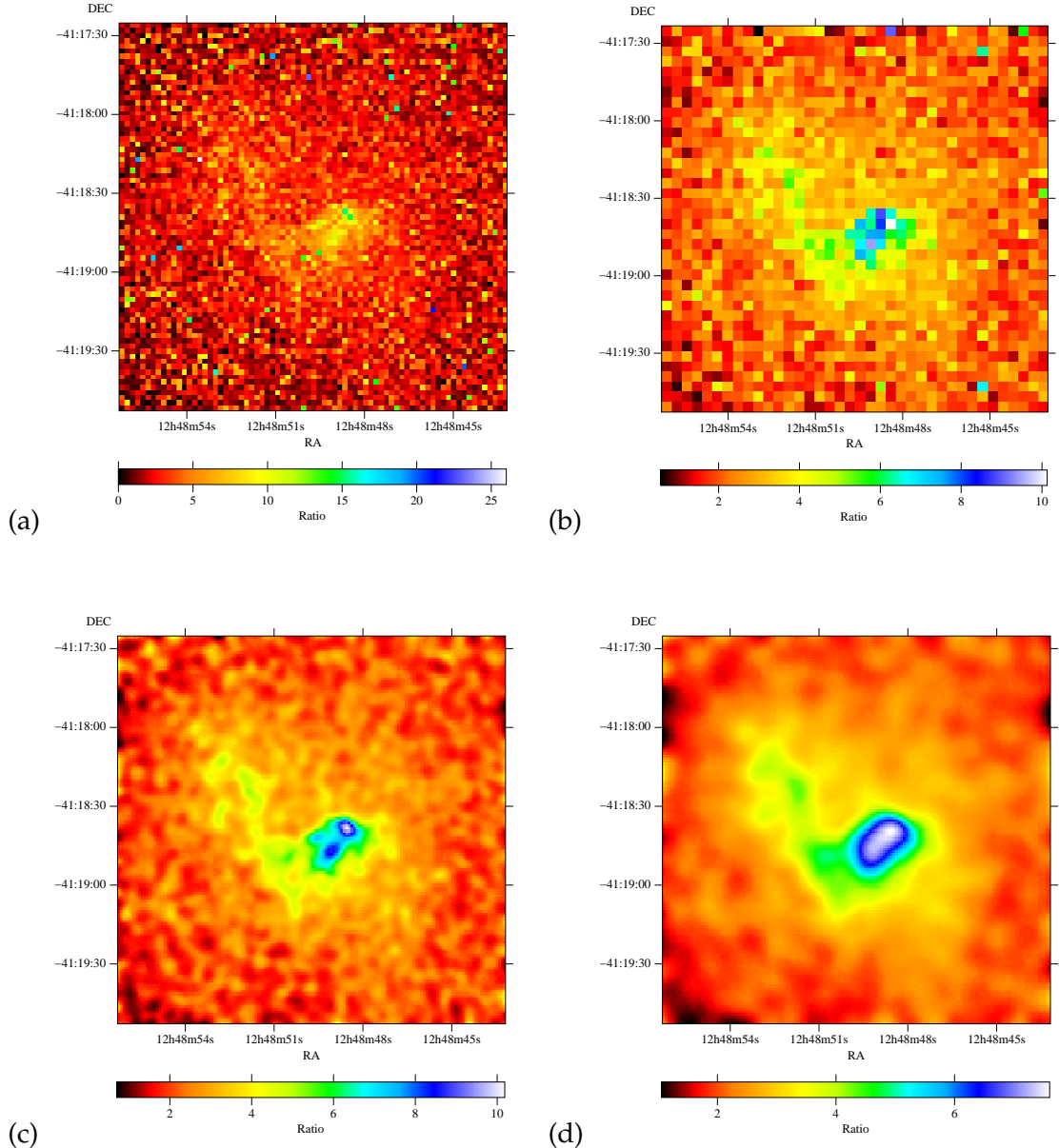


Figure 3.1: Colour images of the centre of the Centaurus. The images were made from the ratio of two energy bands 0.5-1.5 keV and 1.5-7 keV. (a) Images in each band were binned to give 2 arcsec pixels before dividing; (b) images in each band were binned with 4 arcsec pixels before dividing; (c) images in each band were binned by 1 arcsec, then smoothed with a Gaussian with a σ of 1 arcsec; (d) images in each band were binned by 1 arcsec, then smoothed with a Gaussian with a σ of 2 arcsec.

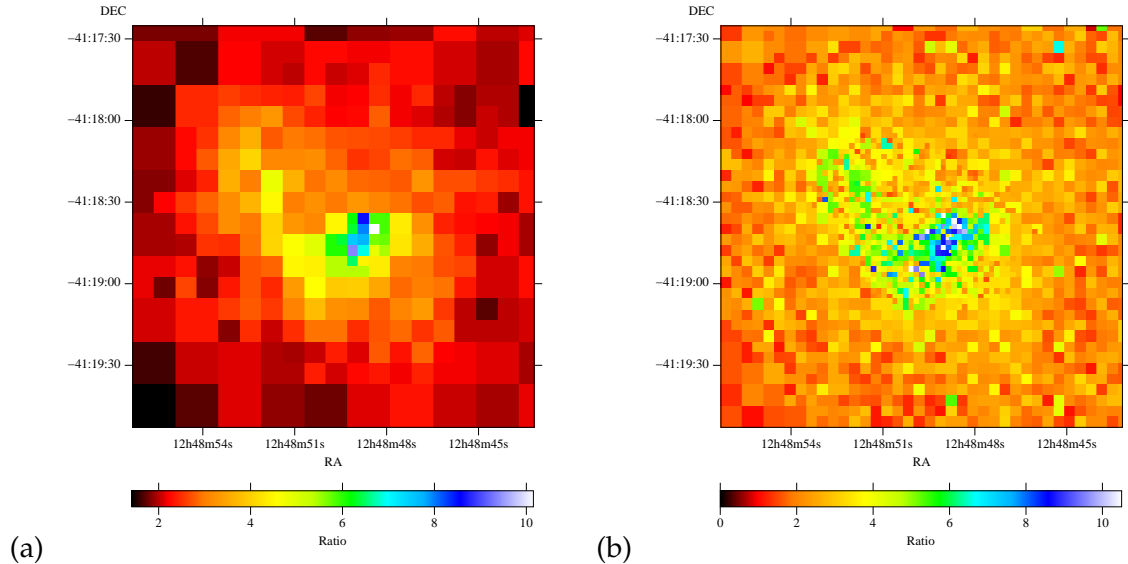


Figure 3.2: Adaptively-binned colour images of the centre of the Centaurus cluster. (a) was adaptively binned to give a colour with an error threshold of 12 per cent, whilst (b) was binned with a threshold of 30 per cent.

The kernel for Gaussian smoothing has the form

$$\mathcal{K}(\vec{r} - \vec{r}', \sigma(\vec{r})) = \frac{1}{2\pi\sigma(\vec{r})^2} \exp\left(-\frac{|\vec{r} - \vec{r}'|^2}{2\sigma(\vec{r})^2}\right), \quad (3.2)$$

where σ gives the characteristic size of the kernel as a function of position, or the top-hat function

$$\mathcal{K}(\vec{r}', \sigma) = \begin{cases} 1/(\pi\sigma^2) & \text{where } |\vec{r}'| < \sigma \\ 0 & \text{elsewhere} \end{cases}, \quad (3.3)$$

The routine converts τ_{\min} and the optional parameter τ_{\max} into minimum and maximum numbers of counts to be covered by the kernel, N_{\min} and N_{\max} . The formula used is

$$\tau_{\min|\max} = \frac{N_{\min|\max} - N_{\text{bkg}}}{\sqrt{N_{\min|\max} + N_{\text{bkg}}}}, \quad (3.4)$$

where N_{bkg} is the integral number of background counts under the kernel. The relationship relating N_{min} and N_{max} to I' and \mathcal{K} is

$$N_{\min} \leq I'(\vec{r})/\mathcal{K}(\vec{0}, \sigma(\vec{r})) \leq N_{\max}. \quad (3.5)$$

The algorithm increases the smoothing scale using discrete steps, accumulating the smoothed image:

$$I'_{\text{AKS}}(\vec{r}) = \sum_i I'_i(\vec{r}) = \sum_i I_i(\vec{r}) \otimes \mathcal{K}(\vec{r}, \sigma_i), \quad (3.6)$$

where σ_i starts from an initial value matched to the pixel size ($1/\sqrt{\pi}$ for a Gaussian, or

$1/\sqrt{9\pi}$ for a top-hat), and $I_i(\vec{r})$ is given by

$$I_i(\vec{r}) = \begin{cases} I(\vec{r}) & \text{where } N_{\min} \leq I'(\vec{r})/\mathcal{K}(\vec{0}, \sigma_i) \leq N_{\max} \\ 0 & \text{elsewhere.} \end{cases} \quad (3.7)$$

It is worth mentioning that data smoothing in general has a somewhat murky reputation. However, to quote from Press et al. (1989):

Data smoothing is probably most justified when it is used simply as a graphical technique, to guide the eye through a forest of data points all with large error bars. [...] Data smoothing is least justified when it is used subjectively to massage the data this way and that, until some feature in the smoothed curve emerges, and is pounced on in support of an hypothesis.

ASMOOTH is very good at finding low surface brightness features, such as filaments. It is especially useful for producing images for display, and for identifying bright features against a background. It is not a universal smoothing tool, however, and care needs to be taken before using it in a particular situation. For instance, it is designed to identify positive features against a background, but not to identify ‘holes’ in emission. However, this problem is fixed in the next version of the routine. Owing to the way it identifies significance against the local background, it may produce spurious features in areas where there is bright flat emission, for instance the cores of galaxy clusters, where Poisson noise may become significant. Used with care, ASMOOTH is a useful routine in many situations.

3.1.2 Wavelet transforms

A wavelet transform (Grossmann & Morlet 1984) is a mathematical technique which has come from the field of signal and image analysis. It is particularly good for looking for structure on different scales. In two dimensions the transform is simply (Starck & Pierre 1998)

$$w_a(x, y) = I(x, y) \otimes \psi\left(\frac{x}{a}, \frac{y}{a}\right), \quad (3.8)$$

where a is the scale parameter (which identifies over what scale size we are interested in looking for structure), and ψ is the wavelet function. The wavelet function corresponding to a Mexican hat is

$$\psi(x, y) = (1 - x^2 + y^2) \exp\left(-\frac{x^2 + y^2}{2}\right). \quad (3.9)$$

The so called *à trous* wavelet transform algorithm is generally used in more recent work, as it allows easy image reconstruction (e.g. Slezak et al. 1994). The image is

decomposed into the transformed images, (w_1, \dots, w_n, c_n) , so

$$I(x, y) = c_n(x, y) + \sum_{j=1}^n w_j(x, y). \quad (3.10)$$

Various methods can be used to determine whether the wavelet coefficient $w_j(x, y)$ is significant or not (see Starck & Pierre 1998 for further discussion and references). Once the transform is done, the image can be reconstructed using those wavelet coefficients which have a significance above a certain threshold.

One of the main uses of the transform in the field of X-ray astronomy is to look for substructure in galaxy clusters (e.g. Slezak et al. 1994) The scale length of the wavelet function is adjusted to look for subclusters on a certain scale. The end results of a set of wavelet transforms is a set of output images, each showing the significant of substructure on a certain spatial scale.

The wavelet transform is an interesting alternative to adaptive smoothing for looking for substructure. It may be interesting to apply it in a similar way as ASMOOTH was in Chapter 2, to plot the colour within significance contours. It is difficult to see how it could apply to making colour maps, without assuming as in Chapter 2 that a colour gradient follows a brightness gradient.

3.1.3 Adaptive binning

The analysis method outlined in this chapter, *adaptive binning*, was originally developed to produce temperature, column density and colour maps of the Perseus cluster, the results of which are shown in Chapter 4 and Fabian et al. (2000). I required a simple algorithm to compare the relative fluxes in different X-ray bands to a theoretical plasma emission model. In order to be able to show the variation in colour over space, it is necessary to bin or smooth the data. Binning, rather than smoothing (Gaussian or otherwise), is a better method for producing spatial estimates of counts for analysis, because it does not spread counts around an image beyond the boundaries of the bin. Each bin can be taken as an independent statistical entity.

In this chapter I use data from the 24 ks ACIS-S *Chandra* X-ray observation of the Perseus cluster, Abell 426, which is discussed in Chapter 4, to demonstrate the adaptive binning method. The Perseus cluster is the brightest X-ray cluster in the sky, and contains a large cooling flow (Fabian 1994) with a mass deposition rate of approximately $300 M_\odot \text{ yr}^{-1}$. Interesting substructure in the cluster due to its central radio source makes it an ideal object for my purpose. I will not attempt here to analyse the physics behind the observations, which is left to Chapter 4 and further work. I also study the method by applying it to simulated data.

The algorithm is presented here in a logically consistent way, from intensity adaptive binning to colour adaptive binning. Colour binning, as mentioned above, was the

original motivation, developed to analyse X-ray colour cluster images.

3.2 Intensity binning

Adaptive intensity binning is the simplest case of the algorithm. It attempts to adaptively bin a single image based on the number of photons in each region. The basic method is to bin pixels in two-dimensions by a factor of two, until the fractional Poisson error of the count in each bin becomes less than or equal to a threshold value. When the error is below this value, those pixels are not binned any further. The algorithm, in detail, is as follows.

1. Each pixel in the image is put into its own ‘bin’, the term used in this chapter for a collection of pixels. A pixel here means one of the individual picture elements which form the input image. Essentially the image is initially divided into ‘imaginary’ 1×1 pixel bins.
2. If there are n_i pixels in bin i , the total count in the bin is c_i , and the background per pixel is b , the net count in the bin is simply defined by

$$s_i \equiv c_i - n_i b. \quad (3.11)$$

This assumes there is a constant number of background photons over the image. The algorithm can be modified to allow a varying background.

3. The fractional error on the net count in the bin is

$$\frac{\sigma_{(s_i)}}{s_i} = \frac{\sqrt{c_i + n_i b}}{c_i - n_i b}. \quad (3.12)$$

This is also the error on the average count in each pixel.

4. If the fractional error is less than or equal to a threshold value, then the pixels in the output image which correspond to the pixels in the input bin are set to the mean count, s_i/n . The fractional error of the net count in the bin is also stored in the pixels in an ‘error image’. Additionally the bin is marked as having been processed. If this is the last iteration over the image, and all the remaining pixels are in a single bin, then that bin is treated as having a fractional error less than the threshold.
5. If the bin was not processed, then it is merged into its neighbouring three bins (if they are unprocessed), to make new bins containing 2×2 of the previous bins. The four bins with the lowest x and y coordinates (lowest declination and highest right-ascension) are merged, as is each consecutive set of four bins. Any bins which have already been processed are ignored in the merging. It is useful to remember

(a)	35	43	21	24
	42	105	24	21
	22	23	20	23
	23	21	20	22

(b)	35	43	21	24
	42	105	24	21
	22	23	20	23
	23	21	20	22

(c)	40	40	21	24
	40	105	24	21
	22	23	20	23
	23	21	20	22

(d)	40	40	22	22
	40	105	22	22
	22	22	22	22
	22	22	22	22

Figure 3.3: Example demonstrating the intensity adaptive binning process. The bottom-left pixel is the origin, $(0, 0)$. See the text for details.

we are considering a bin as a list of pixels. Pixels which have already been set in the output image are ignored in future iterations.

6. The process is repeated from 2 until there is only a single bin remaining.
7. A ‘bin-map’ is also produced by the algorithm, giving an identification number for each processed bin in terms of the pixels which it contains. Using the bin-map, any image of that size can be binned using the same bins.

3.2.1 Demonstration

A simple demonstration of the algorithm operating on a 4×4 pixel image is shown in Fig. 3.3. I demonstrate the process using a threshold fractional error of 0.1 and no background counts. (a) shows the image before binning. We first look for individual pixels (bins of 1×1 pixels) with a Gaussian fractional error in the count less than or equal to the threshold. Only one pixel does; it is shown ‘painted’ in (b). We then bin the remaining pixels by a factor of 2. We examine the binned pixels to see whether any have errors less than the threshold. The three pixels in the top-left corner do, so they are averaged together and painted in (c). We then bin again with a 4×4 pixel bin. The remaining pixels have an error less than the threshold, so they are averaged and painted in (d), the final output image. Had the error on the final bin been larger than the threshold, it would have been binned anyway.

3.2.2 Real example

I show in Fig. 3.4 a ‘raw’ image of the Perseus cluster in the 0.5–7 keV band from the *Chandra* observation, binned with 2 arcsecond pixels. The image has been exposure-corrected. It also has been corrected for the readout node lines of the ACIS-S detector (this smears out the point source at the centre). Contours were placed on the image showing 8 levels spaced equally in square-root space between 20 and 300 counts.

The Perseus cluster is very bright, so we see much structure in the data without doing more than simple binning. The contours shown have been smoothed, but even they break up at large radii owing to the count rate being swamped by Poisson noise.

Fig. 3.5 shows the raw image of Perseus adaptively binned with a threshold fractional error of 0.06. The X-ray background was ignored since it was low, even near the image edges. The contours on the image near the centre match the contours in the raw data well, showing the algorithm works in this regime. At the sides, the bins are quite large and blocky, but otherwise there do not appear to be any edge-effects. There is still noise present in the image, but at a level much reduced from the raw data.

Fig. 3.6 shows the cluster again adaptively binned, but now with a threshold error of 0.04. Note how the bins are larger, but the level of noise is significantly less. A real feature has been lost from the image, however. A point source present in the upper left radio lobe has disappeared. Its counts were merged into rest of the emission from that region.

In Fig. 3.7 is shown the error map for the adaptively-binned map above. In it are easily visible the changes in bin size as the count rate decreases towards the outside. As the count rate decreases, the error of the bins increases until it reaches the threshold, and then the bin-size doubles.

For comparison, Fig. 3.8 shows an adaptively-smoothed (AS) image of the cluster calculated from the data in Fig. 3.4. It was smoothed with a minimum significance of 4σ using the ASMOOTH algorithm of Ebeling et al. (2002). The contours are at the same levels as the raw image.

The AS image contains sharp positive features, such as the edges of the radio lobes. It does not perform as well in the determination of the number of counts in the negative features, such as the radio lobes themselves, where the number of counts per pixel is half that of the raw data. However, the algorithm is designed to find positive features, so using it to look at holes is a misapplication. Also apparent are some edge effects, where ASMOOTH does not find enough counts to place a high significance on the generated features. The edge effects are avoidable by smoothing a larger area of sky than required, and cropping the image thereafter. One disadvantage of this is that ASMOOTH running time increases quickly with image size.

In Fig. 3.9 I show another adaptively-binned image of the Perseus cluster. This, however, was created from data from an observation using the ACIS-I detector on *Chandra*,

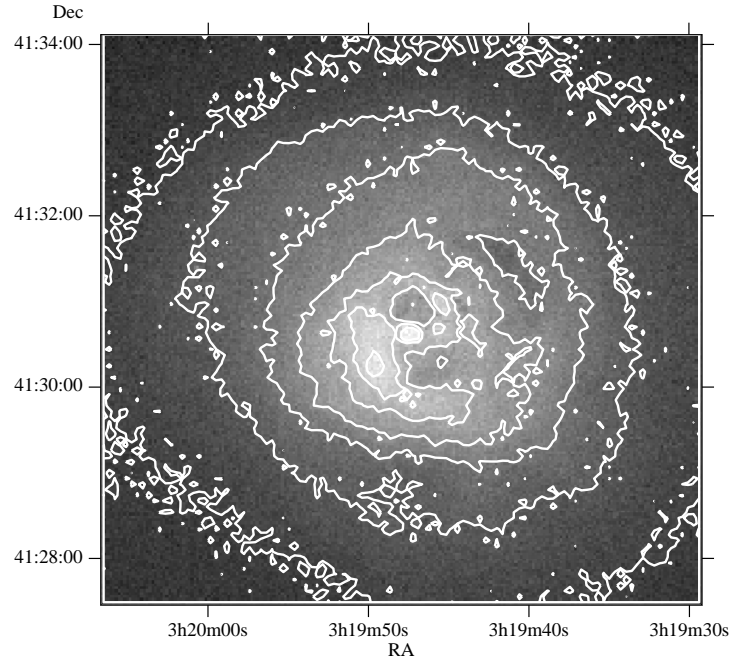


Figure 3.4: Image of cluster binned with 2 arcsec pixels. The image has been corrected for exposure and readout node lines. The 8 contours are spaced on a square-root scale, between 20 and 300 counts per pixel.

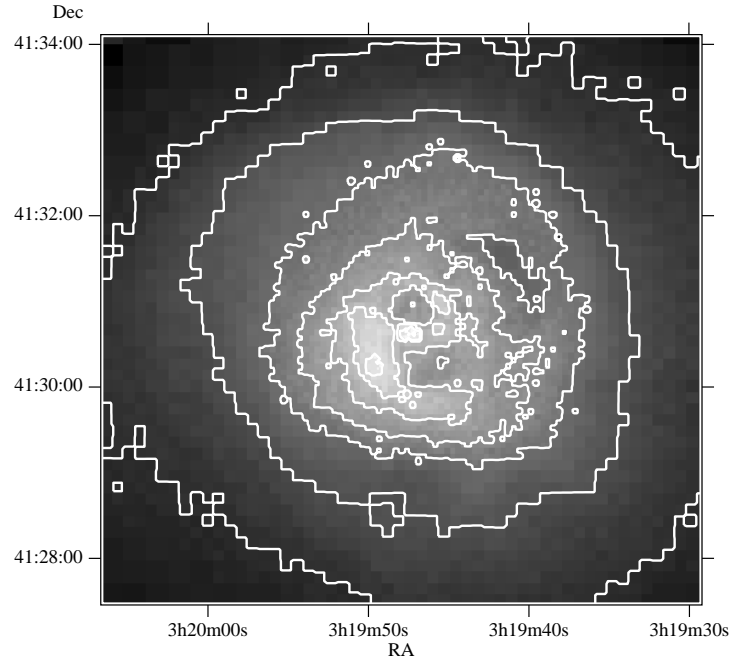


Figure 3.5: Adaptively-binned image of the cluster. The pixel fractional error is set as 0.06. The contours are at the same levels as Fig. 3.4.

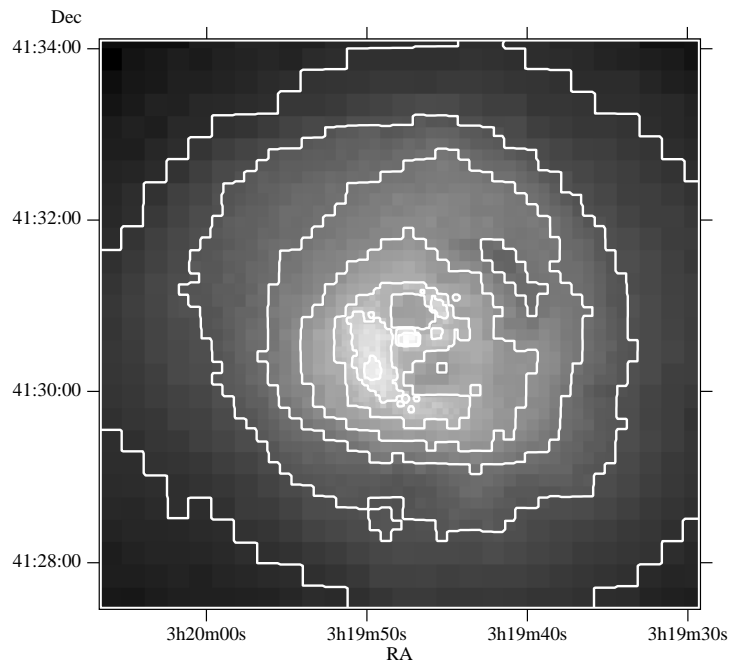


Figure 3.6: Adaptively-binned image of the cluster. The pixel fractional error is set as 0.04. The contours are at the same levels as Fig. 3.4.

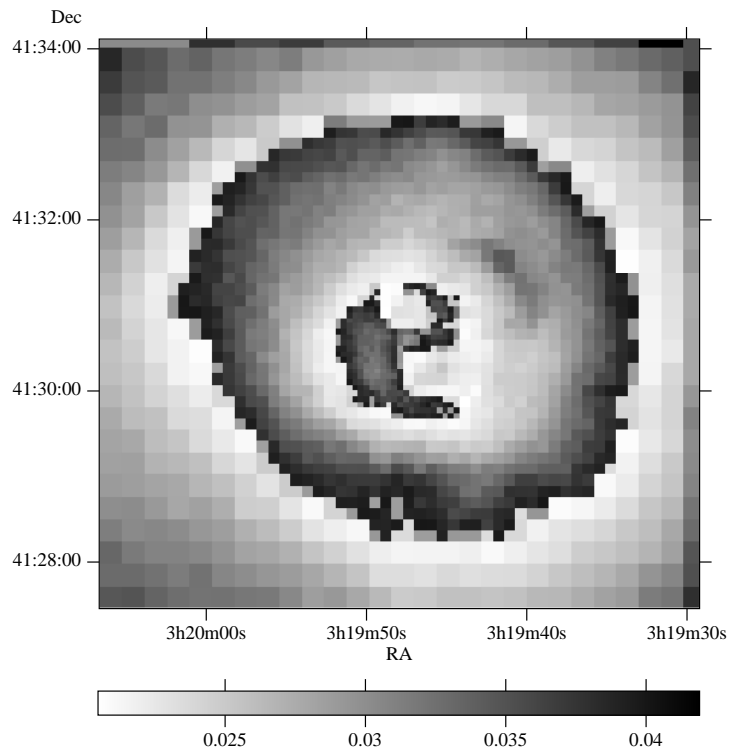


Figure 3.7: Fractional error map for the adaptively-binned image in Fig. 3.6.

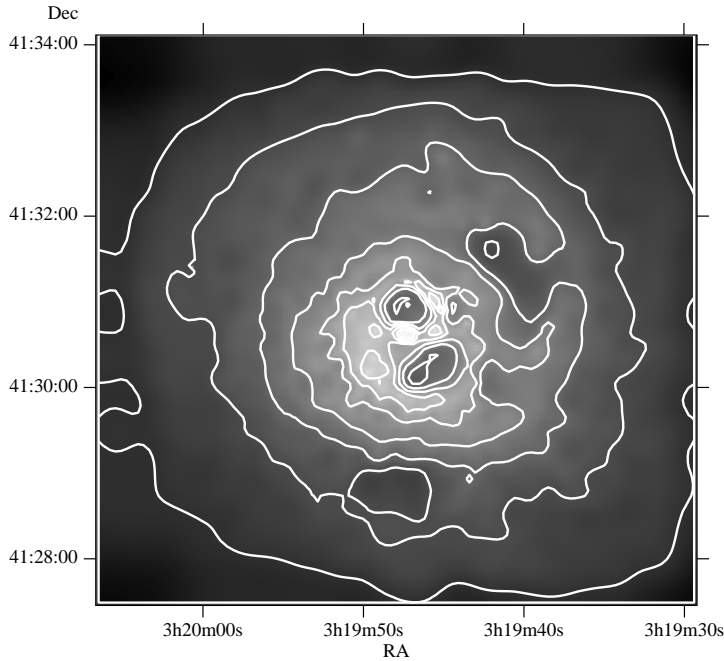


Figure 3.8: Adaptively-smoothed image of the cluster, with a minimum significance of $4-\sigma$. The contours are at the same levels as Fig. 3.4. Note the edge effects in the contours.

with an exposure of 18.6 ks. I present it because the number of counts per pixel is lower than the ACIS-S image, and so it is a good demonstration of the algorithm used on data with more noise.

Adaptive binning of the ACIS-I image brings out an interesting feature of the cluster; it clearly demonstrates that the southern rim of the northern radio lobe (hole) lies south of the nucleus. There is a linear diagonal structure present to the south of the nucleus, running from the north-west to the south-east. This structure is also present in the raw data, but is not clear on the ACIS-S image, despite the longer exposure, as the ACIS-S raw image contains a dark strip owing to the node-line of the detector, where the effective exposure is short.

The dark bin to the south-east of the nucleus shows a ‘stranded bin’, an occasional problem with the algorithm, which I discuss in Section 3.2.3.

3.2.3 Notes on the algorithm

General

1. The algorithm allows bins of width n to contain pixels with coordinates (x, y) in the range $ni \leq x < n(i + 1)$, $nj \leq y < n(j + 1)$, where i and j are integers, and $i \geq 0$, $j \geq 0$. The coordinate origin is $(0, 0)$. x and y increase in the directions of decreasing right-ascension and increasing declination, respectively.
2. If the unbinned image does not have sides which are an equal length of pixels, or

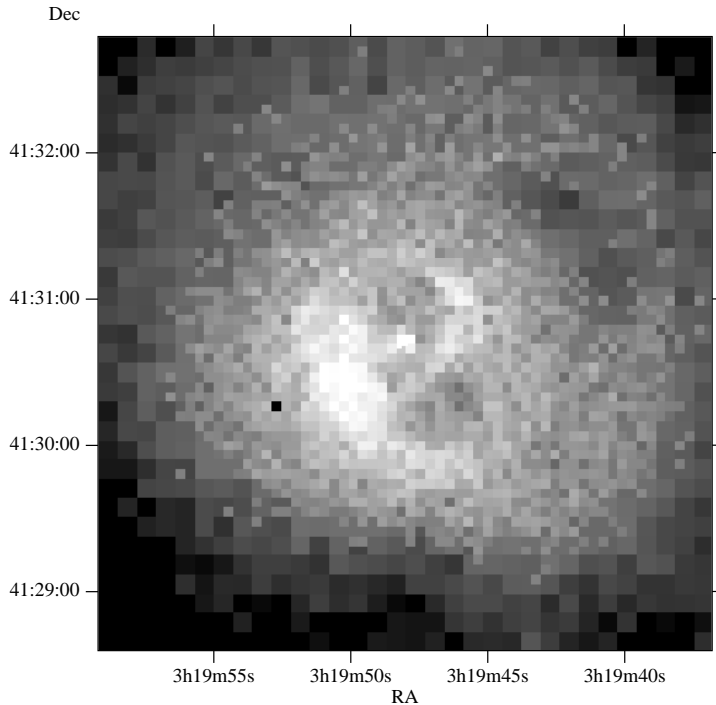


Figure 3.9: ACIS-I adaptively-binned image of the Perseus cluster, using a fractional error of 0.15.

are not a power of two, then the bins on one or both sides will be truncated. This can lead to bins with a small numbers of counts and a large error on the final pass.

3. As is the case with conventional binning, sources with small spatial extent may be split between two bins if they cross a bin boundary. This can be solved by allowing sub-bin positioning, described as follows. For each pass, bins are allowed to be placed at positions displaced by a multiple of some fraction of their length from their conventional positions. The errors are calculated for each possible bin, and the bins are sorted into order of ascending error, discarding those with an error larger than the threshold. The bins are painted in that order, ignoring those bins which had already been partially painted.

The disadvantage of this technique is that the output image appears ‘dithered’. Bins are painted close to one another, but without enough space to put another bin between them. The result is a loose cluster of small bins inside a larger one. The original algorithm appears to produce better results and is less dependent on small variations of errors.

4. The bins are doubled in size between each pass, rather than slowly increased in size, as this ensures a whole number of smaller bins fit inside a larger bin. If this is not the case, then gaps are left between bins in the binning, leading to dithering.

5. Allowing rectangular bins is not useful. It is ambiguous in which direction a rectangle could lie, or be extended. Their use could introduce spurious linear structures into the output image.
6. The use of non-square bins is a possible technique. Any two dimensional object that tiles together could be used, but it is not clear what is the optimal shape. Square bins are a good choice for a number of reasons, including the fact that pixels are naturally square in most detectors; square bins act as scaled pixels. However, there is probably some room for additional work to find better shapes, and I investigate that further in Section 3.4. An alternative idea is to use contour levels in an AS image to define ‘bins’, as demonstrated in Chapter 2.

Overlaid colour images

The adaptive binning algorithm is useful for producing images demonstrating in real colour where the soft, medium and hard areas of emission are. First an intensity image can be binned to produce a bin-map. Then images in three energy bands can be binned themselves using the bin-map. A software package such as GIMP can then be used to combine the three images as, for example, the red, green and blue layers in a single image. The contrast of the image can then be increased to highlight the areas of hard and soft emission.

The advantage of doing this rather than using raw data to make the image, is that the low-intensity regions are not dominated by noise. The technique was used to create the colour image of the Perseus cluster in Chapter 4.

Stranded pixels and contiguous regions

One ‘feature’ of the algorithm is that pixels may become ‘stranded’. If a bin has a reduced count relative to its neighbours, it may be left out on a pass and have no nearby pixels to be binned with on the next. It may be left until the final pass, and that area will be binned with the remaining pixels. Such pixels could be cosmetically removed by replacing them with their original value.

A modified version of the algorithm avoids stranded pixels. If a bin consists of more than one non-contiguous sets of pixels, then the bin is split into several contiguous regions, and each region treated by itself. A stranded set of pixels will remain until the end, where it will be binned by itself as it is isolated. Here, two pixels are said to be connected if one pixel is one of the neighbouring eight pixels of the other pixel.

This modification has a couple of disadvantages. Firstly, finding contiguous sets of pixels is fairly slow. Also, parts of the image which would be connected were the image larger, are treated by themselves, and therefore have a larger statistical error on their count. With these problems in mind, it is probably a useful modification for many

applications of the algorithm. For simplicity, I will use the unmodified version of the algorithm in the following sections, except where explicitly stated.

3.2.4 Simulated cluster

In order to properly test the properties of the algorithm, I attempted to simulate a simple image of a cluster. I used a β -model to simulate the cluster with the following form (Sarazin 1998):

$$S_b(r) = S_0 \left[1 + \left(\frac{r}{r_c} \right)^2 \right]^{0.5-3\beta}, \quad (3.13)$$

where S_b is the surface brightness at a radius r , r_c is a critical radius and β is a parameter. I created an image of 512×512 pixels, where r_c was 128 pixels, S_0 was 100 counts/pixel, and β was 0.67. The meaning of the word count, as used here for surface brightness, is the expectation value of an observation, and is allowed fractional values. The cluster was positioned in the centre of the image. It is shown in Fig. 3.10(a). The contours show constant surface brightness from 10-90 counts in linear 10 count intervals.

To simulate how such a cluster would appear, if observed, I took the surface brightness at a particular pixel, and randomly generated a value from a Poisson distribution with that surface brightness as the expectation value, to which I added a background with an expectation value of 20 counts/pixel. The Poisson image, background subtracted, is shown in Fig. 3.10(b). The data were lightly smoothed in contouring, as it was too noisy to contour otherwise.

I processed the Poisson simulated data with the adaptive binning algorithm to produce Fig. 3.10(c). Here a fractional error threshold of 0.02 was used. Fig. 3.10(d) shows the output of the method using a threshold of 0.04, i.e. twice as large a threshold as (c). The contours are at the same levels as the original surface brightness image.

For comparison, I show the output from the ASMOOTH program using a minimum feature significance of 4σ in Fig. 3.10(e). ASMOOTH, by default calculates the local background and does not take a global value. To create this image I smoothed the simulated data and subtracted the background manually. The count per pixel becomes negative in the outer regions, as ASMOOTH does not know about the global background, which also means features shown may have a lower significance than 4σ .

Spatial distributions of differences

I constructed in Fig. 3.11 images displaying the absolute fractional differences between the reconstructed and model surface brightness images. Spatial correlations in errors should be visible on the images.

Fig. 3.11(a) shows the absolute differences between an adaptively-binned image with 0.02 fractional errors (Fig. 3.10(c)), and the original surface brightness image binned with

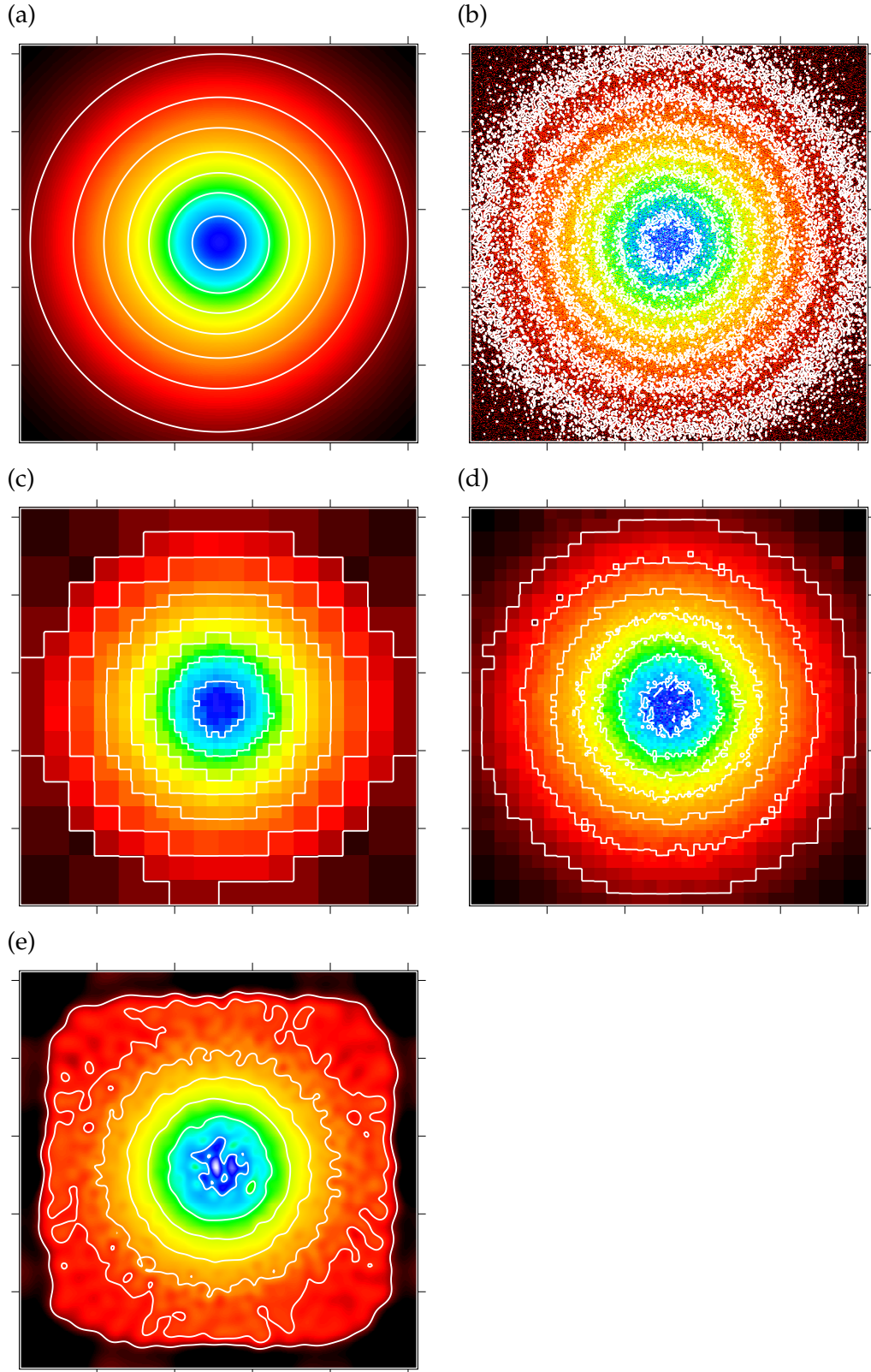


Figure 3.10: Simulated cluster images with equal colour scales. (a) Model surface brightness, contours range 10-90, in 7 steps spaced equally in square-root space. (b) Simulated Poisson image of the cluster (background subtracted). (c) Adaptively-binned image of cluster with error threshold of 0.02. (d) Adaptively-binned image of cluster with error threshold of 0.06. (e) Adaptively-smoothed image of cluster, $\sigma_{\min} = 4$, background subtracted.

the same bins. (b) shows the same except using bins constructed for 0.06 fractional errors (Fig. 3.10(d)). There do not appear to be any correlations between the two images, in terms of where the differences are large and small. The differences appear noise-like and random. Note, however, that if the adaptively-binned image were binned with inappropriate bins, then this would not show in (a) and (b) owing to the surface brightness image being binned with the same bins.

Fig. 3.11(c) is an image showing the absolute differences between adaptively-binned image with 0.02 fractional errors and the unbinned surface brightness image. Owing to the count rate varying across the bin, only the centres have a low absolute fractional difference. This would be the same for any binning process.

Fig. 3.11(d) shows the differences between the AS image in 3.10(e) and the surface brightness image for comparison. Visible are the edge effects of the algorithm. Also present are some peaks at the cluster core. These are due to the local background estimation of the algorithm measuring significant detections against the flat core of the cluster centre.

Histograms of differences

A more useful and quantitative analysis of the performance of the adaptive binning algorithm can be made by plotting the fractional differences (the absolute value of which is in the above images) as histograms, shown in Fig. 3.12. (a) displays the difference between the 0.02 error adaptively-binned image and the surface brightness image binned using the same bins *for each pixel*. (b) is the same as (a), except using 0.06 error binned images. (c) shows a histogram of the differences between the 0.02 error adaptively-binned image and the unbinned surface brightness image. The difference between an image produced by ASMOOTH (Fig. 3.10(d)) and the surface brightness image is shown in (d) for comparison.

Fig. 3.12(a) and (b) approximate Gaussian distributions. The widths of the distributions are close to the threshold fractional error values used by the algorithm, 0.02 and 0.06. (c) shows a wider distribution, which is obtained due to the count varying across the bin in the surface brightness image, but not in the adaptively-binned image. The results in (a) and (b) give confidence in the effectiveness of the algorithm, as the distributions are symmetric and Gaussian.

The histogram for the AS image in (d) has a very narrow peak, but there are long tails, mainly due to the edge-effects. Excluding the outer region almost removes the tail.

I also analysed the differences between the input surface brightness image and the adaptively-binned image using the χ^2 statistic. If there are S_i total counts in the surface brightness image in bin i , and s_i in the adaptively-binned image, and n_i pixels in the bin, then the statistic is

$$\chi_i^2 = \frac{(S_i - s_i)^2}{S_i + n_i b}. \quad (3.14)$$

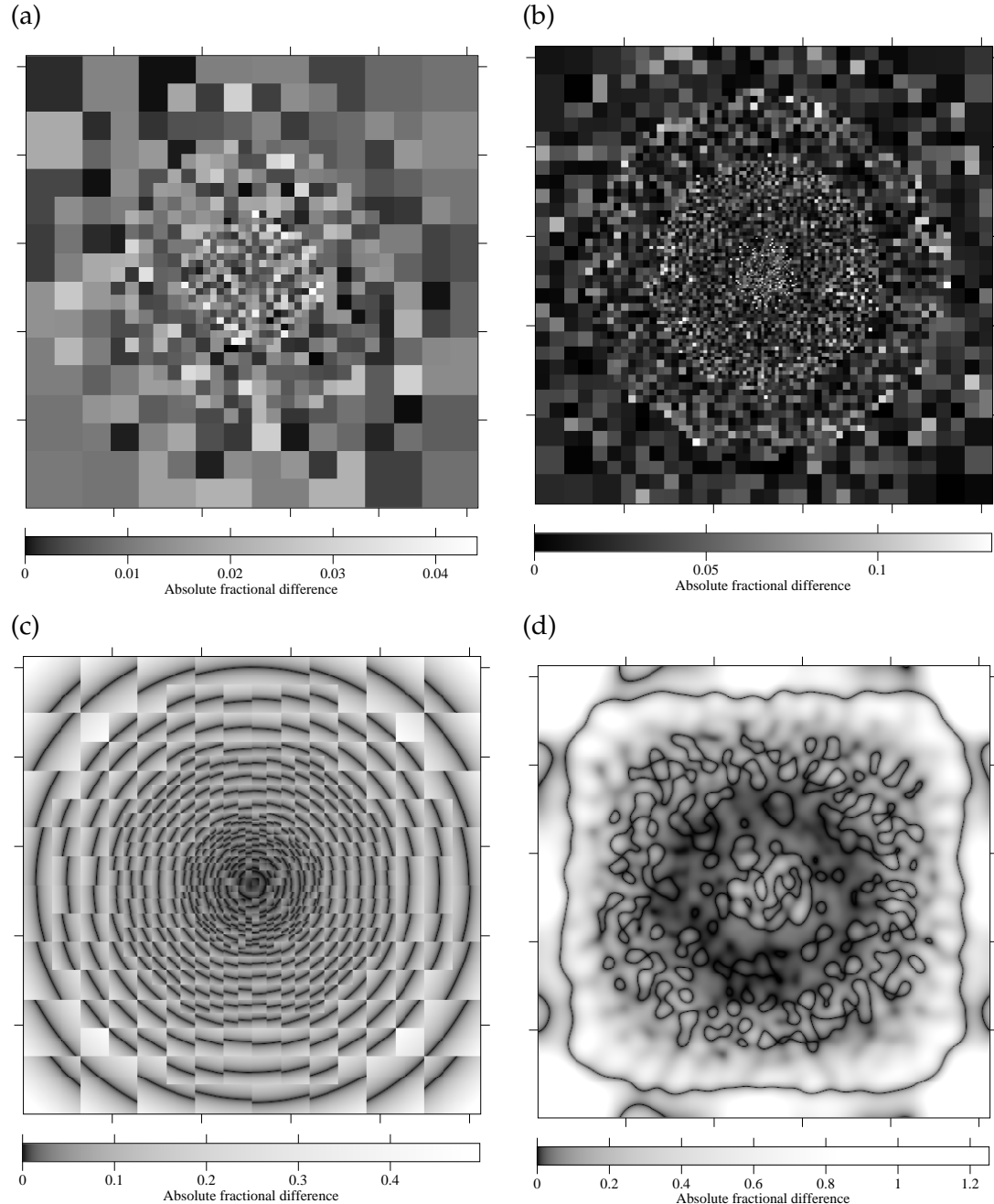


Figure 3.11: Absolution fractional differences between the reconstructed images and original surface brightness image. (a) adaptively-binned image, error 0.02, and binned surface brightness image. (b) adaptively-binned image, error 0.06, and binned surface brightness image. (c) adaptively-binned image, error 0.02 and unbinned surface brightness image. (d) Adaptively-smoothed image, $\sigma_{\min} = 4$ and unbinned surface brightness image.

I plotted the distribution of χ^2 for the bins in the adaptively-binned image. It showed reasonable agreement with the distribution predicted for one degree of freedom.

3.3 Colour binning

A simple way to investigate the inner structure of a cluster is to create X-ray images in different energy bands. The images can then be divided to show the areas of hard and soft X-ray emission, known as a colour image. Additionally plasma codes, such as the MEKAL thermal model, can be fitted to the relative counts, enabling one to map temperature, metallicity and absorption.

One faces a similar problem to the simple intensity binning problem. How can ratios of counts be formed so that the error on the result is accurate enough? A binning algorithm must be able to use the same size bins on the images to be divided, plus it must adapt its bin size to the counts in each of the bands, rather than just one.

The colour adaptive binning algorithm is similar to the intensity algorithm, except it uses an input image for each band, to produce an output image for each band. Each input image is binned using the same bins. The bins are defined by the error on a ‘combined colour’, which folds the ratios of all the bands, not the error on the intensity. If s_k^i is the background-subtracted count in band i for bin k , the combined colour is defined as

$$C_k = \left[\left(s_k^1 / s_k^2 \right) / s_k^3 \right] / \dots \quad (3.15)$$

The fractional error on the combined colour, if there are N bands, is

$$\frac{\sigma_{(C_k)}}{C_k} = \left[\sum_{i=1}^N \frac{c_k^i + n_k b^i}{(c_k^i - n_k b^i)^2} \right]^{1/2}. \quad (3.16)$$

This error is a useful quantity because it takes into account the count in each band in a symmetric way. To make an actual colour map, two binned output images are divided.

An alternative approach is to adaptively bin a total intensity image. The resultant bin-map can then be applied individually to each of the X-ray bands. Ratios can be formed by dividing the output images. This approach has its advantages when several bands are being used. If a sharp feature is only present in one band, then the source will be binned with a large bin using the combined-colour method, owing to the large statistical uncertainty on the colour. However, binning using the total intensity leads to colours with larger range of errors than the combined-colour approach.

3.3.1 Real example

The combined colour adaptive binning method has been applied to the Perseus data shown earlier. Three images of the cluster were created in different bands, labelled from

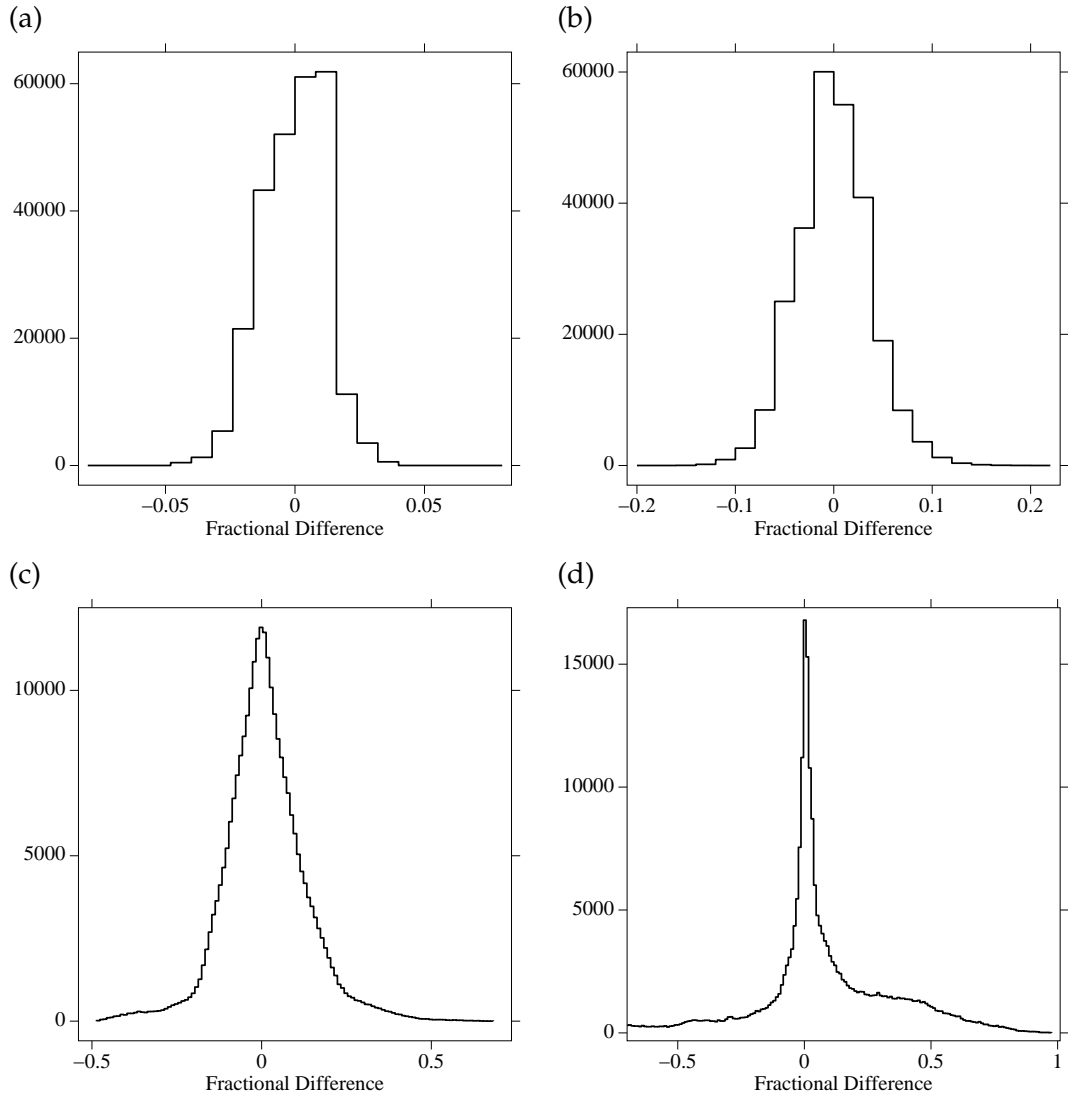


Figure 3.12: The distribution of fractional differences between pixels in binned images. (a) is between an adaptively-binned (0.02 fractional error) image and the original surface brightness image binned with the same bins. (b) is the same as (a) except using 0.06 fractional error image. (c) is between an adaptively-binned image (0.02 fractional error) and the original surface brightness image. (d) is between a $\sigma_{\min} = 4$ AS image and the original surface brightness image.

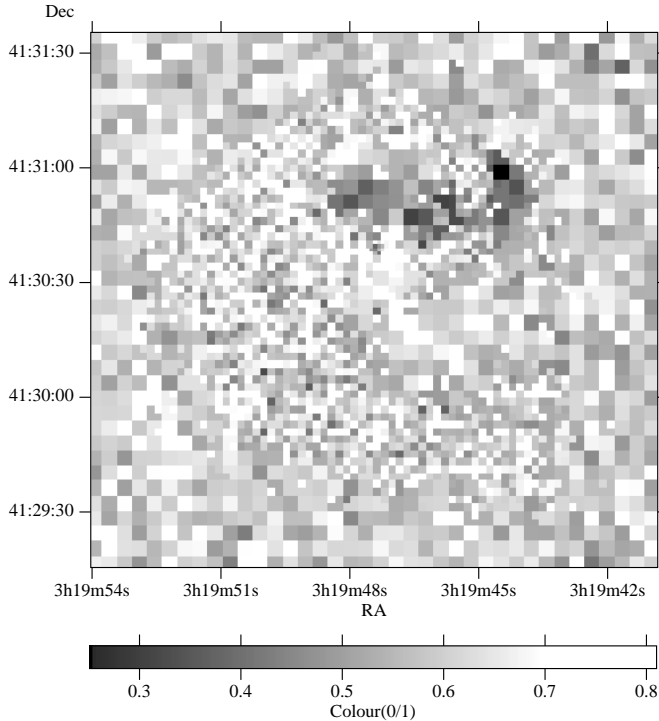


Figure 3.13: Colour map showing the ratio of counts in band 0 (0.5–1 keV) to band 1 (1–2 keV) for the Perseus cluster, adaptively binned with a fractional error of 0.2. This colour map highlights regions of high photoelectric absorption.

0–2, in the energy ranges 0.5–1, 1–2 and 2–7 keV.

The colour adaptive binning algorithm above was applied to the data using a fractional errors on the combined colour, $(s^0/s^1)/s^2$, of 0.12 and 0.2. Again the background counts in each image were small enough to be neglected.

Fig. 3.13 shows the s^0/s^1 colour image produced with a fractional error of 0.2, which is sensitive to X-ray absorption; darker shades indicate more absorption. The absorption shadow of an infalling dwarf galaxy, discussed by Fabian et al. (2000), is clearly seen close to the centre of the image. The rest of the image has approximately uniform colour, indicating there are no further strong absorption features.

Fig. 3.14 shows the s^1/s^2 colour image produced with a fractional error of 0.12, which is sensitive to temperature; lighter shades indicate lower temperature. From this simple analysis, there appears to be a temperature gradient in the cluster, with cooler temperatures towards the centre and the brighter regions. This agrees with cooling flow models. The analysis emphasises a spiral structure, which is present right down to the cluster centre (compare with Fig. 3.9).

Using the combined colour method to generate the bins, the fractional errors on the bins for the individual colours, both range from 0.05 to 0.1 using a fractional error of 0.12. I have shown the colours with different fractional errors owing to the relative strengths of features in the colours.

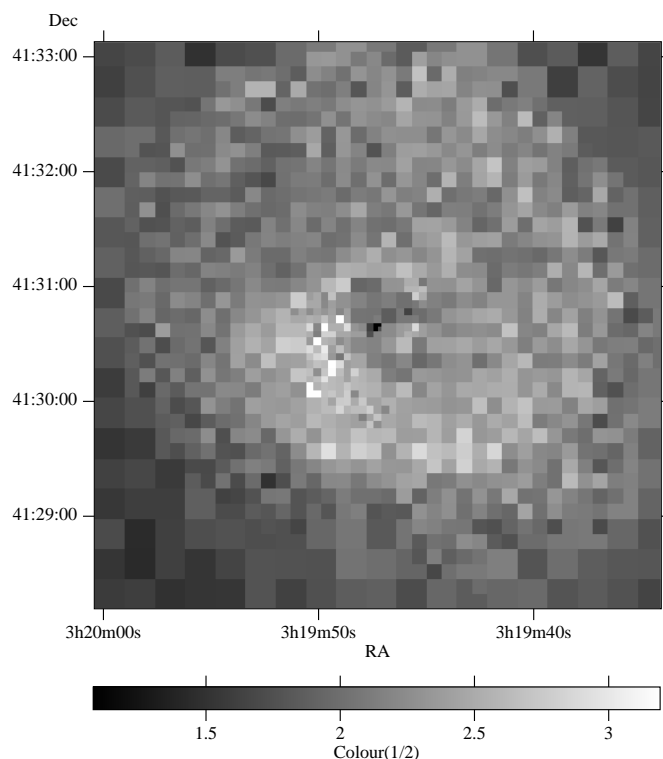


Figure 3.14: Colour map showing the ratio of counts in band 1 (1–2 keV) to band 2 (2–7 keV) for the Perseus cluster, adaptively binned with a fractional error of 0.12. This colour map highlights regions of low temperature.

3.3.2 Spectral fitting

As mentioned above, one can fit the relative counts in different X-ray bands against the relative counts predicted by a plasma code, to estimate physical properties, such as temperature and metallicity. To fit many parameters, several bands are required. It is useful to choose bands with approximately the same number of counts, the choice of which can be derived from the spectrum.

For a more detailed analysis, full spectral fitting is necessary. I have investigated taking an intensity-binned image of the object, automatically extracting spectra for each of the bins, automating XSPEC to fit each spectrum, and then plotting the fitted parameters spatially. A response of the telescope and the X-ray background can be calculated for each bin. I used this technique when I examined the Centaurus cluster (discussed in Chapter 5).

3.4 Non-square bins

It would be expected that introducing additional steps in size between doubling the length of the bins would reduce the ‘granularity’ of the binning process. I have investigated adding another step between the doubling of the length of the bin, so that the area of the bin doubles between each iteration rather than quadruples. This version of the method I will call the ‘half-bin modification’.

Fig. 3.15 shows a set of six simple ways in which the area of the bin can be cut into two approximately equal parts. As there are an even number of pixels along the length of a bin (except in the first step), there is an ambiguity over which half the pixels on the diagonal line lie in if the bin is cut diagonally. This leads to the six possible ways to cut the bin, rather than four. If one type is chosen preferentially over the other then the binning becomes asymmetric. In order to resolve this problem the error for each of the six shapes of bin is measured, and if any have an error less than the threshold value, the one with the lowest error is allowed to propagate through to the output image.

A summary of the procedure used is as follows:

1. Test to see whether any 1×1 pixel bins have a fractional error less than the threshold. If they do, copy them to the output image.
2. Using a 2×2 pixel grid over the image, test to see whether, any of the half-bin patterns shown in Fig. 3.16 have errors below the threshold. If they do, copy the one with the lowest error to the output image.
3. Test to see whether any of the 2×2 bins have an error less than the threshold. If they do, copy them to the output image.

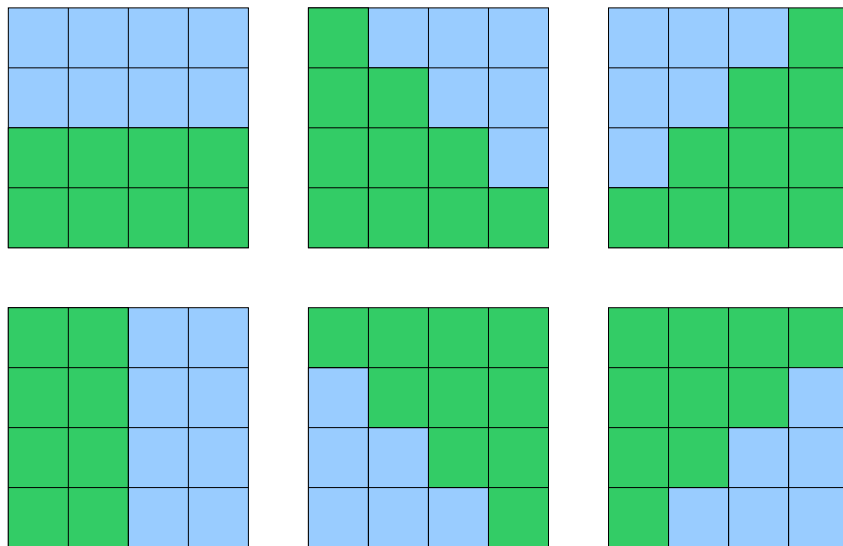


Figure 3.15: Possible ways to cut a 4×4 bin into two approximately equal parts.

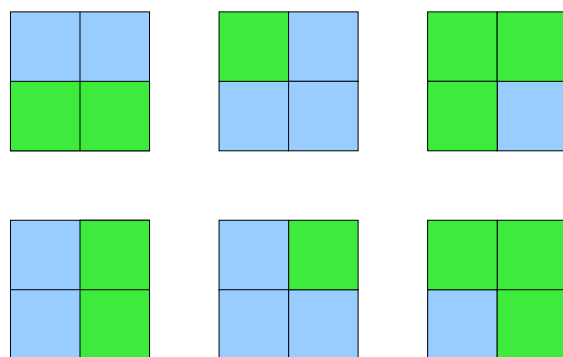


Figure 3.16: Possible ways to cut a 2×2 bin into two approximately equal parts.

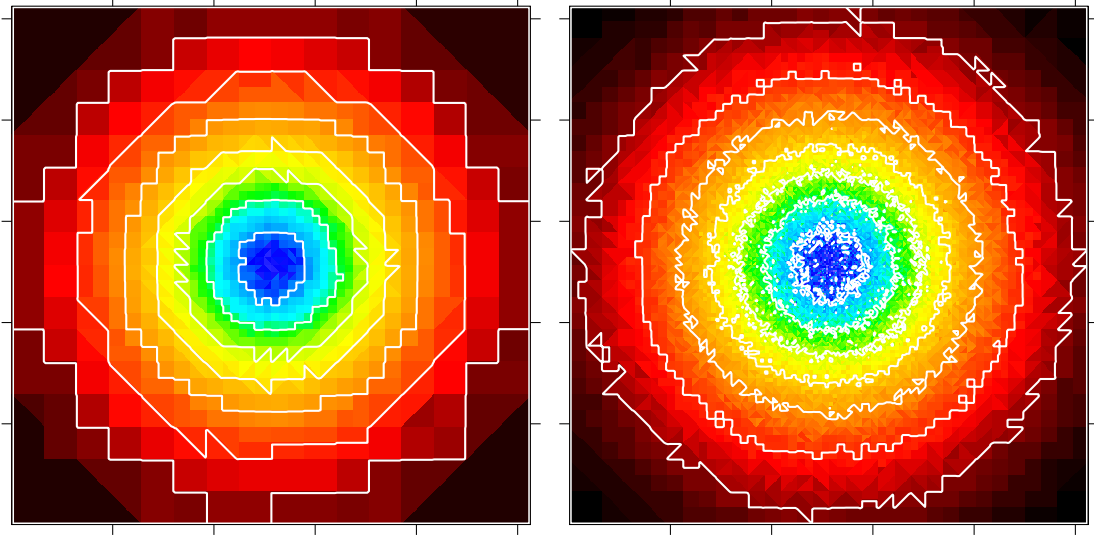


Figure 3.17: Adaptively-binned images using the half-bin modification, of the simulated cluster shown in Fig. 3.10, with the same contours and colour scheme. Left image uses a fractional error threshold of 0.02, and the right image uses a threshold of 0.06.

4. Using a 4×4 pixel grid, test to see whether any of the patterns in Fig. 3.15 have an error less than the threshold. If at least one does, copy the one with the lowest error to the output image.
5. Test to see whether any of the 4×4 bins are allowed by the threshold.
6. Continue enlarging bin size by a factor of two in area until the final step, where the remainder of the image is binned.

Another factor which may be important are stranded pixels (Section 3.2.3). Using half-binning appears to result in many more stranded pixels than simple-binning. For this reason, the results shown in this section use contiguous bins.

Fig. 3.17 show images of the simulated cluster (Section 3.2.4) binned using the half-bin modification. Compared to Fig. 3.10 the isophotes appear less blocky, especially where the bin size is large. Fig. 3.18 shows the fractional differences between the original surface brightness image and the reconstructed image. The distributions are very similar to those of normal adaptive binning (Fig. 3.12), although they look slightly more Gaussian.

Adaptive binning with the half-bin modification is shown applied to real data for the Centaurus cluster in Fig. 3.19 (a colour map) and for the Perseus cluster in Fig. 3.20 (an intensity map). Compare these images to those in Fig. 3.2 and Fig. 3.6. The contours in these images are certainly smoother and less blocky, however there appears to be some slight dithering effects. There are some features in the half-binned images which do not appear in the originals (for instance the green blob on the plume in the Centaurus cluster), but it is difficult to know whether they are real features or are noise. It might

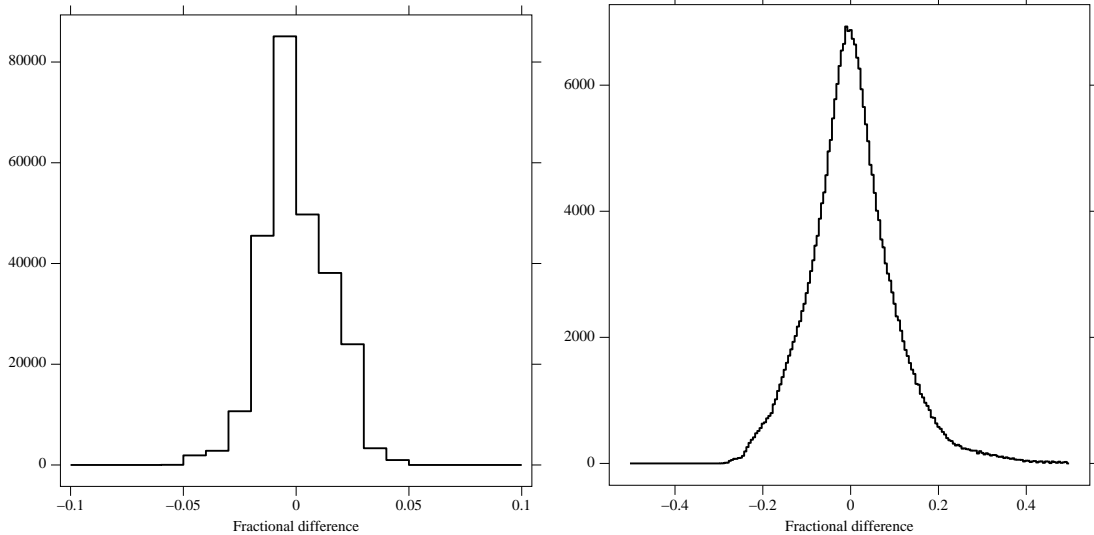


Figure 3.18: Histogram of fractional differences between the original surface brightness image (in Fig. 3.10) and the 0.02 adaptively-binned image with the half-bin modification (Fig. 3.17). The left image shows the differences using the surface brightness image with the same binning as the adaptively-binned image, and the right image shows the difference with the unbinned surface brightness image.

be argued that the diagonal bins are visually unappealing, but given that the statistics of the binning processes are similar, the decision to use normal binning or the half-binning is probably aesthetic. If the count rate in the image is poor, the half-binning process may give needed extra resolution.

3.5 Binning by spectral fit

In Section 3.3.2 I discussed taking a spectrum from each bin to fit a model to find one or more of its parameters. Doing this it is possible to build a map, say of temperature, over a cluster. This problem can be turned around slightly. If one is mapping a physical quantity over a cluster then it is the error on the quantity which is the interesting thing to choose the bin size by. If there is a patch of high metallicity then the error on that metallicity may be fractionally low, despite there being few counts in that area.

Theoretically, one would extract a spectrum from each 1×1 bin, fit a model to it, and if the error on the parameter is sufficient low, output the results of the fit to an output image. The remaining bins would be merged together to make 2×2 bins as in Section 3.1.3, and the process repeated. Basically, this is the same as the original adaptive binning algorithm, but using the spectrum of the bin to decide how large the bin is.

In practise, however, this approach results in a few problems:

1. Fitting spectra and finding the errors on parameters is very slow compared to counting the number of photons in a bin. Therefore if one is fitting the spectrum of

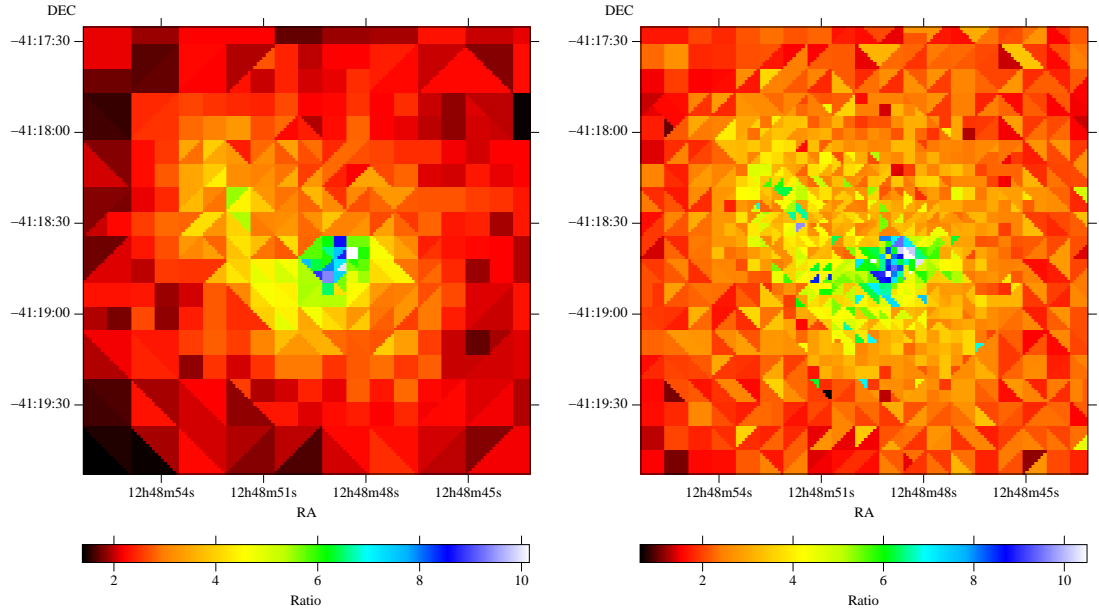


Figure 3.19: Adaptively-binned images using the half-bin modification, of the Centaurus cluster also shown in Fig. 3.1 and Fig. 3.2. The left image is binned with an fractional error threshold of 0.12, and the right image is binned with a threshold of 0.2.

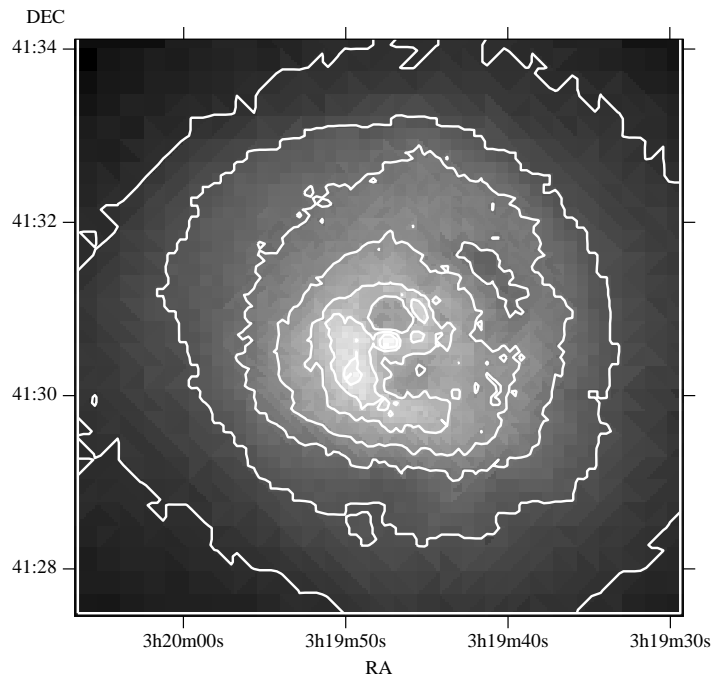


Figure 3.20: Adaptively-binned image of the Perseus cluster with the half-bin modification, the fractional error threshold is 0.04. Compare with Fig. 3.6.

every possible bin it would take weeks or years to bin an image. A work-around is to exclude bins where the number of counts is probably too low to get a reasonable spectral fit. Despite this fix, it may take several days to do the tens of thousands of spectral fits required to make a detailed map. A mistake in the input parameters may only be visible some time later.

2. If one makes a temperature map by specifying the error on the temperature, and makes a column density map by specifying its error, then the bins are located in different positions. This makes it hard to compare the maps of different physical quantities. However, one can make one map whilst binning on another, knowing that the errors will be distributed less regularly in the second map.
3. A change in model or fixed parameters requires that the spectral fits need to be done again.
4. The fractional error may not be useful on a parameter. 100 ± 50 keV is probably less useful than 1 ± 0.5 keV. However, absolute errors could be used if this is a problem.

The main problem is that of the speed of the spectral fits. A possible way of speeding the process up would be to use several X-ray colours and do a simple χ^2 fit, however it may be difficult to improve on the fitting speeds of specialised software such as XSPEC (Arnaud 1996).

3.6 Availability

An implementation of the adaptive binning algorithm is available written in the C++ programming language. See the URL <http://www-xray.ast.cam.ac.uk/~jss/adbin/> for instructions for download.

4

The Perseus and Abell 1795 clusters

Summary

This chapter describes the results from observations of the Perseus and Abell 1795 galaxy clusters using the *Chandra X-Ray Observatory*. Some of this work was published in *Chandra imaging of the complex X-ray core of the Perseus cluster* (Fabian et al. 2000) and *Chandra imaging of the X-ray core of A1795* (Fabian et al. 2001c).

The *Chandra* sub-arcsec resolution image of the core of the Perseus cluster shows the holes which are associated with the radio lobes of 3C 84 and were previously observed by *ROSAT*. The rims of the holes are X-ray bright and consist of cooler gas than their surroundings, indicating that they were not formed as the result of shocks. A spiral structure in the cool X-ray gas is seen, which may have been caused by angular momentum in the cooling flow. A filament-like structure of strong photoelectric absorption is seen across the core of the cluster, which appears to be associated with a small infalling irregular galaxy. Two outer X-ray holes, one of which was previously known, appear to be correlated with spurs of low-frequency radio emission.

The observation of the Abell 1795 galaxy cluster reveals a 40 arcsec long filament in the core of the cluster. The feature is coincident with a H α +[N II] filament found by Cowie et al. (1983), which was later resolved into two *U*-band components by McNamara et al. (1996a). I construct a temperature map of the region around the filament, which shows the gas along the filament has a temperature of 2.5-3 keV, and a mean radiative cooling time of 3×10^8 yr. The cD galaxy at the north end of the filament is probably oscillating through the core of the cluster, and the filament is formed by gas

cooling from the intracluster medium.

4.1 The Perseus cluster

4.1.1 Introduction

The Perseus Cluster, Abell 426, lies at a redshift of $z = 0.0183$ (distance of 100 Mpc), and is the brightest cluster in the sky in X-rays. It was first detected to be an object with finite angular extent by Forman et al. (1972) using the *Uhura* observatory, and has since been observed by most X-ray missions. It hosts our nearest large cooling flow (e.g. Fabian et al. 1981a; Allen et al. 2001), with a mass deposition rate, \dot{M} (see Section 1.1.3), observed by *ASCA* to be on the order of $300 \text{ M}_\odot \text{ yr}^{-1}$ (Allen et al. 2001). Owing to the cooling flow, the central brightness of the cluster is very highly peaked, and the gas in the core of the cluster is several keV cooler than that of the outer regions (e.g. Fabian et al. 1981a). The cluster has a mean temperature of about 4.5 keV (Allen et al. 2001). Molecular gas has also been detected in NGC 1275 in the sub-mm waveband (Bridges & Irwin 1998), which may have been accumulated by the action of the cooling flow.

The cD galaxy, NGC 1275, contains a central radio source, 3C 84. A radio jet emerges from the nucleus of 3C 84 ending in two radio lobes. The X-ray gas interacts with the radio source, something which was first seen clearly using *ROSAT* observations (Böhringer et al. 1993; Fig. 4.1). The X-ray plasma appears to have been displaced by the radio lobes to leave two large holes in X-ray emission either side of the nucleus. The jet and lobes are embedded in an extended radio halo, which has been observed out to 300 kpc, and has been estimated to be powered by an energy output of at least $10^{43} \text{ erg s}^{-1}$ (Pedlar et al. 1990). This energy output corresponds to roughly one tenth of the X-ray radiation emitted by the cooling flow region in the cluster. The pressure of the relativistic particles and the magnetic field in the radio lobes is found to be $\sim 10^{-9} - 10^{-10} \text{ erg cm}^{-3}$. This is probably larger than the pressure of the X-ray gas of $\sim 2 \times 10^{-10} \text{ erg cm}^{-3}$ (Pedlar et al. 1990).

Optically, NGC 1275 has type E or S0, with a smooth luminosity profile (Rubin et al. 1977). There is a high velocity structure to the north of the nucleus, which is moving at a velocity of $\sim 3000 \text{ km s}^{-1}$ towards the cluster (e.g. Rubin et al. 1977, Unger et al. 1990), and has the appearance of an edge-on galaxy. The infalling object is seen in absorption in the 21 cm band (De Young et al. 1973), and it is also found in Ly α emission (Briggs et al. 1982). Since the object is seen in these two wavebands, it must lie in front of the galaxy NGC 1275.

NGC 1275 also shows a large number of emission line filaments, most of which are angled to point away from the centre of the galaxy (Minkowski 1957; and more recently Conselice et al. 2001, see Fig. 4.2). The origin of these filaments is still not understood (e.g. Sabra et al. 2000). Conselice et al. (2001) have taken images of the galaxy, using a

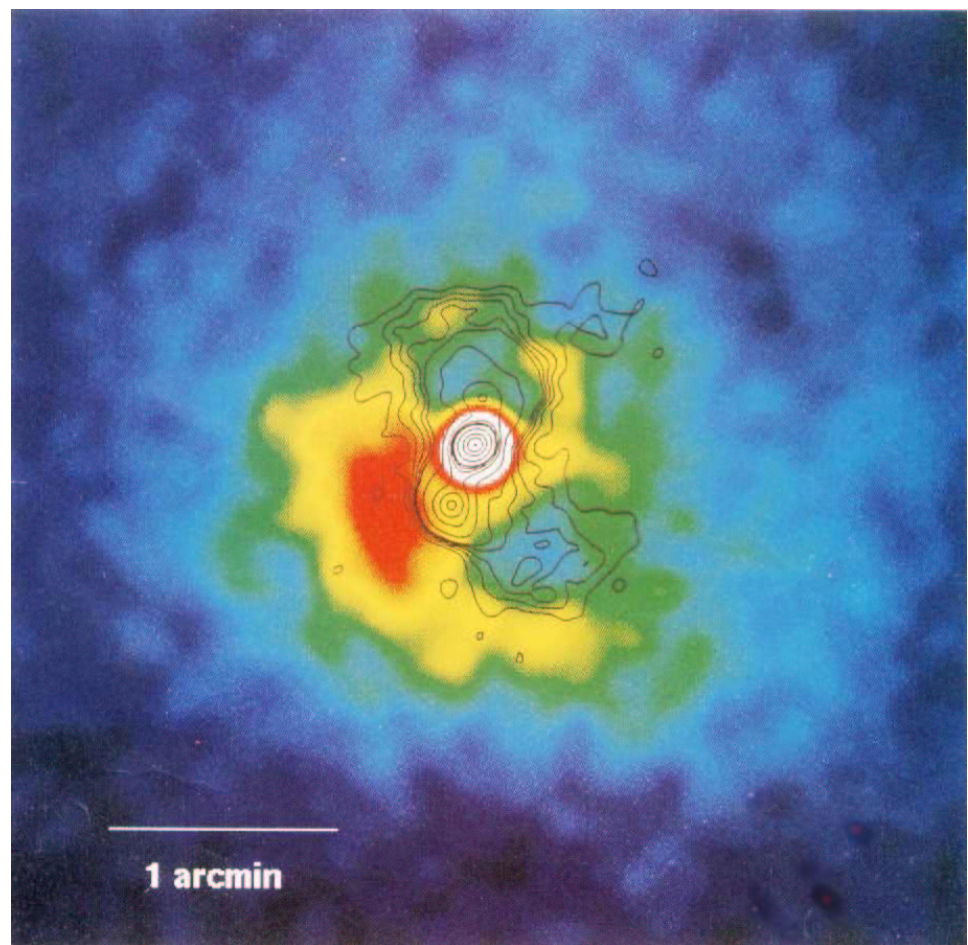


Figure 4.1: Central part of the *ROSAT* HRI image of the region of Perseus cluster around NGC 1275. Overlayed is a contour map of the radio lobes from Pedlar et al. (1990). Image is taken from Böhringer et al. (1993).

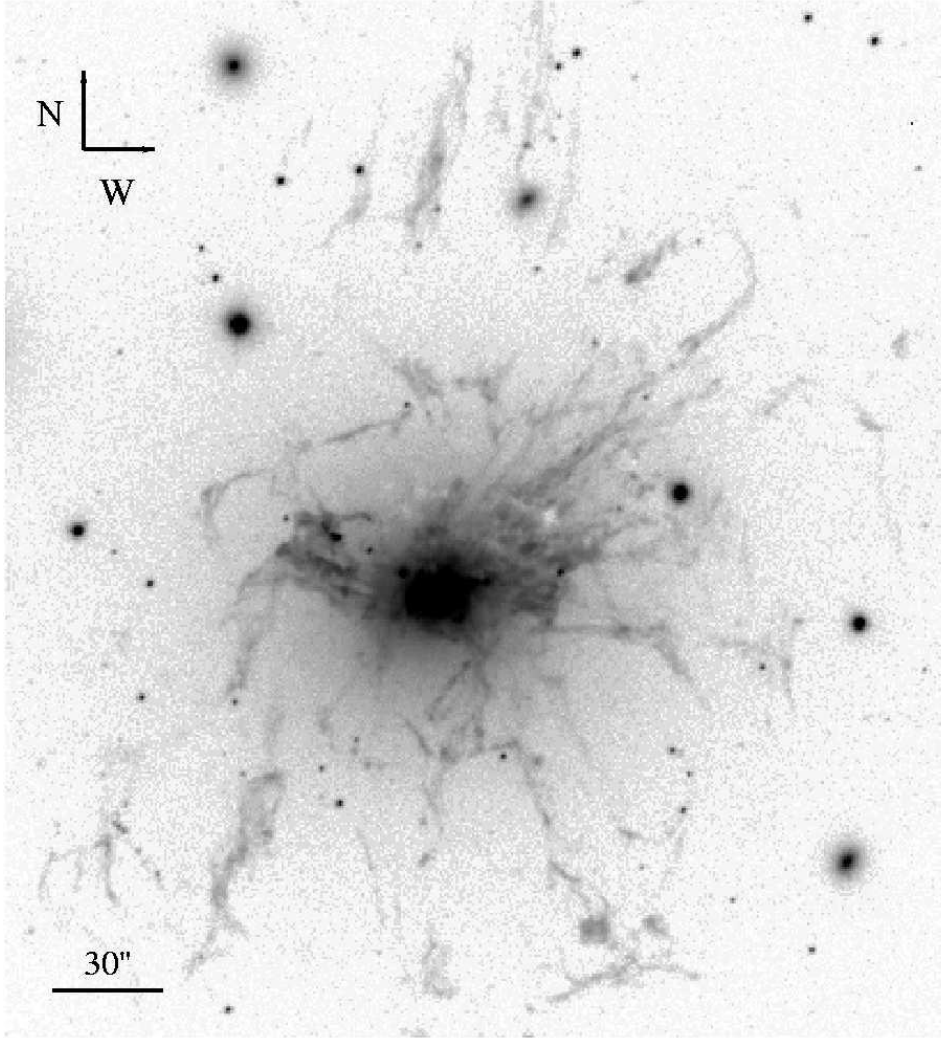


Figure 4.2: H α image of the core of the Perseus cluster, after subtraction by the continuum. The image shows the filaments of the low velocity NGC 1275 system. Taken from Conselice et al. (2001).

filter tuned to the H α wavelength of the gas at the velocity of NGC 1275. They conclude that the features are tubes, or ribbons, of gas. Their preferred model is that the filaments are caused by the interaction with the relativistic plasma from the radio nucleus. However, the distribution of the filaments does not appear to be correlated with the position of the radio lobes or radio jet. The galaxy also contains some regions containing very blue, and probably very young, stellar clusters (Carlson et al. 1998). Star formation is expected if there is a cooling flow depositing cold material in the galaxy (e.g. Fabian 1994).

4.1.2 The *Chandra* observation

The Perseus cluster was observed by *Chandra* on 2000 January 29 for 24,453 s, and on 1999 November 28 for 9,014 s using the ACIS-S detector. Most of the analysis presented here was done on the longer data set, but some of the later sections include data from the second. I will note when the second dataset is also used. Both datasets were taken when the focal plane temperature of the ACIS detector was -110°C . This chapter only examines data from Chip 7 (S3) of the ACIS detector, as this is where the majority of the cluster emission is detected, and is the best calibrated ACIS-S chip.

Fig. 4.3 shows the raw image of the cluster from the ACIS-S3 CCD, binned to have $\sim 1 \text{ arcsec}$ pixels. Contrast the *Chandra* image to the one taken by the *ROSAT* HRI of a slightly smaller region shown in Fig. 4.1. The ACIS image clearly shows the two holes in emission as seen by the PSPC, associated with the inner radio lobes of 3C 84. The image also shows the larger outer hole to the north-west, a feature which was known from *Einstein observatory* images (Fabian et al. 1981a; Branduardi-Raymont et al. 1981). In the energy range 0.5-7 keV the count rate goes down to $\sim 9.0 \times 10^{-4} \text{ s}^{-1} \text{ arcsec}^{-2}$ in the innermost-southern hole, and $1.0 \times 10^{-3} \text{ s}^{-1} \text{ arcsec}^{-2}$ in the innermost-northern hole, compared to a rate of $1.7 \times 10^{-3} \text{ s}^{-1} \text{ arcsec}^{-2}$ on the rim of the holes. The simplest interpretation is that the rims of bright emission are shells enclosing the holes. A bright patch of emission about $50 \times 15 \text{ arcsec}^{-2}$ has a count rate of $2.3 \times 10^{-3} \text{ s}^{-1} \text{ arcsec}^{-2}$. The outer northwestern hole has a count rate of $4.6 \times 10^{-4} \text{ s}^{-1} \text{ arcsec}^{-2}$, and is surrounded by emission of $7.7 \times 10^{-4} \text{ s}^{-1} \text{ arcsec}^{-2}$. A count-rate profile across the image is shown in Fig. 4.4.

The nucleus of NGC 1275 is slightly extended. The source suffers from pileup (see Section 1.2.4), so a second observation with a smaller observing area will be necessary to get accurate spectral information about the nucleus.

4.1.3 X-ray colour analysis

In order to study the X-ray colours of the cluster, I made images in three X-ray wavebands: soft (0.5-1 keV), medium (1-2 keV) and hard (2-7 keV). The images were then exposure-map corrected to remove the nodal readout boundary structures. I adaptively binned (Chapter 3) the total intensity image with a maximum error on the count in each bin of 30 per cent. That bin map was then applied to each of the individual bands in turn. By adaptively binning the image the noise in the outer regions of the cluster is reduced. The three binned images were then combined together as red, green and blue (RGB) layers in the software tool GIMP. The result is shown in Fig. 4.5.

It can be seen from the image that there are no strong colour gradients across the cluster, except for some green/blue patches of hard emission to the north-west of the core. The holes in emission are clearly not due to absorption, as they would appear blue in the figure. The rims are also not hard, but moderately soft, and are the same colour as

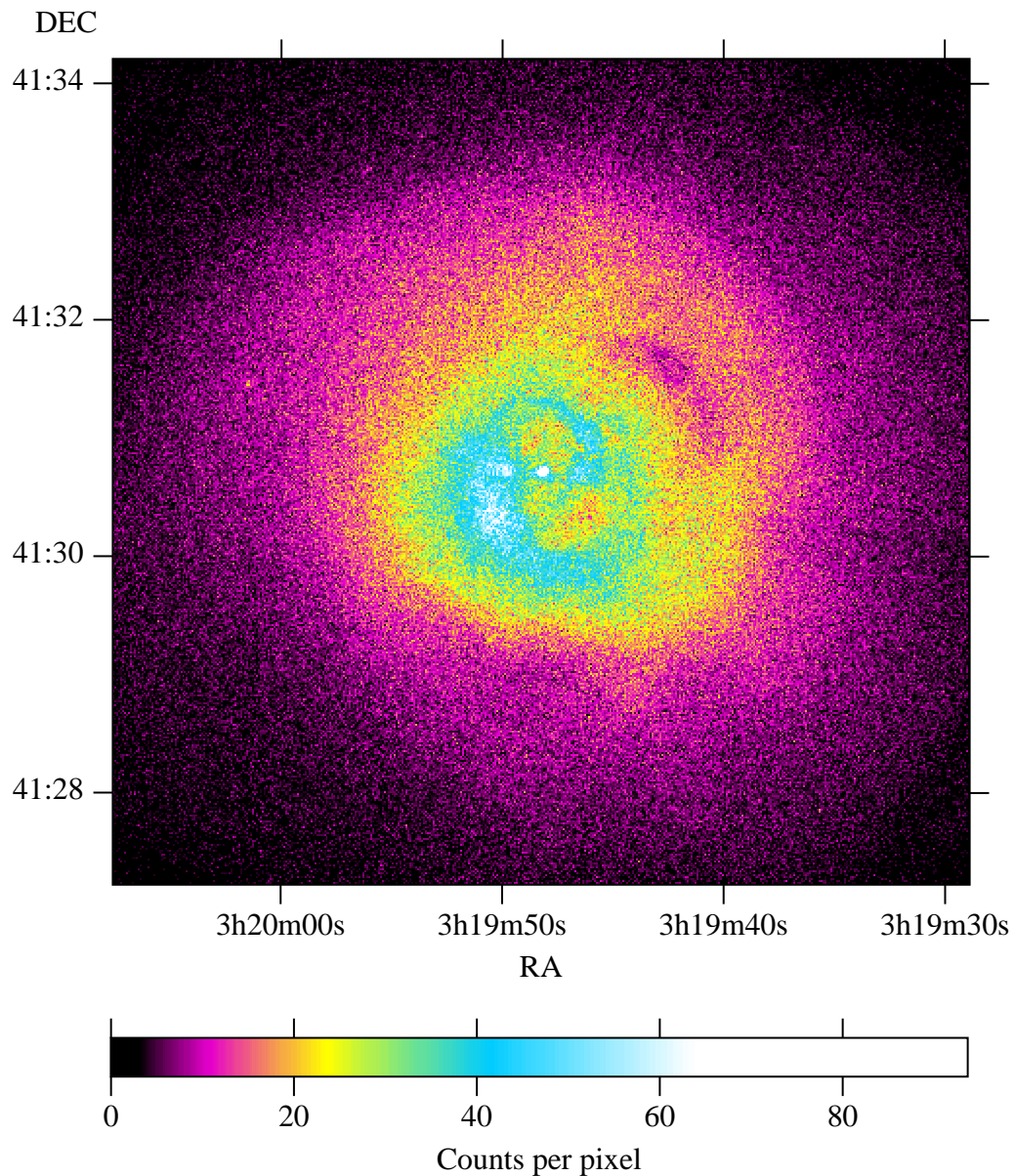


Figure 4.3: Raw (uncorrected) *Chandra* image of the Perseus cluster, made by combining both the observations (and removing X-ray flares; combined exposure 24.0 ks). The image shows counts between 0.5 and 7 keV. ACIS pixels are binned in both directions by a factor of two, giving a pixel size of $\sim 1 \times 1$ arcsec. The nodal readout boundary structures (where the detector is less sensitive to counts) in the 2000 January observation lie across the centre of the cluster, and can be seen faintly running from the lower-mid right to the mid left (Position angle 260°).

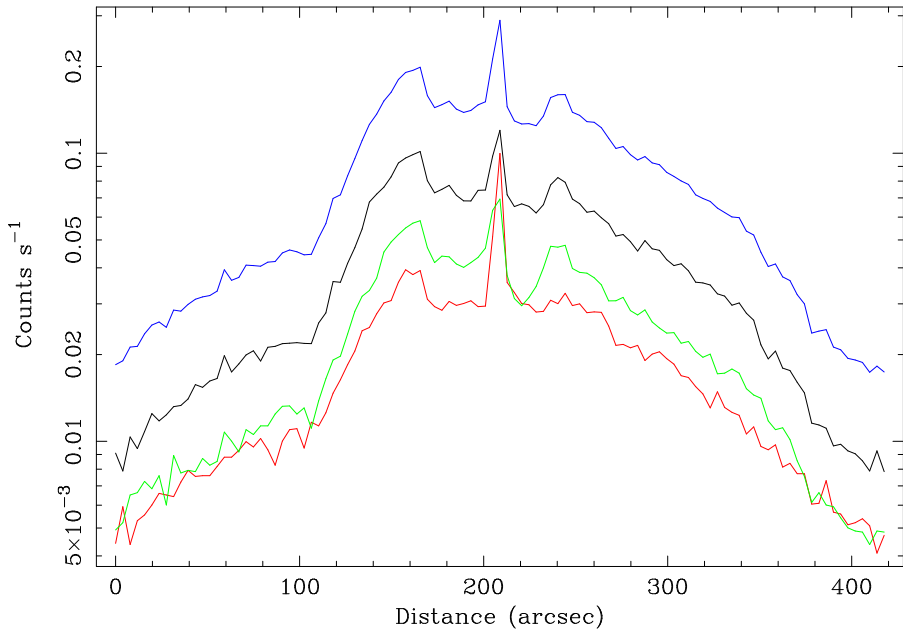


Figure 4.4: Count profile from south to north across the centre of the Perseus cluster for the combined datasets. The count rate in boxes of $27.6 \times 3.9 \text{ arcsec}^2$. The top line is for the 0.5-7 keV band. The profiles below are 1-2, 0.5-1 and 2-7 keV, from the top to the bottom.

the bright eastern patch. As the rims are soft then they cannot be shock features, contrary to the prediction of Heinz et al. (1998), and the holes are not expanding supersonically.

The green/blue patches seen in the RGB image are clearly seen in a soft X-ray intensity map and an optical *B*-band image (Fig. 4.6). The *B*-band image was made by C.S. Crawford from data taken from the Isaac Newton Group Archive. The image is the combination of images taken on 1997 December 25 and 1998 August 22 with the Jacobus Kapteyn Telescope (JKT) using the Tek1024 detector. The total exposure time was 17.7 ks. The data have been bias-subtracted and flat-fielded before their combination. This structure matches coincides in its position and its length with the high-velocity emission-line nebulosity system seen to the north of NGC 1275 (see Section 4.1.1 for references and a description of the system). The system is thought to be associated with a small irregular galaxy which is falling into the centre of the cluster, and lies in front of NGC 1275. Since the object is seen in X-ray absorption, it must lie well in front of the outermost regions or the absorption features would not be so deep, for they would be obscured by further emission in front of the object. A good estimate of the radial distance of the galaxy from the cluster centre is difficult as we do not know its geometry, or the geometry of the X-ray holes. However, the count rate is lower than anywhere in the central 2 arcmin of the cluster, which suggests the galaxy may be more than 60 kpc from the cluster centre. Tantalisingly, the area to the west of the absorption has brighter emission, suggesting the possibility that the infalling galaxy is shocking the gas beneath it.

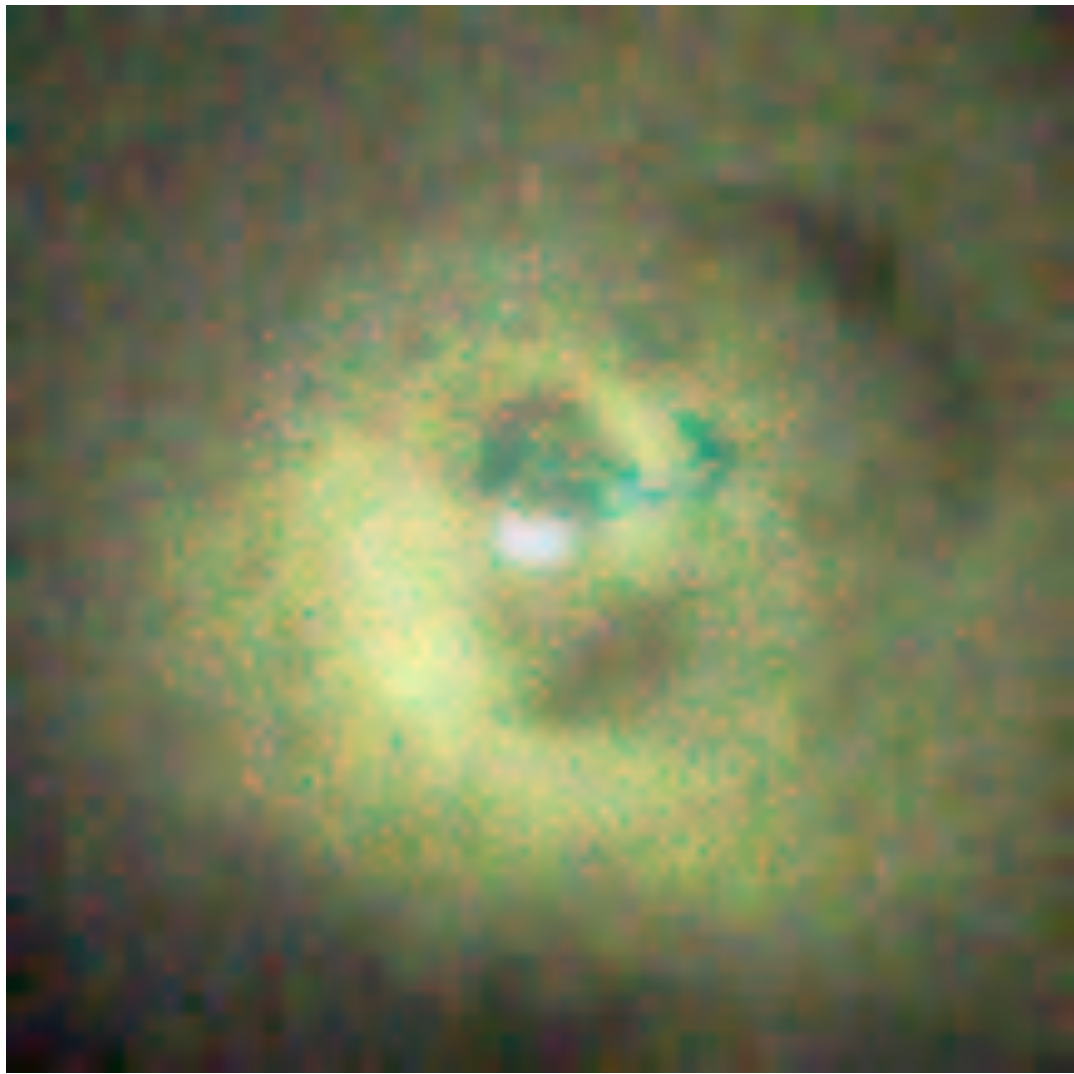


Figure 4.5: Combined RGB image of the Perseus cluster. Composed from a red image (0.5-1 keV), a green image (1-2 keV), and a blue image (2-7 keV). The component images were exposure-corrected, and adaptively binned. The image measures 3.5 arcmin square.

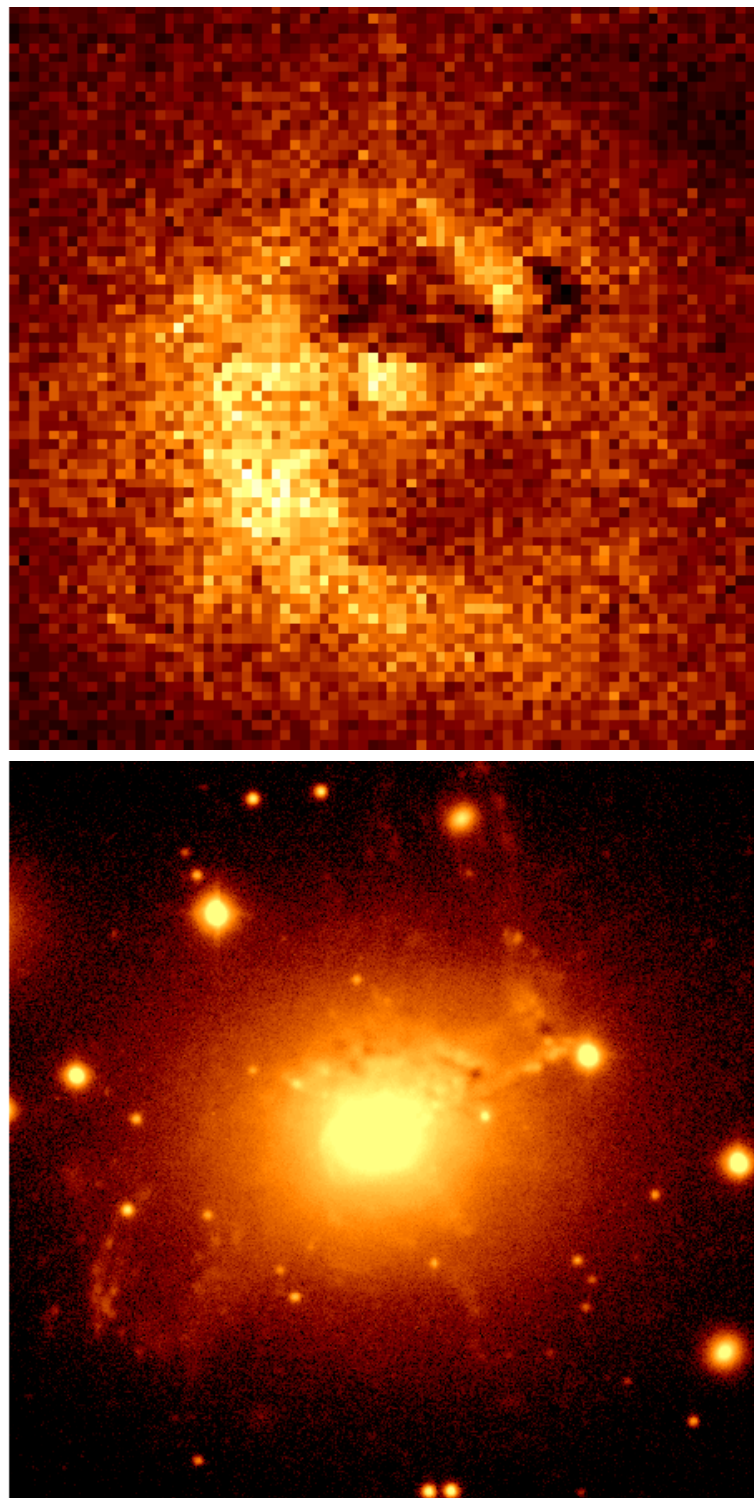


Figure 4.6: A soft X-ray image (0.5-1 keV) map (top) showing the absorption structure, and a *B*-band optical image taken by the JKT (bottom). Both images are on the same scale and measure 150×150 arcsec 2 . North is to the top. Images taken from Fabian et al. (2000).

Temperature and absorption maps

To estimate the distribution of temperature and absorption column density over the cluster, I adaptively binned the image to give bins with a minimum fractional error in the combined-colour (Section 3.3) of the three bands listed in the previous section of 0.15. This gives an approximately equal joint fractional error per bin across the colour ratios, over all the colours. I used XSPEC (Arnaud 1996) to iterate over a grid of parameters (column density and temperature) to a MEKAL model (Mewe et al. 1985, 1986; Liedahl et al. 1995) with an absorbing screen described by a PHABS model (Balucinska-Church & McCammon 1992), recording the relative counts in each of the bands (0.5-1, 1-2 and 2-7 keV) for each set of values of the parameters. The model was fixed at a metallicity of 0.4 times the solar abundance (Using the abundance levels of Anders & Grevesse 1989), and the plasma was placed at the same redshift as the Perseus cluster. For each bin, the count in each of the bins was taken, and a χ^2 minimisation of the observed relative count in each bin against the predicted one was done, by varying the two parameters in the model, the temperature (kT) and column density (N_H). If the counts in each of the bands in the bin are A_d , B_d and C_d , and the predicted counts for a particular value of the model are A_p , B_p and C_p (assuming an arbitrary time for a model observation, and arbitrary brightness of its source), then the χ^2 is calculated using

$$\chi^2(T, N_H) = \frac{[A_d - f A_p(T, N_H)]^2}{A_d^2} + \frac{[B_d - f B_p(T, N_H)]^2}{B_d^2} + \frac{[C_d - f C_p(T, N_H)]^2}{C_d^2}, \quad (4.1)$$

where f is a normalisation factor,

$$f(T, N_H) = \frac{A_d + B_d + C_d}{A_p(T, N_H) + B_p(T, N_H) + C_p(T, N_H)}. \quad (4.2)$$

The best-fitting values of temperature and column density were then plotted as a function of position. Fig. 4.7 shows images of the fitted values of the temperature and column density, with an adaptively-smoothed (Ebeling et al. 2002; Section 3.1.1) intensity image of the cluster at the same scale in Fig. 4.8. The brighter emission comes from a plasma at a temperature of about 2.7 keV, which is less than half the outer temperature, found to be ~ 6.5 keV. The outer temperature agrees well with cluster temperatures measured using ASCA (e.g. Allen et al. 2001). The infalling galaxy has a mean excess column density of $\sim 10^{21}$ cm $^{-2}$. Summing the excess absorption over the face of the galaxy gives an absorbing mass of about $2 \times 10^9 M_\odot$ at cosmic abundance.

Electron density, pressure and cooling time maps

Since we know the count rate and normalisation of the plasma model and we know the total number of counts observed in each of the bands, we can find the normalisation

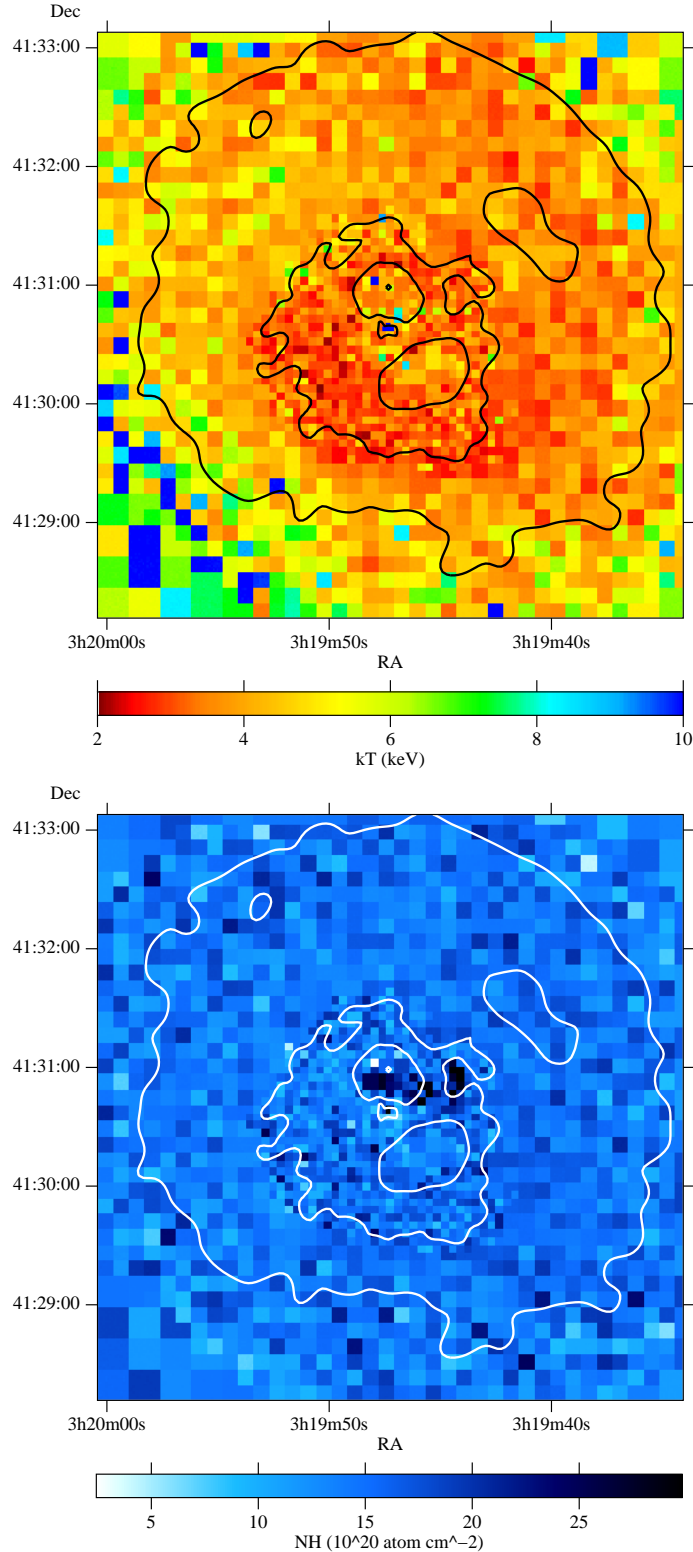


Figure 4.7: Temperature (top) and column density (bottom) maps of the Perseus cluster. Images were made from adaptively-binned X-ray colour images, overlayed with an intensity map of the cluster.

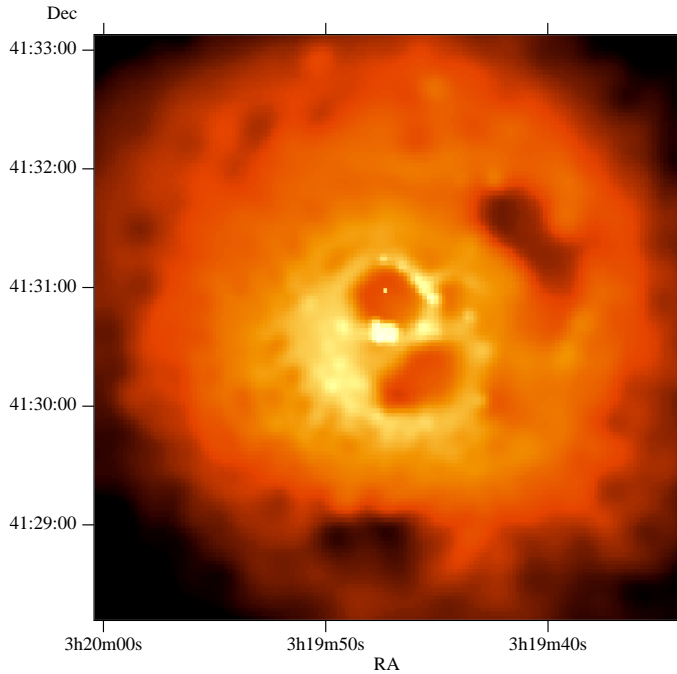


Figure 4.8: Adaptively-smoothed X-ray image of the Perseus cluster, with a minimum significance of 3σ . Data were corrected for exposure effects, and were examined in the 0.5-7 keV range. View along PA 333° for a surprise.

of the source, which measures its brightness. This normalisation can then be used to estimate the electron density in the source. The MEKAL model defines the normalisation of a plasma to be given (in units of cm^{-6}) by

$$K = \frac{10^{-14}}{4\pi[D_A(1+z)]^2} \int n_e n_H \, dV, \quad (4.3)$$

where D_A is the angular diameter distance of the source (cm), z is its redshift, and n_e and n_H are the electron and hydrogen densities (cm^{-3}), and are integrated over the volume of emission (cm^3).

If the number of counts given by the model in the B band per unit normalisation per unit time is denoted by $F(Z, T, N_H)$, then the normalisation of the source is given by

$$K_{\text{source}} = \frac{B_d/t_{\text{data}}}{F(Z, T, N_H)}, \quad (4.4)$$

where t_{data} is the observation length.

Since most of the electrons in the plasma originate from Hydrogen and Helium atoms, the ratio $n_e/n_H \simeq 1.21$ (Sarazin 1998). This value is nearly independent of the state of ionisation, although there is some slight variation with the abundance of the gas. Therefore, combining (4.3) and (4.4) we can calculate n_e , assuming it is constant, and assuming a volume for the part of the source examined.

The electron densities for each pixel in the temperature map were calculated by estimating that the volume of the gas in each pixel is the area of the pixel on the source in cm^2 , multiplied by the distance of the pixel from the centre of the cluster in cm. This volume approximation is gross but probably good enough considering that the temperatures in the temperature map are not deprojected. The electron density map is shown in Fig. 4.9(top). By simply multiplying the density of the gas by the temperature in keV, the pressure of the gas can be estimated in units of keV cm^{-3} . The pressures obtained match those found using the [S II] line ratio in the inner few kpc (Johnstone & Fabian 1988; Heckman et al. 1989).

Assuming that the emission from the X-ray gas is just from bremsstrahlung emission, the cooling time of the gas is approximated by (see e.g. Sarazin 1998)

$$T_{\text{cool}} / \text{yr} = \frac{2 \times 10^{11} \sqrt{11.60 \times 10^6 (k_B T / \text{keV})}}{3.16 \times 10^7 (n_e / \text{cm}^{-3})}, \quad (4.5)$$

therefore a cooling time map can be constructed from the electron density and temperature of the plasma. The above equation does not take account of the effects of line emission, so the actual cooling time may be considerably shorter if the metallicity is high. Fig. 4.10 shows the calculated cooling times as a function of position.

4.1.4 Radio image

The radio image of the cluster (Fig. 4.11), from Fabian et al. (2000), was taken by G.B. Taylor at a frequency of 1.4 GHz using the VLA telescope from several runs of 3-10 h in the A B and C configurations. The image has a synthesised beam of 5 arcsec. The contours start at 1 mJy beam^{-1} , and increase by factors of 2. The peak is at 21.7 J beam^{-1} . The steepest patch of the radio contours abuts the brightest part of the eastern patch.

4.1.5 Discussion

Gas temperatures and cooling times

The temperature of the X-ray gas in the cluster decreases with radius, dropping from about 6.5 to less than 3 keV. The temperature estimates assume that the emission matches a single-phase gas. If more than one temperature component is present, the estimated temperature will approximate the emission-weighted mean. The simple method of estimating the cooling time of the gas shows that the cooling time near the centre of the cluster is of the order of 10^8 yr (none of the gas in Fig. 4.10 has a cooling time of more than 6×10^9 yr). Unless there are significant levels of heating, then the gas is cooling and is part of a cooling flow.

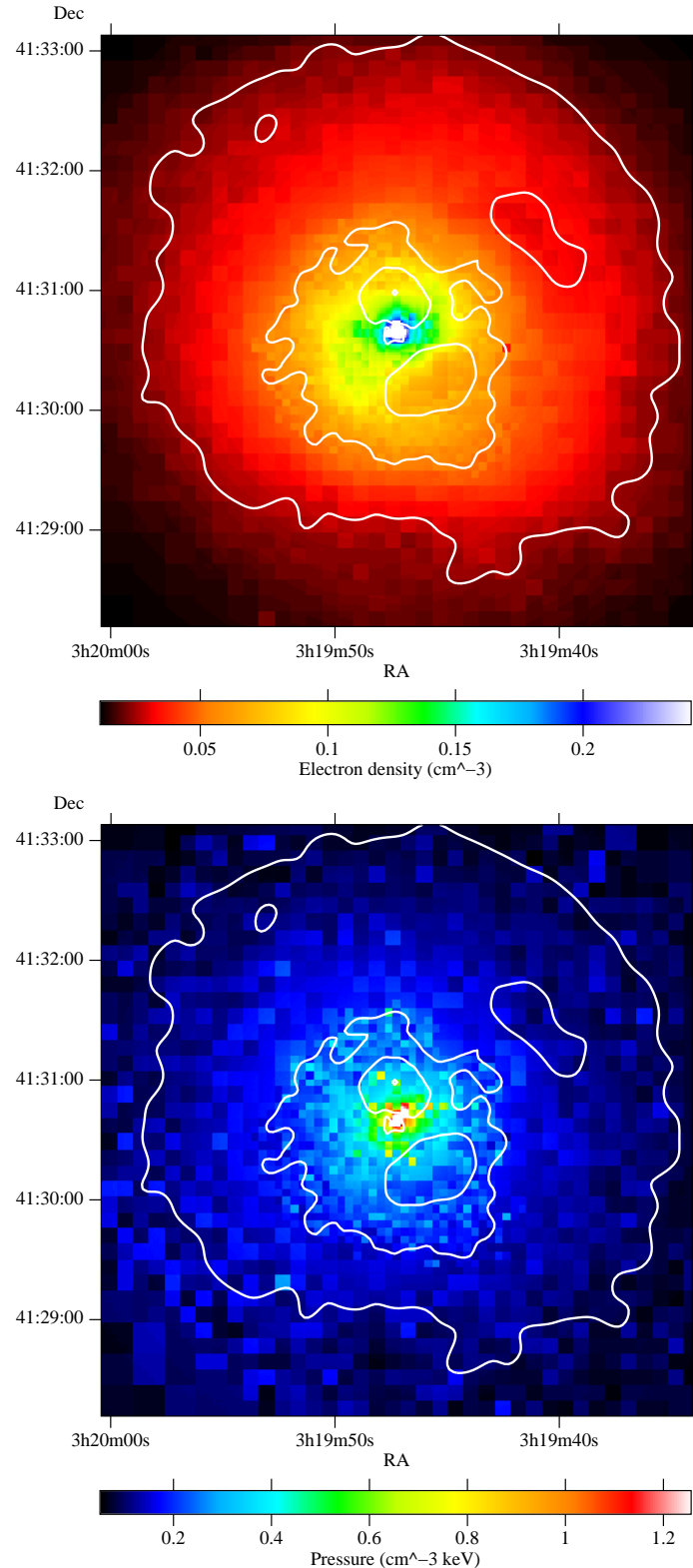


Figure 4.9: Top: Calculated electron density map of the Perseus cluster, overlaid with contours from the intensity image. Bottom: Pressure map derived from the electron density and temperature (Fig. 4.7[top]) maps.

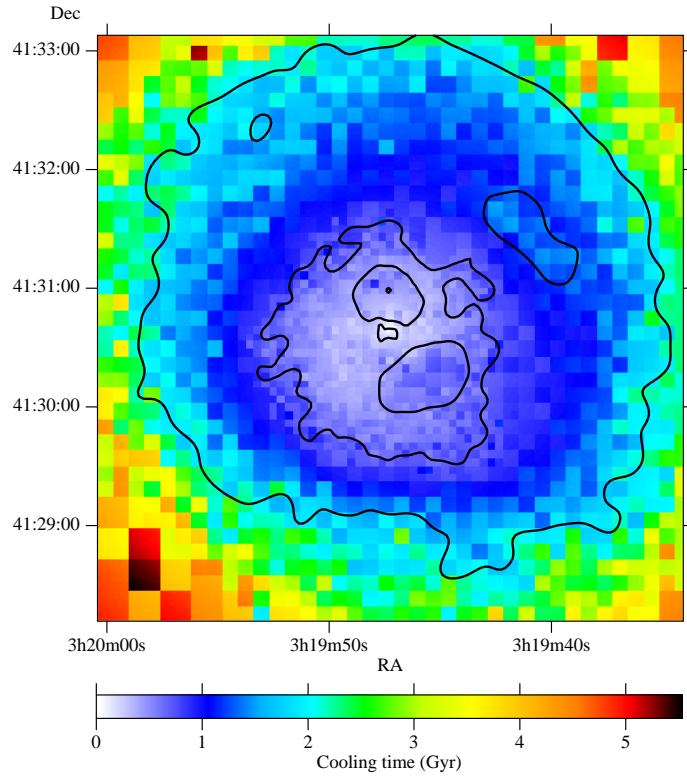


Figure 4.10: Cooling time of the gas in the Perseus cluster, overlaid with contours from the intensity image.

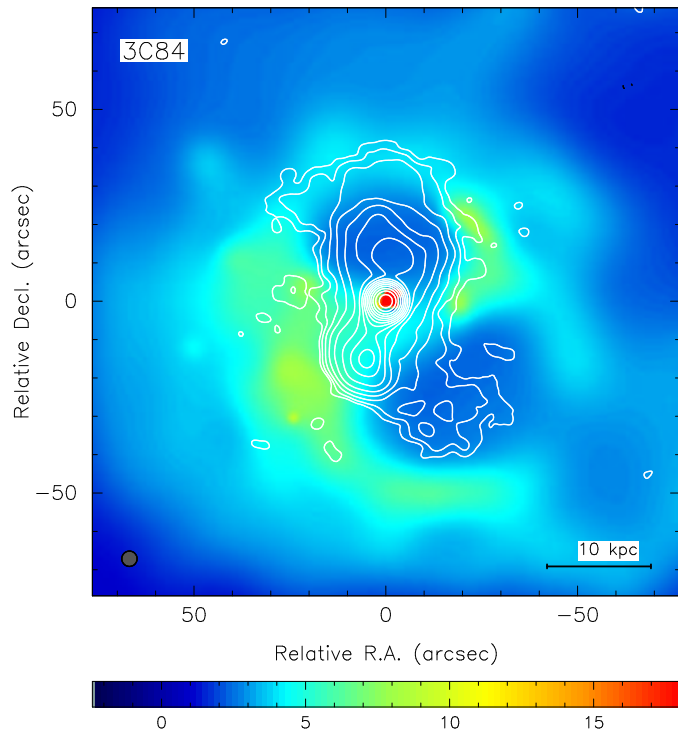


Figure 4.11: *Chandra* X-ray image of Perseus, overlaid with the contours from a VLA radio map. Image taken from Fabian et al. (2000).

The radio lobes

As found by Böhringer et al. (1993), the radio lobes of 3C 84 occupy holes in the X-ray emission of the cluster (Fig. 4.11). It is difficult to disentangle the effects of projection and geometry, but the simplest explanation for the holes is that cosmic rays and magnetic fields have expelled the X-ray gas from these volumes. On the temperature map, there is marginal evidence for hotter emission in the holes, but this may be from material in front or behind them. Since the radio lobes do not feature in the pressure map (Fig. 4.9) they may contain hotter gas. The temperature of gas along the line of sight of the holes is 4–5 keV, but this temperature is projected and emission-weighted.

As mentioned in Section 4.1.3, the X-ray gas along edges of the radio lobes is cool, indicating that any expansion of the lobes must be subsonic. If one knows what the contents of the radio lobes are, then the power output of the radio source can be estimated. By taking the pressure in the holes from the pressure map, and assuming that the lobes are spheres roughly 6 kpc in radius, then the energy contained within them is of the order $P\Delta V \sim 8 \times 10^{58}$ erg, assuming that the holes only contain cosmic rays and magnetic fields. To expand the holes, a similar amount of work was done on the surrounding gas. Since the expansion is subsonic, the work done probably generated a low frequency sound wave which propagated into the outer regions of the cluster, avoiding the local heating of X-ray gas in the core of the cluster. The ages of inner holes have been estimated by Pedlar et al. (1990) using synchrotron ageing, and Churazov et al. (2000) using buoyancy considerations, and are likely to be roughly 10^7 to 10^8 yr. Given the energy content of the lobes and their age, the average power of the nucleus is of the order 10^{44} to 10^{45} erg s $^{-1}$.

This estimate is incorrect if the radio lobes contain hotter, less dense gas than that found in the rims of the lobes. Until the properties of the gas which is possibly in the radio lobes are better understood, then a lower estimate such as that given by the minimum-energy argument of Pedlar et al. (1990) has to be used. They estimate that the pressure of the relativistic gas is ten times less than that of the local gas pressure in the lobes. The relativistic gas only needs to occupy 2 per cent of the volume in order to be in pressure balance. The hot gas may push the cooler gas clouds towards the outer regions of the radio lobes forming the bright rims. If the gas in the holes was pushed to make the rims, then the ratio $\Delta S/S$ (the fractional increase in the surface brightness of the rims to the surrounding gas) should be approximately equal to length of the rims over the radius of the lobes, $\Delta R/R$. This appears to be roughly correct.

It is likely that the nucleus does not have constant activity, having periods where it is ‘switched on’ and periods where it is ‘switched off’. The north-western hole in the X-ray emission could be due to an earlier period of activity which formed a buoyant old radio lobe, as suggested by Churazov et al. (2000). If this is true, then in order for the hole to remain stable it must have a high surface tension, and the likely mechanism for

this is the presence of ordered magnetic fields. A possibility is that the radio lobe was shed by the nucleus, if the galaxy is moving slowly to the south-east. If this is the case, the bright western X-ray emission might have been caused by gas being swept up by the radio lobes.

Blundell et al. (2000) found a spur of low-frequency (74 MHz) radio emission out to the position of the outer north-west hole, and to the south-south-east (to the location of the other hole in Fig. 4.8). The low frequency radio emission is likely to be from the older electron populations, such as those which would be found in fossil radio lobes. The outer holes provide evidence that the central radio source has sporadic outbursts.

The outer holes could be displaced from the current axis of the radio source either due to the motion of the galaxy, or the movement of the gas relative to the galaxy. The swirl nature of the gas in the outer regions of the cluster core (e.g. Fig. 4.7[top] and Fig. 4.3; also noted by Churazov et al. 2000) could be due to the angular momentum of the gas, especially if the gas is flowing inwards due to a cooling flow. The spiral structure is also seen in optical images of the cluster (e.g. Carlson et al. 1998), which may be explained if stars are forming in the gas cooling out from a cooling flow with angular momentum.

A relative movement of the gas or galaxy does not explain why the outer southern hole is along the current radio axis. The position of the outer holes may be due to the beaming directions of the radio source. In M87 the radio-lobes are ‘bent’ indicating that the direction of the jet is changing (Böhringer et al. 1995; Owen et al. 1999). If the direction of the jets can change, then this makes it unlikely that the rapid spin of the black hole could cause the jets. It would require a large addition of angular momentum to the black hole to change its spin.

4.2 Abell 1795

4.2.1 Introduction

Abell 1795 is a rich cluster at a redshift, z , of 0.063 (Hill & Oegerle 1993). It has been especially well studied in optical, radio and X-ray wavelengths. Previous X-ray observations have shown the cluster to be well relaxed; Buote & Tsai (1996) used a power ratio technique on *ROSAT PSPC* images to show the cluster is in a late evolutionary phase. The centre of the cluster shows a strong peak in X-ray emission. This was found using *Einstein* (Jones et al. 1979), *ASCA* (Fabian et al. 1994; Xu et al. 1998), and the *ROSAT PSPC* (Briel & Henry 1996; Allen & Fabian 1997), or using both *ASCA* and *ROSAT* (Allen et al. 2001).

There is also the presence of some strong emission-line nebulosity around the central cD galaxy (Cowie et al. 1983; van Breugel et al. 1984; Hu et al. 1985; Heckman et al. 1989). Cowie et al. 1983 showed the presence of a filamentary system in H α +[N II] extending

$\sim 40h^{-1}$ kpc south¹ of the cD galaxy. Hu et al. (1985) revealed a $\sim 350 \text{ km s}^{-1}$ velocity shear along the H α filament.

The emission-line nebulosity is also accompanied by excess blue light (Johnstone et al. 1987; Smith et al. 1997; Cardiel et al. 1998). The blue light has little if any polarisation, and so is likely to have been emitted by star formation (McNamara et al. 1996a). However, some of the emission is from young globular clusters (Holtzman et al. 1996). Molecular hydrogen emission has also been detected from the cD galaxy (Falcke et al. 1998), indicating the presence of molecular gas. The temperature of this molecular material is estimated to range from 1000-1500 K. Direct evidence for gas of temperatures of $\sim 3 \times 10^5$ K was seen by Oegerle et al. (2001) using *FUSE* in A1795.

The central cD galaxy contains a small radio source in its core. The radio source shows high Faraday rotation measures (Ge & Owen 1993). High Faraday rotations are a good indicator of a cooling flow (Taylor et al. 1994; Taylor et al. 1999). Bright knots of blue continuum are found along the lobes of the radio source, indicating that the radio source has triggered star formation in the central cD galaxy (McNamara et al. 1996b).

An interesting feature of the A1795 cluster is that the central cD galaxy is not at rest in the gravitational potential of the cluster. Hill et al. (1988) found the galaxy has a relative velocity of 365 km s^{-1} relative to average cluster member velocity. This velocity was later revised by Oegerle & Hill (1994) down to $\sim 150 \text{ km s}^{-1}$. However, within a radius of $\sim 200h^{-1}$ kpc, the cD velocity is 374 km s^{-1} greater than the galaxy mean. Oegerle & Hill (1994) argue a subcluster has merged with the main cluster.

Some authors have claimed the detection of excess extreme ultraviolet (EUV) emission from A1795 (Mittaz et al. 1998), but these claims are heavily disputed (e.g. Bowyer et al. 1999).

Recently A1795 was observed with *XMM-Newton* (Tamura et al. 2001). It was found that the volume emission of cool components ($< 1 \text{ keV}$) was less than one per cent of the hot component at the cluster core. If gas is cooling out of the X-ray waveband, then naively there should be cool gas observable. This has been observed in several other clusters (e.g. Peterson et al. 2001). I discussed this further in Section 1.1.5.

4.2.2 The *Chandra* observations

A1795 was observed by *Chandra* on two occasions: firstly for 19,594 s on 1999 December 20 and secondly for 19,421 s on 2000 March 21. The first observation was carried out when the ACIS focal plane temperature was -110°C , but the temperature of the focal plane during the second was -120°C .

Fig. 4.12 shows two *Chandra* images of the combined datasets, one showing counts in the 0.3-1.5 keV waveband, and the other showing 1.5-7 keV. In the soft image a filament like structure runs in the north-south direction, but is much less visible in the hard

¹ h is defined by $H_0 = 100h \text{ km s}^{-1} \text{ Mpc}^{-1}$, where H_0 is the Hubble constant

image. The structure is about 5 arcsec wide, by 40 arcsec long, which corresponds to a projected length of around 80 kpc. Since the object is only visible in the soft image, it is likely to be cool. An adaptively-smoothed (Section 3.1.1; Ebeling et al. 2002) image is shown with an optical image of the filament at the same scale in Fig. 4.13.

It is interesting to make profiles showing the count in some X-ray bands in a box moving across the filament, i.e. in the direction perpendicular to the filament. Fig. 4.14 shows profiles in the bands 0.3-0.8, 0.8-1.5 and 1.5-7 keV, and their total. As in Section 4.1.3, we can adaptively bin the profiles (in one dimension, rather than two), based on the combined colour of the three bands. This procedure gives a roughly equal signal to noise ratio in each of the profile bins. The colours can be fitted to a MEKAL model, as in Section 4.1.3 for Perseus, to generate temperature and absorption profiles, which I show in Fig. 4.15. I also show a two dimensional temperature map of the area around the filament in Fig. 4.16. This map was produced assuming constant galactic absorption.

The maps and profiles show emission weighted temperatures averaged along the line of sight. The temperatures estimated for the inner part of the cluster will be higher than the actual values. The count profile shows that the filament may only produce about a third of the counts from the region which it occupies.

The temperature profile shows that the profile is cooler than the surrounding cluster emission. The average filament temperature is about 2.7 keV, whilst the cluster emission is around 4.3 keV. The southern end of the filament has a temperature of 2.5 ± 0.15 keV, and is cooler than the remainder of the filament which has a temperature of 2.9 ± 0.15 keV. The pixels corresponding to the cD galaxy have the lowest temperature of 2.0 ± 0.15 keV. The column density profile (Fig. 4.15) shows that there is evidence for excess absorption along the filament. A two-dimensional absorption map confirms this and also indicates that there is excess absorption in the cD galaxy.

Using the same assumptions as for the Perseus cluster (Section 4.1.3), maps of the mean electron density and the cooling time of the gas can be made (Fig. 4.17). I assume that the path length through the emitting gas equals the radius of the gas from the centre of the filament, which is the centroid of the surrounding emission. The radiative cooling time is less than 5 Gyr within the inner arcmin radius (corresponding to roughly 120 kpc). The cooling time of the gas along the filament and in the cD galaxy is about 3×10^8 yr.

4.2.3 Comparisons with the optical and radio emission

The X-ray filament is coincident with an H α filament discovered some time ago (Fig. 4.13; Cowie et al. 1983). No galaxies obviously lie along the position of the filament. The filament was found by McNamara et al. (1996a) to resolve into two separate filaments in *U*-band images. They claimed that the brightness requires continuum emission in addition to line emission, which indicates there may be stars present.

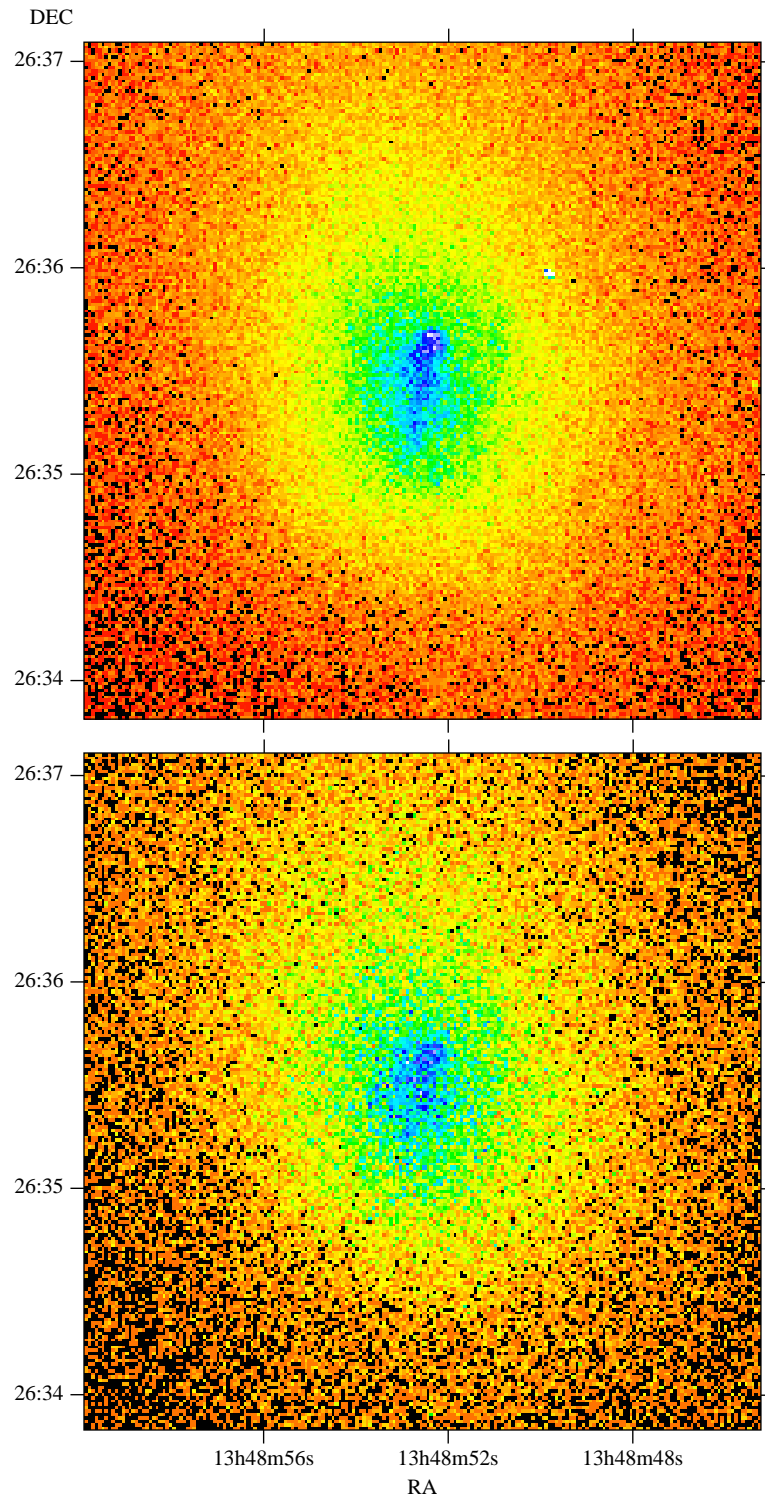


Figure 4.12: Soft (top; 0.3-1.5 keV) and hard (bottom; 1.5-7 keV) *Chandra* images of A1795. Images are binned to give pixels of ~ 1 arcsec.

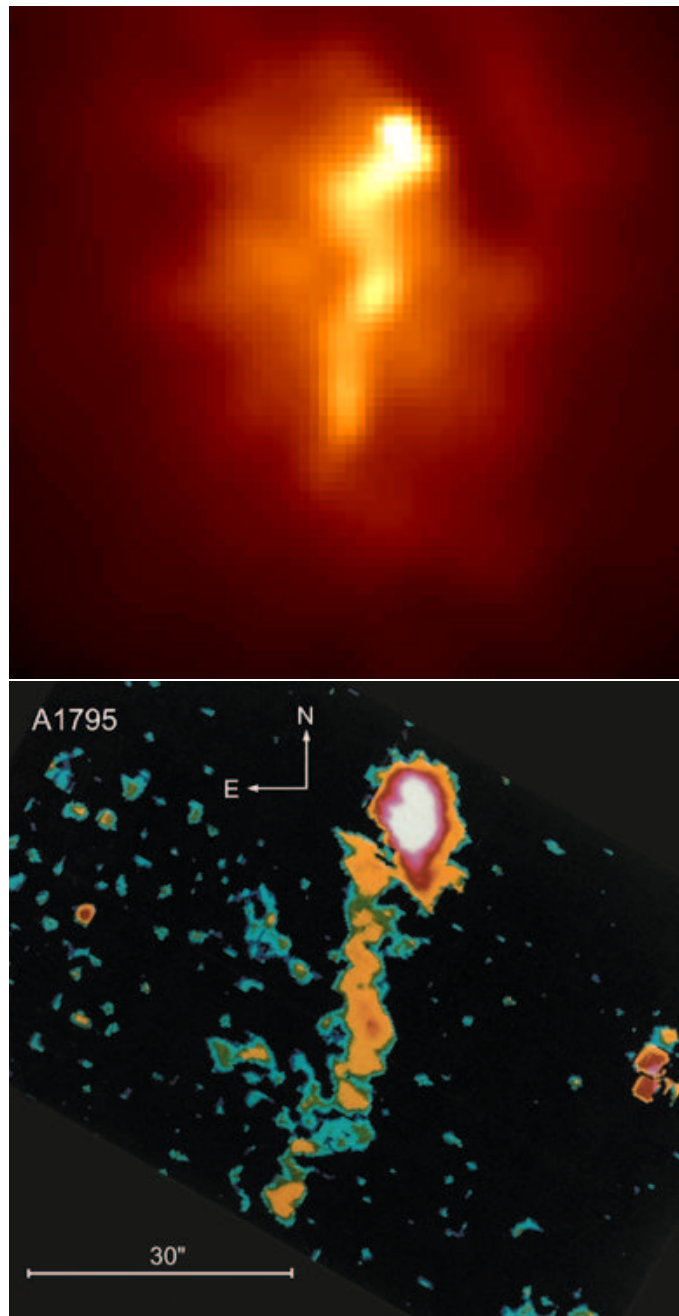


Figure 4.13: Top: adaptively-smoothed X-ray image of the A1795 filament (with $\sigma_{\min} = 3$). Bottom: image of the same region showing emission in H α +[N II], taken from Cowie et al. (1983). North is to the top and east is to the left in both images.

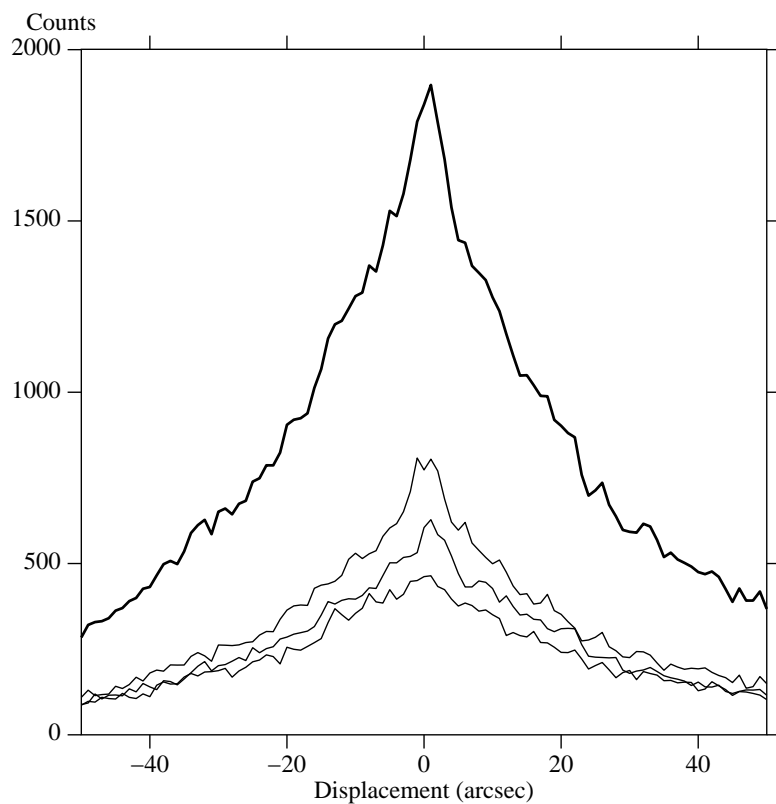


Figure 4.14: Count rate profile across the A1795 filament. Count rates were measured in bins $35 \times 1 \text{ arcsec}^2$, with the long axis parallel to the filament. Top line shows the total count in the 0.3-7 keV band, followed by 0.8-1.5, 0.3-0.8 and 1.5-7 keV.

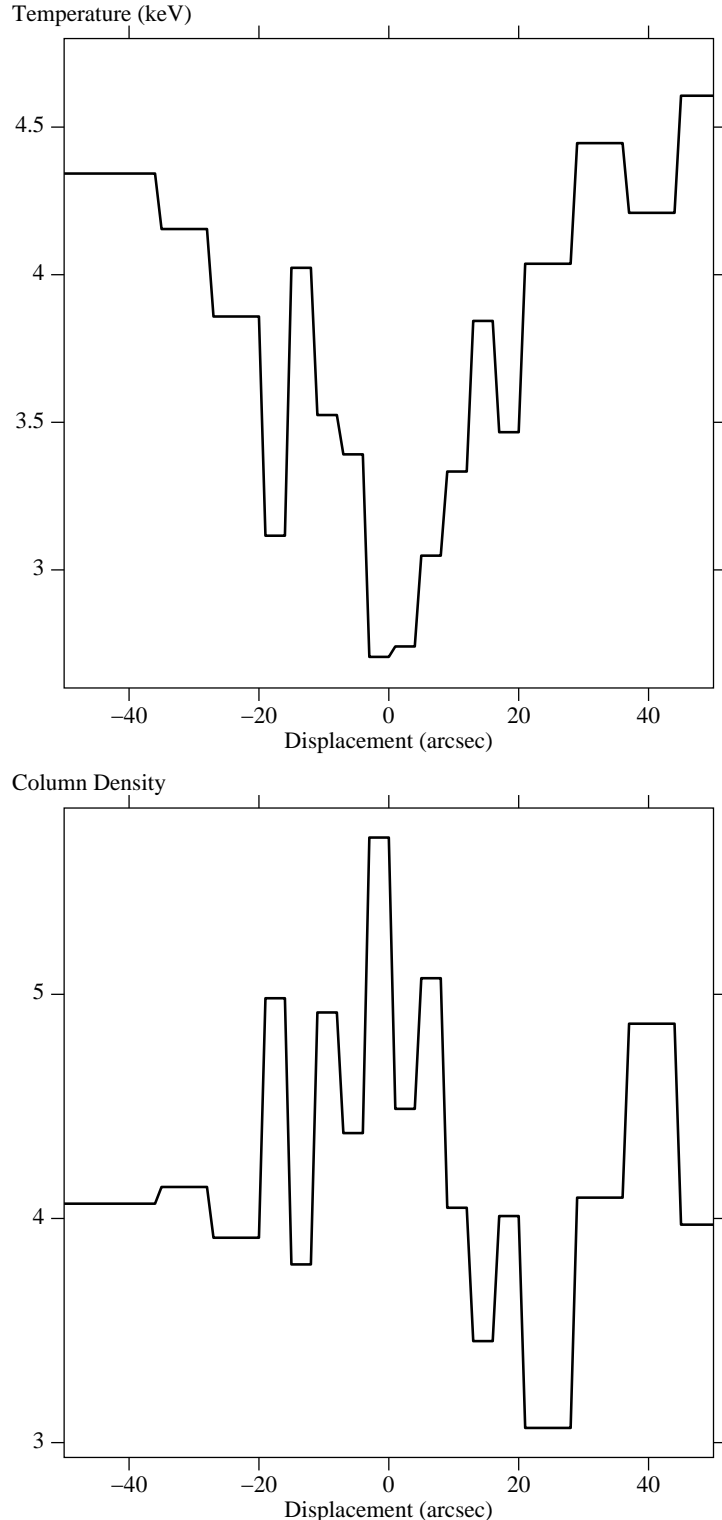


Figure 4.15: Temperature profiles and absorption profile across the filament, generated using adaptively-binned colours from the count rates in Fig. 4.14. The errors in the temperatures are approximately 10 per cent. The column density, N_H is in units of 10^{20} cm^{-2} .

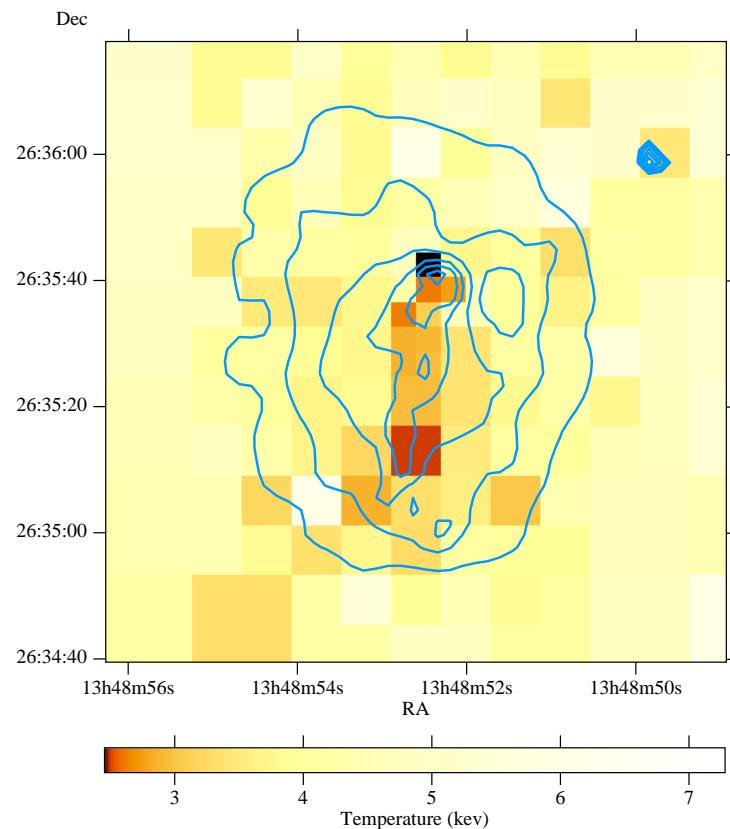


Figure 4.16: Two dimensional temperature map of A1795. The image was by adaptively binning the same three bands as Fig. 4.14. The contours show count levels in the adaptively-smoothed intensity image (Fig. 4.13).

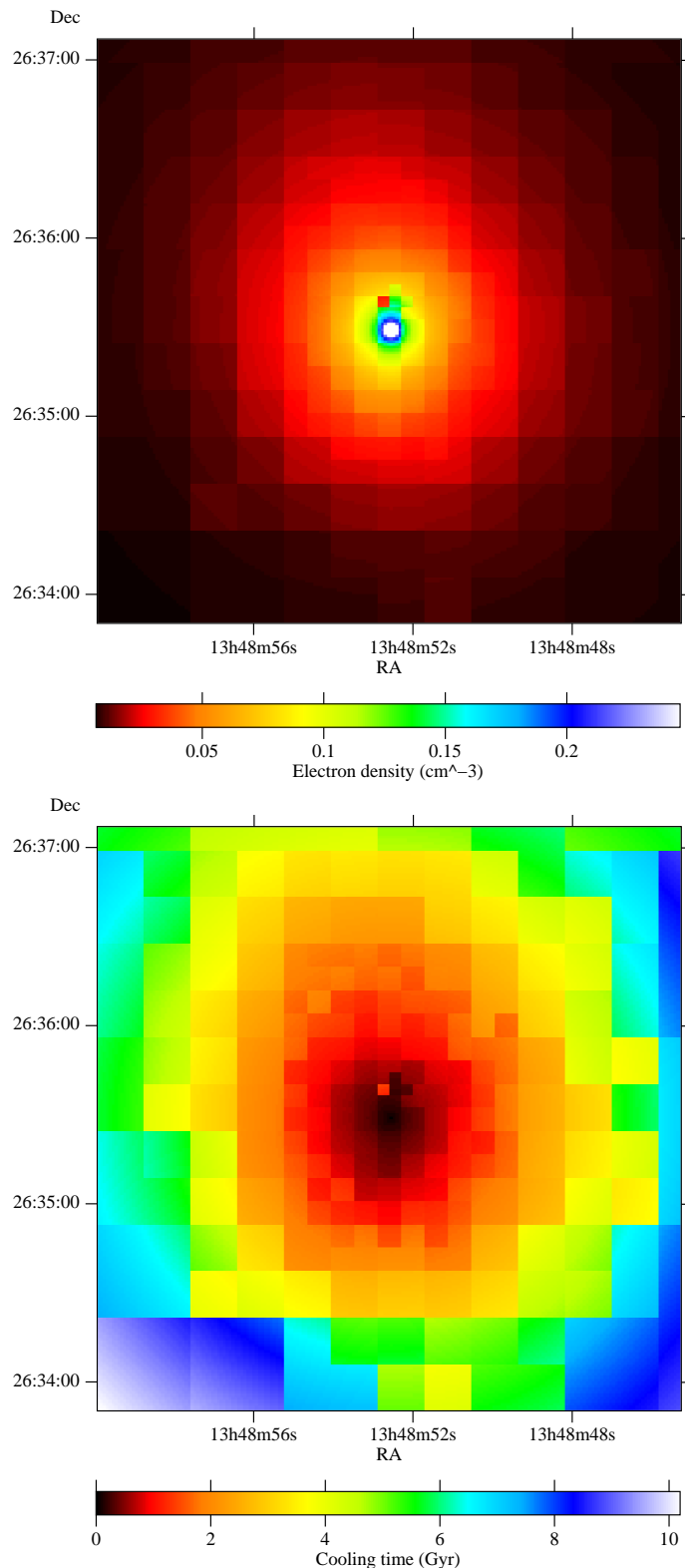


Figure 4.17: Electron density (top) and mean radiative cooling time (bottom) maps for the A1795 cluster. Maps assume that the depth of the emission is the same as the radius from the centre of the filament.

The radio source extends about 5 arcsec in the south-south-west and north-north-east directions (Fig. 4.18[top]). The peak X-ray emission from the cD galaxy is not coincident with the centre of the radio source: the radio source lies about 5 arcsec south of the cD X-ray nucleus. The morphology of the $\text{H}\alpha + [\text{N II}]$ emission is closely related to the radio emission (Fig. 4.18[bottom]), with some anti-correlation between the two. In addition there is also a dust lane associated with the optically bright bluish filamentary and knotty emission features (Pinkney et al. 1996; McNamara et al. 1996b).

There is an anticorrelation between the polarised intensity of the radio emission and the optical line emission, which is likely to be due to the Faraday rotation within the line emitting gas (Ge & Owen 1993). If the line emitting gas is causing Faraday rotation, then it must lie in front of the radio source.

4.2.4 Discussion

The short cooling times in the core of the cluster are consistent with there being a strong cooling flow there. The shortest mean cooling time is approximately 3×10^8 yr, occurring close to the cD galaxy and along the brightest part of the filament.

There is a filament of X-ray emission coincident with the $\text{H}\alpha$ emission filament which was found by Cowie et al. (1983). The X-ray luminosity of the filament can be estimated by assuming it has a width of 5 arcsec and a length of 40 arcsec (corresponding to a real length of 80 kpc). The luminosity is found to be about 2×10^{42} erg s $^{-1}$, only about an order of magnitude greater than the $\text{H}\alpha + [\text{N II}]$ luminosity. If the total optical and ultraviolet luminosities are added, then the total is probably the same or greater than the X-ray luminosity. Providing there is no heating of the filament, then the rate of mass cooling out in the filament is close to $10 \text{ M}_\odot \text{ yr}^{-1}$. In the cD, the X-ray brightest region has the same location as the brightest region of $\text{H}\alpha + [\text{N II}]$ emission.

If the length of the filament is caused by the relative motion of the cD galaxy to the cluster, then given its projected length and assuming an angle of inclination to the sky of 45° , its age is 5×10^8 yr. This time-scale is similar to the cooling time of the gas, which may indicate the cooling time is a constraint on its length. This argument is supported by the coolest point on the filament being the furthest from the cD galaxy. Turbulence in the intracluster medium would be expected to destroy the straightness of the filament. Therefore since the filament is straight, this shows that there probably is not a great deal of turbulence.

We can estimate how far through its orbit the cD galaxy is. The velocity dispersion of the cluster is 920 km s^{-1} (Oegerle & Hill 1994). If the angle of the path of the cD to our line of sight is small (i.e. the measured line-of-sight velocity of 150 km s^{-1} is close to its true velocity), then the cD is close to its position of maximum displacement from the centre of the cluster. If the cD galaxy is moving close to the plane of the sky, then we cannot know its true velocity and the galaxy may have some distance to travel.

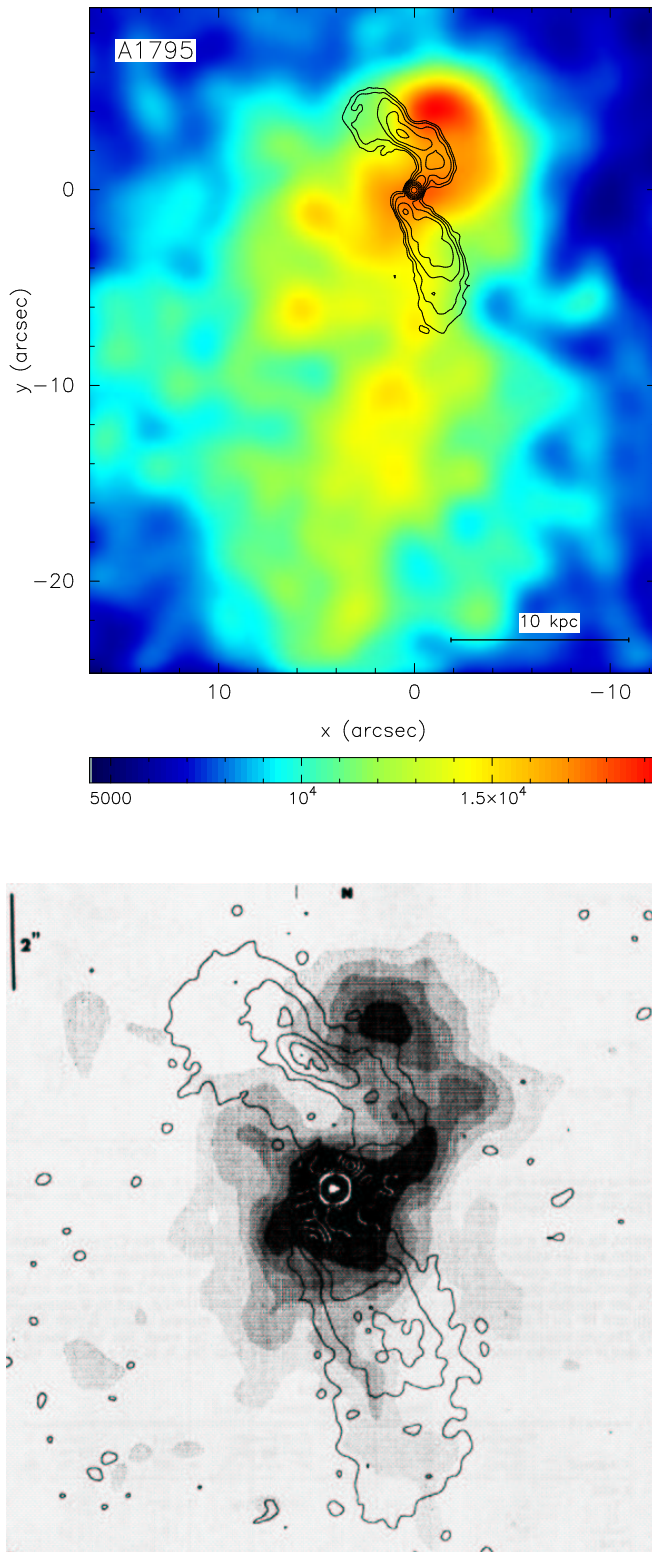


Figure 4.18: Upper: Contours of the 3.6 cm radio emission of the source in A1795 (Ge & Owen 1993) with 0.37 arcsec resolution, overlaid on the *Chandra* X-ray image which has been convolved with a Gaussian with a width of 2 arcsec. The radio contours start at 0.08 mJy beam $^{-1}$, and double with each. The peak radio flux is 33 mJy beam $^{-1}$. Lower: H α +[N II] emission of the cD galaxy overlaid with 6 cm radio contours, taken from van Breugel et al. (1984).

The variations in the brightness of the filament do not correlate well between the X-ray and H α +[N II] images. The brightest part of the H α +[N II] image is 25 arcsec south of the cD galaxy, and this position corresponds with a minimum in the X-ray emission. The brightest X-ray emission 20 arcsec from the cD has little associated optical emission. There also appears to be no evidence in the X-ray band for the SE pointing tail to the filaments which are seen in H α +[N II] and the U-band.

As stated in Section 4.2.2, the centroid of the X-ray emission is not located on the cD galaxy, but 10-20 arcsec south of the cD on the filament. This suggests that the cD is oscillating in the core of the cluster about the centroid. The X-ray surface brightness profile in the core of the cluster does not indicate there is a deep cusp in the cluster potential, as would be expected from the peaked outer X-ray emission. Therefore there is unlikely to be a static dark matter cusp at the centre of the cluster. Since there is no extensive peak (> 10 arcsec) in the surface brightness about the cD, there is no evidence for a dark matter halo associated with the cD, moving with the cD along its path.

The nature of the filament is uncertain, but several of the possibilities are listed below.

1. The filament could be a *cooling wake*, where the gas is cooling onto the moving galaxy (as was seen by ROSAT observations of NGC 5044; David et al. 1994). The gas would be cooling very slowly and steadily, in almost hydrostatic equilibrium with the potential of the cluster. The gas with longer cooling times ($> 10^9$ yr) would only see the mean gravitational potential of the cD, which averages to a line. The cD itself focuses the inner part of the cooling flow (the gas which has short cooling times). The length of the wake would be limited by the cooling time of the gas. This is suggested as the coolest gas is furthest from the cD galaxy.
2. The filament could be a *contrail caused by the ram pressure of the radio source as it moves through a multiphase medium*. It is more likely, however, that the passing galaxy would heat gas rather than cool it.
3. The filament could be caused by *evaporation of cold gas which was ram-pressure stripped from the cD galaxy*. Assuming a tube-like geometry for the filament, the total mass of X-ray visible gas is $5 \times 10^9 M_\odot$. Therefore if this scenario is correct there must have been at least this much gas within the cD galaxy initially. In M86 in the Virgo cluster, the ram-pressure stripped wake is very broad (White et al. 1991a; Forman et al. 1979), so it is not clear whether the gas can be stripped in a straight, even filament. There is unlikely to have been a significant amount of hot interstellar medium intrinsic to the cD galaxy, since a 1 keV component would have a cooling time of 10^8 yr and would only be replenished from stellar mass loss at the rate of a few $M_\odot \text{ yr}^{-1}$ (Takeda et al. 1984). Therefore the cool gas at the position of the cD would be made up of stellar mass loss and inflow from the ICM.

4. The filament could be *an accretion wake, where the gas is gravitationally focused and cooled in the wake of the moving galaxy* (Sakelliou et al. 1996). Since the velocity and velocity dispersion of the cD are at least a factor of two smaller than the sound speed of the gas, it is unlikely that gravitational focusing of the gas could be solely responsible.

The cooling wake seems the simplest, and most likely explanation. In addition, the emission-line velocity map of Hu et al. (1985) shows that most of the filament has the same velocity as the cluster (which is blueshifted by $\sim 150 \text{ km s}^{-1}$ with respect to the cD galaxy). The line emission of the cD is stationary with respect to the cD. These results indicate that the cooling wake hypothesis is more likely than the stripping hypothesis, as a strong velocity gradient would be expected along the filament.

In most clusters with cooling flows, the cooling flow is coincident with the core of the cD galaxy. It is therefore difficult to identify the source of the energy which is energising and ionising the optical nebulosity seen in many cooling flow clusters (see Section 1.1.6). This cluster has the advantage of having the cooling gas removed from the main body of stars in the cD galaxy. A detailed study of the spatial distribution of the optical emission, in particular how clumpy it is, would be useful to understand further the processes of cooling and star formation. The small scale differences between the optical and X-ray emission may be due to the densest gas cooling out on small scales.

The filament also helps us to understand conduction in the ICM. If conduction occurred at the Spitzer value, then the filament would be destroyed in a timescale of $\sim 10^8 \text{ yr}$. Therefore conduction is suppressed by at least an order of magnitude.

5

The Centaurus cluster

Summary

In this chapter I analyse data from a 31.7 ks observation of the Centaurus cluster taken using the ACIS-S detector on *Chandra*. Some of the work in this chapter is currently in press as *Spatially-resolved X-ray spectroscopy of the core of the Centaurus cluster* (Sanders & Fabian 2002). Images of the X-ray emission show a plume-like feature at the centre of the cluster, of extent 60 arcsec (20 kpc in projection). The feature has the same metallicity as gas at a similar radius, but is cooler. A radial abundance profile shows that the previously known steep abundance gradient peaks with a metallicity of $1.3 - 1.8 Z_{\odot}$ at a radius of about 45 arcsec (15 kpc), before falling back to $0.4 Z_{\odot}$ at the centre of the cluster. A radial temperature profile shows that the temperature decreases inwards. Using adaptive binning, I generate temperature, abundance and absorption maps of the cluster core. I determine the spatial distributions of each of two temperature components, where applicable. The radiative cooling time of the cooler component within the inner 10 arcsec (3 kpc) is less than 2×10^7 yr. X-ray holes in the image coincident with the radio lobes are seen, as well as two outer sharp temperature drops, or cold fronts. The origin of the plume is unclear. The existence of the strong abundance gradient is a strong constraint on extensive convection or gas motion driven by the central radio source.

5.1 Introduction

The Centaurus cluster, Abell 3526, at a redshift $z = 0.0104$ (Lucey et al. 1986) is a nearby, X-ray bright galaxy cluster. Analysis of *ASCA*, and earlier data (e.g. Allen et al. 2001) indicates it hosts a cooling flow (see Fabian 1994 for a review) of $30\text{--}50 \text{ M}_\odot \text{ yr}^{-1}$, centred on the cD galaxy NGC 4696. Previous observations of Centaurus (e.g. Allen & Fabian 1994) show a system with smooth, elliptical, X-ray isophotes, indicating the system is relatively relaxed. However, there is evidence for a current or past merger event (Allen & Fabian 1994; Churazov et al. 1999; Furusho et al. 2001). The neighbouring subcluster, Cen 45, centred on NGC 4709, has a velocity which is 1500 km s^{-1} higher than the main Centaurus cluster, also known as Cen 30 (Lucey et al. 1986).

Observations of the cluster using *ROSAT* and *ASCA* show that the central region of the cluster is rich in metals, with a large abundance gradient (Fukazawa et al. 1994; Ikebe et al. 1999; Allen et al. 2001).

5.2 The X-ray image

The data presented here are from a 31.7 ks observation of the Centaurus cluster by the *Chandra Observatory*, using the ACIS-S detector. The temperature of the focal plane was -120°C at the time of the observation. No period in the observation was affected by flares, so no data were excluded from the analysis. The interaction of the radio source PKS 1246-410 with the X-ray plasma is discussed elsewhere (Taylor et al. 2002). All errors quoted are $1\text{-}\sigma$ uncertainties. Distances assume $H_0 = 50 \text{ km s}^{-1} \text{ Mpc}^{-1}$. Data were fitted using the *xSPEC* package (version 11.0.1; Arnaud 1996) and metallicities are relative to solar abundances defined by Anders & Grevesse (1989).

Fig. 5.1 shows a coloured raw (~ 1 arcsec pixels) image of the inner 140 arcsec of the S3 chip. Events are coloured according to the energy recorded (0.5–1 keV red, 1–2 keV green, 2–7 keV blue). The plume-like structure to the NE resembles a twisted sheet, and was seen in an observation of the cluster using the *ROSAT* HRI (Sparks et al. 1993).

Fig. 5.2 shows an adaptively-smoothed (Ebeling et al. 2002) image of the raw data. It has been smoothed with a minimum significance of $3\text{-}\sigma$. The image highlights that the emission is diminished from the north-east to the south-west close to the nucleus. It clearly shows the spiral plume-like feature, appearing to emerge from the nucleus in the south, and heading towards the north-east. The plume is approximately 60 arcsec long (20 kpc in projection). The energy-coloured image (Fig. 5.1) shows the centre of the cluster, and the plume is cooler (redder) than the rest of the cluster. The two deficits or ‘holes’ in emission immediately to the NE and NW of the core are associated with the lobes of the radio source (Taylor et al. 2002). The continuation of the holes to the SE and SW is probably also related with the southern extension to the radio lobes.

In Chapter 4 it was hypothesised that the filament-like feature seen in X-ray emission

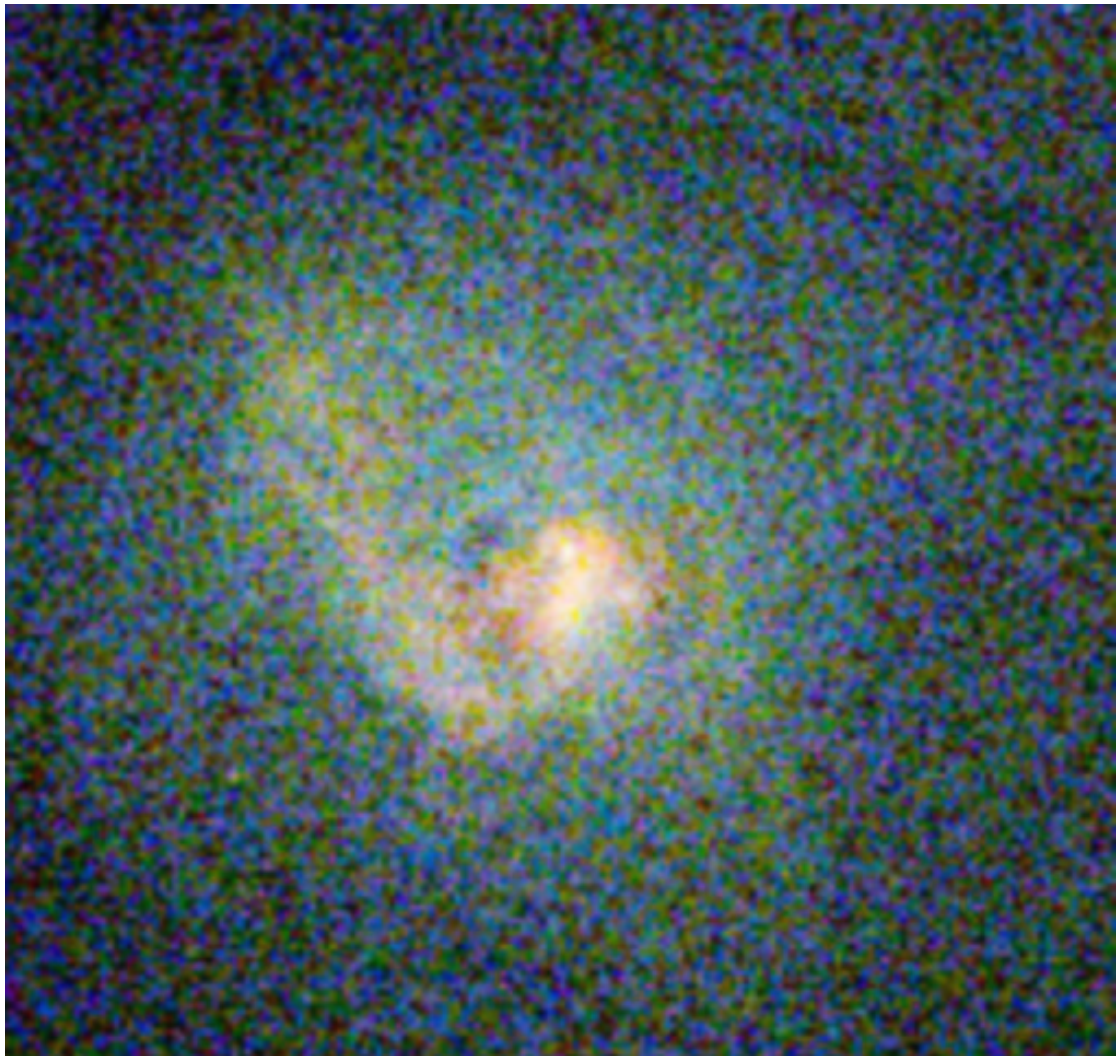


Figure 5.1: Colour X-ray image of the inner part of the ACIS-S3 chip centred on the core of the Centaurus cluster. Events between 0.5 and 1 keV are coloured red, those between 1 and 2 keV green, and those between 2 and 7 keV blue. The pixel size is ~ 1 arcsec. The image measures ~ 140 arcsec (46 kpc) vertically. The emission peaks at around 110 counts per square-arcsecond between 0.5 and 7 keV.

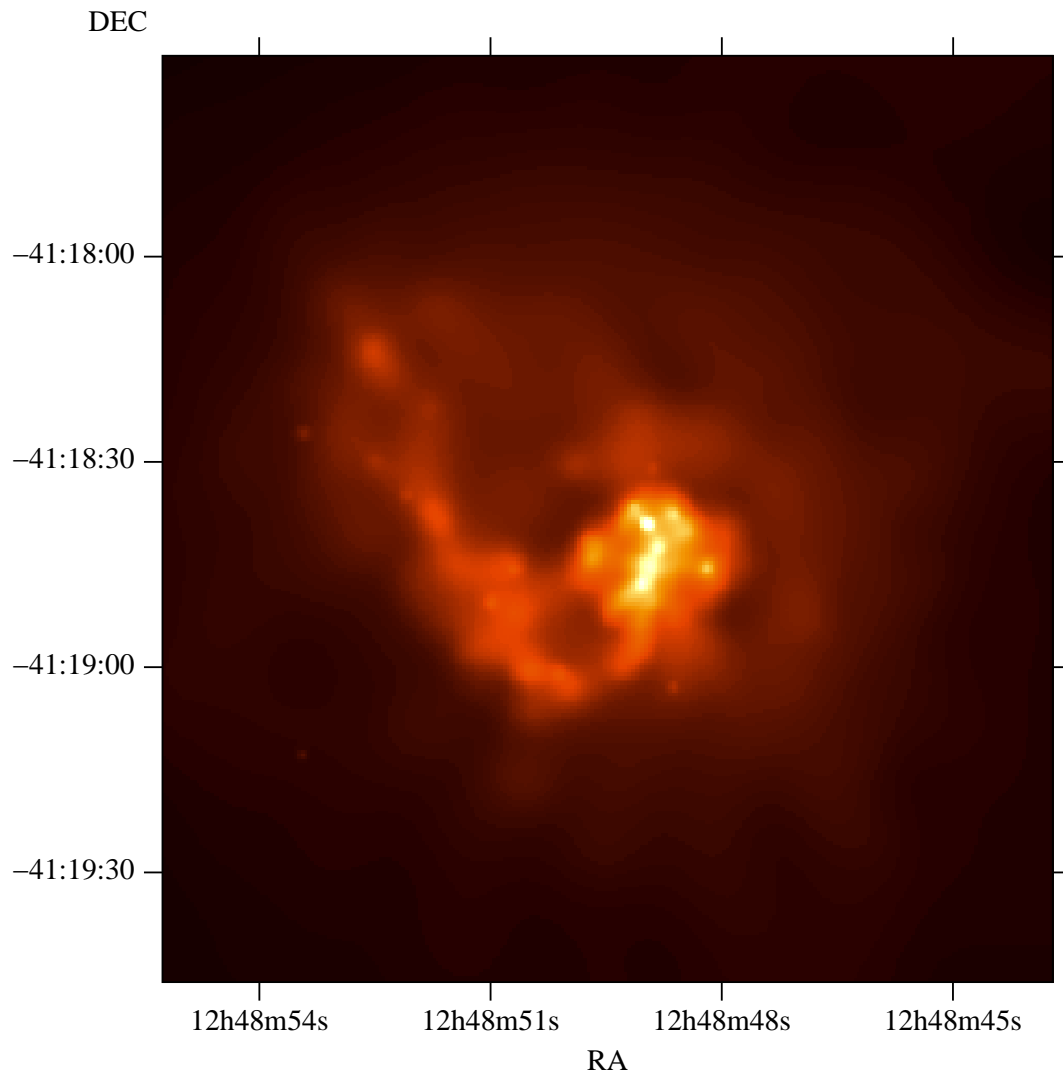


Figure 5.2: Adaptively-smoothed image of the centre of the Centaurus cluster in the energy range 0.5 to 7 keV with ~ 0.5 arcsec pixels. The image measures 175 arcsec vertically, which corresponds to a distance of 58 kpc. The minimum ASMOOTH significance is 3σ .

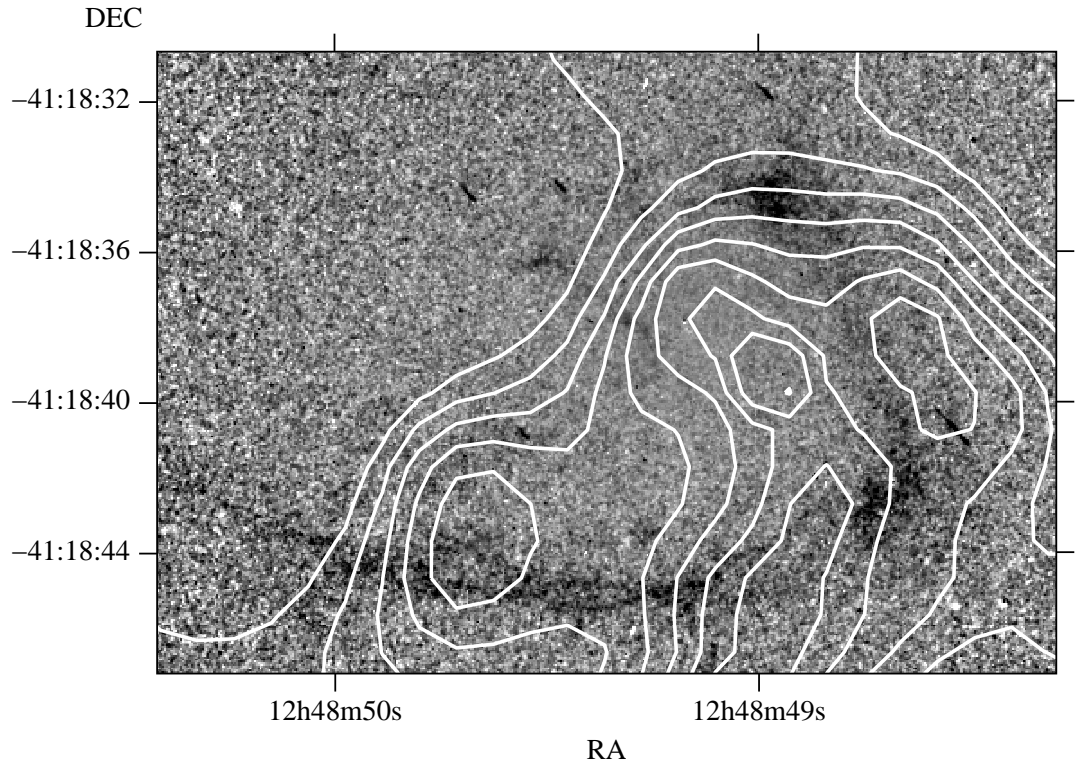


Figure 5.3: Optical *HST* image showing the dust lane in the centre of NGC 4696 overlaid by contours from the adaptively-smoothed image of the X-ray data (Fig. 5.2). The optical image shows the ratio of the emission in a band with a central wavelength of 5407 Å relative to one at 7940 Å.

in the core of the Abell 1795 cluster may be caused by the relative motion of the cD galaxy to the rest of the cluster (estimated to be at least 150 km s^{-1}). The results of Dickens et al. (1986) show that NGC 4696 lies close to the mean velocity of Cen 30. However, the radio maps of Taylor et al. (2002) show that the radio lobes bend to the south of the core. This indicates that NGC 4696 is moving north relative to the local intracluster medium. The aspect of the radio lobes could include a projection effect, with a velocity component along our line of sight of $100\text{-}200 \text{ km s}^{-1}$.

Observations of the core of the cluster at optical wavelengths show a dust-lane in NGC 4696 (Shobbrook 1963). It has been noted that the X-ray emission has a similar morphology to the dust lane (Sparks et al. 1993). Using four *HST* archived observations (datasets U3560101T, U3560102T, U62G8401R and U62G8402R) of the galaxy at 5407 Å and 7940 Å, I made a ratio image of the optical emission in two bands highlighting the dust-lane. This is shown in Fig. 5.3, overlaid with a contour map of the centre of the adaptively-smoothed image, Fig. 5.2. The swirling morphology of the dust-lane is similar to, but smaller than, the X-ray plume.

I find no evidence for hard X-ray emission (between 2-7 or 4-7 keV) from the core of the radio source PKS 1246-410 (position taken from Taylor et al. 2002) at the 2σ level.

Hard X-ray emission was seen in Centaurus using *ASCA* (Allen et al. 2000), which has a hundredfold larger point-spread function than *Chandra*. There is tentative evidence for diffuse hard X-ray emission in the *Chandra* data which will be studied elsewhere.

5.3 Spectral fits

5.3.1 Spectrum of central 10 arcsec

I extracted a spectrum from the central 10 arcsec radius of the cluster. The spectrum was fitted with an absorbed single-temperature (1-T) MEKAL model (Mewe et al. 1985; Liedahl et al. 1995), in the energy range of 0.5 to 7 keV, where the *Chandra* response-matrix is well calibrated. The spectrum was binned to ensure a minimum number of counts per spectral bin, chosen here to be 22 arbitrarily. I generated an effective response and ancillary matrix, averaged from the matrices applicable to each part of the region, but weighted according to the relative number of counts. The background was removed using a blank field background-spectrum of the same part of the detector, created using the prescription of Markevitch (2001). Although the background fields have lower galactic absorption ($N_{\text{H}} = 0.02 \times 10^{22} \text{ cm}^{-2}$) than the region observed ($0.081 \times 10^{22} \text{ cm}^{-2}$, obtained using the FTOOLS NH program; Dickey & Lockman 1990) its level is insignificant compared with the bright cluster emission studied here.

The results of the fit are summarised in Table 5.1. I found a temperature of 0.71 keV, a metallicity of $0.16 Z_{\odot}$, absorbed by $N_{\text{H}} = 0.26 \times 10^{22} \text{ cm}^{-2}$. The 1-T model poorly fits the spectrum (Reduced $\chi^2 = 660/128 = 5.2$).

In regions of cooling flow clusters where radiative cooling dominates, i.e. where the radiative cooling time is shorter than the age of the flow (about 3–5 Gyr; Allen & Fabian 1997, corresponding to about one arcmin radius in the Centaurus cluster), the X-ray surface brightness profiles indicated if there is no balancing heat source, that the inferred mass deposition of cooled gas is roughly proportional to radius ($\dot{M} \propto r$). This requires that the gas there is multiphase (Nulsen 1986; Thomas et al. 1987). The spectrum of multiphase gas should be fit better with a two-temperature (2-T) model than a 1-T model (e.g. Allen et al. 2001). An even better model should be a cooling flow (CF: Johnstone et al. 1992), possibly with intrinsic absorption.

Studies of several cooling flow clusters using the *XMM-Newton* RGS (e.g. Peterson et al. 2001; Tamura et al. 2001) have shown that soft X-ray emission lines expected from gas cooling to low temperatures are absent in the data. A model (cooling flow to a minimum temperature, CFMT) which does fit the data, is a cooling flow in which gas cools from the upper temperature to a lower temperature, which may be one third to one fifth of the upper one. Such a model requires that the gas disappears once it reaches the minimum temperature, perhaps because of intrinsic absorption for which the absorbed CF model is an approximation, because of mixing or because of rapid heating which

turns the cool phase into the hot one (see Fabian et al. 2001b).

In this chapter I try all these models (1-T, 2-T, CF and CFMT) on the data. Previous work with *ASCA* has shown that more than one temperature component is required in the core of the Centaurus cluster (Fukazawa et al. 1994; Ikebe et al. 1999; Allen et al. 2001). Projection effects due to hotter outer gas being along the line of sight to cooler gas are also examined for the plume. I do not however carry out an exhaustive set of modelling due to the unknown three-dimensional geometry of the cooler gas and the limitations of the models themselves, which do not include effects due for example to gravitational heating in a flow. Moreover, as I show, the metallicity of the gas is spatially complex, which further complicates detailed modelling. It is my intention here to identify the gross behaviour of the gas in terms of its temperature and abundance distributions with position.

I fitted the spectrum of the core with a 2-T MEKAL model, fixing the abundances of the two phases to be the same, as there is not enough information in the spectrum to measure the abundances separately and accurately. The results of this fit are also shown in Table 5.1. The temperatures of the two phases are around 0.7 keV and 1.4 keV. The metallicity ($\sim 0.6 Z_{\odot}$) is much larger than for the 1-T result ($\sim 0.2 Z_{\odot}$). The quality of the fit is considerably better than the 1-T model (Reduced $\chi^2 = 200/132 = 2.4$), but still not good. Allowing the two abundances to vary did not significantly improve the fit. The best-fitting metallicities were $1.0^{+1.7}_{-0.4} Z_{\odot}$ (cold-phase) and $0.46^{+0.08}_{-0.06} Z_{\odot}$ (hot-phase), but the temperatures were unaffected. Adding a third temperature to the 2-T model did not significantly improve the fit. However, adding a third component fixed at 4 keV to account for projected emission was an improvement. The radiative cooling time of the cooler component in the 2-T fit is about 2×10^7 yr.

The fits can be improved further by switching from a MEKAL model to an APEC model (Brickhouse et al. 2000). The reduced χ^2 for an APEC 2-T fit is 2.0. The residuals of the fit show there is some excess emission above 3 keV. This emission can be fit either using a power-law or a high-temperature plasma. I show in Table 5.1 the slight changes induced by adding a plasma of fixed temperature 4 keV and metallicity $0.4 Z_{\odot}$. Adding this component is justified as it is expected that there is contributing emission from the cluster in front of the core.

The spectrum can also be fitted (but with a poorer goodness-of-fit) using an intrinsically absorbed cooling flow model (RJCOOL; Johnstone et al. 1992), plus a plasma fixed at 4 keV and $0.4 Z_{\odot}$. I absorbed both components by a fixed galactic absorber, and allowed the intrinsic absorption of the cooling flow to vary. Normally I would add another plasma component to account for the local emission of the cluster near the cooling gas, and gravitational work done. However, at the centre of the cluster the cooling flow dominates, so no extra component was necessary.

I derive a cooling flow mass deposition rate of $11 M_{\odot} \text{ yr}^{-1}$. The gas cools from a temperature of 1.1 keV and has a metallicity of $0.7 Z_{\odot}$. The cooling flow is intrinsically

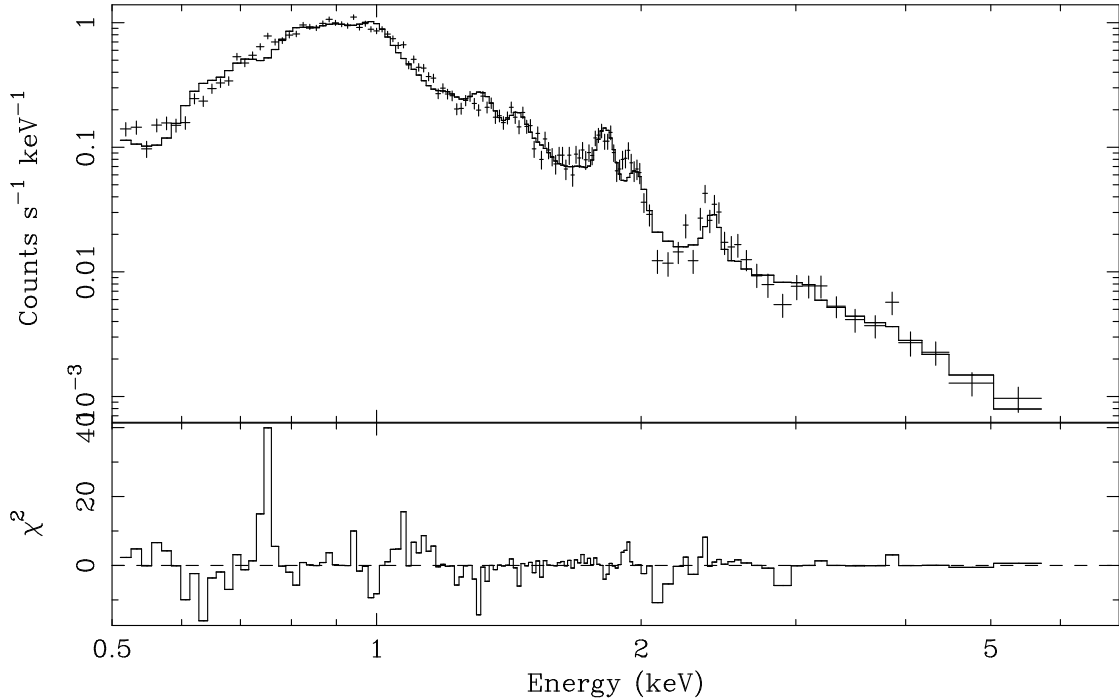


Figure 5.4: Spectrum of the inner 10 arcseconds of the cluster, fitted with a 1-T MEKAL model (fixed at 4 keV and $0.4 Z_{\odot}$), plus an intrinsically absorbed RJC0OL cooling flow.

absorbed by $2.4 \times 10^{21} \text{ cm}^{-2}$. The spectrum, fitted with the cooling flow model, is shown in Fig. 5.4. The cooling flow model calculates its emission using MEKAL plasmas. I speculate that an APEC version of the code would fit the spectra better, but unfortunately this code is still under development.

Using a CFMT model (Table 5.1) I found the mass deposition rate and upper temperature to be unchanged, a decrease in the intrinsic absorption of the cooling flow to a value similar to that found using 2-T fits, and a lower cooling temperature of 0.40 keV. The fit is better than a single cooling flow, but not as good as a 2-T model.

All the fits I have tried to the core spectrum show a large residual around 0.75 keV, independent of the model used (shown for the RJC0OL model in the lower panel of Fig. 5.4). MEKAL and APEC models with varying elemental abundances do not improve the fit to this feature. The emission is well fitted with a δ -function. By examining the spectra of annuli, I have determined that this feature is not significant outside a radius of 10 arcsec (3 kpc) from the centre. It is also present in the inner 5 arcsec. The effective area of the telescope varies smoothly over the energy range of the emission, making the feature unlikely to be a calibration error.

There are also negative-residuals just above 2 keV. The effective area per unit energy of the telescope almost halves in the range 2 to 2.1 keV, so this feature may be a calibration issue. Accounting for these two spectral features would greatly improve the fit to the data, and would lead to a much smaller reduced χ^2 .

I show in Fig. 5.5 the contributions towards χ^2 for three different fits to the spectrum

of the core. The feature at 0.75 keV, in all spectra, has been removed by fitting it with a Gaussian. I also included a plasma fixed at 4 keV and $0.4 Z_{\odot}$ to model the projected cluster emission. The top panel shows a 2-T MEKAL model, the middle panel a 2-T APEC model, and the lower panel an intrinsically absorbed RJCOOL model with fixed galactic absorption.

5.3.2 Spectrum of the plume

I extracted a spectrum from the plume-like region in the cluster. It, like the core, is poorly fit by a 1-T model. Using a 2-T model, the fitted temperature of the hot component is ~ 0.1 keV larger than the hot component in the core. The cooler component has a similar temperature. The abundance of this region is significantly higher than the core (an increase of $0.2 - 0.3 Z_{\odot}$).

I also fitted the spectrum of an area at a similar radius to the plume (but not including the plume) with a 2-T model. The results are shown in Table 5.6 as ‘plume radius’. The plume appears to be ~ 0.25 keV cooler (in both fitted temperatures). There is no significant abundance difference. A cooling flow model (with a component to account for local cluster emission) gives a mass deposition rate of $4 M_{\odot} \text{ yr}^{-1}$, with a high metallicity of $1.6 Z_{\odot}$.

My next task was to test whether the multi-temperature nature of the plume is a projection effect. I compared the emission measure of the upper temperature component of a 2-T model fitted to the plume, with the emission measure of a 1-T fit to the spectrum in another region with the same size and radius as the plume, but at an angle of 90° to it. The emission measure of the upper-temperature component of the plume was 70 per cent greater than the emission measure of this comparison region. Therefore, the multi-temperature nature of the plume is not wholly a projection effect but is intrinsic to the plume.

By assuming a cylindrical geometry for the plume (20 kpc long, radius 2.3 kpc), and fitting a 1-T model to its spectrum, the emission measure implies an electron density of $\sim 0.13 \text{ cm}^{-3}$. The total gas mass of the plume is therefore $\sim 10^9 M_{\odot}$. This mass is compatible with the hypothesis that this gas was stripped off an infalling galaxy. The mean cooling time of the gas in the plume is approximately 10^8 yr, so the gas, or galaxy, must have a velocity of $\gtrsim 200 \text{ km s}^{-1}$ in order to not have cooled. The similarity of the abundance of the plume to the other gas at that radius raises a problem for the stripping hypothesis.

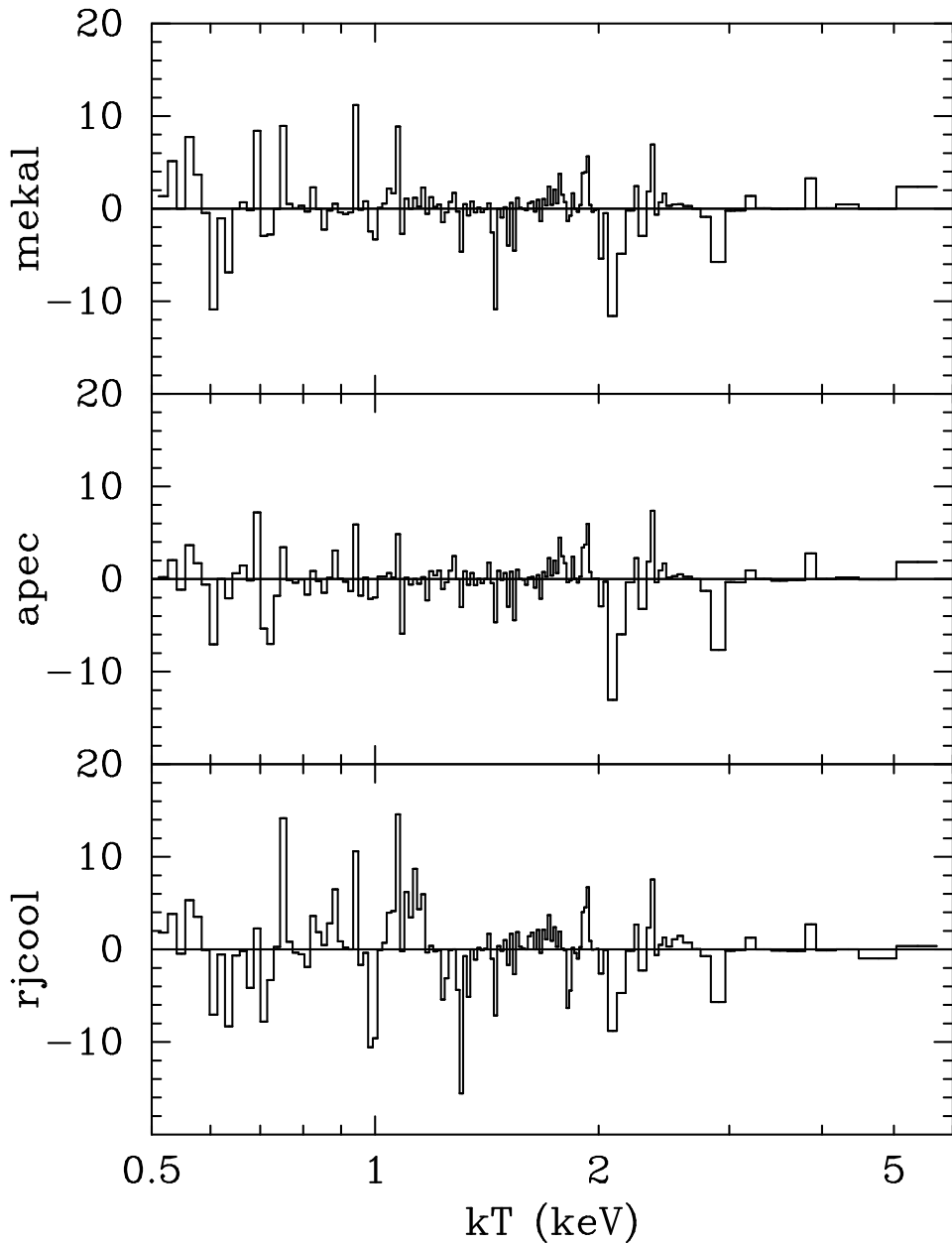


Figure 5.5: Contribution to χ^2 (times sign of the difference between model and spectrum) of fitting the spectrum of the inner 10 arcsec with three different models, including the contribution of the emission at 0.75 keV. (top) 2-T MEKAL model plus a fixed component at 4 keV and $0.4 Z_{\odot}$. (middle) 2-T APEC model with a fixed component. (bottom) RJCOOL component plus another fixed component.

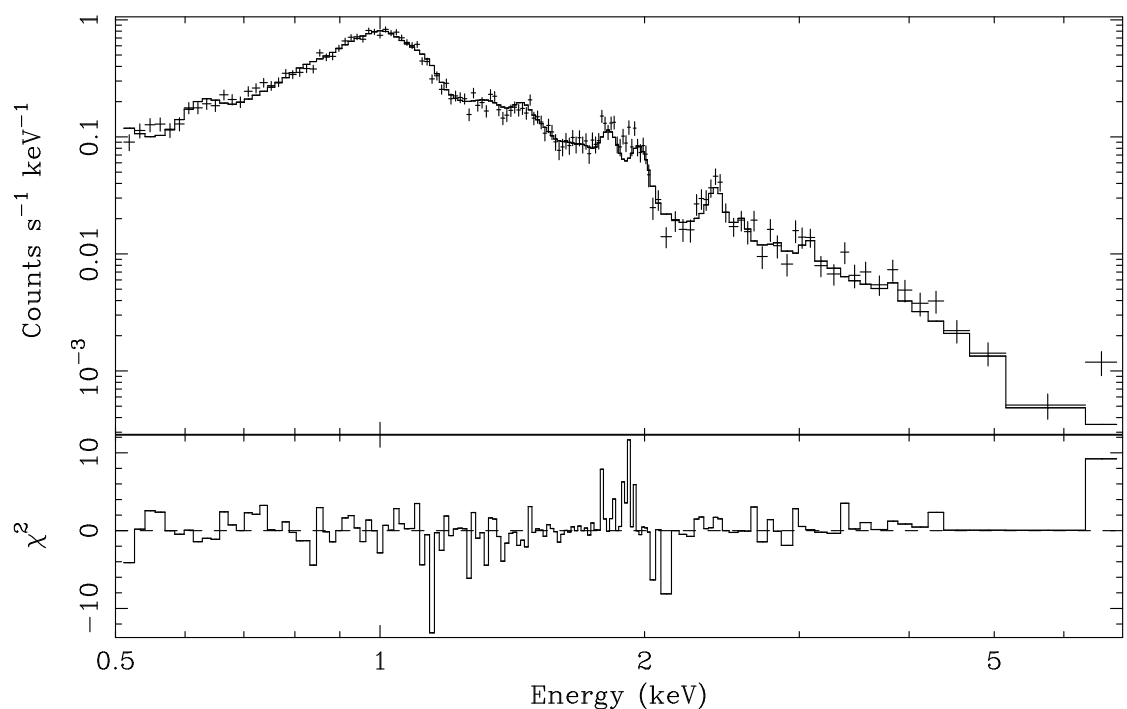


Figure 5.6: Spectrum of the plume, fitted with a 2-T APEC model.

Area	Counts	Model	N_{H} (10^{22} cm^{-2})	kT_1 (keV)	kT_2 (keV) or \dot{M} ($M_{\odot} \text{ yr}^{-1}$)	Z (Z_{\odot})	Reduced χ^2
Central 10 arcsec	17835	phabs(mekal)	0.26 ± 0.01	0.71 ± 0.01		0.16 ± 0.01	$660/128 = 5.2$
		phabs(apec)	0.23 ± 0.01	0.76 ± 0.01		0.14 ± 0.01	$671/128 = 5.2$
		phabs(mekal + mekal)	0.19 ± 0.01	0.67 ± 0.01	1.41 ± 0.05	$0.59_{-0.05}^{+0.07}$	$299/126 = 2.4$
		phabs(apec + apec)	0.16 ± 0.01	0.68 ± 0.01	1.45 ± 0.03	0.62 ± 0.06	$256/126 = 2.0$
		phabs(apec+apec+[apec])*	0.16 ± 0.01	0.66 ± 0.01	1.33 ± 0.03	$0.64_{-0.05}^{+0.08}$	$243/125 = 1.9$
		phabs(zphabs(rjcool) + [mekal])†	0.24 ± 0.02	1.14 ± 0.02	$\dot{M} = 11.3 \pm 0.7$	$0.71_{-0.08}^{+0.11}$	$371/127 = 2.9$
		phabs(zphabs(rjcool - rjcool) + [mekal])‡	0.16 ± 0.02	1.15 ± 0.03	$\dot{M} = 11.0 \pm 0.7$	$0.49_{-0.05}^{+0.05}$	$339/126 = 2.7$
Plume	14206	phabs(mekal)	0.18 ± 0.01	1.14 ± 0.01		0.28 ± 0.01	$583/138 = 4.2$
		phabs(apec)	0.17 ± 0.01	1.22 ± 0.01		0.30 ± 0.02	$451/138 = 3.3$
		phabs(mekal + mekal)	0.17 ± 0.01	0.79 ± 0.02	1.58 ± 0.04	$0.89_{-0.08}^{+0.10}$	$278/136 = 2.0$
		phabs(apec + apec)	0.16 ± 0.01	0.82 ± 0.02	1.62 ± 0.03	0.81 ± 0.08	$219/136 = 1.6$
		phabs(mekal + [mekal] + zphabs(rjcool))§	0.28 ± 0.02		1.56 ± 0.06	$1.58_{-0.23}^{+0.35}$	$289/136 = 2.1$
		phabs(mekal + [mekal] + zphabs(rjcool-rjcool))	0.11 ± 0.03	$1.94_{-0.18}^{+0.26}$	$\dot{M} = 4.1 \pm 0.3$	1.15 ± 0.15	$254/135 = 1.9$
Plume radius	24694	phabs(apec + apec)	0.16 ± 0.01	1.05 ± 0.03	1.89 ± 0.04	0.97 ± 0.07	$281/192 = 1.5$

Table 5.1: Results of spectral fits. Model names are shown in XSPEC notation. *Fit with a 2-T model, with an additional component fixed at 4 keV and $0.4 Z_{\odot}$. †Intrinsically-absorbed cooling flow plus a plasma component fixed at 4 keV and $0.4 Z_{\odot}$. These are both absorbed by a fixed absorber, set to the galactic value of absorption ($0.081 \times 10^{22} \text{ cm}^{-2}$). The temperature shown is the upper temperature of the cooling flow. N_{H} is the intrinsic cooling flow absorption. ‡Like (†), but subtracting another cooling flow component with the same normalisation and abundance, but different upper temperature as the first cooling flow. This simulates a cooling flow cooling from an upper temperature to a lower temperature (shown on the second line). §Like (†), but with an additional MEKAL component to account for the local cluster emission. Its temperature is set to the upper temperature of the cooling flow, and its abundance is set to the same as the cooling flow.

5.4 Imaging analysis

5.4.1 Radial profiles

In order to quantify the properties of the X-ray emitting gas as a function of radius, I analysed the spectra of circular annuli around the core of the cluster. This assumes that the properties of the gas are largely symmetric, an assumption I will test in Sections 5.4.2 and 5.4.3. Spectra were extracted, and appropriate background spectra, response and ancillary matrices were created as in Section 5.3.1 for every annulus. I fitted each spectrum with 1-T and 2-T MEKAL models, leaving metallicity and absorption as free parameters. To identify whether a 2-T fit was substantially better than a 1-T fit for a particular annulus, I computed the F -statistic. If the probability of the observed value of F (or a larger value) was less than or equal to 0.01, I chose the 2-T fit for that annulus. The annuli were allowed to vary in width to ensure that there were 8000 counts in each spectrum (except for the outer annulus). Point sources were excluded from the analysis.

Fig. 5.7 shows the radial profiles of temperature, abundance, absorption and the reduced χ^2 of the fits. The values of the reduced χ^2 show the fits are relatively poor in the centre. Two temperature points are given at the radii where the F -statistic gave reason to do so, showing the temperatures of the two temperature components. The vertical error bars show the $1-\sigma$ errors to the fit for each variable, whilst the horizontal error bars mark the maximum and minimum radii of each annulus.

The temperature in the outer regions of the cluster is ~ 3.4 keV. Towards the centre of the cluster, inside a radius of ~ 50 arcsec (17 kpc), a 2-T model is required to fit the spectra. The two temperatures drop to 1.35 and 0.66 keV at the centre (consistent with Section 5.3.1). The abundance rises from a value of $\sim 0.4 Z_\odot$ in the outer regions, to a maximum of $\sim 1.3 Z_\odot$ at a radius of ~ 45 arcsec (15 kpc). It then drops in the centre to $\sim 0.4 Z_\odot$. The intrinsic absorption rises from a value of $\sim 10^{21} \text{ cm}^{-2}$ in the outer regions, to $\sim 2 \times 10^{21} \text{ cm}^{-2}$ at the centre. The second-lowest panel shows the temperature results of fitting with 2-T and 1-T APEC models, rather than MEKAL models. The abundance and absorptions are very similar to the MEKAL results, so I do not plot them here.

Using models with variable abundances (VMEKAL and VAPEC), I found the relative abundances near the core to be more similar to those found in Type Ia supernovae rather than in Type II supernovae (defined by ratios given in Dupke & Arnaud 2001), tieing together those elements which are produced by the same process in each type of supernova. An even better fit is found by allowing the abundances to be free: I found abundances (relative to solar), for an annulus 35 arcsec away from the core using VAPEC, of O=0.5, Mg=0.8, Ne = 2×10^{-6} , Si=1.3, S=1.5, Ar=1.5, Ca=2.3, Fe=1.1, and Ni=1.8. VMEKAL gives different results: O=0.7, Mg=0.2, Ne=0, Si=1.8, S=2.3, Ar=2.4, Ca=3.4, Fe=2.1, and Ni=2.1. The level of Mg depends in detail on how the Fe L emission is modelled.

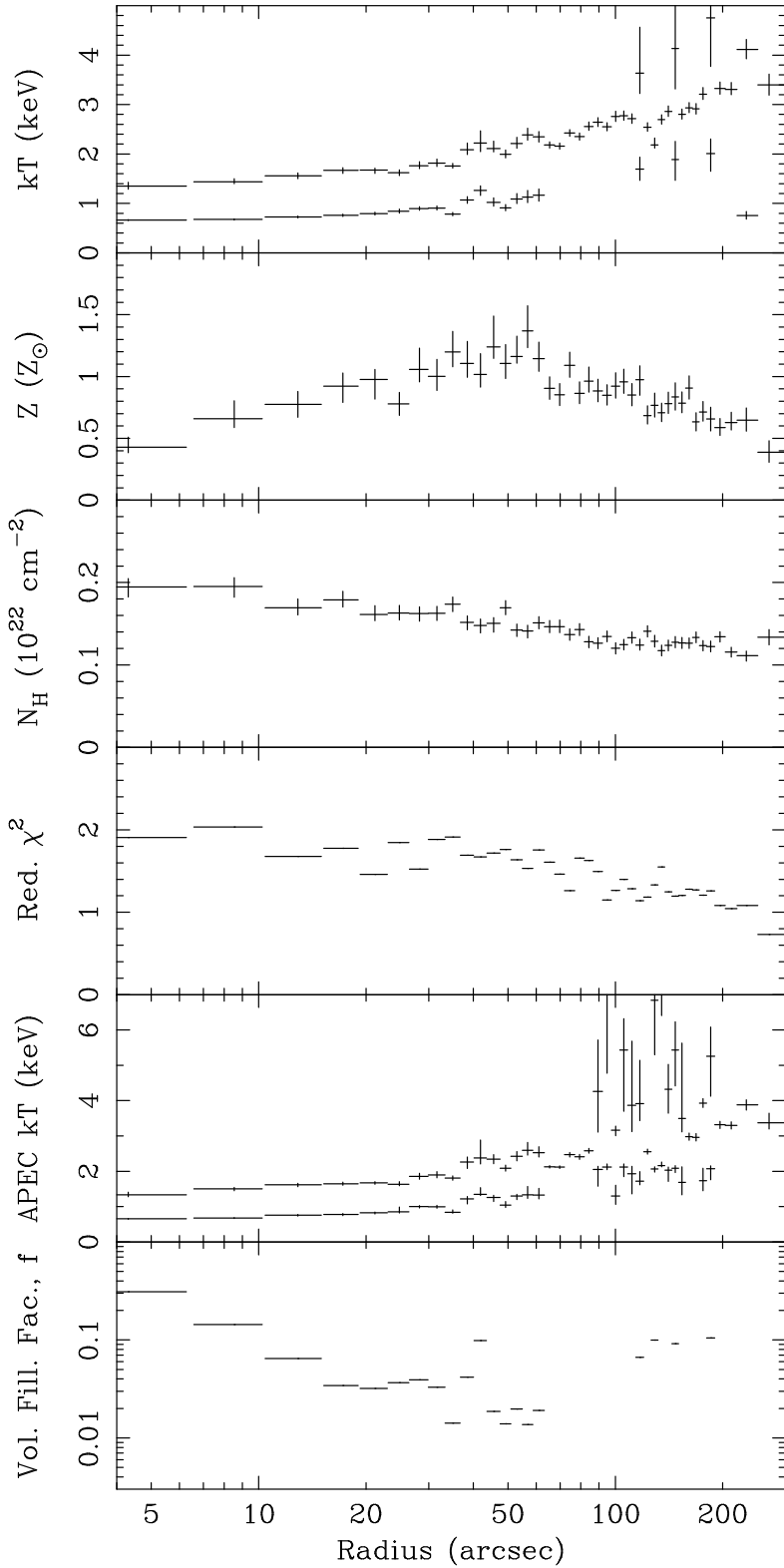


Figure 5.7: Results of fits taken of spectra taken from radial annuli. Errors are $1-\sigma$. A radius of 1 arcsec corresponds to 2.04 detector coordinates, or a distance of 0.33 kpc. Radii at which there are two points have been fitted with a 2-T spectral model. The second-lowest panel shows the results of fitting with APEC models, rather than MEKAL models. The lowest panel shows the volume filling factor, f , of the cool component (where appropriate).

If there are two phases, and assuming there is pressure balance between them, we can write

$$n_1 T_1 = n_2 T_2, \quad (5.1)$$

where n_1 is the density of Phase 1 (the hotter phase), and T_1 is its temperature. The quantities for the colder phase (Phase 2) are labelled similarly. The emission-measure of component X is related to its density and volume by $EM_X \propto n_X^2 V_X$, therefore the fraction of the total volume occupied by the cooler phase, f , where $f = V_2/(V_1 + V_2)$, is

$$\begin{aligned} f &= \frac{EM_2/n_2^2}{EM_1/n_1^2 + EM_2/n_2^2} \\ &= \left[1 + \frac{EM_1}{EM_2} \left(\frac{n_2}{n_1} \right)^2 \right]^{-1} \end{aligned} \quad (5.2)$$

Therefore, substituting (5.1) into (5.2), f can be expressed in terms of emission-measures and temperatures of the phases by

$$f = \left[1 + \frac{EM_1}{EM_2} \left(\frac{T_1}{T_2} \right)^2 \right]^{-1}. \quad (5.3)$$

The radial profile of f (Fig. 5.7), the volume filling factor of the cold phase, shows that the cooler gas is detected when it exceeds about one per cent of the volume; it exceeds 10 per cent within the inner 10 arcsec.

The absorbed cooling flow model was also fitted to each annulus. I used an intrinsically absorbed cooling flow (RJCOOL) plus a MEKAL model, both absorbed by fixed galactic absorption. The temperature and metallicity of the plasma model were fixed to the upper temperature and abundance of the RJCOOL model. Fig. 5.8 (top) shows a plot of the cumulative mass deposition rate as a function of radius: the combined mass deposition rate of all the annuli inside a particular radius. The plot rises from a value of $\sim 7 M_\odot \text{ yr}^{-1}$ in the central 6 arcsec, to $\sim 50 M_\odot \text{ yr}^{-1}$ at large radii (300 arcsec; 100 kpc), in agreement with previous measurements for the mass deposition rate (Allen et al. 2001). Also shown in Fig. 5.8 are the intrinsic absorption of the cooling flow, its upper temperature, its metallicity, and the reduced χ^2 of each fit.

As with the spectrum of the core of the cluster, I fitted each annulus with a CFMT model (the minimum temperature for each annulus rises from 0.4 keV at the centre to 1 keV at a radius of 1 arcmin). This model is only a significant improvement to the standard CF model inside a radius of around 6.5 arcsec from the core.

I note that the level of absorption found is always higher than the expected galactic value. This may, in part, be an ACIS-S calibration issue. When fitting cooling flow spectra it may also characterise the lack of low temperature emission lines, such as are absent from *XMM-Newton/RGS* spectra of cooling flows. I do not have the spectral res-

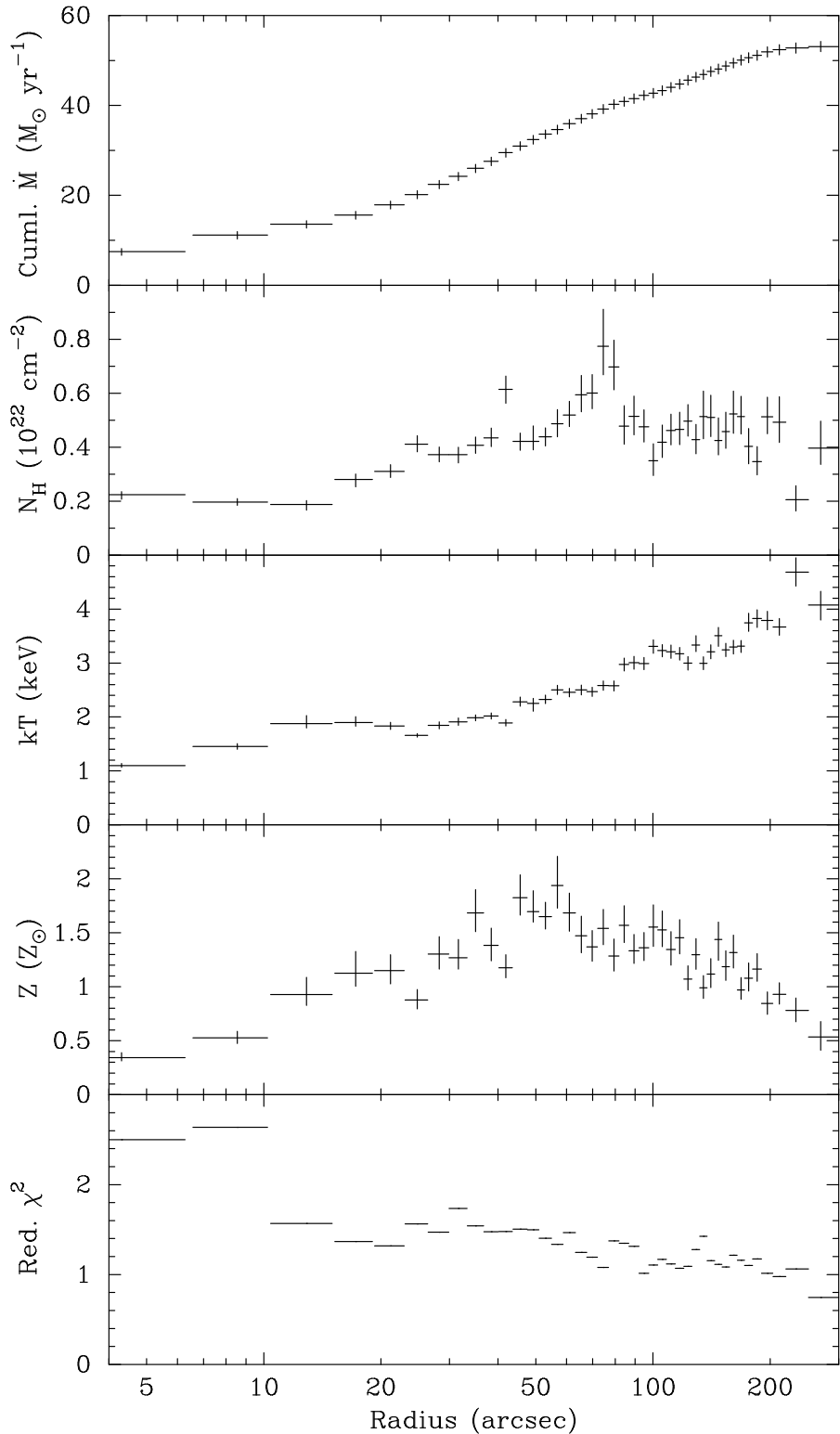


Figure 5.8: Cumulative mass deposition profile, calculated by fitting the mass deposition rate in annuli, and summing from the centre outwards. Also shown are the intrinsic absorption of the cooling flow, its upper temperature, the abundance of the gas, and the reduced χ^2 of the fit. The radiative cooling time of the gas at 300 arcsec is $\sim 10^{10}$ yr, decreasing inward to $< 10^9$ yr within about 60 arcsec.

olution or sensitivity to detect absorption edges which would demonstrate the presence of intrinsic absorption.

5.4.2 East-west anisotropy

The east side of the cluster contains the plume-like feature. To investigate whether there is significant difference between the east and west sides of the cluster, I analysed annuli cut in a north-south direction. Fig. 5.9 shows the two temperature and abundance profiles for the cluster. The annuli were chosen to contain 20 000 counts between 0.5 and 7 keV, and then were split into east and west parts. 1-T and 2-T MEKAL models were fitted using the same procedure as in Section 5.4.1, and an F -test was used to decide whether the 2-T model was a significant improvement over the 1-T model.

The plot shows significant differences in abundance between the two sides at radii of $\sim 40\text{--}50$ arcsec. There are also sharp outward rises in temperature in the east and west, at radii of ~ 70 and 160 arcsec, respectively. I will discuss these further in the next section. Between these radii, there are temperature differences between the two halves of the cluster. These radii match the region in MEKAL and APEC radial plots where two temperature components are often preferred (Fig. 5.7). The anisotropy shows that more detailed analysis is required to map out the structure of the cluster.

5.4.3 Fits to adaptively-binned areas

I adaptively binned (see Chapter 3) the central 3 arcmin of the cluster, using a fractional error threshold of 0.03. Adaptive binning uses a bin size which changes to ensure a minimum number of counts in each bin. A threshold of 0.03 gives 1100 counts per bin (except in certain cases). Fig. 5.10(a) shows the adaptively-binned image of the cluster. Point-sources were excluded from the analysis and are marked as white areas. The core of the cluster is shown to the south-east of the centre of the image.

I extracted spectra from each bin, and generated appropriate background spectra, response and ancillary matrices, as in Section 5.3.1. I then fitted each bin with 1-T and 2-T MEKAL models, finally using an F -test to decide whether the 2-T fit was a significant improvement over the 1-T fit. The results for the two types of fit were then combined to create images showing the spatial distribution for each fitted parameter. Fig. 5.10(b) shows either the fitted temperature from the 1-T fit, or the upper temperature of the 2-T fit. Fig. 5.10(c) shows the lower temperature of the 2-T fit, where appropriate. Figs. 5.10(d) and (e) show the fitted abundance and absorption levels from the relevant fit. Fig. 5.10(f) shows the appropriate reduced χ^2 value.

The value of a parameter in the images is indicated by a colour scale. Subtracted point sources are marked by the maximum value. I plot the $1-\sigma$ errors to the fit as a pair of diagonal boxes in the centre of each bin. The top-right box shows the upper bound,

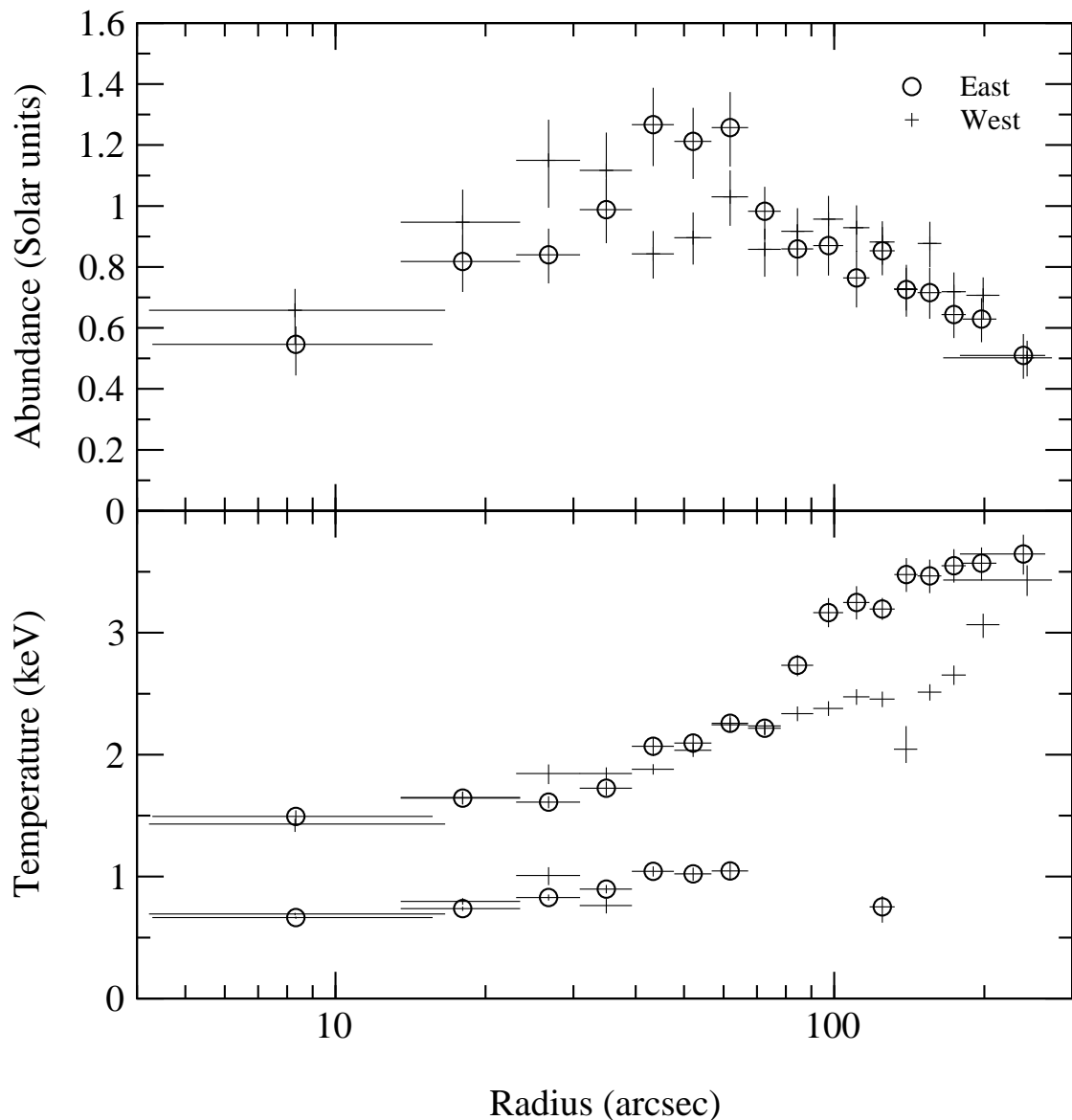


Figure 5.9: Radial abundance and temperature profiles of the east and west of the cluster.

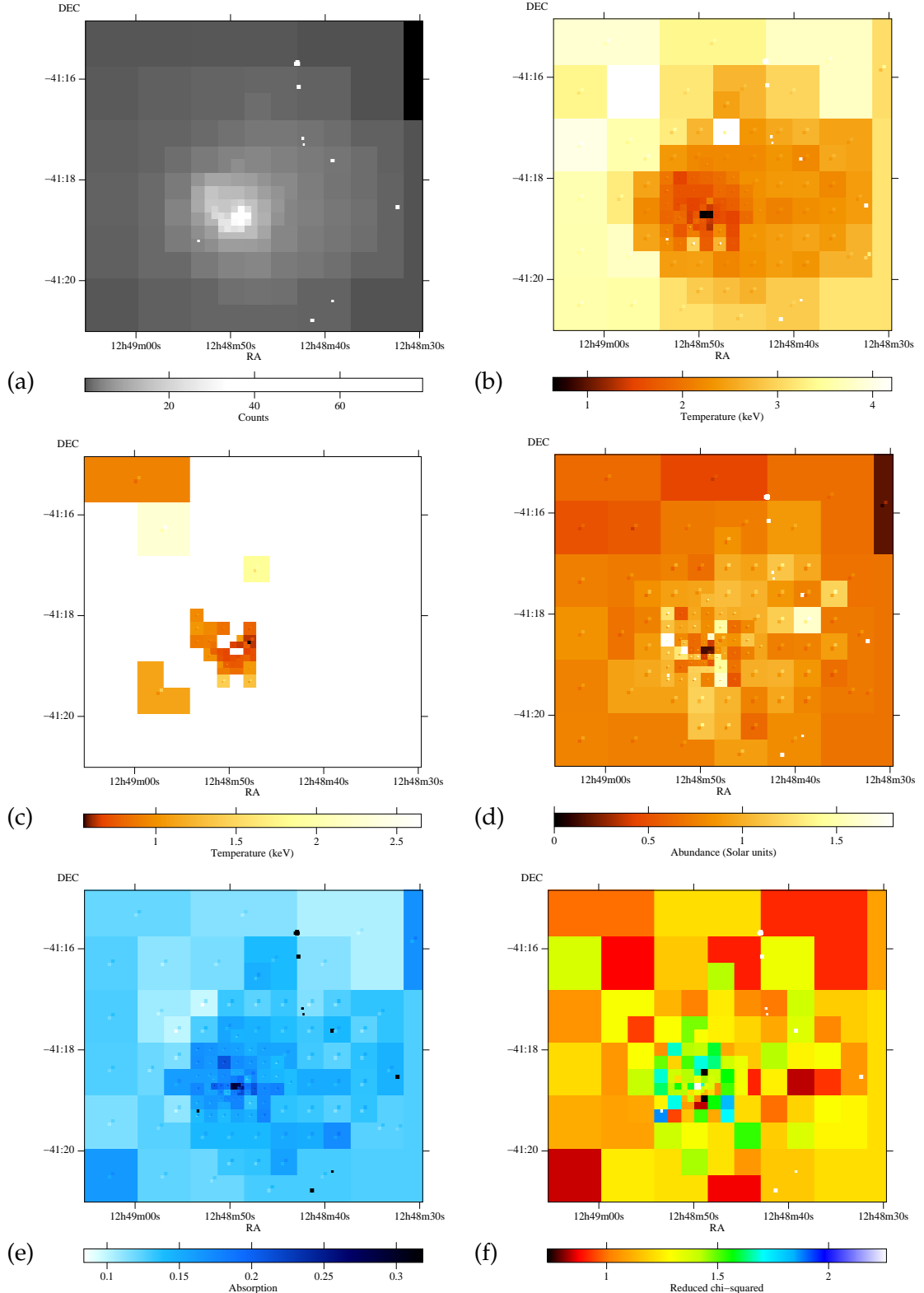


Figure 5.10: (a) Adaptively-binned image of the cluster, counts are average values per arcsecond pixel. (b) Upper-temperature results (for 2-T fits) or the 1-T fit results. The diagonal boxes inside each bin indicate the bounds of the $1-\sigma$ error of the temperature. The white spots are excluded point-sources. (c) Lower-temperature fit results for the 2-T fits. White regions are where 1-T fits were used. (d) Abundance results for fits. (e) Absorption results of fits. (f) Reduced χ^2 of the fits.

and the bottom-left shows the lower bound. Masked-out point sources are shown as areas coloured with the maximum value.

2-T models are required to fit the spectra in the inner 30 arcsec. The 2-T temperature results in the centre (~ 0.7 and 1.2 keV) are cooler than the 1-T results in the outer regions (~ 3 keV). The abundance of the gas in the outer regions has a similar value to that in the core ($\sim 0.5 Z_{\odot}$), but there is a rise in the metallicity about 1 arcmin away from the core to $\sim 1.3 Z_{\odot}$, as in Section 5.4.1.

The images show that the properties of the emitting gas are not spherically symmetric. The temperature sharply increases between 70 and 160 arcsec radius, depending on position angle (Fig. 5.9). Such features have been seen in other clusters, and are termed cold fronts (Markevitch et al. 2000). The most striking front is to the north-east of the core in the Centaurus cluster, where the emission suddenly drops. There is an extensive cooler region to the west of the core (~ 2.4 keV; Fig. 5.10(b)). This area has a higher abundance than an equivalent region to the east (Fig. 5.10(d)). In addition, there is more absorption (Fig. 5.10(e)) to the west.

In the innermost core of the cluster (at a radius of less than 4 arcsec) there are a few bins for which a 1-T fit is preferred using an F -test (probabilities for F of ~ 0.03). Owing to this, they have much lower abundances than the surrounding bins. If their spectra are combined, a 2-T fit is easily preferred, and the results of the fit closely match the values of the surrounding bins. This is likely to be due to the difficulties of detecting two low (~ 1 keV) temperatures close together. More counts at that temperature appear to be required to detect two temperatures.

In order to examine whether there is significant non-radial variation in the bins, the fitted parameters (with $1-\sigma$ errors) to each bin as a function of the radius of the bin are plotted in Fig. 5.11. The radius plotted is the mean radius of the pixels of the bin. The plot brings out the features in Fig. 5.7. There is some significant variation in metallicity between radii of 7–50 arcsec. Examining those bins in the east and those to the west, I find that most of the variation in the abundance is to the west (the opposite side to the plume). The metallicity to the west is scattered between 0.5 and $1.7 Z_{\odot}$ at radii of 7–50 arcsec. The profile to the east is much smoother, except for an obvious high abundance point (Fig. 5.10(d), roughly 7 arcsec from the core). The east-west difference in metallicity and temperature is highlighted by Fig. 5.9, which shows east-side and west-side profiles of the cluster.

Given that the cluster contains a strong radio source (Taylor et al. 2002) there may be significant non-thermal emission in the X-ray band. Any non-thermal emission will increase the continuum of the X-ray emission and lower the apparent metallicity. The presence of non-thermal emission was tested by fitting the spectrum in each bin with a 1-T plus power-law model. I then used an F -test to decide whether adding the power-law component made a significant improvement to the fit (using the same criterion as Section 5.4.1) for each bin.

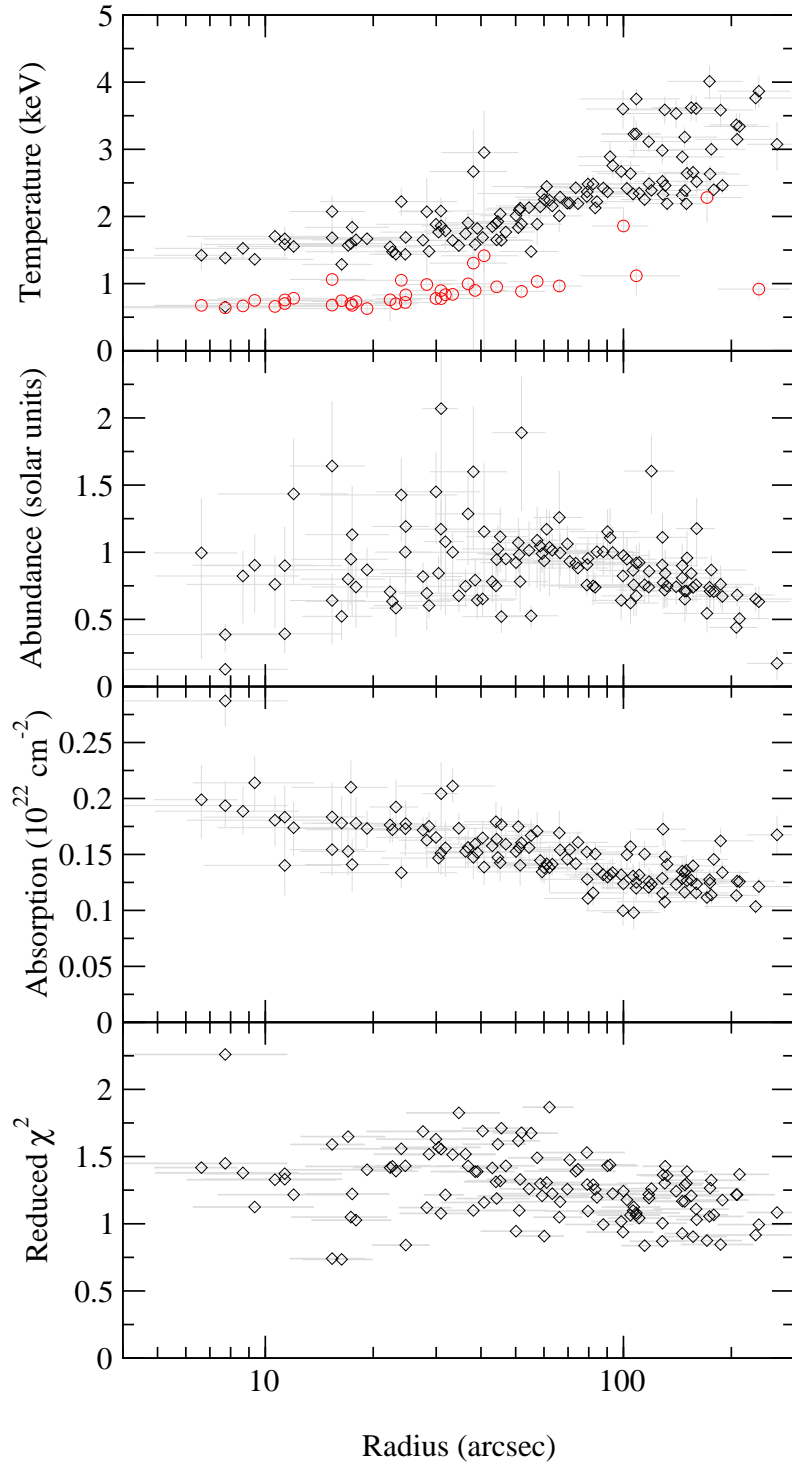


Figure 5.11: Distribution of the fitted values for the bins in Fig. 5.10 as a function of radius. The radius of a bin is the mean displacement from the centre of the cluster, and the error bars indicate the maximum and minimum radius of each pixels in the bin. The errors on the value are the $1-\sigma$ fitted errors also shown in Fig. 5.10. Two points are plotted in the temperature plot for bins fitted with a 2-T model. Bins at a radius of less than 4 arcsec are excluded, due to an incorrect fitted model (see text).

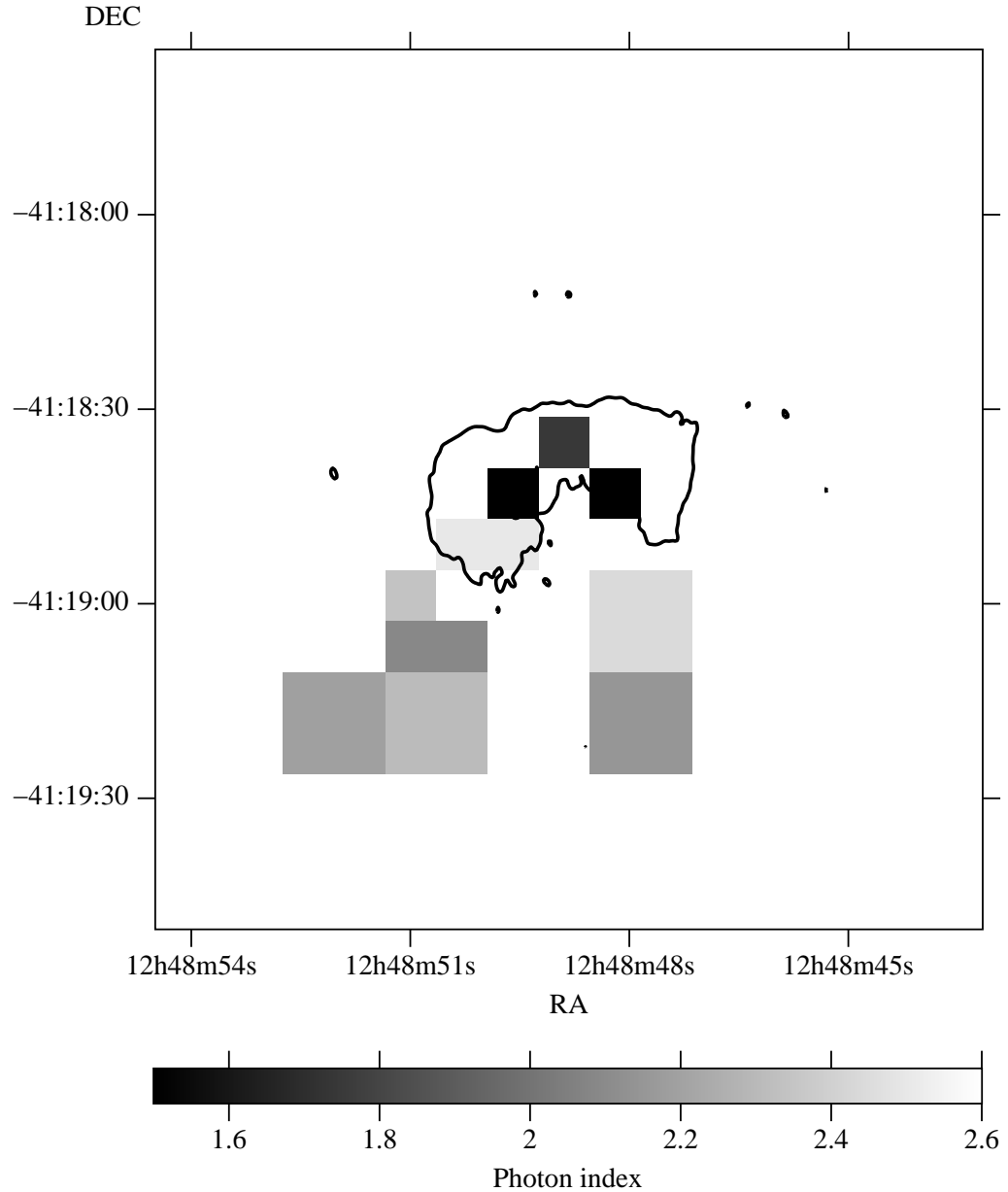


Figure 5.12: Regions in the centre of the cluster where a power-law plus 1-T is an improvement over a 1-T fit. White areas indicate where the F -test gives no significant improvement over a 1-T fit. The other regions are shaded to show the photon index of the best-fitting power-law. The photon index was constrained to lie between 1.5 and 2.5. The contour marks where the radio emission is $0.2 \text{ mJy beam}^{-1}$ at 4.8 GHz, taken from the data of Taylor et al. (2002).

I show in Fig. 5.12 the areas where the power-law component is suggested by the *F*-test. Interestingly the morphology of the radio source approximately matches those areas in the centre where the power-law component is a significant improvement. I also find that those areas 1 arcmin south of the core where the power-law is preferred match the low-intensity regions of the radio source (see Taylor et al. 2002 for detailed maps of the radio source morphology). However, only a small fraction of the emission from the core of the cluster appears to have a significant non-thermal component, and the peak in the abundance still exists if I exclude those regions where it may be important. Therefore the peak in abundance 15 kpc from the core is not an effect of non-thermal emission.

5.5 Discussion

The most interesting conclusion of this analysis is that the metallicity of the cluster peaks at $\sim 1.3 Z_{\odot}$ (or $1.8 Z_{\odot}$ with a cooling flow model) at a radius of ~ 15 kpc, declining to $0.4 Z_{\odot}$ at the centre. Previous observations (Fukazawa et al. 1994; Ikebe et al. 1999) of the cluster did not have high enough spatial resolution to resolve this feature, showing only an increasing gradient in metallicity to the centre. Böhringer et al. (2001) found using *XMM-Newton* data that the abundances in the Virgo Cluster peak ~ 1 arcmin from the centre. Molendi & Gastaldello (2001) later saw this to be an effect of using a 1-T fit where more temperature components were required; within 1 arcmin from the centre the actual metal profile is flat.

The abundance gradient in Centaurus was modelled by Reisenegger et al. (1996), but no decrease was expected. A peak in abundance is still found just fitting spectra between 3 and 7 keV where Fe K emission occurs (Fig. 5.13), so the peak is not an artefact of the Fe L complex. Resonant absorption is a possible mechanism for the metallicity decline in the core of the cluster. However, since the abundance peak is seen in the Fe K lines too, resonant absorption is unlikely.

In the future, it will be important to study the chemical composition of the plasma, and handle projection effects fully. I also would like to understand why the statistical quality of the fits to the spectra in the centre are poor, and how to improve them. These effects are probably due to the high metallicity of the core: a feature which is particular to this cluster. I would like to draw attention to the fact that there are differences in the qualities of fits using different plasma codes. The fits to the adaptively-binned image spectra (Fig. 5.10(c)) suggest that the 2-T fits are required in specific regions, rather than at specific radii.

Using a CF model produces a radial abundance profile with a similar shape, but with a higher peak metallicity, than that found using the 2-T model, indicating that the peak is not a model-dependent effect. The upper-temperature of the CF fit also matches the upper-temperature of the 2-T fit. In general, excluding the very central bins, the CF model gives a smaller reduced χ^2 than the 2-T model.

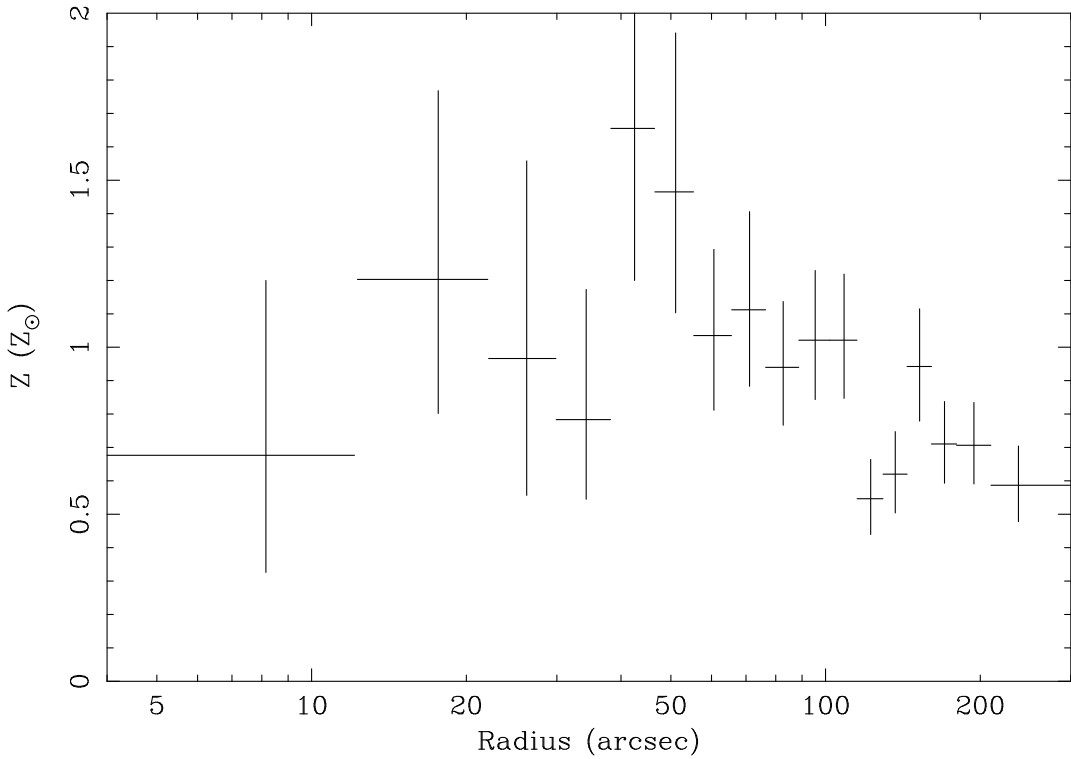


Figure 5.13: Radial metallicity plot generated by fitting spectra between 3 to 7 keV with a 1-T model (above 3 keV only one temperature component is necessary). Each radial bin contains $\sim 20\,000$ counts from 0.5–7 keV.

It is difficult to conclude in general which model gives the better fits to the regions of the cluster. When the data are binned in annuli, a standard cooling flow model (CF) is a significant improvement (measured using an F -test with a maximum probability of 0.01) over a 1-T fit for nearly every annulus. 2-T and CFMT models are only a significant improvement over a 1-T model within about 60 arcsec of the cluster core. A 2-T model or CFMT model are a significant improvement to the CF model within the inner ~ 7 arcsec. A CF model probably fits the spectra of the annuli better as the cluster is not radially symmetric, so there are a number of temperatures at each radius, which the CF model includes.

The comparison gives different conclusions when fitting the regions in the adaptively-binned image. A 2-T, CF or a CFMT model is a significant improvement (with the same F -test criterion) over the 1-T model inside much of the inner 40–50 arcsec. The area in the central arcmin for which the CF model is an improvement over the 1-T model is roughly 2/3 that for which the CFMT and 2-T models are an improvement. The CFMT and 2-T models show a significant improvement in the fit over the CF model for areas about 50 arcsec away for the nucleus, and some of the area inside. Fig. 5.14 shows that the radiative cooling time of the gas is less than a Gyr within that radius. Outside the core, there are some areas which show a significant improvement using a CF, 2-T or CFMT model over a 1-T model. It may be that there are local variations in temperature in these

regions, or this could be a statistical effect. Using a larger bin size, with the corresponding increase in counts in the spectra, still results in areas outside the core which show a significant improvement using a 2-T or CFMT model over a 1-T model, although using a larger bin size includes more gas, which is probably at different temperatures. Note that if there is a cooling flow, then the models used here do not incorporate the gravitational work done on the gas in the flow. Therefore no firm statement can be made on the level of the mass deposition rate. The data support a rate of several tens $M_{\odot} \text{ yr}^{-1}$.

It is difficult to speculate on the cause of the plume-like feature in the core of the cluster. The galaxy velocity data cannot rule out a 100-200 km s^{-1} line of sight motion of NGC 4696 in Cen 30 similar to that of the cD in A1795 (Chapter 4). The real velocity could of course be larger and there may be significant motion of the intracluster gas within its potential well. The plume does, however, touch the east-most extent of the radio lobes (Taylor et al. 2002), indicating there may be some interaction between the lobes and the plume. However, the direction of the plume is not aligned with the radio lobes. The plume has a higher metallicity than the core, suggesting the cooling flow is depositing enriched material in this area.

Sparks et al. (1989) and de Jong et al. (1990) have proposed that the cooler central gas around NGC 4696 originates from an infallen dust-rich dwarf galaxy, which also accounts for the dust lane. The fact that the metallicity of the plume matches its surroundings argues against this stripping hypothesis (as mentioned in Section 5.3.2). Moreover, cool gas is found in the majority of clusters.

As in M87, the plume could be due to a radio bubble dragging out cooler gas (Böhringer et al. 1995; Churazov et al. 2001). The cold front at the end of the plume could in fact be the edge of the bubble. However, I have shown that the metallicity of the plume is similar to the surrounding material, and higher than the central gas, which argues against that gas having originated close to the central radio source. Of course, the drop in metallicity within the inner 20 kpc (60 arcsec) could be due to bubbles transporting higher metallicity gas to larger radii (Churazov et al. 2001; Brüggen & Kaiser 2001). However, it is not then clear where the present lower-abundance gas has come from. More detailed models of the convection and exchange of gas are required, but at first inspection, such models are unlikely to reproduce the abundance profile seen here.

The main conclusion of this chapter is that the steep abundance gradient in this cluster does not persist within 15 kpc, but decreases inward to a value similar to that seen at large radii. This may be a feature of radiative cooling of the gas, if composed of small metal-rich clumps in a metal-poor surrounding environment (Morris & Fabian, in preparation). *The presence of an abundance gradient means that there has not been significant widespread convection or mixing extending beyond 15 kpc driven by the nucleus of NGC 4696.* The spectra within ~ 60 kpc also indicate that the temperature structure of the gas has at least two phases, both decreasing towards the centre. The present data are not capable of testing for the presence of further phases.

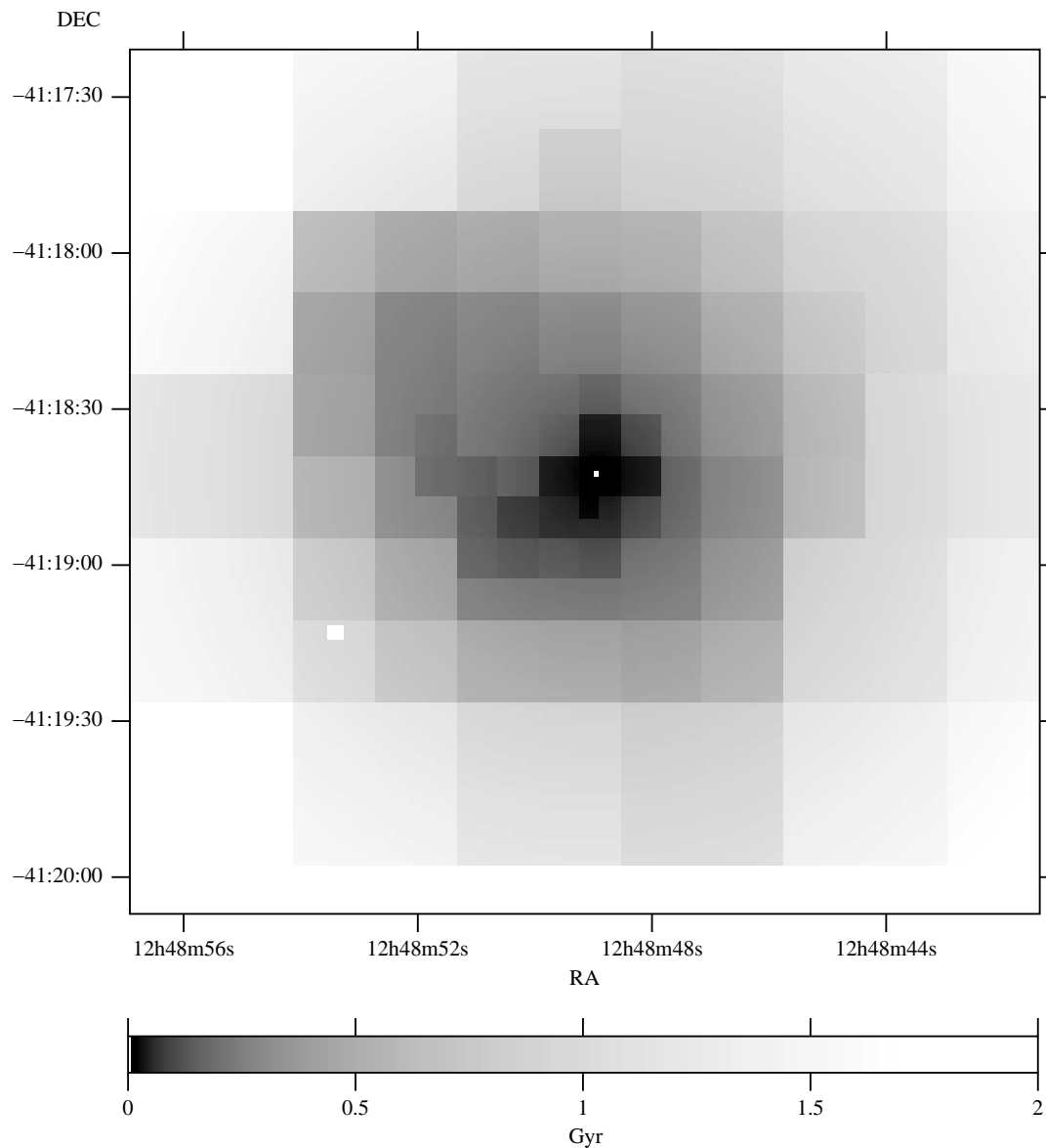


Figure 5.14: Mean radiative cooling time of the gas, estimated from the X-ray surface brightness (see Section 4.1.2). The mean cooling time is less than 5×10^8 yr inside a radius of 45 arcsec, below 10^8 yr inside 10 arcsec (3 kpc) radius, and falls to 3×10^7 yr within 5 arcsec of the centre.

6

Conclusions

Summary

In this chapter I summarise this dissertation and make some concluding remarks.

6.1 Introduction

It is clear that the arrival of the *Chandra* and *XMM-Newton* telescopes have given us a wealth of data on the subject of galaxy clusters. Unfortunately, as is almost always the case in astronomy, the arrival of new data shows that reality is far more complex than our models! We have observed the complex structure of X-ray emitting gas in the *Chandra* images of many clusters, including those which I have studied in this dissertation (Perseus, A1795 and Centaurus), and elsewhere (e.g. Vikhlinin et al. 2001a; Fabian et al. 2001a; McNamara et al. 2000; Markevitch et al. 2000). The spatial resolution of *Chandra* is unsurpassed, and will be for many years since the future planned X-ray missions will focus on effective area and spectral resolution, so *Chandra* will be vital for the understanding of galaxy clusters.

Standard cooling flow models seemed the final description of what was observed in galaxy clusters in the days of *ROSAT* and *ASCA*. Now we must either abandon cooling flows altogether, or explain the lack of low energy emission lines (e.g. Fabian et al. 2001b). If we are to abandon cooling flows altogether, then we must also explain the optical nebulosity, blue continuum emission, UV line emission and infrared emission (Section 1.1.6), not to mention the evidence of gas cooling down to ~ 2 keV.

The next few years will be interesting times for the understanding of cooling flows and galaxy clusters. Data from *Chandra* and *XMM-Newton* will push the theoretical models, and gradually we will understand more about the largest gravitationally bound objects in the universe.

In this dissertation I have examined several clusters and found a variety of structure, including infalling galaxies, radio lobes, filaments, plumes, and metallicity peaks. Some of these features are easily explained, but some are not. This work has made some progress to understanding them. Small-scale structure is what differentiates between clusters: relaxed clusters look very similar on large scales, but *Chandra* has shown unique features in the cores of many clusters. The key to understanding clusters as a whole is understanding the features which make them unique, and what makes them alike.

6.2 Summaries of chapters

6.2.1 Colour maps of cluster cores

In Chapter 2 I made a study of 33 bright clusters from the brightest 55 X-ray clusters, using *ROSAT* archival data. I used the X-ray colour technique of Allen & Fabian (1997) to spatially analyse the clusters for temperature and absorption gradients. The method used in this chapter took account of the spatial structure in the image, rather than forming simple radial contours. Using this data I showed that there is significant evidence for the presence of cooler X-ray gas in the centres of those clusters with known cooling flows. Those clusters without coolings flows did not show evidence for the cooler gas. There was also evidence of increased absorption above galactic column density in those clusters with cooling flows.

6.2.2 Adaptive binning

In Chapter 3 I discussed a method which has been developed for the spatial analysis of X-ray data, which I then demonstrated in use on the Perseus, A1795 and Centaurus clusters (Chapters 4 and 5).

Adaptive binning is a method to bin images according to the local count rate. It attempts to use a bin size which leads to a maximum error in all parts of the image. The method can be used to create X-ray colour maps or intensity maps. It can also be used to generate areas for spectral fitting, or the error on the parameters of spectral fits can be used to choose the bin size.

6.2.3 The Perseus and Abell 1795 clusters

In Chapter 4 I showed the results from *Chandra* observations of two nearby galaxy clusters: the Perseus and Abell 1795 clusters. The image of the core of the Perseus cluster

showed the holes which are associated with the radio lobes of 3C 84 and were previously observed by *ROSAT*. The rims of the holes are X-ray bright and consist of cooler gas than their surroundings, indicating that they were not formed as the result of shocks. A spiral structure in the cool X-ray gas was seen in the images, which may have been caused by angular momentum in the cooling flow. A filament-like structure of strong photoelectric absorption was seen across the core of the cluster. The absorption appears to be associated with a small infalling irregular galaxy. Two outer X-ray holes, one of which was previously known, appear to be correlated with spurs of low-frequency radio emission.

The *Chandra* observation of A1795 reveals that there is a 40 arcsec long filament in the core of the cluster. The feature is coincident with a $\text{H}\alpha + [\text{N II}]$ filament found by Cowie et al. (1983), which was later resolved into two *U*-band components by McNamara et al. (1996a). By fitting X-ray colours to the colours of an adaptively binned image of the cluster, I constructed a temperature map of the region around the filament. The filament has a temperature of 2.5–3 keV, and a mean radiative cooling time of 3×10^8 yr. The cD galaxy at the north end of the filament is probably oscillating through the core of the cluster, and the filament was formed by gas cooling from the intracluster medium.

6.2.4 The Centaurus cluster

In Chapter 5 I showed the analysis of an observation of the Centaurus cluster using *Chandra*. An image of the cluster showed a plume-like feature at the centre of the cluster. The feature has the same metallicity as gas at a similar radius, but is cooler. Radial profiles showed that the previously known steep abundance gradient peaks with a metallicity of $1.3 - 1.8 Z_\odot$ at a radius of about 45 arcsec (15 kpc), before falling back to $0.4 Z_\odot$ at the centre of the cluster. A radial temperature profile showed that the temperature decreases inwards. I created adaptively binned maps of the temperature, abundance and absorption in the cluster core. The spatial distributions of each of two temperature components were determined. The radiative cooling time of the cooler component within the inner 10 arcsec (3 kpc) is less than 2×10^7 yr. X-ray holes coincident with the radio lobes were found, as well as two outer sharp temperature drops, or cold fronts. The origin of the plume is unclear. The existence of the strong abundance gradient is a strong constraint on extensive convection or gas motion driven by a central radio source.

6.3 Future work

The recent observations by *Chandra* have shown that to understand the structure of galaxy clusters, high spatial resolution is necessary. Detailed imaging of small-scale structure is far easier for clusters which lie close to us at low redshift. Improvements to our knowledge about the processes occurring in the cores of galaxy clusters are likely to come from imaging nearby clusters for extended periods of time, allowing us to look at

the properties of the gas in areas with small spatial scales.

An ideal cluster to study is the Perseus cluster. It is the clearest example of a cluster where a central radio source is interacting with the cooling X-ray gas. A detailed study of this cluster may allow us to finally rule out that heating is significant in this cluster. Understanding what fills the radio lobes in NGC 1275 will give a better understanding of radio lobes in general, the energy budget in the cores of clusters, and the nature of the central radio sources in these objects. The metallicity structure in the Perseus cluster would also be an interesting area of study.

The Abell 1795 cluster is also an interesting target since it appears that the cooling gas is located away from the cD galaxy, allowing us to separate galactic phenomena in the cD from the cooling in the cluster. Multi-wavelength studies of the filament will allow us to pinpoint the mechanism for its creation, and understand better the process of star formation from cooling flows.

The Centaurus cluster is a wonderful target. Firstly there is much work to do on the plume, as its origins are not yet understood. Also the presence of the peak in the metallicity away from the core may be telling us something fundamental about the processes of cooling and metal enrichment in galaxy clusters.

There is also work to be done studying complete samples of clusters, such as the brightest 55 cluster sample, looking for trends in their properties, as I did in Chapter 2. The analysis I did was heavily limited by the characteristics of *ROSAT*. An analysis of *Chandra* and *XMM-Newton* data would give a much more complete study, with more spatial and spectral resolution.

The key to understanding cooling flows will be the analysis of grating data (such as that from *XMM-Newton*) in combination with detailed spectral models (e.g. Morris & Fabian, in preparation) and imaging data. As we receive more data from *Chandra* and *XMM-Newton*, we will need to develop more advanced methods of analysing the data spectrally and spatially, possibly from more than one telescope at the same time.

7

References

- Abell G. O. 1958. *The Distribution of Rich Clusters of Galaxies*, ApJS, 3, 211
- Allen S. W. 1995. *Starbursts in cooling flows: blue continua and emission-line nebulae in central cluster galaxies*, MNRAS, 276, 947
- . 1998. *Resolving the discrepancy between X-ray and gravitational lensing mass measurements for clusters of galaxies*, MNRAS, 296, 392
- Allen S. W., Di Matteo T., & Fabian A. C. 2000. *Hard X-ray emission from elliptical galaxies*, MNRAS, 311, 493
- Allen S. W., Edge A. C., Fabian A. C., Böhringer H., Crawford C. S., Ebeling H., Johnstone R. M., Naylor T., & Schwarz R. A. 1992. *Optical spectroscopy of the ROSAT X-ray brightest clusters*, MNRAS, 259, 67
- Allen S. W. & Fabian A. C. 1994. *A ROSAT PSPC Investigation of the Centaurus Cluster of Galaxies*, MNRAS, 269, 409
- . 1997. *The spatial distributions of cooling gas and intrinsic X-ray-absorbing material in cooling flows*, MNRAS, 286, 583
- . 1998. *The relationship between cooling flows and metallicity measurements for X-ray-luminous clusters*, MNRAS, 297, L63
- Allen S. W., Fabian A. C., Johnstone R. M., Arnaud K. A., & Nulsen P. E. J. 2001. *ASCA and ROSAT observations of nearby cluster cooling flows*, MNRAS, 322, 589

- Allen S. W., Fabian A. C., Johnstone R. M., White D. A., Daines S. J., Edge A. C., & Stewart G. C. 1993. *A ROSAT PSPC observation of Abell 478 - The distribution of X-ray absorbing matter in a massive cooling flow*, MNRAS, 262, 901
- Anders E. & Grevesse N. 1989. *Abundances of the elements - Meteoritic and solar*, Geochim. Cosmochim. Acta, 53, 197
- Arnaud K. & Dorman B. 2001, XSpec User's Guide, 11th edn., HEASARC, <http://legacy.gsfc.nasa.gov/docs/xanadu/xspec/manual/>
- Arnaud K. A. 1996, Astronomical Data Analysis Software and Systems V. ASP Conf. Ser. Vol. 101. eds Jacoby, G. and Barnes, J. (Astron. Soc. Pac.), 17
- Arnaud M., Rothenflug R., Boulade O., Vigroux L., & Vangioni-Flam E. 1992. *Some Constraints on the Origin of the Iron Enriched Intracluster Medium*, A&A, 254, 49
- Aschenbach B. 1990. ROSAT Notiz, Tech. rep., MPE
- Ball R., Burns J. O., & Loken C. 1993. *The radio properties of cD galaxies in Abell clusters. II - The VLA sample*, AJ, 105, 53
- Balucinska-Church M. & McCammon D. 1992. *Photoelectric absorption cross sections with variable abundances*, ApJ, 400, 699
- Begelman M. C. & Fabian A. C. 1990. *Turbulent mixing layers in the interstellar and intra-cluster medium*, MNRAS, 244, 26P
- Bevington P. R. & Robinson D. K. 1992, Data reduction and error analysis for the physical sciences, 2nd edn. (WCB/McGraw-Hill)
- Bijleveld W. & Valentijn E. A. 1983. *The trivariate (radio, optical, X-ray) luminosity function of cD galaxies. I - New Westerbork observations of 22 cD galaxies and Einstein observations of A1918 and A2317. II - The fuelling of radio sources*, A&A, 125, 217
- Blundell K. M., Kassim N. E., & Perley R. A. 2000. *3C radio sources as they've never been seen before*, ASP Conf. Ser., Astron. Soc. Pac., San Francisco, astro-ph/0004005
- Böhringer H., Nulsen P. E. J., Braun R., & Fabian A. C. 1995. *The interaction of the radio halo of M87 with the cooling intracluster medium of the Virgo cluster*, MNRAS, 274, L67
- Böhringer H., Belsole E., Kennea J., Matsushita K., Molendi S., Worrall D. M., Mushotzky R. F., Ehle M., Guainazzi M., Sakelliou I., Stewart G., Vestrand W. T., & Dos Santos S. 2001. *XMM-Newton observations of M 87 and its X-ray halo*, A&A, 365, L181
- Böhringer H. & Hensler G. 1989. *Metallicity-dependence of radiative cooling in optically thin, hot plasmas*, A&A, 215, 147

- Böhringer H., Voges W., Fabian A. C., Edge A. C., & Neumann D. M. 1993. *A ROSAT HRI study of the interaction of the X-ray-emitting gas and radio lobes of NGC 1275*, MNRAS, 264, L25
- Bowyer S., Berghöfer T. W., & Korpela E. J. 1999. *Extreme-Ultraviolet Emission in Abell 1795, Abell 2199, and the Coma Cluster*, ApJ, 526, 592
- Bradt H., Mayer W., Naranan S., Rappaport S., & Spada G. 1967. *Evidence for X-Radiation from the Radio Galaxy M87*, ApJ, 150, L199
- Branduardi-Raymont G., Fabricant D., Feigelson E., Gorenstein P., Grindlay J., Soltan A., & Zamorani G. 1981. *Soft X-ray images of the central region of the Perseus cluster*, ApJ, 248, 55
- Bregman J. N., McNamara B. R., & O'Connell R. W. 1990. *Infrared emission from central dominant galaxies in X-ray luminous clusters*, ApJ, 351, 406
- Brickhouse N. S., Smith R. K., Raymond J. C., & Liedahl D. A. 2000. *The Astrophysical Plasma Emission Code*, AAS/High Energy Astrophysics Division, 32, 2701
- Bridges T. J. & Irwin J. A. 1998. *Molecular gas in the Perseus cooling flow galaxy, NGC 1275*, MNRAS, 300, 967
- Briel U. G. & Henry J. P. 1996. *An X-Ray Temperature Map of Abell 1795, a Galaxy Cluster in Hydrostatic Equilibrium*, ApJ, 472, 131
- Briggs S. A., Snijders M. A. J., & Boksenberg A. 1982. *Ly- α absorption at a high velocity in NGC1275*, Nature, 300, 336
- Brüggen M. & Kaiser C. R. 2001. *Buoyant radio plasma in clusters of galaxies*, MNRAS, 325, 676
- Buote D. A. 2001. *On the Origin of Radio Halos in Galaxy Clusters*, ApJ, 553, L15
- Buote D. A. & Tsai J. C. 1996. *Quantifying the Morphologies and Dynamical Evolution of Galaxy Clusters. II. Application to a Sample of ROSAT Clusters*, ApJ, 458, 27
- Byram E. T., Chubb T. A., & Friedman H. 1966. *Cosmic X-Ray Sources-Galactic and Extra-galactic.*, AJ, 71, 379
- Cardiel N., Gorgas J., & Aragón-Salamanca A. 1998. *Spectral gradients in central cluster galaxies: further evidence of star formation in cooling flows*, MNRAS, 298, 977
- Carlson M. N., Holtzman J. A., Watson A. M., Grillmair C. J., Mould J. R., Ballester G. E., Burrows C. J., Clarke J. T., Crisp D., Evans R. W., Gallagher J. S., Griffiths R. E., Hester J. J., Hoessel J. G., Scowen P. A., & Stapelfeldt K. R. 1998. *Deep Hubble Space Telescope Observations of Star Clusters in NGC 1275*, AJ, 115, 1778

- Cavaliere A., Gursky H., & Tucker W. H. 1971, *Nature*, 231, 437
- Chandra X-ray Center. 2000, Chandra Proposers' Observatory Guide, <http://asc.harvard.edu/udocs/docs/POG/MPOG/>
- Chandran B. D. G. & Cowley S. C. 1998. *Thermal Conduction in a Tangled Magnetic Field*, *Physical Review Letters*, 80, 3077
- Churazov E., Brüggen M., Kaiser C. R., Böhringer H., & Forman W. 2001. *Evolution of Buoyant Bubbles in M87*, *ApJ*, 554, 261
- Churazov E., Forman W., Jones C., & Böhringer H. 2000. *Asymmetric, arc minute scale structures around NGC 1275*, *A&A*, 356, 788
- Churazov E., Gilfanov M., Forman W., & Jones C. 1999. *Evidence for Merging in the Centaurus Cluster*, *ApJ*, 520, 105
- Colafrancesco S. 1999, in Diffuse Thermal and Relativistic Plasma in Galaxy Clusters, 269
- Conselice C. J., Gallagher J. S., & Wyse R. F. G. 2001. *On the Nature of the NGC 1275 System*, *AJ*, astro-ph/0108019
- Cowie L. L. & Binney J. 1977. *Radiative regulation of gas flow within clusters of galaxies - A model for cluster X-ray sources*, *ApJ*, 215, 723
- Cowie L. L., Hu E. M., Jenkins E. B., & York D. G. 1983. *Two-dimensional spectrophotometry of the cores of X-ray luminous clusters*, *ApJ*, 272, 29
- Crawford C. S., Allen S. W., Ebeling H., Edge A. C., & Fabian A. C. 1999. *The ROSAT Brightest Cluster Sample - III. Optical spectra of the central cluster galaxies*, *MNRAS*, 306, 857
- Crawford C. S., Edge A. C., Fabian A. C., Allen S. W., Böhringer H., Ebeling H., McMahon R. G., & Voges W. 1995. *Optical spectroscopy of the ROSAT X-ray brightest clusters - II*, *MNRAS*, 274, 75
- David L. P., Jones C., & Forman W. 1995. *Cosmological implications of ROSAT observations of groups and clusters of galaxies*, *ApJ*, 445, 578
- David L. P., Jones C., Forman W., & Daines S. 1994. *Mapping the dark matter in the NGC 5044 group with ROSAT: Evidence for a nearly homogeneous cooling flow with a cooling wake*, *ApJ*, 428, 544
- De Grandi S. & Molendi S. 2001. *Metallicity Gradients in X-Ray Clusters of Galaxies*, *ApJ*, 551, 153

- de Jong T., Nørgaard-Nielsen H. U., Jørgensen H. E., & Hansen L. 1990. *IRAS observations of NGC 4696 - Cooling or evaporation flow?*, A&A, 232, 317
- De Young D. S., Roberts M. S., & Saslaw W. C. 1973. *Detection of 21-cm Hydrogen Absorption in the High-Velocity Component of the Radio Galaxy Perseus A*, ApJ, 185, 809
- den Herder J. W., Brinkman A. C., Kahn S. M., Branduardi-Raymont G., Thomsen K., Aarts H., Audard M., Bixler J. V., den Boggende A. J., Cottam J., Decker T., Dubbeldam L., Erd C., Goulooze H., Güdel M., Guttridge P., Hailey C. J., Janabi K. A., Kaastra J. S., de Korte P. A. J., van Leeuwen B. J., Mauche C., McCalden A. J., Mewe R., Naber A., Paerels F. B., Peterson J. R., Rasmussen A. P., Rees K., Sakelliou I., Sako M., Spodek J., Stern M., Tamura T., Tandy J., de Vries C. P., Welch S., & Zehnder A. 2001. *The Reflection Grating Spectrometer on board XMM-Newton*, A&A, 365, L7
- Dickens R. J., Currie M. J., & Lucey J. R. 1986. *The Centaurus cluster of galaxies. I - The data*, MNRAS, 220, 679
- Dickey J. M. & Lockman F. J. 1990. *H I in the Galaxy*, ARA&A, 28, 215
- Dreher J. W., Carilli C. L., & Perley R. A. 1987. *The Faraday rotation of Cygnus A - Magnetic fields in cluster gas*, ApJ, 316, 611
- Dressler A. 1984. *The Evolution of Galaxies in Clusters*, ARA&A, 22, 185
- Dupke R. A. & Arnaud K. A. 2001. *Central Elemental Abundance Ratios in the Perseus Cluster: Resonant Scattering or SN IA Enrichment?*, ApJ, 548, 141
- Dupke R. A. & White R. E. 2000. *Metallicity Gradients in the Intracluster Gas of Abell 496*, ApJ, 537, 123
- Ebeling H., White D. A., & Rangarajan F. V. N. 2002. *ASMOOTH: A simple and efficient algorithm for adaptive kernel smoothing of two-dimensional imaging data*, submitted to MNRAS
- Edge A. C. 2001. *The detection of molecular gas in the central galaxies of cooling-flow clusters*, MNRAS, in press, astro-ph/0106225
- Edge A. C., Ivison R. J., Smail I., Blain A. W., & Kneib J.-P. 1999. *The detection of dust in the central galaxies of distant cooling-flow clusters*, MNRAS, 306, 599
- Edge A. C. & Stewart G. C. 1991. *EXOSAT observations of clusters of galaxies. I - The X-ray data. II - X-ray to optical correlations*, MNRAS, 252, 414
- Edge A. C., Stewart G. C., & Fabian A. C. 1992. *Properties of cooling flows in a flux-limited sample of clusters of galaxies*, MNRAS, 258, 177

- Edge A. C., Stewart G. C., Fabian A. C., & Arnaud K. A. 1990. *An X-Ray Flux-Limited Sample of Clusters of Galaxies - Evidence for Evolution of the Luminosity Function*, MNRAS, 245, 559
- Ettori S. & Fabian A. C. 1999. *ROSAT PSPC observations of 36 high-luminosity clusters of galaxies: constraints on the gas fraction*, MNRAS, 305, 834
- . 2000. *Chandra constraints on the thermal conduction in the intracluster plasma of A2142*, MNRAS, 317, L57
- Ezawa H., Fukazawa Y., Makishima K., Ohashi T., Takahara F., Xu H., & Yamasaki N. Y. 1997. *Discovery of a Large-Scale Abundance Gradient in the Cluster of Galaxies AWM 7 with ASCA*, ApJ, 490, L33
- Fabian A. C. 1994. *Cooling Flows in Clusters of Galaxies*, ARA&A, 32, 277
- Fabian A. C., Arnaud K. A., Bautz M. W., & Tawara Y. 1994. *ASCA observations of cooling flows in clusters of galaxies*, ApJ, 436, L63
- Fabian A. C. & Barcons X. 1992. *The origin of the X-ray background*, ARA&A, 30, 429
- Fabian A. C., Crawford C. S., Ettori S., & Sanders J. S. 2001a. *Chandra detection of the intracluster medium around 3C 294 at z=1.786*, MNRAS, 322, L11
- Fabian A. C. & Daines S. J. 1991. *The X-ray subcluster in A2256 - Cluster mergers, cooling flows and diffuse radio sources*, MNRAS, 252, 17P
- Fabian A. C., Hu E. M., Cowie L. L., & Grindlay J. 1981a. *The distribution and morphology of X-ray-emitting gas in the core of the Perseus cluster*, ApJ, 248, 47
- Fabian A. C., Mushotzky R. F., Nulsen P. E. J., & Peterson J. R. 2001b. *On the soft X-ray spectrum of cooling flows*, MNRAS, 321, L20
- Fabian A. C. & Nulsen P. E. J. 1977. *Subsonic accretion of cooling gas in clusters of galaxies*, MNRAS, 180, 479
- Fabian A. C., Nulsen P. E. J., & Canizares C. R. 1982. *Star formation in a cooling flow*, MNRAS, 201, 933
- . 1984. *Cooling flows in clusters of galaxies*, Nature, 310, 733
- Fabian A. C., Nulsen P. E. J., Stewart G. C., Ku W. H.-M., Malin D. F., & Mushotzky R. F. 1981b. *The discovery of optical filaments surrounding the central galaxy in A496 - Evidence for a cooling flow*, MNRAS, 196, 35P
- Fabian A. C., Sanders J. S., Ettori S., Taylor G. B., Allen S. W., Crawford C. S., Iwasawa K., & Johnstone R. M. 2001c. *Chandra imaging of the X-ray core of Abell 1795*, MNRAS, 321, L33

- Fabian A. C., Sanders J. S., Ettori S., Taylor G. B., Allen S. W., Crawford C. S., Iwasawa K., Johnstone R. M., & Ogle P. M. 2000. *Chandra imaging of the complex X-ray core of the Perseus cluster*, MNRAS, 318, L65
- Falcke H., Rieke M. J., Rieke G. H., Simpson C., & Wilson A. S. 1998. *Molecular Hydrogen and PA- α Emission in Cooling Flow Galaxies*, ApJ, 494, L155
- Ford H. C. & Butcher H. 1979. *The system of filaments in M87 - Evidence for matter falling into an active nucleus*, ApJS, 41, 147
- Forman W. & Jones C. 1982. *X-ray-imaging observations of clusters of galaxies*, ARA&A, 20, 547
- Forman W., Kellogg E., Gursky H., Tananbaum H., & Giacconi R. 1972. *Observations of the Extended X-Ray Sources in the Perseus and Coma Clusters from UHURU*, ApJ, 178, 309
- Forman W., Schwarz J., Jones C., Liller W., & Fabian A. C. 1979. *X-ray observations of galaxies in the Virgo cluster*, ApJ, 234, L27
- Fritz G., Davidsen A., Meekins J. F., & Friedman H. 1971. *Discovery of an X-Ray Source in Perseus*, ApJ, 164, L81
- Fukazawa Y., Ohashi T., Fabian A. C., Canizares C. R., Ikebe Y., Makishima K., Mushotzky R. F., & Yamashita K. 1994. *Metal concentration and X-ray cool spectral component in the central region of the Centaurus cluster of galaxies*, PASJ, 46, L55
- Furusho T., Yamasaki N. Y., Ohashi T. S. R., Kagei T., Ishisaki Y., Kikuchi K., Ezawa H., & Ikebe Y. 2001. *ASCA Temperature Maps of Three Clusters of Galaxies: Abell 1060, AWM 7, and the Centaurus Cluster*, PASJ, 53, 421
- Ge J. P. & Owen F. N. 1993. *Faraday rotation in cooling flow clusters of galaxies. I - Radio and X-ray observations of Abell 1795*, AJ, 105, 778
- Govoni F., Enßlin T. A., Feretti L., & Giovannini G. 2001. *A comparison of radio and X-ray morphologies of four clusters of galaxies containing radio halos*, A&A, 369, 441
- Grabelsky D. A. & Ulmer M. P. 1990. *Search for cold gas in clusters with and without cooling flows*, ApJ, 355, 401
- Grossmann A. & Morlet J. 1984. *Decomposition of Hardy functions in square integrable wavelets of constant shape*, J. Math. Anal., 15, 723
- Gursky H., Kellogg E. M., Leong C., Tananbaum H., & Giacconi R. 1971. *Detection of X-Rays from the Seyfert Galaxies NGC 1275 and NGC 4151 by the UHURU Satellite*, ApJ, 165, L43

- Hasinger G., Altieri B., Arnaud M., Barcons X., Bergeron J., Brunner H., Dadina M., Dennerl K., Ferrando P., Finoguenov A., Griffiths R. E., Hashimoto Y., Jansen F. A., Lumb D. H., Mason K. O., Mateos S., McMahon R. G., Miyaji T., Paerels F., Page M. J., Ptak A. F., Sasseen T. P., Schartel N., Szokoly G. P., Trümper J., Turner M., Warwick R. S., & Watson M. G. 2001. *XMM-Newton observation of the Lockman Hole. I. The X-ray data*, A&A, 365, L45
- Heckman T. M. 1981. *Optical emission-line gas associated with dominant cluster galaxies*, ApJ, 250, L59
- Heckman T. M., Baum S. A., van Breugel W. J. M., & McCarthy P. 1989. *Dynamical, physical, and chemical properties of emission-line nebulae in cooling flows*, ApJ, 338, 48
- Heinz S., Reynolds C. S., & Begelman M. C. 1998. *X-Ray Signatures of Evolving Radio Galaxies*, ApJ, 501, 126
- Hill J. M., Hintzen P., Oegerle W. R., Romanishin W., Lesser M. P., Eisenhamer J. D., & Batuski D. J. 1988. *Peculiar velocities of cD galaxies - MX spectroscopy of Abell 1795*, ApJ, 332, L23
- Hill J. M. & Oegerle W. R. 1993. *Dynamics of cD clusters of galaxies. I - Redshift data for seven clusters*, AJ, 106, 831
- Holtzman J. A., Watson A. M., Mould J. R., Gallagher J. S., Ballester G. E., Burrows C. J., Clarke J. T., Crisp D., Evans R. W., Griffiths R. E., Hester J. J., Hoessel J. G., Scowen P. A., Stapelfeldt K. R., Trauger J. T., & Westphal J. A. 1996. *Star Clusters in Interacting and Cooling Flow Galaxies*, AJ, 112, 416
- Hu E. M., Cowie L. L., & Wang Z. 1985. *Long-slit spectroscopy of gas in the cores of X-ray luminous clusters*, ApJS, 59, 447
- Huang Z. & Sarazin C. L. 1996. *A High-Resolution ROSAT X-Ray Study of the Hercules Cluster*, ApJ, 461, 622
- Ikebe Y., Makishima K., Fukazawa Y., Tamura T., Xu H., Ohashi T., & Matsushita K. 1999. *Two-Phase Intracluster Medium in the Centaurus Cluster of Galaxies*, ApJ, 525, 58
- Johnstone R. M. & Fabian A. C. 1988. *Extended emission-line gas in NGC 1275 and the central galaxy in A1795 - Evidence for a distributed rather than a central source of ionization*, MNRAS, 233, 581
- Johnstone R. M., Fabian A. C., Edge A. C., & Thomas P. A. 1992. *The spectral signature of the cooling flow in Abell 478*, MNRAS, 255, 431
- Johnstone R. M., Fabian A. C., & Nulsen P. E. J. 1987. *The optical spectra of central galaxies in southern clusters Evidence for star formation*, MNRAS, 224, 75

- Jones C., Mandel E., Schwarz J., Forman W., Murray S. S., & Harnden F. R. 1979. *The structure and evolution of X-ray clusters*, ApJ, 234, L21
- Kaastra J. S. & Mewe R. 1993. *Legacy*, 3, Tech. rep., HEASARC, NASA
- Kent S. M. & Sargent W. L. W. 1979. *Ionization and excitation mechanisms in the filaments around NGC 1275*, ApJ, 230, 667
- King I. 1962. *Density Law in Spherical Stellar Systems.*, AJ, 67, 274
- Liedahl D. A., Osterheld A. L., & Goldstein W. H. 1995. *New calculations of Fe L-shell X-ray spectra in high-temperature plasmas*, ApJ, 438, L115
- Lucey J. R., Currie M. J., & Dickens R. J. 1986. *The Centaurus cluster of galaxies. II - The bimodal velocity structure*, MNRAS, 221, 453
- Markevitch M. 2001, <http://hea-www.harvard.edu/~maxim/axaf/acisbg/>
- Markevitch M., Ponman T. J., Nulsen P. E. J., Bautz M. W., Burke D. J., David L. P., Davis D., Donnelly R. H., Forman W. R., Jones C., Kaastra J., Kellogg E., Kim D.-W., Kolodziejczak J., Mazzotta P., Pagliaro A., Patel S., & Van Speybroeck L. 2000. *Chandra Observation of Abell 2142: Survival of Dense Subcluster Cores in a Merger*, ApJ, 541, 542
- Markevitch M., Vikhlinin A., & Mazzotta P. 2001. *Non-hydrostatic gas in the core of the relaxed galaxy cluster A1795*, ApJ, astro-ph/0108520
- Mathews W. G. & Bregman J. N. 1978. *Radiative accretion flow onto giant galaxies in clusters*, ApJ, 224, 308
- Matsumoto H., Koyama K., Awaki H., Tomida H., Tsuru T., Mushotzky R., & Hatsukade I. 1996. *Discovery of an Abundance Gradient in the Central Region of the Virgo Cluster*, PASJ, 48, 201
- Matthews T. A., Morgan W. W., & Schmidt M. 1964. *A Discussion of Galaxies Identified with Radio Sources.*, ApJ, 140, 35
- Mazzotta P., Markevitch M., Forman W. R., Jones C., Vikhlinin A., & van Speybroeck L. 2001a. *Chandra Observation of MS 1455.0+2232: cold fronts in a massive cooling flow cluster?*, ApJ, astro-ph/0108476
- Mazzotta P., Markevitch M., Vikhlinin A., Forman W. R., David L. P., & VanSpeybroeck L. 2001b. *Chandra Observation of RX J1720.1+2638: a Nearly Relaxed Cluster with a Fast-moving Core?*, ApJ, 555, 205
- McNamara B. R., Jannuzi B. T., Elston R., Sarazin C. L., & Wise M. 1996a. *U-Band Polarimetry of the Radio-aligned Optical Continuum in the Abell 1795 Cluster Central Galaxy*, ApJ, 469, 66

- McNamara B. R. & O'Connell R. W. 1993. *Blue lobe galaxies in the cooling flow clusters Abell 1795 and Abell 2597*, AJ, 105, 417
- McNamara B. R., Wise M., Nulsen P. E. J., David L. P., Sarazin C. L., Bautz M., Markevitch M., Vikhlinin A., Forman W. R., Jones C., & Harris D. E. 2000. *Chandra X-Ray Observations of the Hydra A Cluster: An Interaction between the Radio Source and the X-Ray-emitting Gas*, ApJ, 534, L135
- McNamara B. R., Wise M., Sarazin C. L., Jannuzi B. T., & Elston R. 1996b. *Optical Structure in the Abell 1795 Cluster Central Galaxy: Evidence for Stripping and Deflection of Radio Jets*, ApJ, 466, L9
- Mellier Y. 1999. *Probing the Universe with Weak Lensing*, ARA&A, 37, 127
- Mewe R., Gronenschild E. H. B. M., & van den Oord G. H. J. 1985. *Calculated X-radiation from optically thin plasmas. V*, A&AS, 62, 197
- Mewe R., Lemen J. R., & van den Oord G. H. J. 1986. *Calculated X-radiation from optically thin plasmas. VI - Improved calculations for continuum emission and approximation formulae for nonrelativistic average Gaunt factors*, A&AS, 65, 511
- Minkowski R. 1957, in IAU Symp. 4: Radio astronomy, Vol. 4, 107
- Mitchell R. J., Culhane J. L., Davison P. J. N., & Ives J. C. 1976. *Ariel 5 observations of the X-ray spectrum of the Perseus Cluster*, MNRAS, 175, 29P
- Mittaz J. P. D., Kaastra J. S., Tamura T., Fabian A. C., Mushotzky R. F., Peterson J. R., Ikebe Y., Lumb D. H., Paerels F., Stewart G., & Trudolyubov S. 2001. *UV observations of the galaxy cluster Abell 1795 with the optical monitor on XMM-Newton*, A&A, 365, L93
- Mittaz J. P. D., Lieu R., & Lockman F. J. 1998. *Detection of Luminous Intracluster Extreme-Ultraviolet Emission From Abell 1795*, ApJ, 498, L17
- Molendi S. & Gastaldello F. 2001. *On the metal abundance in the core of M 87*, A&A, 375, L14
- Mushotzky R., Loewenstein M., Arnaud K. A., Tamura T., Fukazawa Y., Matsushita K., Kikuchi K., & Hatsukade I. 1996. *Measurement of the Elemental Abundances in Four Rich Clusters of Galaxies. I. Observations*, ApJ, 466, 686
- Mushotzky R. F., Cowie L. L., Barger A. J., & Arnaud K. A. 2000. *Resolving the extragalactic hard X-ray background*, Nature, 404, 459
- Mushotzky R. F. & Loewenstein M. 1997. *Lack of Evolution in the Iron Abundance in Clusters of Galaxies and Implications for the Global Star Formation Rate at High Redshift*, ApJ, 481, L63

- Navarro J. F., Frenk C. S., & White S. D. M. 1995. *Simulations of X-ray clusters*, MNRAS, 275, 720
- Nulsen P. E. J. 1986. *Thermal instability in cooling flows*, MNRAS, 221, 377
- Oegerle W. R., Cowie L., Davidsen A., Hu E., Hutchings J., Murphy E., Sembach K., & Woodgate B. 2001. *FUSE Observations of Cooling-Flow Gas in the Galaxy Clusters A1795 and A2597*, ApJ, 560, 187
- Oegerle W. R. & Hill J. M. 1994. *Dynamics of cD clusters of galaxies. II: Analysis of seven Abell clusters*, AJ, 107, 857
- Owen F., Eilek J., & Kassim N. 1999, in Diffuse Thermal and Relativistic Plasma in Galaxy Clusters, 107
- Pedlar A., Ghataure H. S., Davies R. D., Harrison B. A., Perley R., Crane P. C., & Unger S. W. 1990. *The Radio Structure of NGC1275*, MNRAS, 246, 477
- Peres C. B., Fabian A. C., Edge A. C., Allen S. W., Johnstone R. M., & White D. A. 1998. *A ROSAT study of the cores of clusters of galaxies - I. Cooling flows in an X-ray flux-limited sample*, MNRAS, 298, 416
- Peterson J. R., Paerels F. B. S., Kaastra J. S., Arnaud M., Reiprich T. H., Fabian A. C., Mushotzky R. F., Jernigan J. G., & Sakelliou I. 2001. *X-ray imaging-spectroscopy of Abell 1835*, A&A, 365, L104
- Pfeffermann E. & Briel U. 1983. *Development and performance of a position sensitive proportion counter for the ROSAT project*, Adv. Space Res., 2, 255
- Pinkney J., Holtzman J., Garasi C., Watson A. M., Gallagher J. S., Ballester G. E., Burrows C. J., Casertano S., Clarke J. T., Crisp D., Evans R. W., Griffiths R. E., Hester J. J., Hoessel J. G., Mould J. R., Scowen P. A., Stapelfeldt K. R., Trauger J. T., & Westphal J. A. 1996. *WFPC2 Observations of the Cooling Flow Elliptical in Abell 1795*, ApJ, 468, L13
- Pistinner S., Levinson A., & Eichler D. 1996. *Can Electromagnetic Instabilities Driven by Temperature Gradients Inhibit Thermal Conduction in Cluster Cooling Flows?*, ApJ, 467, 162
- Pistinner S. & Shaviv G. 1996. *Can Tangled Magnetic Fields Suppress Thermal Conduction in Cluster Cooling Flows?*, ApJ, 459, 147
- Plucinsky P. P., Snowden S. L., Briel U. G., Hasinger G., & Pfeffermann E. 1993. *An Updated Calibration of the ROSAT PSPC Particle Background for the Analysis of Diffuse and Extended Sources*, ApJ, 418, 519

- Press H. P., Flannery B. P., Teukolsky S. A., & Vetterling W. T. 1989, Numerical Recipes: The art of scientific computing (CUP)
- Raymond J. C. & Smith B. W. 1977. *Soft X-ray spectrum of a hot plasma*, ApJS, 35, 419
- Reisenegger A., Miralda-Escudé J., & Waxman E. 1996. *Cooling Flows and Metallicity Gradients in Clusters of Galaxies*, ApJ, 457, L11
- Rubin V. C., Oort J. H., Ford W. K., & Peterson C. J. 1977. *New observations of the NGC 1275 phenomenon*, ApJ, 211, 693
- Rugge H. R. & McKenzie D. L. 1985. *X-ray line ratios for Fe-XVII observed in the solar corona*, ApJ, 297, 338
- Sabra B. M., Shields J. C., & Filippenko A. V. 2000. *Emission-Line Properties of the Optical Filaments of NGC 1275*, ApJ, 545, 157
- Sakelliou I., Merrifield M. R., & McHardy I. M. 1996. *What bent the jets in 4C 34.16?*, MNRAS, 283, 673
- Sanders J. S. & Fabian A. C. 2001. *Adaptive binning of X-ray galaxy cluster images*, MNRAS, 325, 178
- . 2002. *Spatially-resolved X-ray spectroscopy of the core of the Centaurus cluster*, MNRAS, in press, astro-ph/0109336
- Sanders J. S., Fabian A. C., & Allen S. W. 2000. *X-ray colour maps of the cores of galaxy clusters*, MNRAS, 318, 733
- Sarazin C. L. 1998, X-ray emissions from clusters of galaxies (Cambridge University Press)
- Schwarz R. A., Edge A. C., Voges W., Boehringer H., Ebeling H., & Briel U. G. 1992. *The structure of the intracluster medium of the Perseus cluster*, A&A, 256, L11
- Shobbrook R. R. 1963. *A note on a radio source identification in Centaurus*, The Observatory, 83, 36
- Slezak E., Durret F., & Gerbal D. 1994. *A wavelet analysis search for substructures in eleven X-ray clusters of galaxies*, AJ, 108, 1996
- Smith E. P., Bohlin R. C., Bothun G. D., O'Connell R. W., Roberts M. S., Neff S. G., Smith A. M., & Stecher T. P. 1997. *Ultraviolet Imaging Observations of the cD Galaxy in Abell 1795: Further Evidence for Massive Star Formation in a Cooling Flow*, ApJ, 478, 516
- Snowden S. L. & Kuntz K. D. 1998. *Cookbook for ROSAT observations of extended objects*, <ftp://legacy.gsfc.nasa.gov/rosat/software/fortran/sxrb/esas.ps.gz>

- Snowden S. L., McCammon D., Burrows D. N., & Mendenhall J. A. 1994. *Analysis procedures for ROSAT XRT/PSPC observations of extended objects and the diffuse background*, ApJ, 424, 714
- Sparks W. B., Jedrzejewski R. I., & Macchetto F. 1993, in AIP Conf. Proc., Vol. 313, The Soft X-ray Cosmos, ed. E. M. Schlegal & R. Petre (AIP, Woodbury), 389
- Sparks W. B., Macchetto F., & Golombek D. 1989. *Imaging observations of gas and dust in NGC 4696 and implications for cooling flow models*, ApJ, 345, 153
- Spitzer L. 1956, Physics of Fully Ionized Gases (Physics of Fully Ionized Gases, New York: Interscience Publishers, 1956)
- Starck J. & Pierre M. 1998. *Structure detection in low intensity X-ray images*, A&AS, 128, 397
- Stewart G. C., Fabian A. C., Jones C., & Forman W. 1984a. *The prevalence of cooling flows in clusters of galaxies*, ApJ, 285, 1
- Stewart G. C., Fabian A. C., Nulsen P. E. J., & Canizares C. R. 1984b. *The mass profile and gas content of M87*, ApJ, 278, 536
- Takeda H., Nulsen P. E. J., & Fabian A. C. 1984. *Ram pressure stripping in a changing environment*, MNRAS, 208, 261
- Tamura T., Day C. S., Fukazawa Y., Hatsukade I., Ikebe Y., Makishima K., Mushotzky R. F., Ohashi T., Takenaka K., & Yamashita K. 1996. *Uniformity in the Temperature and Metallicity of the X-Ray Emitting Gas in the Abell 1060 Cluster of Galaxies*, PASJ, 48, 671
- Tamura T., Kaastra J. S., Peterson J. R., Paerels F. B. S., Mittaz J. P. D., Trudolyubov S. P., Stewart G., Fabian A. C., Mushotzky R. F., Lumb D. H., & Ikebe Y. 2001. *X-ray spectroscopy of the cluster of galaxies Abell 1795 with XMM-Newton*, A&A, 365, L87
- Taylor G. B., Allen S. W., & Fabian A. C. 1999, in Diffuse Thermal and Relativistic Plasma in Galaxy Clusters, 77
- Taylor G. B., Barton E. J., & Ge J. 1994. *Searching for cluster magnetic fields in the cooling flows of 0745-191, A2029, and A4059*, AJ, 107, 1942
- Taylor G. B., Fabian A. C., & Allen S. W. 2002. *Magnetic fields in the Centaurus cluster*, submitted to MNRAS, astro-ph/0109337
- Thomas P. A., Fabian A. C., & Nulsen P. E. J. 1987. *Mass deposition in cooling flows - Analysis of the X-ray data*, MNRAS, 228, 973
- Trimble V. 1987. *Existence and nature of dark matter in the universe*, ARA&A, 25, 425

- Trümper J. 1983. *The ROSAT mission*, Adv. Space Res., 2, 241
- Unger S. W., Taylor K., Pedlar A., Ghataure H. S., Penston M. V., & Robinson A. 1990. *The nature of the high-velocity gas in NGC 1275 - First results with TAURUS-2 on the William Herschel telescope*, MNRAS, 242, 33P
- van Breugel W., Heckman T., & Miley G. 1984. *Optical line emission associated with the radio galaxy 4C 26.42 in the cluster of galaxies Abell 1795*, ApJ, 276, 79
- van Speybroeck L. P., Jerius D., Edgar R. J., Gaetz T. J., Zhao P., & Reid P. B. 1997. *Performance expectation versus reality*, Proc. SPIE, 3113, 89
- Vikhlinin A., Markevitch M., Forman W., & Jones C. 2001a. *Zooming in on the Coma Cluster with Chandra: Compressed Warm Gas in the Brightest Cluster Galaxies*, ApJ, 555, L87
- Vikhlinin A., Markevitch M., & Murray S. S. 2001b. *Chandra Estimate of the Magnetic Field Strength near the Cold Front in A3667*, ApJ, 549, L47
- Voges et al. W. 1996, MPE Report, 263, 637
- Weisskopf M. C., Tananbaum H. D., Van Speybroeck L. P., & O'Dell S. 2000, in X-Ray Optics, Instruments, and Missions, ed. J. Trümper & B. Aschenbach, Proc. SPIE No. 4012, astro-ph/000412
- White D. A. 2000. *Deconvolution of ASCA X-ray data - II. Radial temperature and metallicity profiles for 106 galaxy clusters*, MNRAS, 312, 663
- White D. A. & Fabian A. C. 1995. *Einstein Observatory evidence for the widespread baryon overdensity in clusters of galaxies*, MNRAS, 273, 72
- White D. A., Fabian A. C., Forman W., Jones C., & Stern C. 1991a. *Ram-pressure stripping of the multiphase interstellar medium of the Virgo cluster elliptical galaxy M86 (NGC 4406)*, ApJ, 375, 35
- White D. A., Fabian A. C., Johnstone R. M., Mushotzky R. F., & Arnaud K. A. 1991b. *The discovery of large amounts of cold, X-ray absorbing matter in cooling flows*, MNRAS, 252, 72
- Wilman R. J., Edge A. C., Johnstone R. M., Crawford C. S., & Fabian A. C. 2000. *Molecular hydrogen emission in Cygnus A*, MNRAS, 318, 1232
- Xu H., Makishima K., Fukazawa Y., Ikebe Y., Kikuchi K., Ohashi T., & Tamura T. 1998. *Discovery of the Central Excess Brightness in Hard X-Rays in the Cluster of Galaxies Abell 1795*, ApJ, 500, 738
- Zwicky F. 1933, Helv. Phys. Acta, 6, 110

Zwicky F., Herzog E., Wild P., Karpowicz M., & Kowal C. T. 1961, in California Inst. Techn. (1961)